UNIVERSITY OF SOUTHAMPTON

Faculty of Engineering, Science and Mathematics

Optoelectronics Research Centre

Novel All-Optical Switching and Processing Techniques for Optical Networking

A thesis submitted for the degree of Doctor of Philosophy

by

Paulo Jorge dos Santos Almeida

December 2006

UNIVERSITY OF SOUTHAMPTON

ABSTRACT

FACULTY OF ENGINEERING, SCIENCE AND MATHEMATICS
SCHOOL OF ELECTRONICS AND COMPUTER SCIENCE

Doctor of Philosophy

Novel All-Optical Switching and Processing Techniques for Optical Networking

by Paulo Jorge dos Santos Almeida

In this thesis, the possibility of processing optical time-division multiplexing (OTDM) signals in both the temporal and spectral domains is investigated. The technique relies on the conversion of high-speed OTDM signals into a mixed time and wavelength division multiplexing (TDM-WDM) format. Depending on the specific network function, it may be advantageous to process the signal in one rather than the other domain. For example, channel add/drop multiplexing can be performed directly by passive filtering in the spectral domain.

The OTDM to mixed TDM-WDM conversion is achieved by the nonlinear switching of linearly-chirped pulses with a rectangular-like temporal envelope, and a wide spectral-bandwidth with flat spectral-density. Two main approaches were investigated for the generation of these pulses. One was based on the re-shaping of the spectrum of short optical pulses broadened via self-phase modulation in a highly nonlinear fibre using a broadband filter. Another was based on the pre-shaping of the seed pulse injected into the highly nonlinear fibre to ensure that this evolves nonlinearly into the desired linearly-chirped pulse form.

An investigation into the switching of the linearly-chirped pulses in a nonlinear optical loop mirror (NOLM) revealed that the product of the control-pulse duration and the chirp-rate of the linearly-chirped pulse should be above a minimum value to ensure a one-to-one relation between the temporal and spectral waveforms after the switching. Below this minimum value, severe spectral distortion of the mixed TDM-WDM signal was observed. The physics behind this distortion is unveiled and shown to be related to the interference between the spectral content in the switched pulse and the unavoidable residual components of the linearly-chirped pulse transmitted through the NOLM switch. These effects were identified in experiments which aimed at compressing/expanding waveforms at 40 Gb/s by control of the group delay of the converted TDM-WDM signal in a dispersive medium.

Apart from the packet compression/expansion experiments, demultiplexing and channel add/drop multiplexing of 40-Gb/s OTDM signals were also experimentally demonstrated. The technological challenges of implementing this technique at higher repetition rates are discussed.

Contents

List of Figures

List of Tables

Principal Abbreviations

ASE amplified spontaneous emission

BER bit-error rate

CW continuous wave

DCF dispersion compensating fibre

DFF dispersion-flattened fibre

DSF dispersion-shifted fibre

EAM electro-absorption modulator

EDFA erbium-doped fibre amplifier

EFRL erbium-fibre ring laser

FBG fibre Bragg grating

FROG frequency-resolved optical gating

FWHM full-width at half-maximum

FWM four-wave mixing

GVD group-velocity dispersion

HNLF highly-nonlinear fibre

MUX Multiplexer

NOLM nonlinear optical-loop mirror

NLSE nonlinear Schrödinger equation

OSA optical spectrum analyser

OTDM optical time-division multiplexing

PMD polarisation mode dispersion

PRBS pseudo-random binary sequence

RB resolution bandwidth

RZ return-to-zero

SHG second-harmonic generation

SPM self-phase modulation

SSFBG superstructured fibre Bragg grating

SSMF standard single mode fibre

TDM time-division multiplexing

WDM wavelength-division multiplexing

XPM cross-phase modulation

Declaration of Authorship

I, Paulo Jorge dos Santos Almeida, declare that the thesis entitled:
Novel All-Optical Switching and Processing Techniques for Optical Networking
and the work presented in the thesis are both my own, and have been generated by me as the result of my own original research. I confirm that:

- this work was done wholly or mainly while in candidature for a research degree at this University;
- where any part of this thesis has previously been submitted for a degree or any other qualification at this University or any other institution, this has been clearly stated;
- where I have consulted the published work of others, this is always clearly attributed;
- where I have quoted from the work of others, the source is always given. With the exception of such quotations, this thesis is entirely my own work;
- I have acknowledged all main sources of help;
- where the thesis is based on work done by myself jointly with others, I have made clear exactly what was done by others and what I have contributed myself;
- parts of this work have been published (See *List of Publications*).

Paulo Almeida

December 2006

Acknowledgements

This thesis book is the outcome of the great effort of many people and, therefore, many people I wish to thank. I hope they feel, as I feel, the joy of another long and hard journey completed when browsing throughout these pages.

I first want to thank Professor David Richardson for welcoming me into his group and for his supervision throughout my PhD studies. I learned a great deal from him about research skills. In many occasions, he has impressed me much with his sharp analysis of my research results. Dave always had time to listen and advise me either as supervisor or as a friend. I have great respect and admiration for him.

I have no less admiration for Dr. Periklis Petropoulos, who together with Prof. David Richardson supervised my PhD studies. I am immensely grateful to Periklis for his constant encouragement and guidance. He has many times shown me the way through the difficulties of my research work.

I want to thank my colleagues, friends, from optical communications group: Dr. Anoma McCoy, for her understanding and solace when I insisted in testing the limits of operation of devices in her setup, some of which eventually end-up being limited in their operation (oops-a-daisy); Dr. Michaël Roelens, his studies of high-speed systems and pulse characterisation intersected with many aspects of my work, also for the amazing experience of paragliding in the Isle of Wight; Dr. Benn Thomsen, for teaching me his outstanding laboratory skills; Dr. Ju Han Lee, from whom I learned a lot about nonlinear fibre switching; Chun Tian, for his very complete photo album of our trip around Scotland after ECOC 2005; Symeon Asimakis, for making me believe that I was working on something important. Last, because she contributed most to my thesis work, Francesca Parmigiani. Her patience and ability to verify the details

of my mathematical work were outstanding. She was also involved in much of the experimental work in this thesis.

I would like to thank Dr. Morten Ibsen for producing the fibre-Bragg-gratings used in this work, and for teaching me about fibre-Bragg-grating technology, and for much more support. I also would like to thank Dr. Ridzuan Mokhtar for producing a tunable mounting for the gratings used in the add/drop experiments. I am also grateful for the brief collaboration with Dr. Jerry Prawiharjo and Dr. Katia Gallo in their experiments using $\chi^{(2)}$ nonlinear effects in $LiNbO_3$.

I would like to thank Dr. Eleanor Tarbox for her careful proofreading of my papers and thesis's manuscripts. Mrs. Eveline Smith has made all the process of administrative documentation 'easy-peasy', thank you Eve. I would like to thank Simon Butler, Chris Nash, and Timothy McIntyre for their help with various electrical and mechanical issues concerning my thesis experimental work, and for not laughing at me when I could not find the correct English words and depicted the situation with weird sounds and gestures. My thanks go also to Dave Oliver and Kevin Sumner for their computer support.

I would like to thank all my friends in Southampton; their friendship surely helped me to get through difficult moments. Although being far away from home, because of you, I have never felt homesick during the last four years.

Last, but always first in my heart, I am deeply grateful to my parents (Rosinha e Luis) and Francesca for their constant support and unconditional love, even when they cannot understand my choices. Thank you Francesca for coping with me during the thesis's writing.

Finally, I would like to acknowledge the financial support from Fundação para a Ciência e Tecnologia through the PhD grant SFRH/6994/2001.

To my parents

"I shall be telling this with a sigh, somewhere ages and ages hence:
Two roads diverged in a wood, and I – I took the one less traveled by.
And that has made all the difference"
— Robert Frost

Chapter 1

Introduction

Optical technology is invading the entire telecommunication network within the backbone and progressively reaches closer to the end user, even though it may take sometime to reach the home in the UK, since other technologies can provide enough bandwidth to support upcoming home services, such as video-on-demand (broadband connections up to 100 Mb/s can be implemented either using microwave-radio antennas or the telephone copper cable [7]). These are obviously preferred solutions by service providers since installation only requires setting up a box at the consumer end. It is a requirement, however, that fibre comes to the neighbourhood, since both copper and radio transmission, at the above connection speed, can only reach a few hundred metres. Fibre in the neighbourhood serves many broadband connections, and transfers data between home users and an ultra-high speed backbone optical network [8].

In this imminent scenario of optical fibre being used throughout the network infrastructure, routing and switching nodes capable of ultra-high-speed throughput and of adapting data format at the network interface are an essential technology. Flexible optical-signal-processing may be a solution to implement these ultrafast network-node functions [9]. However, this requires several functions to be performed in the optical domain such as packet buffering, packet wavelength conversion and routing, packet compression and expansion, address recognition, and packet clock extraction among others [10]. Basic network functions have already been demonstrated at speeds well beyond the electronic-speed limit by using several optical switching technologies. In

particular, fibre and semiconductor technologies have shown the capability of switching at bit-rates close to one terabit per second [11, 12].

However, due to the different nature of photons and electrons, it is very unlikely that optics can mimic electronics. Currently, it seems practically impossible that an all-optical processor can achieve the functional complexity of an electronic processor. This is mainly because an all-optical transistor, i.e. a diode which emits light when controlled by light, has never been invented, even though electronic transistors have recently been made to emit light [13]. Complex signal-processing functions may thus be challenging to implement in the optical domain, as unrealistic lattices of optical switches, delay lines, and optical amplifiers may be required.

Ultrafast network routers will therefore have to adapt to the limited functionality of the available optical-signal-processing blocks. Nonetheless, agile manipulation of optical signals in the time, frequency and space domains has been widely demonstrated and much of the utilised technology has matured. A possible approach to achieve more complex and flexible optical-signal-processing is then to combine together techniques from the different domains.

1.1 Optical-Signal-Processing of Time-Wavelength Multiplexed Signals

My PhD research project began with an investigation of the insufficiently explored idea that a high-speed signal, converted into a mixed time and wavelength multiplexing format, allows the implementation of networking functions by manipulating the signal in both the temporal and spectral domains. The motivation of this approach is that some functions can be easier to implement in one of the domains, while others may be easier in the other domain. For example, functions such as channel demultiplexing and channel add/drop multiplexing can be performed directly by passive filtering and channel coupling in the spectral domain. By contrast, functions such as clock recovery require beating with a local oscillator in the temporal domain.

Hence, the ability to change between time multiplexed and wavelength multiplexed signals allows the selection of the most efficient and simplest processing techniques to

be used on the signal and allows for the construction of optical subsystems capable of relatively complex all-optical functions. Figure 1.1 shows the concept of multiplexing and converting between OTDM and mixed TDM-WDM signals. An OTDM signal is usually an aggregate of low bit-rate channels, which can be processed electronically, commonly referred to as tributary channels, into an ultrafast optical data stream, whose typical speed is beyond the electronic processing speed. The tributary channels are, in this case, aggregated through a bit-interleaving structure. An OTDM to WDM converter shifts the carrier wavelength of each tributary onto a different wavelength without affecting the temporal bit-interleaving. In this mixed TDM-WDM format the ultrafast signal can then be manipulated using both spectral filtering and temporal gating. The output signal, however, needs to be converted back to its original OTDM format. A WDM to OTDM converter is therefore used to shift the carrier wavelength of each tributary onto the same wavelength.

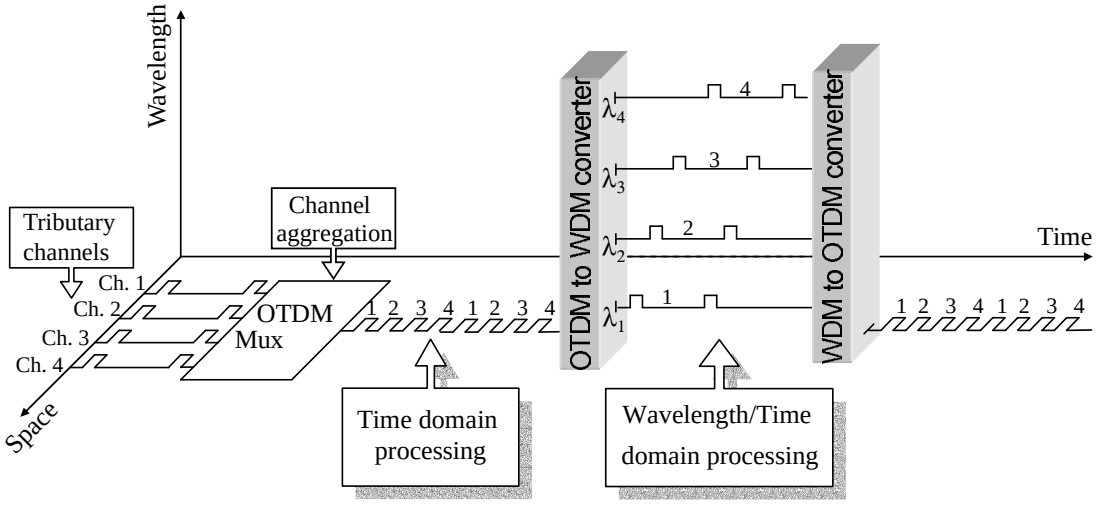

Figure 1.1: Representation of four tributary channels multiplexed in the time and wavelength domains for time/wavelength optical signal processing.

Table 1.1 shows various network functions and the critical components required for their implementation according to the signal multiplexing-format. For instance, demultiplexing of an OTDM signal is performed, in the time domain, with an ultrafast switch capable of operating at the signal bit-rate. Instead, in a mixed TDM-WDM signal, the same function can also be achieved with an optical filter which transmits the tributary channels into separate optical paths.

Compression or expansion of the aggregate-rate of an OTDM signal may be required at the interface between networks that operate at different line bit-rates [8]. For example: the interconnection of two ultra-high-speed backbone networks, one serving a metropolitan area, and the other connecting many metropolitan areas in the country. Direct aggregate-rate compression in the time domain would require complicated and generally impractical structures, such as a recirculating loop facilitating bit interleaving. When the ultrafast signal is converted into a TDM-WDM signal, on the other hand, the tributary channels can be delayed independently by propagating them in a dispersive element, which imposes a different group-delay onto each carrier wavelength. This could be, for instance, an optical fibre with superimposed fibre-Bragg-gratings, which are precisely spaced in the fibre, where each grating reflects off a different tributary-channel. Aggregate-rate compression can be achieved when the reflection delay between subsequent tributaries is negative, which implies that the tributaries are sequentially reflected earlier in the fibre. In the case that some dispersion can be tolerated by the individual channels, a dispersive element such as a chirped fibre-Bragg-grating or a dispersive fibre can be used to impart the differential group delay.

Another function that may be required in an all-optical network is the reordering of the tributary channels into the bit-slots. To reduce the cost of the network infrastructure, network nodes at the interface with the access network might not be reconfigurable, and might be designed to only add and drop from a specific bit-slot. It is thus required that at a higher-hierarchy node the tributary channels are

Table 1.1: Comparison between the critical components required for processing optically an OTDM signal and alternative components that can be used when the signal is converted in a mixed TDM-WDM format considering different network functions.

Function	OTDM	Mixed TDM-WDM
Demultiplexing	ultrafast switch	optical filter
Add/drop multiplexing	ultrafast switch	optical filter
Aggregate-rate compression/expansion	e.g. recirculating loop	e.g. dispersive fibre
Channel-slot exchange	—	e.g. FBGs
Clock recovery	local oscillator	—

allocated to a bit-slot according to their destination. This can be challenging to implement with time-division signals, requiring a complex lattice of ultrafast switches and optical-delay-lines, whereas with a TDM-WDM signal a similar FBG scheme to that described above can be a much more practical approach.

Although WDM technology is considered to be more mature than OTDM technology, one can also find examples where processing in the temporal domain might be preferable. For instance, regeneration of WDM signals could be achieved simultaneously for all channels by converting the WDM signal onto a TDM signal and using well studied nonlinear switching regenerators [14]. The WDM alternative would require each channel to be processed separately.

1.2 Multiplexing Format Conversion Review

The conversion from an OTDM to a mixed TDM-WDM signal is, however, by itself a difficult process to perform. Multiplexing format conversion between time and wavelength division multiplexed signals has been studied in the last decade and several techniques have been reported. Pioneering work focused on four-wave mixing in semiconductor optical amplifiers (SOA), where the conversion of a 700 Mb/s TDM signal onto a 2 × 350 Mb/s WDM signal was demonstrated in [15]. This scheme used two pump diode-lasers centred at different wavelengths and on-off modulated at 350 MHz. The modulation was delayed between the two pumps by a phase difference of 180°, which ensured that the pumps overlapped with alternate bits of the TDM data stream. Data signal and pumps were then coupled together into an SOA, which gave rise to four-wave mixing between them. Idler signals were then filtered and coupled together concluding the multiplexing format conversion. The same scheme was also demonstrated using cross-gain modulation in an SOA: 40-Gb/s TDM onto 2×20-Gb/s WDM was shown in [16], and 2-Gb/s TDM onto 4×500-Mb/s WDM in [17]. In [18], a similar scheme based on the NOLM switching of a multi-wavelength clock signal, which consists of pulses with alternate carrier-wavelengths, with the OTDM data pulses was proposed for high-speed OTDM-to-WDM conversion.

A different approach was demonstrated in [19], where conversion of a 40-Gb/s TDM signal to a 4×10-Gb/s WDM signal was reported, based on super-continuum generation from the original TDM signal, followed by spectral slicing at different centre wavelengths. Each spectral slice thus contained the original 40-Gb/s TDM data, and therefore, to complete the multiplexing-format conversion required each channel to be delayed from the one preceding it by one bit-period, and subsequently, temporally gated at the baseline rate of 10 Gb/s.

The approach presented in this thesis involves generating pulses with a linear chirp, which encompasses the full range of channel wavelengths that need to be generated, at a clock rate that corresponds to the base rate of the individual OTDM channels, and a pulse duration that ensures that the pulse temporally overlaps each multiplexed OTDM channel. These pulses can then be input to an all-optical switch and the OTDM channels used as control pulses to switch the linearly chirped pulses in regions of temporal overlap. The switching process thus maps the OTDM channels into the wavelength domain on a straight one-to-one relation, see Fig. 1.2(a).

A few advantages of this technique, as compared to those previously described, is that it requires only one laser source in the OTDM-to-WDM converter independently of the number of incoming tributary channels, and complete conversion occurs without splitting the tributary channels into separate optical paths, which eliminates the need for additional channel synchronisation.

This technique has been reported by other research groups as a means of simultaneous demultiplexing of all the tributary channels of a high-speed OTDM signal [20, 21]. However, it has been strictly applied to the demultiplexing function, and assessment of the possibility of performing further signal processing with the mixed TDM-WDM signal was missing. In this thesis the conditions under which the technique shown in Fig 1.2(a) can be applied to network functions, such as rate compression/expansion and add/drop multiplexing, are fully investigated.

Subsequently to the time/wavelength domain signal-processing, it may be required to convert the processed signal back into the network signal-format. In this case, it is necessary to perform mixed TDM-WDM to OTDM format conversion. This function can be achieved, for instance, by using the pulses in the temporally-interleaved WDM

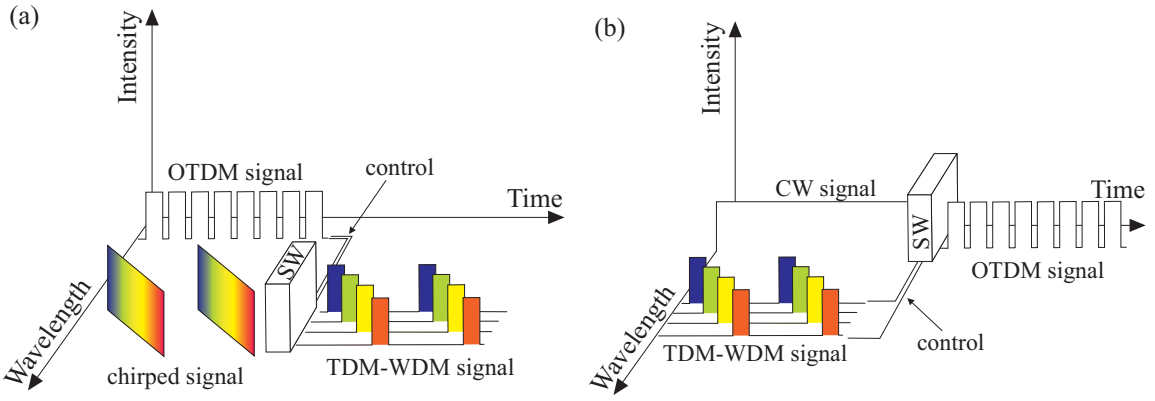

Figure 1.2: Scheme for conversion from (a) OTDM to mixed TDM-WDM signal, and (b) mixed TDM-WDM to OTDM signal. SW: optical switch.

channels to control the switching of a CW signal. This maps the temporal sequence of the mixed TDM-WDM signal onto the CW signal, see figure 1.2(b).

1.3 Thesis Outline

Chapter 2 contains the general background for the work in this thesis. First it gives an overview of nonlinear fibres for optical signal processing. Nonlinear fibres have been critical components in the implementation of all the basic blocks in the scheme that I have developed, namely: the generation of linearly-chirped pulses, and the all-optical switches for conversion between OTDM and WDM signals. Several fibre-based switches are described and discussed with emphasis on the nonlinear-optical-loop-mirror (NOLM) and the Kerr-switch, which were used in my experimental work. Numerical modelling of the propagation of pulses in a nonlinear fibre, as well as their transmission through a fibre-based switch, was a valuable tool in the understanding and design of most of the experiments presented in this thesis. The modelling technique is described in this chapter, whereas details of the approximations made on the NOLM-switch model are given in Appendix A. This chapter concludes with an overview of Fibre-Bragg-Gratings (FBG). Optical filters, as described above, can be used to process the mixed TDM-WDM signal, and FBGs are demonstrated to be a flexible and suitable technology. In particular, linearly-chirped FBGs and high-reflectivity FBGs are described due to their application in channel add/drop multiplexing and dispersion control.

Chapter 3 relates to the generation of linearly-chirped pulses for the OTDM to mixed TDM-WDM multiplexing-format conversion. The chirp generation is achieved via strong self-phase modulation in a low-dispersion nonlinear fibre. This is evidenced by a large spectral broadening. Two main criteria are required to implement the conversion technique: a flat spectral-density and steep spectrum edges. The former is important to ensure that the converted WDM channels have equal power. The latter is to prevent long tails from being formed when the linearly-chirped pulse is stretched to overlap all the tributary channels. To follow these two criteria, the chirp generation mechanism was investigated numerically and experimentally, taking into consideration different dispersion regimes. To better achieve the two criteria, a novel approach was introduced which considered the shaping of the input pulses to the nonlinear fibre so that the pulses evolve into the desired spectral shape. The pulse shaping function is obtained by numerical calculation of the reverse propagation of the desired pulse amplitude and phase. This technique is described and experimentally demonstrated at the end of this chapter.

In Chapter 4, the OTDM to mixed TDM-WDM multiplexing format conversion, using a NOLM-switch, is demonstrated. An original contribution of this work involves the detailed experimental and theoretical assessment of the amplitude, phase and spectrum of the converted pulses. It is shown that severe spectral beating can be formed when residual components of the non-overlapped part of the linearly-chirped pulses is transmitted through the NOLM switch. These are very important aspects mainly in applications involving dispersive effects such as temporal compression/expansion. In the last part of this chapter, the linearly-chirped pulse bandwidth, required to achieve optimum conversion, was estimated as function of the OTDM signal bit-rate. The associated channel spacing and crosstalk level were also estimated.

In the subsequent chapters, I describe the experimental demonstration of several network functions using the concept illustrated in Fig. 1.1. In Chapter 5, I first describe the demultiplexing of 10-Gb/s tributaries, from a 40-Gb/s OTDM signal, based on the nonlinear gating of linearly-chirped pulses in a fibre Kerr-switch. The influence of the residual birefringence of the nonlinear fibre in the polarisation extinction of the Kerr-switch was investigated theoretically and compared to the experimental results. In the second part of this chapter, I describe add/drop multiplexing of 10-Gb/s channels from a 40-Gb/s OTDM signal using a high-reflectivity FBG whose Bragg

wavelength was tuned to reflect off a tributary channel. The mixed TDM-WDM signal, after add/drop multiplexing, is converted back onto an OTDM signal which completes all the stages shown in Fig. 1.1.

In Chapter 6, I describe experimental and theoretical work on the compression and expansion of the OTDM signal bit-rate. The compression/expansion is achieved in a dispersive medium which imposes a linear group-delay across the bandwidth of the linearly-chirped pulses. This dispersion also induces compression/broadening of the individual pulses. The chapter first investigates the chirp condition required to keep the pulse duration of the compressed/expanded signal within an interval of negligible crosstalk between adjacent channels. In the theoretical analysis, it was taken into consideration that the mixed TDM-WDM signal is obtained by nonlinear switching of linearly-chirped pulses in a NOLM. Compression/expansion experiments under different chirp conditions are compared with the theoretical predictions, which support the good understanding of the proposed schemes.

The thesis concludes with Chapter 7, where I summarise the key results and discuss future directions for further work.

Chapter 2

The Enabling Technology

Overview: In this chapter I describe the technology that I used to implement the multiplexing-format conversion scheme based on the switching of linearly-chirped pulses, and also the numerical modelling techniques used to simulate the underlying physical effects.

2.1 Introduction to highly-nonlinear dispersion-shifted optical fibres

Highly-nonlinear germania-doped silica fibres were used in this work on nonlinear switching and pulse generation schemes. In this section, therefore, I describe the properties of these fibres and their use in optical signal processing techniques.

All-optical switching in fibre exploits the nonlinear-response of a medium to an intense optical field. In particular, the nonlinear Kerr effect leads to an ultrafast change of the fibre refractive-index which subsequently induces a phase modulation onto the propagating optical field. The fibre refractive-index responds to an intense optical field according to [22]:

$$n(\omega) = n_0(\omega) + n_2 I \tag{2.1}$$

where n_0 is the linear refractive-index, I is the intensity of the optical field in the fibre. The nonlinear refractive-index (n_2) is related to the third-order susceptibility ($\chi^{(3)}$), which is an intrinsic property of the medium, by:

$$n_2 = \frac{3}{8n_0}\mathrm{Re}\left(\chi^{(3)}\right) \tag{2.2}$$

The nonlinear refractive-index, in general, can be considered to be frequency independent within the spectral region used for optical-fibre communications. Although, significant frequency dependency has been measured when the electrostriction effect is excited [23]. The electrostriction effect is associated with Brillouin scattering, and therefore, occurs when long pulses ($> 1\,\mathrm{ns}$) are used.

The strength of the fibre nonlinearity is commonly estimated by the fibre nonlinear coefficient (γ), which considers the fibre nonlinear refractive-index, and the guided-mode confinement in terms of the guided-mode effective area (A_{eff}), and is defined as:

$$\gamma = \frac{2\pi}{\lambda}\frac{n_2}{A_{\mathrm{eff}}} \tag{2.3}$$

where λ is the wavelength of the guided-mode.

Silica optical fibre is a weakly nonlinear medium as the third-order susceptibility of silica is relatively low when compared to other materials. One path, to developing highly nonlinear fibres, is to use glasses with higher optical susceptibilities than silica, such as chalcogenides [24]. Typically, the $\chi^{(3)}$ of chalcogenides is two orders of magnitude larger than silica. However, several optical properties of these materials such as high refractive-index, and high absorption makes the design and fabrication of single-mode fibres challenging in the spectral window used for optical-fibre communications. A review of the nonlinearity of different glasses for fibres is given in [25]. A significant enhancement of the nonlinearity can also be achieved by tighter confinement of the guided light. Holey fibres have shown extreme optical confinement. For example, a guided-mode effective area of 2 $\mu\mathrm{m}^2$ has been achieved in a single material structure comprising a small solid-core surrounded by air holes which form the cladding. Furthermore, these structures can be fabricated in a large variety of glasses, and record levels of fibre nonlinearity have been demonstrated [26]. Although

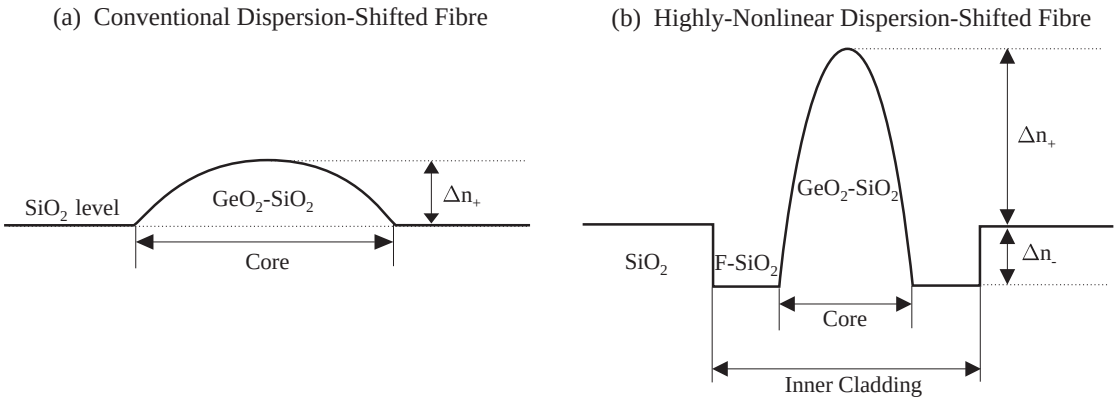

Figure 2.1: Typical refractive-index profile of (a) a conventional dispersion-shifted fibre, (b) a highly-nonlinear dispersion-shifted fibre. Figure adapted from [1].

the holey fibre concept allows a wide range of guiding properties, these are highly sensitive to fabrication imperfections in the holes' size and arrangement. Modelling the drawing process of holey fibres is an active research area, which has provided relevant information on the best drawing parameters [27]. Also, a novel design of holey fibres with higher resilience to fabrication imperfections has been demonstrated [28]. However, hitherto, it has been difficult to produce more than a few tens of metres of length of holey fibre with a uniform structure. Furthermore, low loss splicing between nonlinear holey-fibre and standard single-mode fibre is still an ongoing research topic, and lens coupling is currently a better option. Use of holey fibres, therefore, has been limited to the demonstration of simple nonlinear devices [29].

More widely used in fibre based nonlinear switching techniques, however, are the highly-nonlinear dispersion-shifted fibres (HNL-DSF) [30]. These are fibres where the core-cladding refractive-index contrast results from heavily doping the fibre core with germania. The typical refractive-index profile of a HNL-DSF is shown in Fig. 2.1(b), which can be compared to the refractive-index of a conventional dispersion-shifted fibre shown in Fig. 2.1(a). In these fibres, the high nonlinearity results mainly from tighter confinement of the optical guided-mode by decreasing the core region area and increasing the core-cladding index contrast by heavily doping the fibre core with germania. The index contrast can be further enhanced by doping the cladding with fluorine, since this decreases the refractive-index of pure silica. A confinement of the optical mode to an effective area of about $10\,\mu\mathrm{m}^2$ and an associated nonlinear-coefficient of 20–30 $\mathrm{W}^{-1}\cdot\mathrm{km}^{-1}$ has typically been demonstrated [31]. Although the mode confinement is the main factor in increasing the fibre nonlinearity, it has also to

be appreciated that germania doping increases the nonlinear index (n_2) of the pure silica fibre [32]. Whilst the nonlinear refractive-index of pure silica is [33, 34]:

$$n_2\,(\mathrm{SiO_2}) = 2.2 \times 10^{-20}\,\left(\mathrm{m^2/W}\right), \tag{2.4}$$

the nonlinear index of germania-doped silica fibre is given by [33]:

$$n_2\,(\mathrm{GeO_2} - \mathrm{SiO_2}) = [2.2 + 0.033 \cdot X_{\mathrm{GeO_2}}] \times 10^{-20}\,\left(\mathrm{m^2/W}\right). \tag{2.5}$$

where $X_{\mathrm{GeO_2}}$ is the mole fraction of germania in percentage in the silica glass, which is typically about 80 mol.% for a HNL-DSF [35].

An interesting feature of the HNL-DSFs is that the zero-dispersion-wavelength is shifted to the 1550-nm window, as a consequence of decreasing the guided-mode effective area while increasing the core-cladding index contrast by germania doping the fibre core. Furthermore, the dispersion slope can be significantly reduced in a depressed-cladding index profile [36], as shown in Fig. 2.1(b), which allows the fabrication of highly-nonlinear dispersion-flattened fibre (HNL-DFF). An optimum core-cladding index contrast ($\Delta \mathrm{n_+}$) of about 3% has been suggested, because it was found that for higher index contrast the fibre becomes multimode at 1550 nm [1]. At this contrast level, the mode area is about $10\,\mu\mathrm{m}^2$ and the nonlinear index is $5 \times 10^{-20}\,\mathrm{m^2/W}$, which, according to Eq.(2.3), give a typical nonlinear coefficient of $\sim$20 $\mathrm{W^{-1}{\cdot}km^{-1}}$. In Table 2.1 the typical parameters of the highly-nonlinear fibres used in this work are shown. The HNL-DSFs were fabricated by Sumitomo Electric Industries, while the HNL-DFFs were fabricated by Furukawa Electric Company. The fibres were spliced to standard single-mode fibre by the respective companies, and splicing losses of between 0.06 and 0.2 dB were achieved. Sumitomo Electric Industries [1] and Furukawa Electric Company [37] have produced 500 m HNL-DSF modules within dimensions of 10×10 cm wide and 1-cm high, by coiling the HNL-DSF in a spool of 6 cm diameter.

There are, however, limitations in increasing the fibre nonlinearity by heavily doping the silica core with germania. One is that germania increases the fibre attenuation in terms of both the loss due to Rayleigh scattering, and the loss due to the waveguide imperfection. Another is that the zero-dispersion-wavelength is shifted to longer

Table 2.1: Highly-nonlinear fibre parameters measured at 1550 nm

Fibre	attenuation [dB/km]	dispersion [ps/nm/km]	slope [ps/nm^2/km]	γ [W^{-1}·km^{-1}]	PMD [ps/$\sqrt{km}$]	length [m]
HNL-DSF1	0.53	+0.01	+0.03	20	0.02	220
HNL-DSF2	0.49	−0.64	+0.03	20	0.05	490
HNL-DSF3	0.59	+0.32	+0.03	19	0.03	1010
HNL-DFF1	3.45	−0.75	+0.0031	21	0.1	500
HNL-DFF2	1.05	−0.87	−0.0006	21	0.015	500
HNL-DFF3	1.44	+0.06	+0.0035	21	0.14	500

wavelengths, out of the 1550-nm window. Furthermore, as mentioned above, the fibre cutoff wavelength is also shifted in the 1550-nm window and the fibre may support more than one mode. Hence, the fibres in Table 2.1 are actually a good reference to the limits of this technology.

2.2 Nonlinear Fibre-based Switches

Nonlinear fibre based switches have been proposed for data signal processing applications. The electronic polarisation, induced by an intense optical field in the fibre, occurs on a femtosecond timescale and, consequently, allows bit-by-bit switching at terabit-per-second data rates. In Table 2.2, the reported record switching speed of different types of nonlinear fibre based switches are given. The fibres used in the switches are germania-doped silica fibres, as described in the previous section. The criteria I considered, in selecting the references in this table, is the demonstration of the best error-free switching performance. A detailed review of the several nonlinear fibre based switches is given in [38]. As for the latest comparison between semiconductor and fibre based switches used in all-optical signal processing, the reader is referred to [39]. In the next subsections, I describe the nonlinear optical loop mirror (NOLM) and the Kerr switch, as these were used in my PhD thesis work.

2.2.1 NOLM Switch

The nonlinear optical loop mirror (NOLM) was first proposed for all-optical signal processing in [44], where a bulk crystal was used as the nonlinear element. A NOLM

Table 2.2: Record speed operation of nonlinear fibre switches.

Type	Bit rate (Gb/s)	Operation	Ref.
NOLM switch	640	demux	[40]
Kerr switch	640	demux	[41]
XPM switch	160	demux	[42]
FWM switch	500	demux	[43]

switch using nonlinear fibre was proposed later in [2]. The NOLM switch is based on the Sagnac interferometer and consists of a coupler and a fibre connected to its output ports, as shown in Fig. 2.2. A signal launched into the NOLM, via the coupler input port, is split into two counter-propagating beams which interfere back at the coupler. As both beams follow the same optical path, albeit in opposite directions, the phase of both fields is the same at the recombination in the coupler and the NOLM acts as a mirror, reflecting the signal back into the coupler input-port.

There are, however, several means to induce a phase-shift between the two beams using the nonlinear Kerr-effect in the fibre in the loop. One means is to unbalance the power of the counter-propagating beams by using a coupler with an unequal splitting ratio. When the two beams are equally split, the phase-shift induced by the intensity dependent nonlinear refractive-index is the same. In contrast, when the splitting ratio differs, the two beams can suffer a significantly different phase-shift, which increases in proportion to the splitting-ratio difference. The NOLM transmission can then be characterised by the switching-ratio, which is defined as the ratio between the light on and off at the output port. The highest switching-ratio occurs for a nearly equal splitting-ratio of the two beams, however the energy required to turn light from on to off is also the highest near an equal splitting-ratio [2].

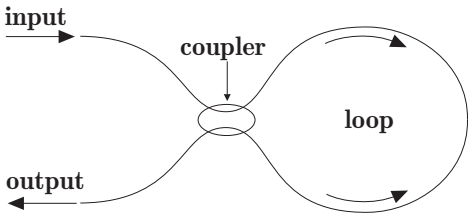

Figure 2.2: The nonlinear optical loop mirror (NOLM). Figure adapted from [2].

One means to reduce the switching energy, required to achieve a high switching-ratio, is to introduce amplification in the loop. The nonlinear amplifying loop mirror (NALM) consists of a coupler with an equal splitting-ratio (50:50) and a loop with two sections: a fibre amplifier, and a nonlinear fibre. In one direction the signal is first amplified and suffers subsequently a large nonlinear phase-shift. Instead, in the other direction, the signal suffers first a small nonlinear phase-shift and is afterwards amplified. As the power of the two counter-propagating beams is equal at the recombination in the coupler, the signal is completely reflected into the coupler input port when no amplification occurs. The signal is completely switched into the coupler output-port when the phase difference induced by the amplifier between the two counter-propagating beams is 180°. Hence, in principle, this scheme allows to completely turn light from on to off at the output of the NOLM-switch coupler.

Another means to achieve a high switching-ratio, but without using an active component in the loop, is by combining different dispersive elements in the loop. The dispersion-imbalanced nonlinear optical loop mirror (DI-NOLM) consists of a 50:50 coupler and a loop with two sections: a low-dispersion nonlinear fibre, and a highly dispersive fibre. This scheme can only be used when the signal consists of a stream of pulses, since dispersion induces both pulse-duration broadening and peak-power lowering. In one direction the signal suffers first a large nonlinear-phase shift and is subsequently dispersed. In the other direction, the signal is first largely dispersed, and consequently, suffers a very small phase-shift in the nonlinear fibre.

These NOLM schemes, based on signal self-switching, have been widely used in pulse compression and pedestal suppression schemes, see for example [45]. Most signal-processing functions, however, require a three-port switch, which consists of an input, output and control port. The three-port NOLM scheme was first proposed in [46] and is shown in Fig. 2.3, which illustrates both the wavelength conversion and all-optical modulation functions. In this scheme, the signal is injected into the loop, which consists of a nonlinear fibre, via a 50:50 coupler and, consequently, it is reflected back into the coupler input-port in the absence of a control signal. The control signal is coupled into the loop in co-propagation with one of the loop directions. Hence, the signal in co-propagation suffers a phase shift, proportional to the peak intensity of the control pulses, which is induced by cross-phase modulation (XPM). In contrast, the signal in counter-propagation suffers a phase shift proportional to the average power

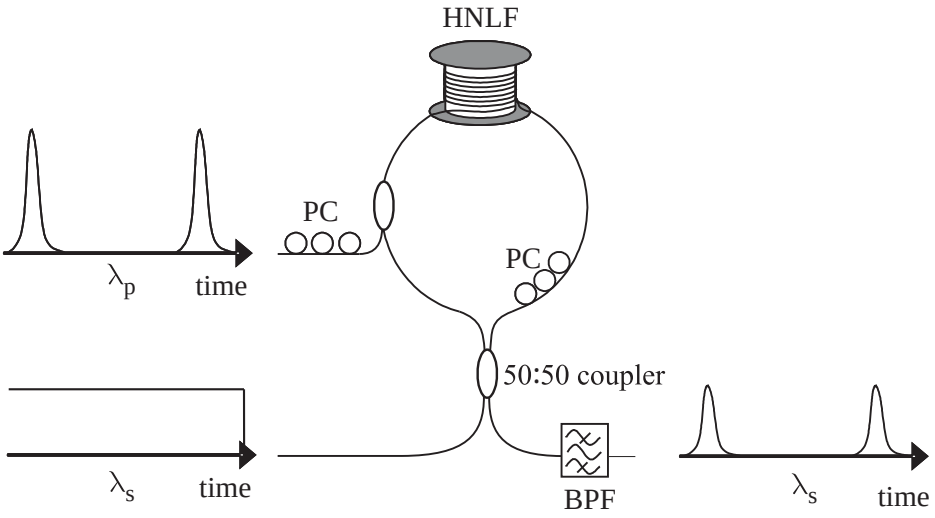

Figure 2.3: Three-port nonlinear optical loop mirror used for wavelength conversion and all-optical modulation.

of the control pulses only. A phase-shift difference of 180° switches, completely, the signal into the coupler output-port. A bandpass optical-filter, centred at the signal wavelength, then filters out the control pulses. This scheme is often referred to either as XPM-NOLM or 2λ-NOLM.

Typically, complete switching is achieved in a NOLM with a loop length of a few hundred metres, by using recently developed nonlinear fibres and optical amplifiers. For instance, in a loop consisting of a nonlinear fibre with a nonlinear coefficient of $20\,\mathrm{W}^{-1}\cdot\mathrm{km}^{-1}$, a phase shift of 180° is induced by the XPM of a control pulse with a peak power of 0.5 W in a nonlinear-fibre length of 160 m, according to $\Delta\phi = 2\gamma L P_0$ where γ is the nonlinear coefficient, L is the fibre length, and P_0 is the control pulse peak-power. In such long media, the polarisation of the signal and control changes randomly in the loop which severely degrades the switching performance. In [47], the switching performance, as a function of the deviation between the signal and control polarisations, was investigated and it was found that the deviation should be less than 10° for error-free performance. Two polarisation controllers, one in the loop and another at the control-port input, can be used to enhance the switching performance, however, in this configuration, the NOLM is a polarisation sensitive device. Another detrimental effect in long-length interaction media is a large walk-off between signal and control, which occurs due to the inherent medium dispersion and imposes a different propagation delay between control and signal. To reduce

walk-off, the typical approach applied is to use a nonlinear fibre in the loop with the zero-dispersion-wavelength in-between the signal and control carrier wavelengths.

In the case of a continuous-wave (CW) or a high duty-cycle (such as NRZ) signal, the counter-propagation XPM effect induces a permanent de-phasing between the two counter-propagating beams of the signal, which can prevent the NOLM from completely switching off. Recently, a new NOLM scheme has been suggested to overcome this issue [48]. This scheme basically introduces in the loop an additional section which induces a phase shift between the two counter-propagating beams based on linear birefringence controlled by strain. This can then be adjusted to compensate the permanent nonlinear phase-shift, so that the NOLM achieves a high switching-ratio.

2.2.2 Kerr Switch

The Kerr switch, also referred to as Kerr shutter, consists essentially of a nonlinear fibre and a polariser, as depicted in Fig. 2.4. It uses the ultra-fast nonlinear polarisation-rotation which can be induced in a medium with a large third-order susceptibility (χ_3) through the intensity dependent refractive-index. A linearly polarised high-intensity signal propagating through a medium with a large χ_3 induces an anisotropic change of the medium's refractive-index. A probe signal, oscillating in a different plane from the high-intensity signal, suffers polarisation rotation due to the induced anisotropy. The Kerr switch is thus implemented to gate an ultra-high speed signal by changing the polarisation of the probe signal between two orthogonal states, one of which is aligned with the axis of the polariser. First, the state-of-polarisation of the probe signal is transformed into a linear polarisation and aligned to its minimum transmission through the polariser, i.e. at a direction perpendicular to the axis of the polariser. To transmit the signal through the polariser, a control signal can then be injected into the nonlinear fibre to induce polarisation rotation of the signal, which results in transmission through the polariser of the part of the signal overlapping with the control. The part of the control that passes through the polariser can be removed with a bandpass filter centred at the signal wavelength. In the Kerr switch, the switching-ratio is fundamentally limited by the polarisation

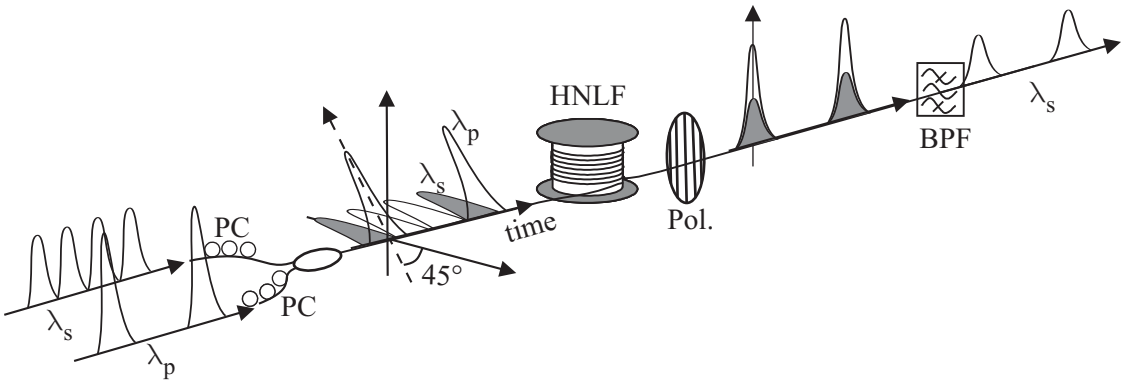

Figure 2.4: Schematic of the Kerr switch using the nonlinear-polarisation-rotation in a highly nonlinear fibre (HNLF) and polariser (Pol.).

extinction-ratio of the polariser. The minimum switching-energy is required when the signal and control are linearly polarised at 45°.

The polarisation rotation can be explained by considering that the electric-field vector of a signal propagating through an optical fibre can also be interpreted as the sum of two fields oscillating in orthogonal directions. The rotation of the polarisation angle of a signal is induced by changing the phase difference between the two orthogonal polarisation components of the signal. For a phase difference between the two polarisation components of 180°, the signal polarisation-angle rotates by 90°. Hence, when the signal is polarised at 45° from the control (high-intensity field), there is one signal-component parallel to the control, and another perpendicular. Both components suffer nonlinear phase-modulation, induced via the XPM effect, but the XPM amplitude between cross-polarised fields is one-third of that between co-polarised fields [34]. The phase difference between the two perpendicular components after the XPM effect is, therefore, given by:

$$\Delta\phi = 2\gamma L P_0 \left(1 - \frac{1}{3}\right) = \frac{4}{3}\gamma L P_0 \tag{2.6}$$

where γ is the nonlinear coefficient, L is the length of the nonlinear medium, and P_0 is the peak power of the control signal. Full-swing operation of the Kerr-switch is achieved by varying the control peak-power between 0 and $\frac{3\pi}{4\gamma L}$. It can be inferred that the Kerr-switch requires a slightly higher switching-energy than the 2λ-NOLM.

The practical implementation of the Kerr-switch for all-optical signal processing was thoroughly investigated in [49, 50]. It was shown, therein, that the intrinsic linear-birefringence of the nonlinear-medium can severely hinder the Kerr-switch performance. Firstly, it induces polarisation mode dispersion which narrows the operation bandwidth. Secondly, it can scramble the linear polarisation of the control signal into an elliptical polarisation, for which the nonlinearly induced anisotropy nearly vanishes.

These limiting effects can, however, be eliminated with polarisation-maintaining nonlinear fibres, which are high-birefringence fibres. In this case, the linear polarisation of the control is maintained along the nonlinear fibre when this is initially aligned with a birefringence axis of the optical fibre. However, since the probe signal is aligned at 45° with the birefringence axes, the strong birefringence of the medium induces a large differential-group-delay in the probe signal. This effect can be largely reduced by splicing two identical sections of the same highly-birefringent fibre with their birefringence axes perpendicularly aligned. Consequently, the differential-group-delay induced in the first section is reversed in the second section.

Although, in principle, this scheme eliminates the degradation induced by intrinsic birefringence, a small difference on the length of the two fibre sections associated with variation of the fibre birefringence due to temperature fluctuation can lead, in highly birefringent media ($B_0 \approx 10^{-4}$, where B_0 is the modal birefringence [34]), to significant degradation of the performance of the Kerr switch [50]. The practical implementation of the Kerr-switch scheme can thus be challenging.

More recently, the development of highly-nonlinear fibres with ultra-low polarisation-mode-dispersion allowed the use of much shorter lengths of nonlinear-medium [41], which largely reduces the detrimental effects of intrinsic birefringence. For instance, a 90° polarisation rotation of the signal corresponds to a 180° phase shift, given by Eq. (2.6). For a nonlinear coefficient of $21\,\mathrm{W^{-1}{\cdot}km^{-1}}$, and a control peak-power of 10 W, the nonlinear fibre length required is only 11 m.

2.3 Modelling nonlinear fibre-based switches

The numerical modelling of the nonlinear effects in the optical fibre was a valuable tool in my investigation of the chirped-pulse generation and the fibre-based switches. The nonlinear Schrödinger equation (NLSE) governs the propagation of light in optical fibres, and can be written as [34]:

$$\frac{\partial A}{\partial z} = \left(\hat{D} + \hat{N}\left[A\right]\right) \cdot A \tag{2.7}$$

where the amplitude A is the slow-varying envelope of the optical field, and its module square is the optical power. $\hat{D}$ is the differential operator given by:

$$\hat{D} = -i\frac{\beta_2}{2!}\frac{\partial^2}{\partial\tau^2} + \frac{\beta_3}{3!}\frac{\partial^3}{\partial\tau^3} - \frac{\alpha}{2} \tag{2.8}$$

where β_2 is the second-order dispersion coefficient, β_3 is the third-order dispersion coefficient, α is the power attenuation coefficient, and $\hat{N}$ is the nonlinear operator given by:

$$\hat{N}\left[A\right] = i\gamma\left|A\right|^2 \tag{2.9}$$

where z is the propagation distance, τ is the time in a frame of reference moving at the group velocity ($v_g = 1/\beta_1$). Higher-order dispersive effects and nonlinear scattering effects were not incorporated in the fibre model as, for the signals and power levels involved in this work, the various proposed schemes were well modelled by the above effects.

The NLSE is derived from the Maxwell equations, which are proven fundamental laws of the interaction between electromagnetic waves and propagation medium properties. The details of the derivation are written in several published books such as, for example, Ref. [34]. Despite that, I decided to briefly summarise herein the conditions of validity of the NLSE. Firstly, it assumes the paraxial propagation of the guided light or, in other words, total light confinement in the fundamental mode, and therefore, the above NLSE is not valid for multi-mode propagation. Secondly, it is written in the slow varying envelope amplitude approximation, which is a valid representation

of the optical signal if the carrier frequency is much larger than the spectral width of the signal, consequently the NLSE is not valid for few cycle pulses, i.e. pulses with a duration of a few femtoseconds.

The most commonly used algorithm to solve the NLSE is the split-step Fourier method (SSFM) [34]. The propagation of a pulse over the full length of an optical fibre is simulated by dividing the fibre into relatively small segments such that changes in the complex envelope can be considered sufficiently small. Consequently, at each step, the nonlinear and differential operators of the NLSE are decoupled and can be applied separately. While the nonlinear operator is algebraic in the time domain, the differential operator, assuming that the signal is a superposition of forward propagating harmonic-waves, is algebraic in the frequency domain as $\frac{\partial}{\partial\tau} \rightarrow -i\omega$. Under this condition the differential operator can be written in the frequency domain as:

$$\hat{D}_\omega = i\frac{\beta_2\omega^2}{2!} + i\frac{\beta_3\omega^3}{3!} - \frac{\alpha}{2} \tag{2.10}$$

Consequently, in the SSFM, the nonlinear operator manipulates the signal in the time domain, while the differential operator is used in the frequency domain. The signal representation is changed between time and frequency domains by using the Fourier transform defined as:

$$F(\omega) = \int_{-\infty}^{\infty} f(t)\exp(i\omega t)dt \tag{2.11}$$

For a small propagation step h, in which the nonlinear operator is approximately constant, Eq. (2.7) can be solved analytically, and its solution is given by:

$$A(z+h,\tau) = \exp\left(\hat{D}h + \hat{N}h\right)\cdot A(z,\tau) \tag{2.12}$$

Although the accuracy of the SSFM is mainly defined by the step length, better accuracy is obtained with a smaller step, also the splitting scheme of the nonlinear and differential operators introduces numerical error. This is so because the nonlinear and differential operators are non-commuting operators, and $\exp\left(\hat{D}+\hat{N}\right) =$

$\exp\left(\hat{D}\right)\exp\left(\hat{N}\right)$ if and only if the two operators commute, this is $\hat{D}\hat{N} = \hat{N}\hat{D}$. Otherwise:

$$\exp\left(\hat{D}\right)\exp\left(\hat{N}\right) = \exp\left(\hat{D} + \hat{N} + \frac{1}{2}\left[\hat{D}, \hat{N}\right] + \frac{1}{12}\left[\hat{D}, \left[\hat{D}, \hat{N}\right]\right] + \cdots\right) \tag{2.13}$$

Physical intuition can prove that $\hat{D}$ and $\hat{N}$ are non-commuting operators. For example, the induced nonlinear phase-modulation is different if it occurs before or after a length of highly dispersive fibre, because the pulse intensity at the input of the nonlinear fibre is different in the two cases.

The simplest scheme of the SSFM is based on Lie splitting [51, 52], for which the numerical error is of second order in the step length (h):

$$A\left(z + h, \tau\right) = \exp\left(\hat{D}_\omega h\right)\exp\left(\hat{N} h\right) \cdot A\left(z, \tau\right) + O(h^2) \tag{2.14}$$

A more accurate scheme is based on Strang splitting [51, 53], also known as the symmetric SSFM, for which the numerical error is of third order in the step size:

$$A\left(z + h, \tau\right) = \exp\left(\frac{\hat{D}_\omega h}{2}\right)\exp\left(\int_z^{z+h} N\left[A\left(z'\right)\right] dz'\right)\exp\left(\frac{\hat{D}_\omega h}{2}\right) \cdot A\left(z, \tau\right) + O(h^3) \tag{2.15}$$

In this form the operator is symmetric with respect to the direction of the propagation step, i.e. defining $A(z + h, \tau) = \hat{H}(h) \cdot A(z, \tau)$ then $\hat{H}(h)\hat{H}(-h) = 1$, which allows forward and backward propagation calculations. This property is used in Sec. 3.5 to calculate the reverse propagation of a target pulse at the output of a HNL-DSF. In my work the integral in Eq. (2.15) was calculated using the midpoint approximation:

$$A\left(z + h, \tau\right) \approx \exp\left(\frac{\hat{D}_\omega h}{2}\right)\exp\left(\hat{N}\left[A\left(z + h/2\right)\right] h\right)\exp\left(\frac{\hat{D}_\omega h}{2}\right) \cdot A\left(z, \tau\right) \tag{2.16}$$

All the simulations, in this thesis, involving nonlinear propagation in an optical fibre are based on the algorithmic implementation of Eq. (2.16), whose flow diagram is shown in Fig. 2.5.

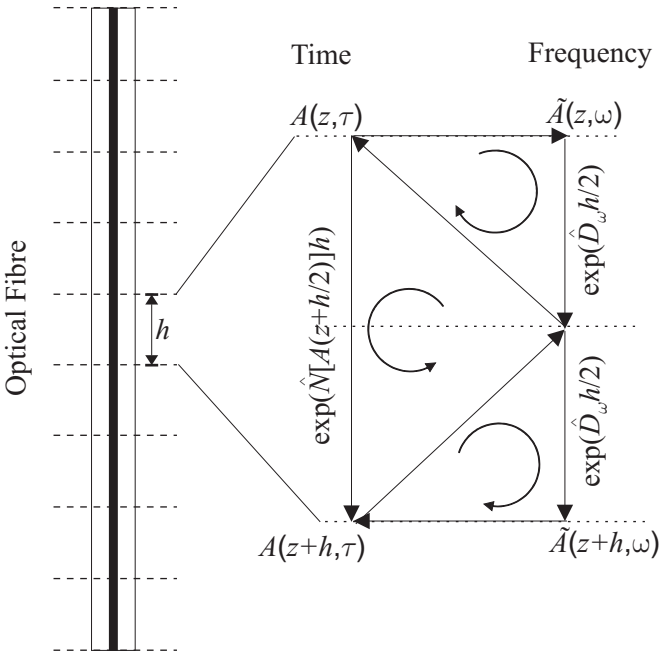

Figure 2.5: Diagram of the symmetric split-step Fourier method algorithm.

There are a few guidelines to estimate the optimum SSFM step-length (h). For example, one can estimate the step-length as a fraction of the smallest value between the nonlinear and dispersive lengths of the fibre. The fibre nonlinear-length (L_{NL}) is the fibre length over which a nonlinear phase-rotation ($\phi(z) = \gamma P_0 z$) of 1 rad is induced, and is defined as:

$$L_{\mathrm{NL}} = \frac{1}{\gamma P_0} \tag{2.17}$$

where P_0 is the peak power of the optical field.

The dispersion length (L_{D}), instead, is the length over which the pulse broadens by $\sqrt{2}$, and is defined as:

$$L_{\mathrm{D}} = \frac{\tau_0^2}{|\beta_2|} \tag{2.18}$$

where τ_0 is the initial pulse-width.

The propagation regime is dominantly dispersive when $L_{\mathrm{D}} \ll L$ and $L_{\mathrm{NL}} \gtrsim L$, where L is the fibre length. On the other hand, the propagation regime is dominantly nonlinear when $L_{\mathrm{NL}} \ll L_{\mathrm{eff}}$ and $L_{\mathrm{D}} \gtrsim L$, where L_{eff} is the effective length of the fibre,

in which the same overall nonlinear interaction would occur if attenuation were zero, and is defined as:

$$L_{\text{eff}} = \int_0^L \exp\left(-\alpha z\right) dz = \frac{1 - \exp\left(-\alpha L\right)}{\alpha} \tag{2.19}$$

where α is the fibre attenuation coefficient.

In the nonlinear regime, it is common to estimate the step-length over which the nonlinear phase-rotation does not exceed a certain limit [54], often chosen as 0.5°, which corresponds to $h \approx 0.01 L_{\text{NL}}$. However, this method is not valid for all propagation problems. Overestimation of the four-wave mixing (FWM) between two or more channels due to the power resonance effect in the SSFM simulation, using a constant step-length, has been reported [55, 56]. Significant reduction of this effect was shown using a non-constant step-length along the fibre [54].

Moreover, when modelling the interaction between pulses at different wavelengths, the SSFM step-length should also be smaller than the walk-off length (L_{W}), which is the length two pulses at different wavelengths go when walking through each other, and is defined as [34]:

$$L_{\text{W}} = \frac{\tau_0}{|D \Delta\lambda_{12}|} \tag{2.20}$$

where D is the fibre chromatic dispersion, $\Delta\lambda_{12}$ is the pulses' wavelength separation, and considering that both pulses have the same pulse-width τ_0.

All these criteria were taken into consideration when applying the split-step Fourier method to the numerical investigation of the nonlinear propagation in the HNL-DSFs. The characteristic lengths of the fibres, shown in Table 2.1, are $L_{\text{NL}} \sim$ 10–100 m, $L_{\text{D}} \sim$ 1–10 km, and $L_{\text{W}} \sim$ 100–500 m. The propagation regime, in the HNL-DSFs is, therefore, predominantly nonlinear and an SSFM step-length of 1 m was typically considered.

2.4 Fibre Bragg gratings

2.4.1 Background

In a simple description, a fibre Bragg grating (FBG) is a nearly periodic variation of the fibre core refractive-index along the fibre longitudinal-axis. The refractive-index grating is obtained by exposing the germanium-doped core to an intense UV pattern [57, 58]. The magnitude of the refractive-index variation depends on the intensity of the UV laser, the exposure time, and the photosensitivity of the fibre, which can be enhanced by soaking the fibre in hydrogen gas at high pressure and temperature [59]. The physical mechanism underpinning photosensitivity in optical fibres is, however, still not a fully understood process. Several mechanisms for photoinduced refractive-index changes have been proposed. For a detailed review of grating formation mechanisms, I refer the reader to [60, 61].

The color-centre model, which supports the formation of UV-absorbing atomic bonds is, however, the most widely accepted mechanism. In standard single mode fibres, enhancement of the core refractive-index is achieved by doping the fibre core with germania (GeO_2). During the doping process, the germania bonds to silica through their oxygen atoms, forming germanosilicate (GeO_2-SiO_2). However, the high temperatures during the fibre drawing process can cause large germania oxygen deficiency (GeO), and in this case the germanium and silicon atoms can bond directly, forming Ge-Ge, Si-Si and Ge-Si bonds [61]. These bonds can be broken by absorption of a 245 nm UV photon, releasing an electron. The free electron moves until it gets trapped into another oxygen-deficient bond. These new atomic bonds absorb UV light at different wavelengths, forming, therefore, new absorption bands [62]. Absorption and refractive-index are properties of the same material characteristic, the complex electric-permittivity, and can be mathematically related through the Kramers-Krönig integrals. A change in the absorption spectrum is, therefore, also observed as a change of the refractive-index.

The fibre Bragg grating refractive-index can be expressed, for small changes of the core refractive-index, as [63]:

$$n(z) = n_{\mathrm{dc}} + \Delta n_{\mathrm{ac}}(z) \cdot \cos\left(\frac{2\pi \mathrm{z}}{\Lambda} + \theta(\mathrm{z})\right) \tag{2.21}$$

where z is the length along the fibre longitudinal-axis, n_{dc} is the average constant change of the core refractive-index, Δn_{ac} is the amplitude of the refractive-index modulation, which is often referred to as the apodisation profile, Λ is the grating period, and θ is the spatial grating-phase. An example of the refractive-index of an FBG, in this case a chirped FBG with a Gaussian apodisation, is illustrated in Fig. 2.6. Although not clear in the figure, the refractive-index grating is a small perturbation of the core refractive-index in the absence of the grating (n_{co}). In fact, typically, the index change is $\sim [10^{-4}, 10^{-3}]$, while $n_{\mathrm{co}} \sim 1.5$.

The spatial grating-phase term, θ, locally changes the grating period. The derivative of the phase gives the change rate of the grating period. In this example, the parabolic phase imposes a linear variation of the grating period along the grating length, where the grating period is unchanged at the centre of the grating.

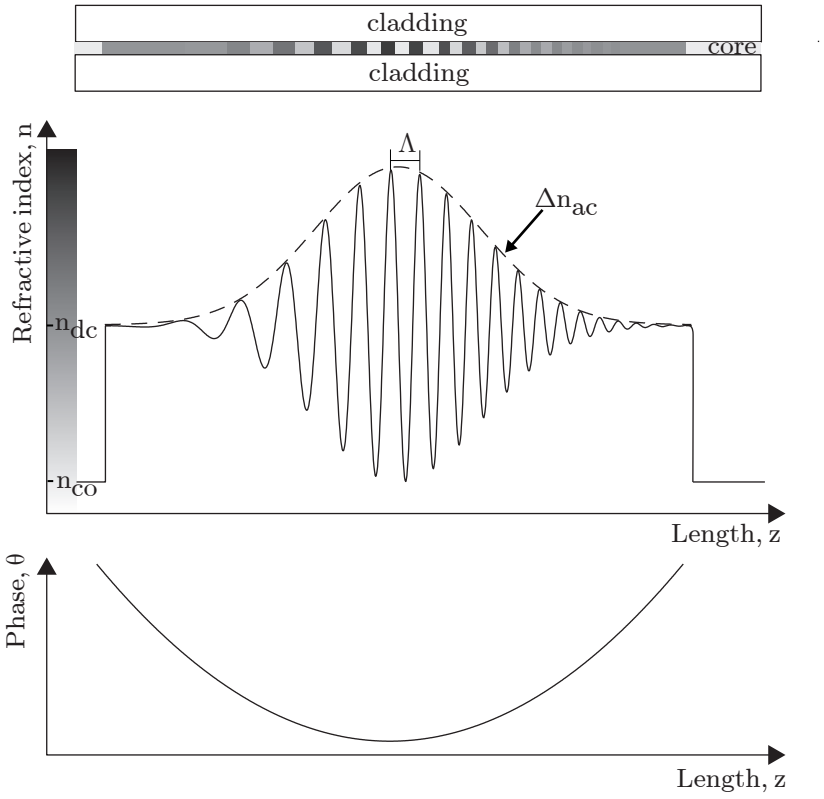

Figure 2.6: Fibre Bragg grating refractive-index profile and phase.

An FBG works as a distributed reflector, since light guided along the fibre core is partially reflected at each grating plane in the transition from a low to a high refractive-index region. The reflections from the subsequent grating planes add in-phase, in a backward propagating guided-mode, when the grating period is equal to half of the guided-light wavelength. This leads to the first-order Bragg condition:

$$\lambda_B = 2n_{\text{eff}}\Lambda, \tag{2.22}$$

where λ_B is the Bragg wavelength, n_{eff} is the effective modal index, which lies in-between the cladding and core refractive indices, and Λ is the grating period. The Bragg condition is valid for a uniform grating with grating planes perpendicular to the fibre longitudinal-axis, and for paraxial propagation of a single guided-mode.

For wavelengths shorter or longer than the Bragg wavelength, the successive reflections add out-of-phase, which reduces the power coupled into the backward propagating mode. The reflection dephasing increases with the detuning from the Bragg wavelength, and consequently, the power reflected off the grating is a function of the wavelength, which determines the FBG reflection bandwidth. A general expression for the full-bandwidth at half-maximum of a uniform FBG, is given by [61, 63]:

$$\Delta\lambda = \lambda_B \alpha_{\text{gr}} \sqrt{\left(\frac{\Delta n_{\text{ac}}}{2n_{\text{eff}}}\right)^2 + \left(\frac{\Lambda}{L_{\text{gr}}}\right)^2} \tag{2.23}$$

where α_{gr} is a parameter that relates to the grating strength, Δn_{ac} is the maximum amplitude of the refractive-index modulation, L_{gr} is the total length of the grating.

This relation shows that for a strong grating (large Δn_{ac}), since most of the light reflection occurs in the first grating planes, the detuning from the Bragg condition has a small effect and, therefore, the reflection bandwidth can be large. On the other hand, for a long and weak grating (small Δn_{ac} and large L_{gr}), the light propagates deeper in the grating and the detuning from the Bragg wavelength has a larger impact, which narrows the reflection bandwidth.

2.4.2 High reflectivity Fibre Bragg Gratings

High reflectivity FBGs have been mainly developed for optical channel add/drop multiplexing (ADM). The main requirements for efficient ADM operation are high suppression of the dropped channel without affecting the through channels, which requires a FBG with high in-band reflectivity and strong side-lobe extinction, efficient bandwidth utilisation, which relates to the squareness of the FBG filter, and negligible distortion of the dropped channel due to the FBG in-band dispersion. These conditions have pushed forward the FBG technology and significant progress has been reported [64].

The maximum reflectivity of a uniform grating, which occurs at the Bragg wavelength, is given by [60]:

$$R = \tanh^2(\kappa L_{\mathrm{gr}}) \tag{2.24}$$

where κL_{gr} is the grating strength, κ is the coupling coefficient between forward and backward propagating guided modes, and L_{gr} is the grating length. The coupling coefficient is related to the induced refractive-index modulation (Δn_{ac}) by:

$$\kappa = \eta \frac{\pi \cdot \Delta n_{\mathrm{ac}}}{\lambda_B} \tag{2.25}$$

where η is the fraction of the guided-mode optical power confined in the core. For $\lambda_B = 1550\,\mathrm{nm}$, the typical maximum value of the coupling coefficient (κ) achieved in the ORC fabrication laboratories is about $3000\,\mathrm{m}^{-1}$. This corresponds, according to Eq. (2.25), to a maximum refractive-index modulation of about 1.5×10^{-3}. According to Eq. (2.24), a reflectivity of 99.9% is possible when $\kappa L_{gr} = 4$. This corresponds to a grating length of 1.3 mm when the above coupling coefficient is considered, while the grating bandwidth, given by Eq. (2.23), is about 1 nm. It can thus be challenging to produce uniform gratings with a reflectivity higher than 99.9% (30 dB), and an associated bandwidth wider than 1 nm.

A problem that, early on, affected high reflectivity FBGs was the strong growth of side-lobes in the FBG reflection spectrum. These side-lobes result from multiple

reflection, to and fro, between the opposite ends of the grating. To reduce the effect of these unwanted reflections, apodisation of the grating refractive-index was proposed [65]. This consists in gradually diminishing to zero the refractive-index variation at both grating ends. A consequence of grating apodisation is, however, an increasing of the dispersion in the reflection band. Significant improvement came from applying inverse-scattering modelling techniques to the design of apodised non-uniform FBGs [66]. This allowed the production of FBGs with a reflectivity higher than 99.9%, a bandwidth utilisation of 75%, no dispersion in the reflection band, and more than 40-dB side-lobe extinction, as shown in [67].

2.4.3 Tuning the Bragg wavelength

The use of FBGs in telecom applications often requires the tuning of the Bragg wavelength to the optical-carrier of a specific channel. As can be inferred from Eq. (2.22), the Bragg wavelength can be shifted by changing the grating period and the grating effective refractive-index. These can be controlled by thermal or mechanical effects. The small thermo-optic and thermo-elastic coefficients of glass fibre require, however, a high temperature variation to significantly shift the Bragg wavelength.

In contrast, stress-induced strain of the grating period, which also changes the refractive-index through the elasto-optic effect, can substantially shift the Bragg wavelength. The Bragg-wavelength shift induced by mechanical stress is given by [60]:

$$\Delta\lambda_B = \lambda_B \left(1 - p_e\right) \varepsilon \tag{2.26}$$

where p_e is the elasto-optic coefficient, which is typically 0.22 for silica, and ε is the grating-period strain. Equation (2.26) can thus be approximated for silica fibre by:

$$\frac{\Delta\lambda_B}{\lambda_B} \approx 0.78\varepsilon \tag{2.27}$$

The maximum tensile-strain that a coated glass-fibre can withstand is typically about 1% (see details in [68]), which corresponds to a Bragg-wavelength shift of 12 nm according to Eq. (2.26) for λ_B =1550 nm. Special coatings, which can increase the mechanical strength of the optical fibre, have been investigated and axial straining of

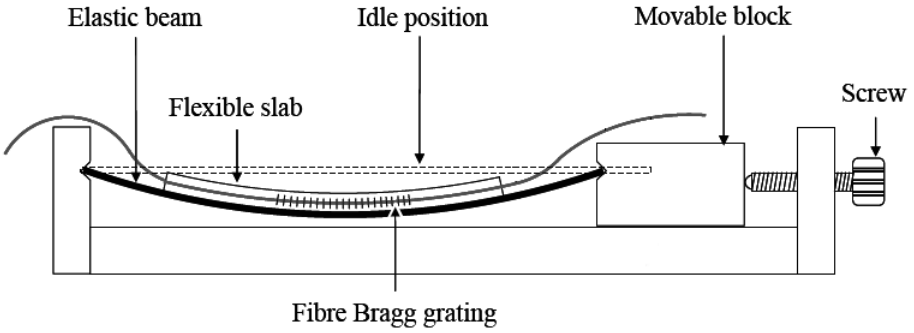

Figure 2.7: Schematic of the tunable package used to induce compressive strain of the fibre-Bragg-grating period. Figure adapted from [3].

5% has been demonstrated [69]. A bare fibre, however, snaps when strained by more than $\sim 0.3\%$. This was the case for the fibre Bragg gratings used in this work, whose polymer coating was stripped off for the UV writing of the grating, and re-coating was usually not done.

On the other hand, the optical glass-fibre is very resistant to compressive strain, and a grating-period compression of more than 10%, which corresponds to a Bragg wavelength shift of about 100 nm, was demonstrated using the tunable mounting technique shown in Fig. 2.7. This tuning technique was developed in the ORC by the fibre-Bragg-grating group led by Dr. Morten Ibsen [3].

2.4.4 Super-structured Fibre Bragg Gratings

A relevant application of fibre Bragg gratings is the shaping of ultrashort pulses [70]. Many all-optical systems can perform better when the intervening pulses are shaped in some specific form. For instance, a time division demultiplexer is more resilient to the data signal timing-jitter when its switching window is rectangular, as shown for example in [71]. A wide variety of pulses have already been shaped with FBGs, such as rectangular, Gaussian and parabolic pulses. Although, many other technologies can be used for pulse shaping such as, for example, acoustooptic and spatial light modulators [72]. FBGs, however, have the advantage of simpler integration in more complex systems.

The most commonly used pulse-shaping techniques are based on linear filtering in either the spatial or spectral domain. When the input pulse has a well-defined optical

field, the filter transfer-function can be specifically designed to produce the desired output optical field. A FBG acts as a spectral filter, and therefore, can finely shape the spectral amplitude and phase of input pulses. The spectral response of the reflectivity of a FBG is, thus, given by:

$$H(\omega) = \frac{Y(\omega)}{X(\omega)} \tag{2.28}$$

where $Y(\omega)$ is the desired output spectral-amplitude, and $X(\omega)$ is the well-defined input spectral-amplitude.

The fibre Bragg gratings used in pulse shaping typically have non-uniform amplitude and phase profiles and, therefore, are often referred to as superstructured fibre Bragg gratings (SSFBGs). In the weak grating limit, the grating refractive-index variations are small enough to allow the incident light to penetrate the full device length, such that the whole grating contributes equally to the reflected signal. This occurs when the peak reflectivity is less than 10–40%. It can be shown that, in this limit, the grating reflectivity and complex coupling-coefficient relate through the Fourier-transform [73]. This can be written, mathematically, as [74]:

$$-\frac{1}{2}q^*\left(\frac{z}{2}\right) \approx \frac{1}{2\pi}\int_{-\infty}^{+\infty} r(\delta)e^{-i\delta z}d\delta \tag{2.29}$$

where z is the length along the grating, $q(z)$ is the grating complex coupling-coefficient, δ is the wave-number detuning from the Bragg wavelength, and $r(\delta)$ is the complex reflection spectrum. The wave-number detuning is defined as:

$$\delta = 2\pi n_{\text{eff}}\left(\frac{1}{\lambda} - \frac{1}{\lambda_B}\right) = \frac{n_{\text{eff}}\omega}{c} \tag{2.30}$$

where ω is the angular-frequency detuning from the Bragg angular-frequency, and c is the speed of light in vacuum.

As Eq.(2.28) gives the desired impulse-response of the FBG, it is then necessary to write Eq.(2.29) in the time-frequency domain (t-ω). Whilst the wave-number and angular-frequency relate through Eq.(2.30), the time interval between two reflections which occur at a distance difference of z is given by:

$$t = 2 \cdot z \cdot \frac{n_{\text{eff}}}{c} \tag{2.31}$$

This is valid when the light reflected in the grating does not suffer multiple reflections. This assumption is valid in the weak-grating limit, while in general it fails in the strong-grating limit.

Hence, substituting Eqs. (2.30) and (2.31) in Eq. (2.29), it follows that:

$$q^*(z) \equiv -\frac{n_{\text{eff}}}{\pi c} \int_{-\infty}^{+\infty} H(\omega) e^{-i\omega t} d\omega \tag{2.32}$$

Although the right side of the equation is a function of time, the absolute value of the complex coupling-coefficient is unchanged when using Eq.(2.31) to transform between time (t) and space (z).

The SSFBG profile can be obtained from Eq.(2.32), taking into consideration that the complex coupling-coefficient in Eq.(2.29) has been defined as [75]:

$$q(z) = -i\frac{\eta\pi}{\lambda_B} \Delta n_{\text{ac}}(z) \exp\left[-i\theta(z)\right] \tag{2.33}$$

where η is the mode-confinement coefficient, which is typically about 0.9 for standard single-mode fibre.

The amplitude of the refractive-index modulation can, thus, be calculated by:

$$\Delta n_{\text{ac}}(z) = \frac{\lambda_B}{\eta\pi} |q^*(z)| \tag{2.34}$$

It can be inferred from Eq.(2.34) that the impulse response of a weak grating follows its refractive-index modulation.

On the other hand, the phase of the grating, according to Eq.(2.33), is given by:

$$\arg q^*(z) = \theta(z) + \frac{\pi}{2} \tag{2.35}$$

A grating phase-change can be related to a variation of the grating period, assuming a constant average refractive-index (n_{dc}), and consequently, the phase in Eq. (2.21) can be re-written as:

$$\frac{2\pi z}{\Lambda} + \theta(z) = \int_0^z \frac{2\pi}{\Lambda(z')} dz' \tag{2.36}$$

The grating period as a function of the grating length can then be obtained by taking the derivative of Eq. (2.36) and substituting in Eq. (2.35), which yields that:

$$\Lambda(z) = \Lambda \left(1 + \frac{\Lambda}{2\pi} \frac{d}{dz} \arg q^*(z) \right)^{-1} \tag{2.37}$$

The associated shift of the Bragg-wavelength (i.e. grating chirp) is subsequently given by:

$$\lambda_B(z) = 2n_{\mathrm{eff}}\Lambda(z) \tag{2.38}$$

In summary, the design of a weak superstructured FBG, which shapes an input pulse $x(t)$ into an output pulse $y(t)$, involves first the calculation of Eq.(2.28), then the calculation of the complex coupling-coefficient through Eq.(2.32), and finally the calculation of the index modulation and grating phase according to Eqs.(2.34) and (2.35) respectively.

2.4.5 Linearly-Chirped Fibre Bragg Gratings

A linearly chirped fibre Bragg grating (LCFBG) has a linear variation of the grating period (Λ) along its length. As the reflected wavelength relates to the grating period according to the relation (2.38), different points in the LCFBG reflect different wavelengths. LCFBGs are, therefore, dispersive gratings. This property has been widely used for dispersion compensation and pulse compression techniques. The chromatic dispersion (D), induced by the LCFBG, is related to the grating chirp-rate (CR), which is given by:

$$CR(z) \equiv \frac{d\lambda_B}{dz} = 2n_{\mathrm{eff}} \frac{d\Lambda}{dz} \tag{2.39}$$

The dispersion, subsequently, can be expressed as:

$$D(z) \equiv \frac{d\tau}{d\lambda} = \frac{2n_{\text{eff}}}{c}\frac{1}{CR(z)} = \frac{1}{c}\left(\frac{d\Lambda}{dz}\right)^{-1} \tag{2.40}$$

where τ is the reflection delay as function of the grating length, which is given by Eq. (2.31).

LCFBGS can be produced either by direct UV-writing of a non-uniform period, as for those used in this thesis work, or by inducing a non-uniform strain on a uniform grating. As for the latter technique, it was proposed initially that a linear variation of the grating period could be induced by embedding the FBG on a metal beam, and bending one end of the beam while the other end is fixed [76]. This produces a strain gradient along the beam, and consequently, chirps the grating period according to the bending angle. A major limitation of this approach is that the centre wavelength shifts to longer wavelengths, as result of axial tensile-stress at the centre of the grating. Following research proposed S-bending of the beam [77]. In this case both ends of the beam are fixed, one end is on a moving stage that moves perpendicularly to the beam length, this movement deforms the straight beam into an S-shape. It results in a strain gradient along the beam with zero axial stress at the centre of the grating, which avoids the shift of the centre wavelength.

An associated feature of the S-bending technique is that, as the grating length is unchanged, the FBG bandwidth is a function of the induced chirp-rate. Recently, a means for varying the grating length while a gradient-strain changes the grating chirp-rate was demonstrated [78, 79]. In contrast with the above techniques, a movable support, which is free to move along the beam length, defines the length of the grating. These techniques can also be used to tune the linear chirp-rate of a non-uniform grating.

Chapter 3

Generation of Linearly-Chirped Pulses for TDM-WDM Conversion

"Chirps are ubiquitous in nature and man-made systems."

—Patrick Flandrin

Overview: This chapter relates to the generation of the linearly-chirped pulses used in the TDM-WDM conversion stage of the signal processing techniques proposed in this thesis.

I describe the generation and characterisation of the complex amplitude of these pulses based on experimental measurements and numerical calculations. The chapter is divided into three sections: first, the full characterisation of pulses chirped in the normal regime of highly nonlinear fibres is described; in the second section I discuss the sizing of the chirped pulses envelope width for later applications, and finally I describe proposed approaches to shape the spectrum and envelope of linearly chirped pulses.

3.1 Introduction

As discussed in Chapter 1, a basic component of the signal processing schemes proposed in this thesis work, is the generation of linearly-chirped pulses at the repetition rate of the individual tributaries. As illustrated in Fig. 3.1, the incoming OTDM

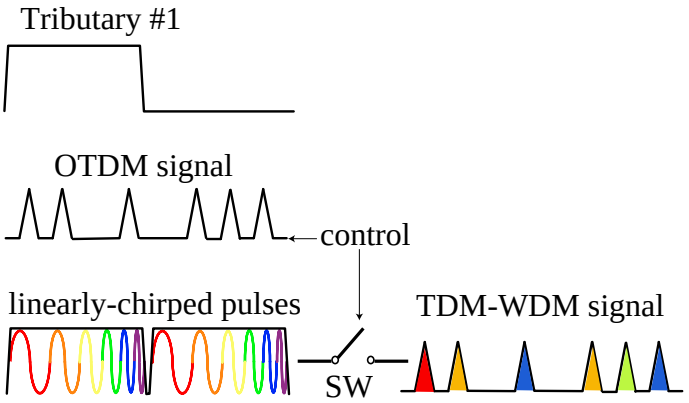

Figure 3.1: OTDM to mixed TDM-WDM multiplexing format conversion with ideal rectangular linearly-chirped pulses. SW: optical switch.

data signal is converted onto a mixed time-frequency division multiplexing signal (TDM-WDM) by gating the linearly-chirped pulses in an ultrafast optical-switch (SW) controlled by the OTDM data.

For the multiplexing-format conversion to be completely and successfully achieved, the generated linearly-chirped pulses should have the following characteristics:

1. The duration of the linearly-chirped pulses at the peak intensity should equal the bit-period of the individual tributary channels, so that each aggregated channel is shifted onto a different centre wavelength. The repetition-rate of the linearly-chirped pulses should be synchronised to the clock of the individual tributaries, so that each channel is shifted onto a precise centre wavelength and data is not lost.

2. The frequency chirp should be perfectly linear to assure that all the tributaries are mapped onto equally spaced channels with identical spectral bandwidths. Furthermore, the full bandwidth of the linearly-chirped pulses should be sufficiently wide to allow spectral separation of all the tributary channels. For example, a 100-Gb/s OTDM signal, composed of 10×10-Gb/s individual tributaries, requires approximately a −3-dB bandwidth of 40 nm, regardless of the switching mechanism. This estimation is obtained by assuming that a 100-Gb/s OTDM signal consists of a stream of 3 ps pulses, which is the maximum pulse duration to prevent significant inter-symbol interference degradation at this bit rate, which have transform-limited −3-dB bandwidth of 1.2 nm (assuming a Gaussian envelope). To avoid increasing adjacent channel crosstalk when either

processing the signal in the time or frequency domains, a one-to-one mapping of the tributary channels from the time to the frequency domain is required. Under these conditions, the tributary channels spectral separation is 3-times the individual channel bandwidth, since the pulse duration is a third of the bit slot, which is equal to 3.6 nm. Consequently, 10 tributary channels occupy approximately a total bandwidth of 40 nm.

3. The top of the linearly-chirped pulses should be flat across the full envelope to ensure that power is equal for all converted channels. Also, a steep edged envelope avoids the situation that the same channel is mapped onto two different spectral bands, caused by simultaneously gating the overlapping tails of two consecutive chirped pulses, which can result in undesired crosstalk effects. The rise and fall times of the chirped pulse intensity-envelope should thus be shorter than half of the OTDM signal bit-period.

Fig. 3.2 shows the ideal temporal and spectral characteristics for the linearly-chirped pulses. The contour plot shows the time-frequency distribution (spectrogram) of the intensity of these pulses, on a logarithmic scale represented by the colour lines shown in the side bar, and normalised to unity. The spectrogram is the set of spectra of all gated parts of the waveform as the delay between the waveform and the gate is varied [80]. In this chapter, the gating function was a 0.5-ps Gaussian pulse (i.e. much shorter than the linearly-chirped pulses), which facilitated a high resolution spectrogram in both the time and frequency domains. The figure shows that the temporal envelope of the 100-ps pulses is mapped in a one-to-one relation to a bandwidth of 4 THz. The pulse duration and bandwidth plotted in the figure are given as an example. Appropriate analysis and discussion of the chirped pulse bandwidth versus line bit-rate for TDM-WDM conversion is provided in chapter 4.

3.2 Pulse Chirping in Highly Nonlinear Fibre

A linear chirp is induced through a quadratic phase-modulation process. A primary issue for the generation of the linearly-chirped pulses shown in Fig. 3.2 is, therefore, the large quadratic phase-modulation required to sufficiently broaden the spectrum of the long rectangular pulses. For instance, the pulses in Fig. 3.2 have a total

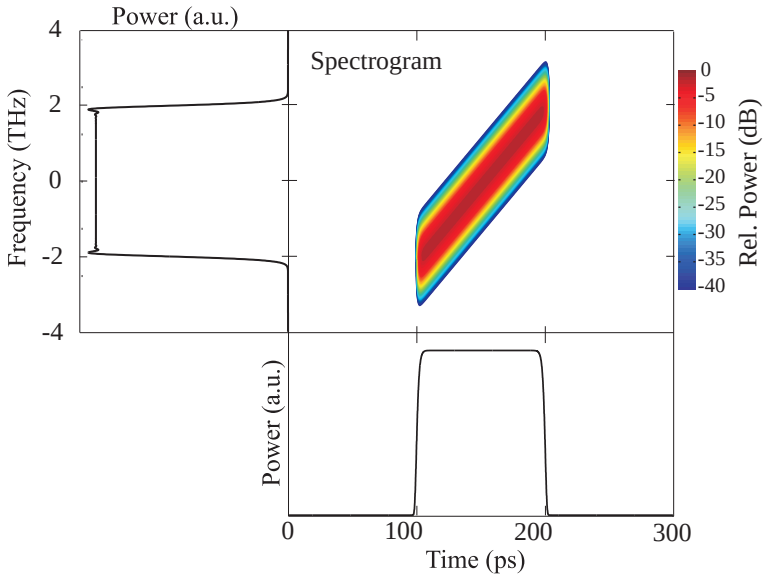

Figure 3.2: Ideal linearly-chirped pulse to enable TDM-WDM conversion at the base bit-rate of 10 Gb/s.

phase-shift of 100π rad. Long rectangular pulses can easily be generated by externally modulating the intensity of a CW laser beam, and electro-optic phase modulators can be used to induce a quadratic phase-modulation. However, state-of-the-art electro-optic phase modulators can induce at most a total phase-shift of about 15π rad. In [81] the generation of highly linearly-chirped pulses using an integrated $LiNbO_3$ phase and intensity modulator, which externally modulates a CW laser beam to produce 50-ps Gaussian pulses with a bandwidth of 7 nm at the repetition rate of 10 GHz, was demonstrated. Generation of broader bandwidth pulses using this technology is, however, a challenging research goal. The above results required the fabrication of a remarkably long 15-cm $LiNbO_3$ waveguide, which was driven at 10 GHz with an RF power of 36 dBm to achieve the 15π-rad phase modulation index. Nonetheless, low drive voltage $LiNbO_3$ phase and intensity integrated modulators are a great research achievement and several applications, including the techniques proposed in this thesis, can benefit from this compact source of highly linearly-chirped pulses.

Large frequency modulation (chirp) in optical pulses can also occur through excitation of the fibre nonlinearities. For example, self-phase modulation (SPM) occurs when the pulse itself induces variation of the medium's refractive-index resulting in a change in the phase of the pulse across the pulse envelope due to the intensity variation. During this process new spectral components are generated and the pulse suffers spectral broadening. The efficiency of the SPM effect depends directly on the pulse's

intensity profile and on the nonlinear coefficient of the medium. However, the group velocity dispersion (GVD) of the medium also chirps the pulse, and the interplay between GVD and SPM determines the pulse evolution. Briefly, if SPM dominates in the anomalous dispersion regime the pulse evolves into a higher-order soliton, while in the normal dispersion regime the chirp due to SPM and GVD add together, which opposes the formation of soliton pulses.

Ultra-wide spectral broadening spanning several hundreds of nanometers has been reported by many research groups based on supercontinuum generation processes. However, pulse breakup, and phase coherence degradation can be severe during the generation process if the spectrum extends into the anomalous dispersion regime. Even at high repetition rates (higher than 1 GHz), where the relatively low pulse energies induce only Kerr nonlinear refractive effects, phase coherence can be severely degraded by modulational instability [82, 83].

For the generation of spectral broadening suitable for telecommunications applications, the use of either dispersion decreasing fibres (DDF) [84], or low normal-dispersion dispersion-flattened fibres (ND-DFF) [85] has been reported. The use of DDFs can give significant spectral broadening. For example, in [86] the generation of 1 μm broad supercontinuum in a nonlinear DDF, from 110-fs pulses emitted by a passive mode-locked fibre laser at a wavelength of 1550 nm is reported. However, in the DDF the flatness of the spectrum is usually compromised by higher-order soliton effects unless adiabatic soliton compression is used. The schemes employing ND-DFFs take care to ensure that the zero dispersion wavelength of the fibre lies well outside the generated wavelength range in order to avoid the onset of modulational instability, which may also compromise the achievable spectral flatness. Several high speed signal processing schemes have been proposed based on the wide, flat supercontinuum generated in ND-DFF [87]. This fact led us to investigate chirped pulse generation in the normal dispersion regime of the dispersion shifted highly nonlinear fibres shown in Table 2.1.

The first measurements we carried out to characterise the chirp generation in these fibres, involved measuring the achievable spectral broadening of 2.5-ps transform limited pulses generated from an actively mode-locked fibre laser at a repetition rate of 10 GHz; the experimental setup is shown in Fig. 3.3. The pulses were externally modulated with a pseudo-random bit-sequence (PRBS), so that higher pulse energies

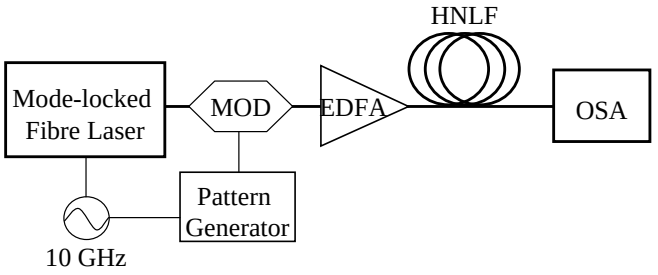

Figure 3.3: Experimental setup to characterise spectral broadening in a HNLF.

could be achieved due to the presence of zeros in the bit stream. The pulses were then amplified to an average power of 19 dBm and launched into the highly nonlinear fibre. Fig. 3.4 shows the measured broadened spectra for the HNL-DSF2, HNL-DFF2, and HNL-DFF3 fibres in Table 2.1. In cases (a) and (b) the pulses were launched in the normal dispersion regime. In both cases, the broadened spectrum had a -3-dB bandwidth of roughly 20 nm, however, the larger dispersion slope of HNL-DSF2 induced asymmetrical broadening of the spectral envelope relative to the seed pulse centre wavelength. The original spectral band of the seed pulses is shown in the dashed trace.

In case (c), the pulses were launched in the anomalous regime of HNL-DFF3. Although the small dispersion-slope ensures symmetrical spectral broadening, large ripples in the spectral envelope are the consequence of higher-order soliton formation. Furthermore, the degradation of the spectral lines in comparison to the previous cases is strikingly clear, which indicates a degradation of the pulse-to-pulse temporal coherence. Note that in this case, the launched average power was limited to 15 dBm to avoid the complete suppression of the spectral lines.

The physical reason for the spectral ripples is that the same frequency appears at different instants across the pulse, which leads to spectral interference that is different for different frequencies. In the case of nonlinear chirping in the anomalous regime, there is a larger contribution to the interference as the induced chirp is oscillating across the full pulse envelope. By contrast, in the normal regime the chirp oscillates just at the pulse edges, and therefore the interference effects are smaller.

It was, therefore, observed that HNL-DSF2 and HNL-DFF2 are more suitable fibres to generate spectrally broad linearly-chirped pulses. At the early stage of this thesis

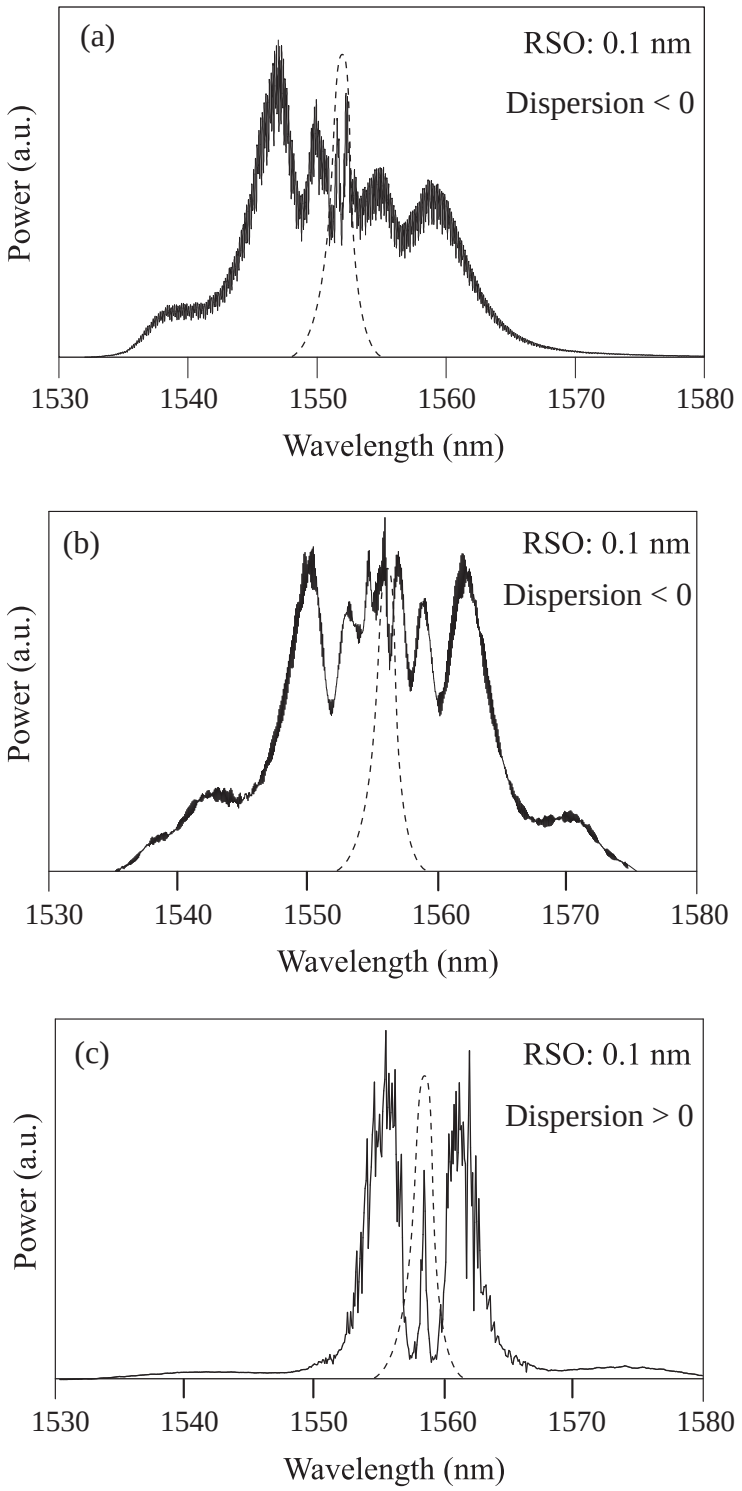

Figure 3.4: Measured spectral broadening of 2.5-ps pulses with an average power of (a) 19 dBm at the repetition rate of 10 GHz in HNL-DSF2, (b) 19 dBm at the bit-rate of 10 Gb/s in the HNL-DFF2, (c) 15 dBm at the bit-rate of 10 Gb/s in the HNL-DFF3. The dashed trace shows the spectrum of the seed pulse.

work, only HNL-DSF2 was available, and we proceeded at that time with investigating the phase and amplitude of the spectrally broadened pulses. The characterisation

of the complex amplitude of short pulses can be determined from a spectrogram of the pulse intensity. A widely established technique to measure spectrograms is frequency-resolved optical-gating based on the second-harmonic generation (SHG-FROG) of the pulses under test, or in other words the pulse frequency resolved autocorrelation. However, to characterise broad spectrum pulses it is necessary to use a nonlinear SHG crystal that provides phase matching across the full bandwidth of the pulses. Broadband phase matching requires a thin crystal to minimize the group velocity mismatch between the second harmonic and the pump pulses, while high SHG efficiency at the 10-GHz pulse rate requires the crystal material to be strongly nonlinear. Unfortunately, the SHG-FROG in our lab has a standard crystal, and thus we were unable to use this technique to characterise experimentally the pulses shown in Fig. 3.4.

Consequently, we proceeded by numerically simulating the pulse electric-field using the modelling techniques described in Chapter 2. The HNL-DSF2 parameters considered in the numerical simulation are shown in Table 2.1.

The model was based on solving the nonlinear Schrödinger equation using the symmetric split-step Fourier algorithm taking into account the fibre attenuation, group-velocity dispersion, dispersion slope and the nonlinear Kerr effect. Considering the relatively low pulse energy available at the 10-GHz repetition rate, and to simplify the analysis, the effects of stimulated Raman scattering and self-steepening were neglected.

The main advantage of the split-step Fourier algorithm compared to other methods is the possibility of computing the complex amplitude of the pulses in time and frequency domains at different distances along the fibre in one simulation run. It is, therefore, a good tool to study pulse envelope and spectral evolution in the fibre. Fig. 3.5 shows the spectrogram of the pulses generated in the HNL-DSF2, when 2.5 ps sech^2-shaped pulses with an energy of about 10 pJ are launched into the fibre. The figure also shows the corresponding pulse envelope and spectrum. The calculated spectrum shows good agreement with the measured spectrum in Fig. 3.4(a). During propagation in the normal dispersion regime of a nonlinear fibre, the pulses evolve initially into a parabolic shape and deform later into a square-like form. The pulse full-width at half-maximum (FWHM) evolution in the HNL-DSF2 is shown in Fig. 3.6(b). It can be seen that the pulse duration broadens from 2.5 ps to 8 ps.

The calculated pulse envelope shows a negative slope on the top towards the trailing edge. The explanation is that the trailing edge is composed of lower frequencies, which travel faster, and therefore the dispersive effects are more significant in this part of the pulse.

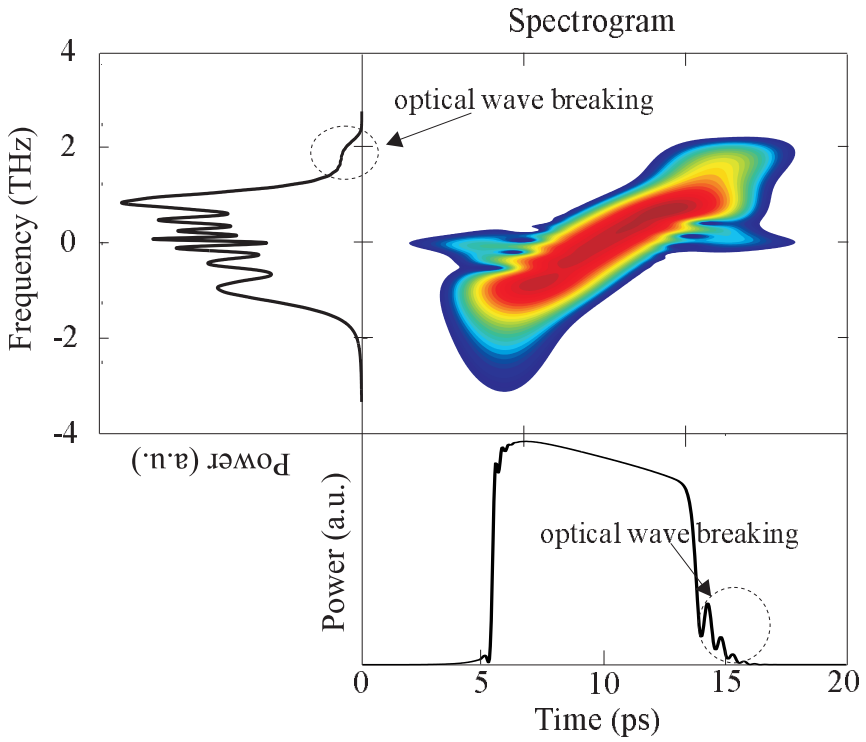

Figure 3.5: Spectrogram of the chirped pulses generated in HNL-DSF2 and correspondingtime and frequency marginals.

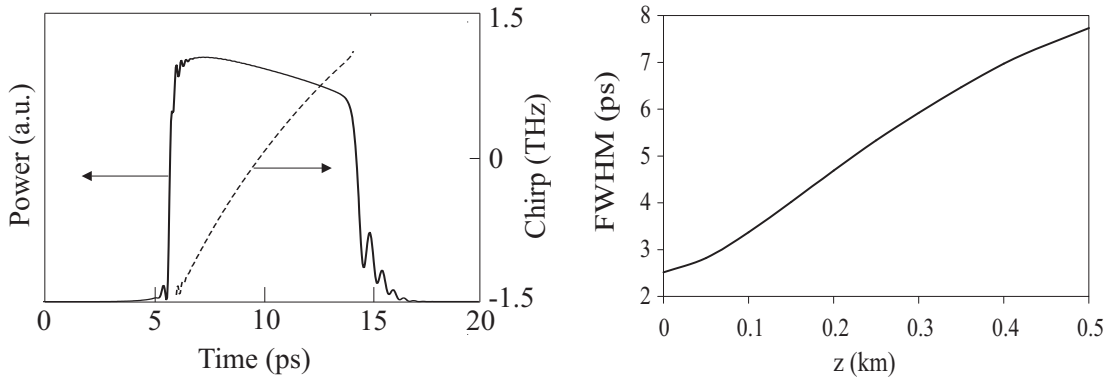

Figure 3.6: (a) Linearly-chirped pulse generated in HNL-DSF2. (b) Pulse duration evolution along the fibre length.

Optical wave breaking occurs when the leading and trailing edges of the pulse overlap the unchirped components in the pulse wings [88]. Consequently, different frequencies with a phase difference overlap temporally, and an oscillating intensity envelope

develops at the pulse wings. This is associated with the formation of spectral side lobes in the pulse spectrum. In the case of HNL-DSF2, shown in Fig. 3.5, the group-velocity dispersion is higher for the higher frequency components due to the large dispersion-slope of the fibre and, as the pulse trailing edge consists of higher frequencies, optical wave breaking occurs first at the trailing edge. In Fig. 3.6(a), the pulse generated at the output of HNL-DSF2 and its corresponding frequency chirp are shown; the effect of the dispersion slope in the chirp linearity is clearly evident.

Having discussed in this section the reasons that led us to choose spectral broadening in the normal dispersion of highly-nonlinear dispersion-shifted fibres, I proceed in the next section to describe the stretching of the envelope of these pulses.

3.3 Fourier Transformation of Stretched Linearly-Chirped Pulses

As shown in Fig. 3.6(b), the pulses after the chirp generation are about 8-ps long, which is insufficient for the target applications of this work. The TDM-to-WDM format conversion requires linearly-chirped pulses wider than 100 ps as discussed in Section 3.1. The obvious solution is to stretch out the previous pulses through linear propagation in an extra length of fibre with well defined GVD. At the input of this fibre, the pulse energy must eventually be reduced to prevent excitation of additional nonlinear effects and consequent chirp distortion. As the pulse stretches, the relative group delay of the different spectral components increases, and this results in an extension of all the frequency components in time. Consequently, the oscillatory structure initially observed on the spectrum is also now observed on the pulse temporal envelope. This results in a fundamental property of highly linearly-chirped pulses, i.e. that the frequency and time components are in a direct one-to-one relation and, therefore, the temporal and spectral envelopes have similar shapes, as demonstrated in Appendix C. In fact, the stretched pulse is, to within a phase factor, proportional to the Fourier transform of the input signal after propagating through a medium with a total dispersion given by:

$$|\beta_2|L \gg \frac{\Delta T}{\Delta \omega} \tag{3.1}$$

Table 3.1: DCF parameters measured at 1550 nm

attenuation [dB/km]	dispersion [ps/nm/km]	slope [ps/nm^2/km]	γ [1/W/km]
0.5	−190	-0.4	5

where ΔT is the initial pulse duration, and $\Delta\omega$ is the −3-dB bandwidth of the chirped pulses. The details of the mathematical derivation that lead to the Fourier transformation condition are given in Appendix D.

Figs 3.7 and 3.8 show calculations of the spectrogram and associated temporal and spectral envelopes of pulses stretched in a length of the dispersion compensating fibre (DCF) shown in Table 3.1 for chirp generated in different highly nonlinear fibres. In Fig 3.7, the pulses are chirped in the normal dispersion regime of the highly nonlinear fibres, and the dispersion-flattened fibre HNL-DFF2 and the dispersion-shifted fibre HNL-DSF2 were considered in cases (a) and (b), respectively. In Fig 3.8, the pulses are, in contrast, chirped in the anomalous dispersion regime of the highly nonlinear fibres, and the dispersion-flattened fibre HNL-DFF3 and the dispersion-shifted fibre HNL-DSF3 were considered in cases (a) and (b), respectively. The pulse stream average-power at the DCF input was attenuated, in all the simulated cases, so that the pulse propagates in the linear regime, and the spectral envelope is not distorted.

The Fourier transformation condition for the pulses in Fig. 3.7 is about $L_{\mathrm{DCF}} \gg 2\,\mathrm{m}$. This estimation was obtained by substituting in Eq. (3.1) a pulse duration of 7 ps, which was inferred from Fig. 3.6(b), a bandwidth of 3 THz, which corresponds to the −3-dB bandwidth of the spectra in Fig. 3.7, and considering the DCF dispersion coefficient (β_2) in Table 3.1. The total amount of dispersion, required to stretch the envelope of the chirped pulses to about 100 ps, was −6 ps/nm and −5 ps/nm in cases (a) and (b), respectively. This corresponds to a length of DCF of about 28 m, which satisfies the above Fourier transformation condition.

As it can be seen in Fig. 3.7(b), the dispersion slope of HNL-DSF2 induces significant asymmetry in the temporal and spectral envelopes. In Fig. 3.7(a), the long tails formed on the temporal envelope are, however, more detrimental to the signal-processing schemes proposed in this thesis. The long tails are a consequence of optical-wave-breaking, and are mapped from the spectral onto the temporal domain through the Fourier transformation effect and, for HNL-DFF2, optical-wave-breaking

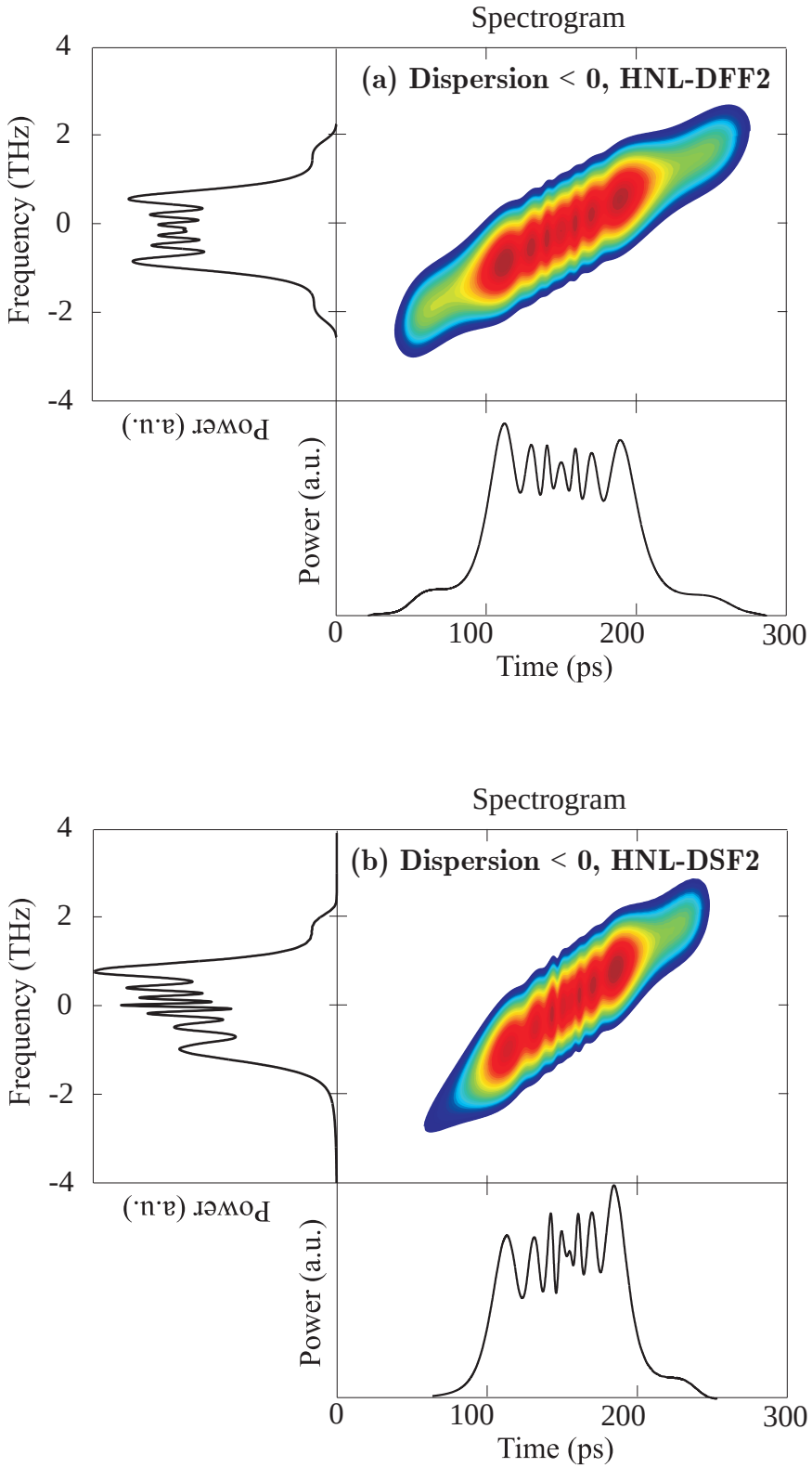

Figure 3.7: Spectrogram and associated temporal and spectral envelopes of a sech^2-pulse chirped in the (a) HNL-DFF2 with an average power of 20 dBm, and stretched in 32 m of DCF (−6 ps/nm), (b) HNL-DSF2 with an average power of 20 dBm, and stretched in 26 m of DCF (−5 ps/nm).

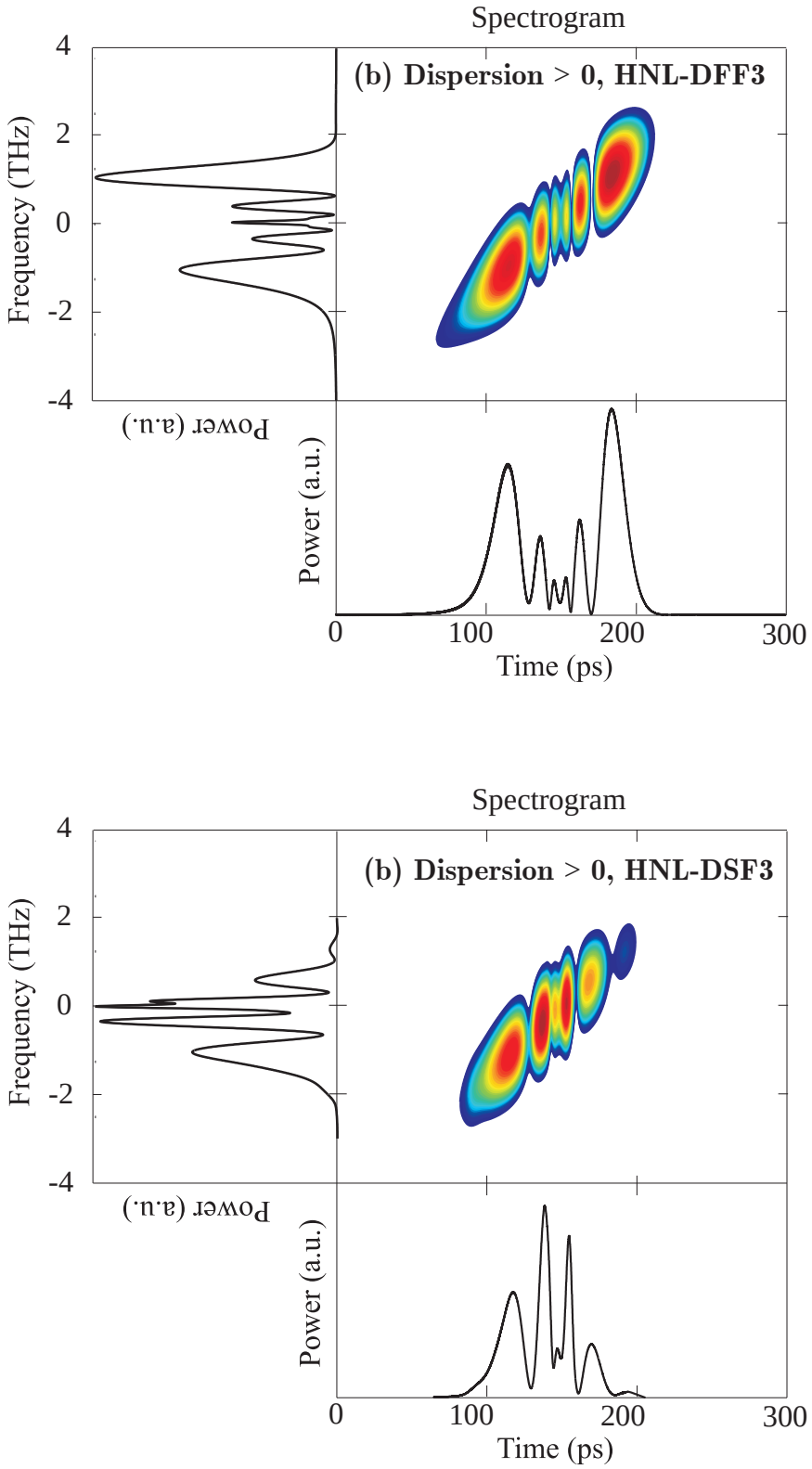

Figure 3.8: Spectrogram and associated temporal and spectral envelopes of a sech^2-pulse chirped in the (a) HNL-DFF3 with an average power of 16 dBm, and stretched in 21 m of DCF (−4 ps/nm), (b) HNL-DSF3 with an average power of 10 dBm, and stretched in 21 m of DCF (−4 ps/nm).

occurs in both the leading and trailing edge of the pulse due to the reduced dispersion slope of the fibre.

In Fig. 3.8, the large oscillations in the spectra are induced by solitonic effects in the anomalous dispersion regime of the highly nonlinear fibres. As the higher-order soliton pulse has a nonlinear chirp in the centre of the pulse, the Fourier transformation condition, given in Eq.(3.1), cannot be applied. Although, the temporal envelope of the stretched pulses is still Fourier transformed, as can be seen. Consequently, due to the large oscillations formed in the temporal envelope of the stretched pulses, these pulses are not suitable for the schemes proposed in this thesis.

To verify experimentally the Fourier transformation effect, the experimental setup in Fig. 3.9 was prepared. Fibre laser pulses at the repetition rate of 10 GHz were gated down in an intensity modulator to 2.5 GHz, so that the pulses would not overlap when their temporal envelope was stretched. The pulses were then amplified and coupled into the highly nonlinear HNL-DSF2, where the pulses were heavily chirped. The chirped pulses were then attenuated, to prevent nonlinear effects in the DCF, and finally coupled into 100-m of DCF, where the pulse envelope was stretched out to about 400 ps. Measurements of the pulse envelope and spectrum at the output of the DCF were carried out, and the measured oscilloscope trace and optical spectrum are shown in Fig. 3.10. As it can be seen, pulse and spectrum have similar oscillating features, which confirms the Fourier transformation effect. The pulse shown in Fig. 3.10 is close to our aimed target of generating linearly-chirped rectangular pulses. The pulse envelope, however, does not possess a flat-topped rectangular shape. The next section describes different approaches to shape the chirped pulses' temporal and spectral envelope.

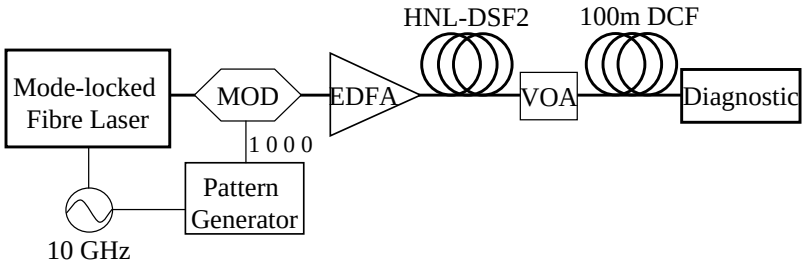

Figure 3.9: Experimental setup to generate stretched linearly-chirped pulses.

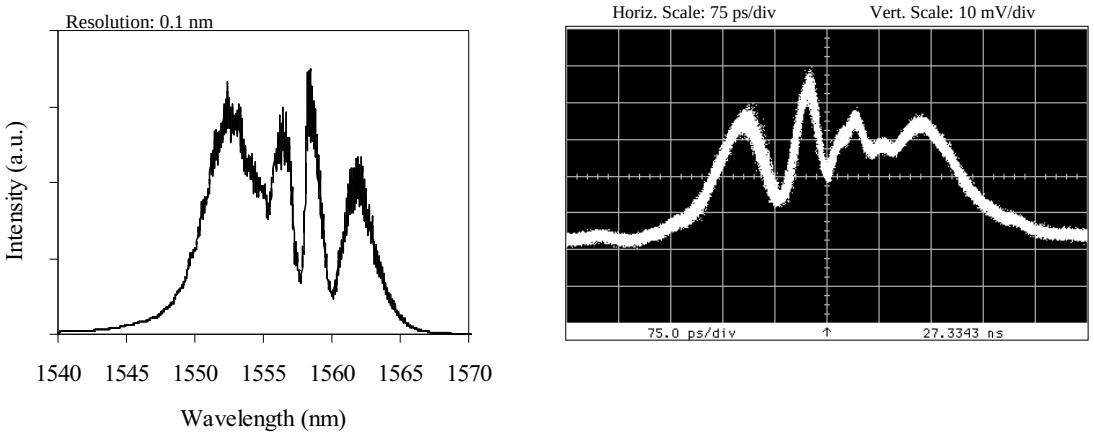

Figure 3.10: Measured pulse envelope and spectrum after propagation in the DCF.

3.4 Shaping of Linearly-Chirped Rectangular Pulses

The origin of oscillations (ripples), in the spectrum of pulses spectrally broadened in a highly-nonlinear fibre, relates to the nonlinear chirp induced by self-phase modulation (SPM) of conventional pulse forms, such as Gaussian or soliton pulses. Moreover, the combination of dispersion and nonlinear effects can lead to optical-wave-breaking, which produces oscillations on the edges of the pulse envelope and the development of side-lobes in the associated spectrum. The depth of the spectral oscillations, which can severely compromise the signal processing schemes proposed in this thesis, is mainly determined by the shape of the intensity envelope of the pulses, the dispersion profile of the nonlinear fibre, and the fibre nonlinear coefficient.

Recently, the generation of smooth (ripple free) SPM broadened spectrum using the nonlinear formation of parabolic pulses in a normal dispersion fibre amplifier has been suggested and demonstrated [89]. A few attempts to generate linearly-chirped parabolic pulses for telecommunication applications have, thereafter, been made. In general, these schemes are based on custom-made fibres, for example a km-long highly-nonlinear erbium-doped fibre was used in [90], while a dispersion-decreasing fibre with a hyperbolic dispersion profile was proposed in [91]. Although parabolic pulse formation has been observed, and spectra free of ripples obtained, these spectra do not have sharply defined edges, as is desired for our applications.

In this section, a novel technique based on pre-shaping the optical pulses at the input of the nonlinear fibre into a form that evolves into a flat spectrum with steep spectral

edges, through SPM in a conventional commercial highly-nonlinear dispersion-shifted fibre (HNL-DSF), is described [92]. By appropriate shaping of the pulses, it is possible to compensate for optical-wave-breaking and pulse distortion effects within the HNL-DSF in order to ensure that the pulse evolves into a highly linearly-chirped pulse with a rectangular shaped optical spectrum. The necessary pulse shaping can be achieved by the flexible linear-filtering associated with the reflection from a superstructured fibre-Bragg-grating (SSFBG), as described in Chapter 2.

3.4.1 Pulse Pre-Shaping Technique using a SSFBG

The concept of the technique used to generate linearly-chirped rectangular pulses is illustrated in Fig. 3.11. Initial pulses of a well defined shape and power, e.g. soliton pulses from a mode-locked fibre laser, are pre-distorted in order to generate linearly-chirped pulses with a flattened spectrum through SPM in a given length of a commercial HNL-DSF. In order to establish the required pulse pre-distortion, the target output spectrum is defined, i.e. pulses with a flat spectrum with sharp edges and a linear chirp, and reverse propagation of these target pulses back through the HNL-DSF is calculated using the nonlinear Schrödinger equation. Once the input pulse shape is established the required complex grating response can be evaluated from a knowledge of the input pulse shape [70]. The required spatial superstructure function of the SSFBG can then be calculated using either the Fourier transform approximation, described in Chapter 2, or an inverse-scattering algorithm.

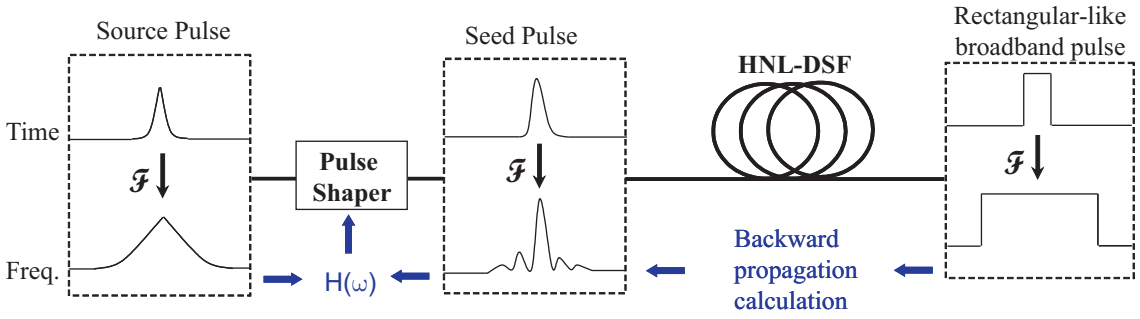

Figure 3.11: Generation of rectangular linearly-chirped pulses in a HNL-DSF using pulse pre-shaping.

3.4.1.1 Design of the SSFBG pulse shaper

As a practical example, the grating response required to generate 8-ps linearly-chirped super-Gaussian pulses with a −3-dB bandwidth of 13 nm and flat topped spectrum, shown in the dashed traces in Fig. 3.12, from 1.8-ps soliton pulses with a central wavelength of 1557.5 nm, was calculated. A launched pulse energy of 15 pJ and the parameters of HNL-DSF2 were considered. This choice corresponds closely to the input pulse characteristics and the fibre used in our proof-of-principle experiments described below.

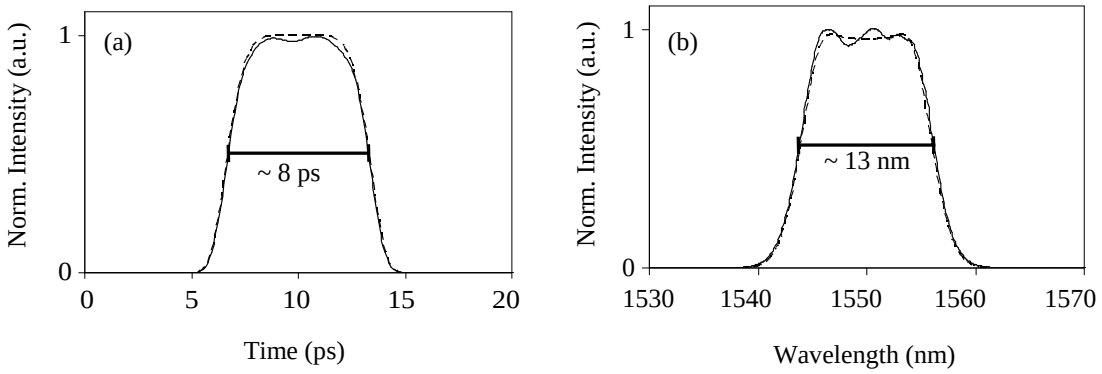

Figure 3.12: Target linearly-chirped pulse (dashed trace) and calculated SPM-broadened pulse after pulse pre-shaping with the designed SSFBG (solid trace) (a) temporal intensity envelope, (b) spectral intensity envelope.

In Figs. 3.13(a) and (b), the temporal and spectral envelopes of both the input 1.8-ps soliton pulse (dashed line) and the shaped pulse at the input of the HNL-DSF2 (solid line), which was retrieved by reverse propagation of the target pulse, are shown. The inset in Fig. 3.13(b) shows the corresponding group-delay of the input and the pre-shaped pulses. The transfer function of the SSFBG shaper was then numerically calculated by dividing the complex spectral amplitude of the calculated seed pulses with that of the input laser pulses. The maximum reflectivity of the SSFBG was limited to 35% so that the Fourier approximation between the grating reflection and impulse response would hold. Fig. 3.13(c) shows the calculated SSFBG refractive-index modulation along the grating length. The SSFBG is 3-mm long with a phase profile showing that the grating period is different in the first and second half of the grating length. The asymmetry of the refractive-index modulation is a consequence of the pulse spectral distortion required to compensate for the dispersion slope of HNL-DSF2.

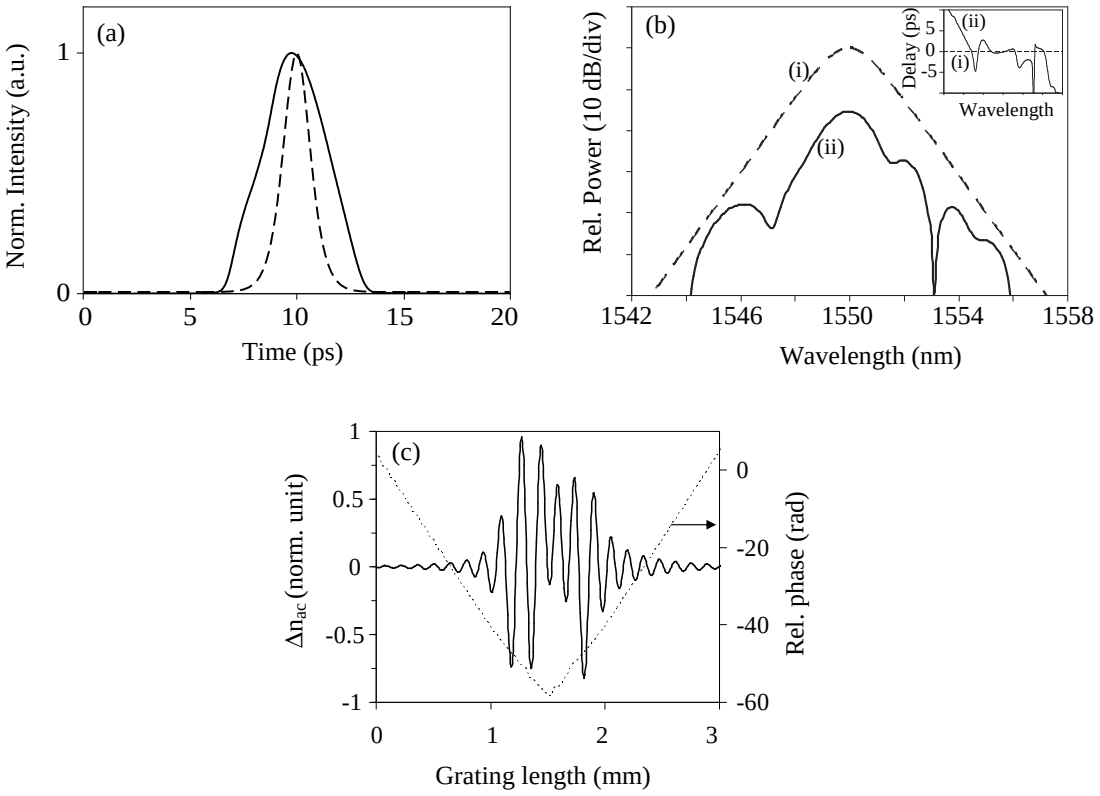

Figure 3.13: (a) Temporal envelope of the source pulses (dashed trace) and of the pulses retrieved by reverse propagating the target pulses in HNL-DSF2 (solid trace), (b) corresponding spectral envelopes, the inset shows the corresponding relative group-delay. (c) Normalised refractive-index modulation and phase of the SSFBG that shapes the 1.8-ps soliton source pulses into the retrieved pulses.

To guarantee that the grating structure was within the resolution limits of the UV-writing technique, it was necessary to limit the bandwidth of the grating by applying an apodisation profile to the grating reflectivity. To assess the impact of this, the same apodisation profile was applied to the pre-distorted pulses, and their nonlinear propagation through HNL-DSF2 was subsequently calculated. The resulting pulse is seen to be very similar to the initial target pulse, although it does possess a small degree of ringing ($\sim$0.25 dB), see Fig. 3.12 − solid trace. This level of distortion is, however, far less than would be obtained without pre-distortion confirming the merit of the pre-shaping approach.

3.4.1.2 Experimental Results

Although the grating design in Fig. 3.13(c) has yet to be produced, a grating with a reasonably similar spectral response to that shown in Fig. 3.13(a), previously used for

square pulse generation, was utilised. Therefore, using this non-ideal grating, some provisional experiments were performed. The experimental setup used is shown in Fig. 3.14. 1.8-ps sech^2 pulses, from a mode-locked fibre laser at the repetition rate of 10 GHz, were first amplified and coupled into the SSFBG via the port-1 of an optical circulator. The reflection of the SSFBG, which shapes the spectral amplitude of the fibre laser pulses, is coupled back into the port-3 of the circulator. The shaped pulses are then amplified to an average power of 22 dBm, which corresponds to a pulse energy of 15 pJ, and coupled into HNL-DSF2. Fig. 3.15(a) shows the spectrum of the 1.8-ps mode-locked fibre-laser pulses, whilst Fig. 3.15(b) shows the spectrum reflected off the SSFBG. A total insertion loss of 16 dB was measured between the circulator ports. From the autocorrelation measurement of the shaped pulses we estimated a full-width at half-maximum of 5 ps.

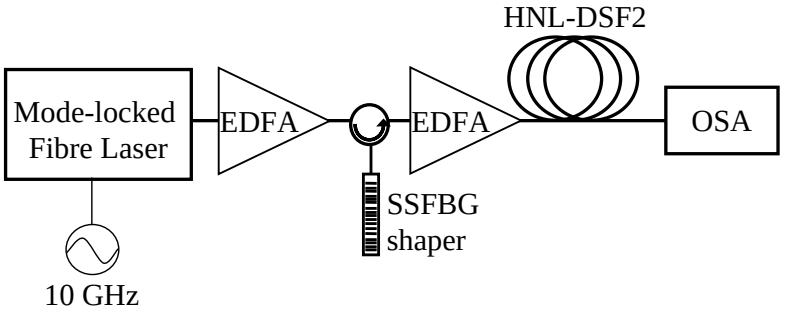

Figure 3.14: Schematic of the experimental setup used to generate rectangular linearly-chirped pulses.

In Figs. 3.16(a) and (b), the SPM-broadened spectra, in the HNL-DSF2, without and with pulse pre-shaping are shown, respectively. To ensure that the same amount of nonlinear phase-shift arose in the HNL-DSF2 in both cases, the average power of the signal at the fibre input was adjusted to 17.5 dBm and 22 dBm, respectively, so that the peak power of the propagating pulses is the same.

Fig. 3.16(a) shows the spectral broadening of the 1.8-ps laser pulses. An asymmetric spectrum with large ripples, with 4.5-dB intensity fluctuation, is observed. Fig. 3.16(b), in contrast, shows the spectral broadening of the pulses pre-shaped in the SSFBG. An almost rectangular spectral envelope is formed and an SPM ripple of less than 1.5 dB is observed in this case. The insets in Fig. 3.16 show the SPM-broadened spectra on a logarithmic scale. Fig. 3.17 gives a close view of the -3-dB bandwidth of the SPM-broadened spectrum using pulse pre-shaping.

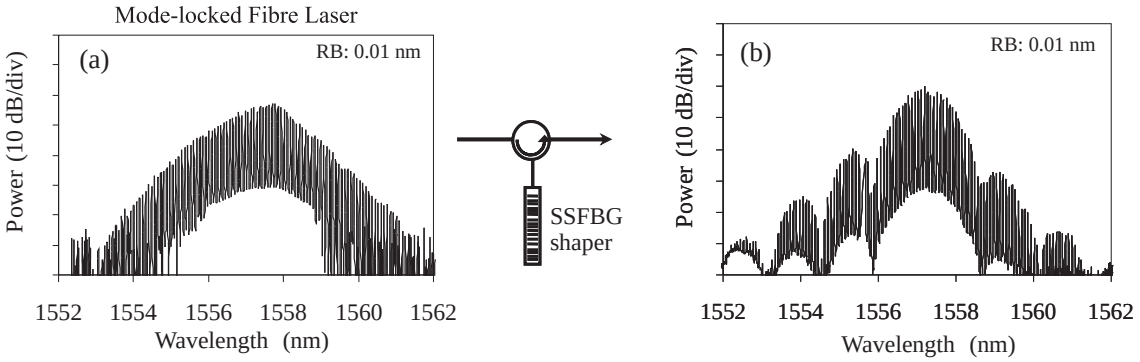

Figure 3.15: Optical spectrum of the (a) source pulses, (b) pulse shaped in the SSFBG.

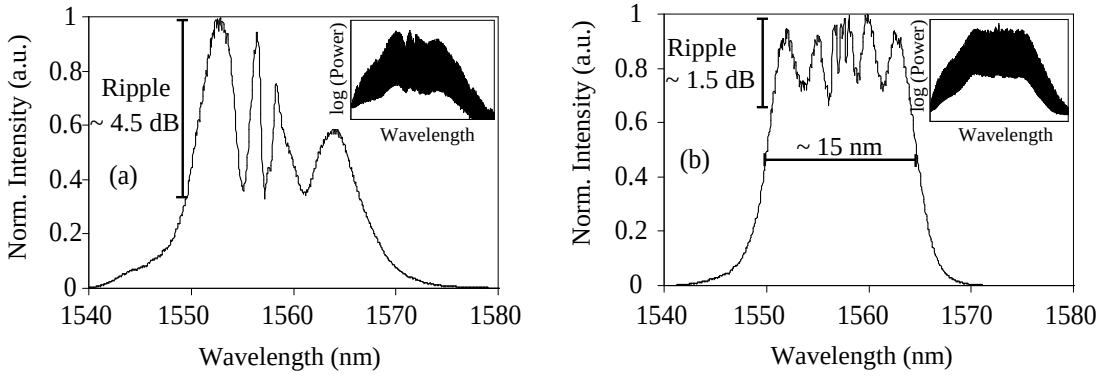

Figure 3.16: Optical spectrum, in a linear scale, of the SPM-broadened pulses (a) without pre-shaping, (b) with pre-shaping, RB: 0.1 nm. The insets show the same traces in a logarithmic scale, RB: 0.01 nm.

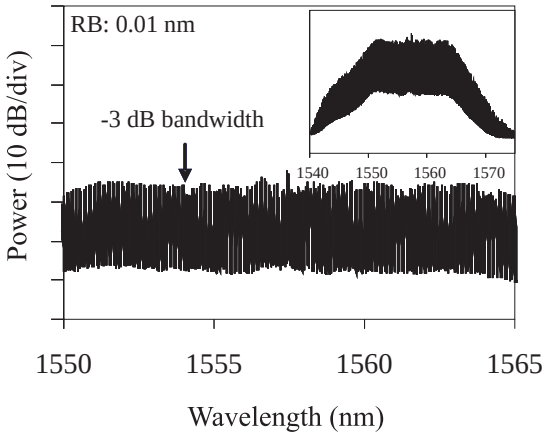

Figure 3.17: Close view of the −3-dB bandwidth of the SPM-broadened pulses with pulse pre-shaping.

The results obtained confirm that adequate pulse pre-shaping can assist the nonlinear evolution of pulses in the normal dispersion regime of an optical fibre. The pulse spectrum shown in Fig. 3.16(b) is close to the ideal spectrum required to implement

the signal-processing schemes proposed in this thesis. This technique, however, as opposed to soliton and parabolic pulses, does not exploit a stable nonlinear propagation regime. The technique is therefore highly sensitive to variations in parameters affecting the nonlinear propagation, such as the pulse energy. The issues of sensitivity and stability therefore need further investigation.

3.4.2 Spectrum-Slicing with a Linearly-Chirped Fibre Bragg Grating

In this section I describe another scheme to shape SPM-broadened pulses. The principle is to use an equalising filter to remove the ripples generated in the chirping process. These gratings were designed to use the full pulse bandwidth and alter its amplitude and phase characteristics in order to obtain the desired waveform.

Although a few sophisticated FBG structures were designed in order to shape the envelope of the linearly-chirped pulses into a rectangular form, several practical issues relating to the FBG fabrication did not make their production possible. Instead, a flat-top linearly-chirped fibre-Bragg-grating (LCFBG) was fabricated, which allowed the demonstration of the shaping principle and generation of rectangular linearly-chirped pulses of limited bandwidth, as I describe in this section.

Figure 3.18 shows the spectral profile of the LCFBG. The grating reflection spectrum shows a bandwidth of 6 nm centred at 1551 nm and a relative group-delay of

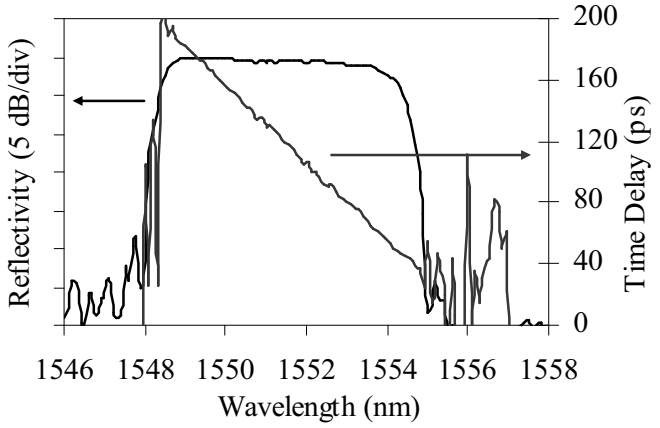

Figure 3.18: Linear-chirp fibre-Bragg-grating spectral response characterisation.

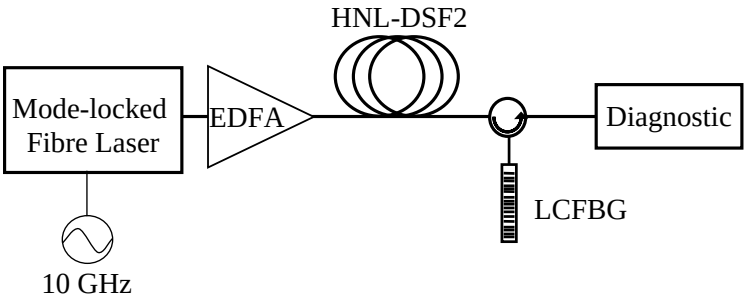

Figure 3.19: Experimental setup to generate rectangular linearly-chirped pulses using a LCFBG.

$-24\,\mathrm{ps/nm}$. The grating can thus be used as a rectangular filter, and can simultaneously apply some additional dispersion to stretch the temporal envelope of the SPM-broadened pulses using the setup in Fig. 3.19. As previously, 2-ps fibre-laser pulses at the 10-GHz repetition-rate were amplified and coupled into HNL-DSF2. The fibre laser centre wavelength was tuned to accommodate the flattest part of the spectrum inside the FBG bandwidth. The resulting SPM-broadened spectrum is shown in Fig. 3.20(a), and as can be seen, due to the dispersion slope of HNL-DSF2, it was possible to produce a flat spectral-region by tuning the fibre-laser centre wavelength. The optical spectrum of the pulses reflected off the LCFBG is shown in Fig. 3.20(b), and as can be seen a 6-nm flat-top rectangular spectrum is obtained. These pulses were then diagnosed in the temporal domain, and Fig. 3.21 shows the corresponding oscilloscope trace and optical spectrum on a linear scale. As shown, the linearly-chirped pulses had an almost flat-top envelope and a duration of 140 ps. If required, a further length of dispersive fibre can be used to adjust the duration of the linearly-chirped pulses.

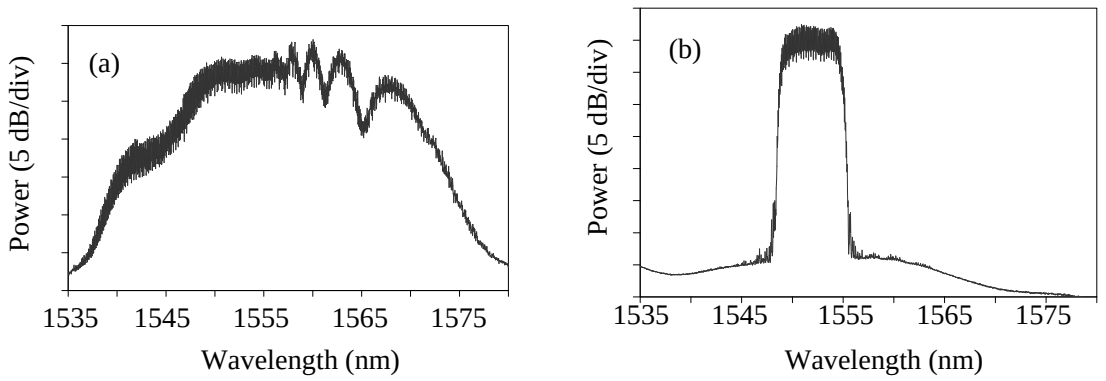

Figure 3.20: Optical spectrum of the (a) SPM-broadened pulses, (b) pulses reflected-off the LCFBG. RB: 0.01 nm.

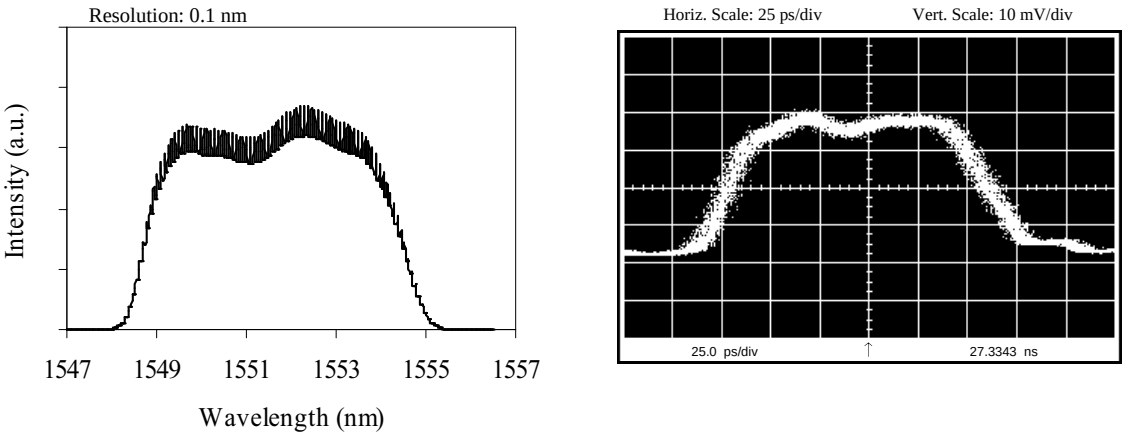

Figure 3.21: Measured spectrum (linear scale) and oscilloscope trace of the pulses reflected off the LCFBG.

3.5 Summary and Discussion

In conclusion, highly linearly-chirped pulses were generated by propagating short fibre laser pulses with high energy in the normal dispersion regime of highly nonlinear fibres. It was demonstrated that the chirp linearity is improved by stretching out the pulse in a normally dispersive medium (an extra length of DCF in our case), where the length of this fibre defines the final chirp-slope and pulse width. However, an oscillatory shape of the pulse envelope is always observed after stretching due to the Fourier transformation of the original shape of the SPM-broadened spectrum. Different approaches were suggested to overcome this issue. Nearly flat-top envelope linearly-chirped pulses were generated either using a pulse pre-shaping technique or a linearly-chirped-fibre-Bragg-grating to slice a flat region of the original SPM-broadened spectrum. The pulses shown in Fig. 3.21 were extensively used in the NOLM switching investigation described in Chapter 4 and in the signal-processing schemes demonstrated in Chapter 5 to map the OTDM signals onto a mixed time and wavelength division multiplexing signal.

Chapter 4

NOLM Switching of Linearly-Chirped Pulses

Overview: In this chapter, I describe the nonlinear optical-gating of linearly-chirped pulses with the nonlinear optical loop mirror (NOLM).

The optical-signal-processing techniques proposed in this thesis rely on converting the incoming TDM signal onto a chirped-WDM replica, so that each tributary can be independently processed in both the temporal and spectral domains. A possible way to achieve this is by gating linearly-chirped pulses at the tributary-channel rate with the high-speed TDM signal using a NOLM switch, see Fig. 4.1. The linearly-chirped pulses are stretched to 100% duty cycle, so that in the NOLM switch each tributary channel gates the linearly-chirped pulse at a different instant across the pulse and thus at a different frequency offset. Consequently, the tributary channels are mapped onto different wavelengths.

Ultrafast optical-gating of linearly-chirped pulses has previously been demonstrated using either fibre or semiconductor nonlinear effects [4, 21, 93, 94]. In all these schemes, the main goal was to spectrally separate the tributary OTDM channels using the linearly-chirped pulses to map the temporal slots into spectral bands. Before this thesis work, the technique that showed the best tributary spectral-separation was based on a semiconductor saturable-absorber [94]. The other techniques, which were based on fibre four-wave mixing [21], semiconductor four-wave mixing [93], and fibre NOLM [4], showed higher-speed operation, as they were based on sub-picosecond

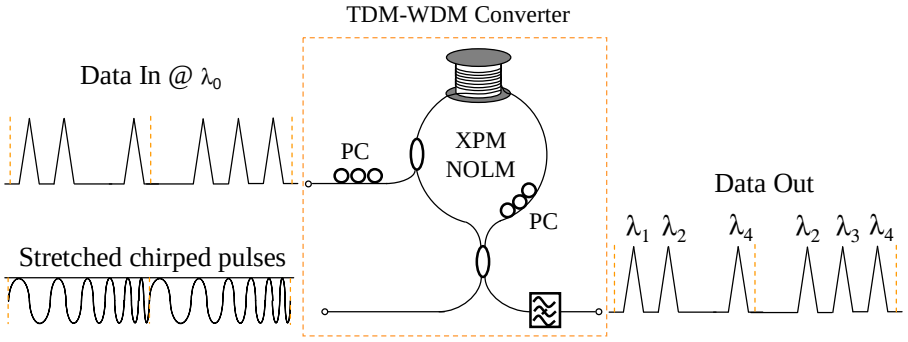

Figure 4.1: Schematic diagram of the TDM to chirped-WDM converter.

response nonlinear effects, but they achieved poor tributary spectral-separation, and therefore, were mainly proposed as demultiplexing schemes to be used at the receiver-end of a transmission system. In particular, in [4], the NOLM switching of linearly-chirped pulses was reported for demultiplexing of 100-Gb/s TDM signals, and to the best-of-my-knowledge this was the only demonstration of optical gating of linearly-chirped pulses with a NOLM-switch previous to my thesis work. Fig. 4.2 shows the optical spectra, which were measured before (figure (a)) and after (figure (b)) the NOLM-switch, reported in [4]. As it can be seen, although the channel separation was about 4 nm, the tributaries were hardly distinguishable.

Much better tributary-channel spectral separation was achieved when a saturable absorber was used as the switch. The reason for that will become clearer as a result of the analysis within this chapter. It is not related to the switching mechanism, but due to the minimum temporal-width of the optical gate required to map the individual tributary channels onto the spectrum of the linearly-chirped pulses. In

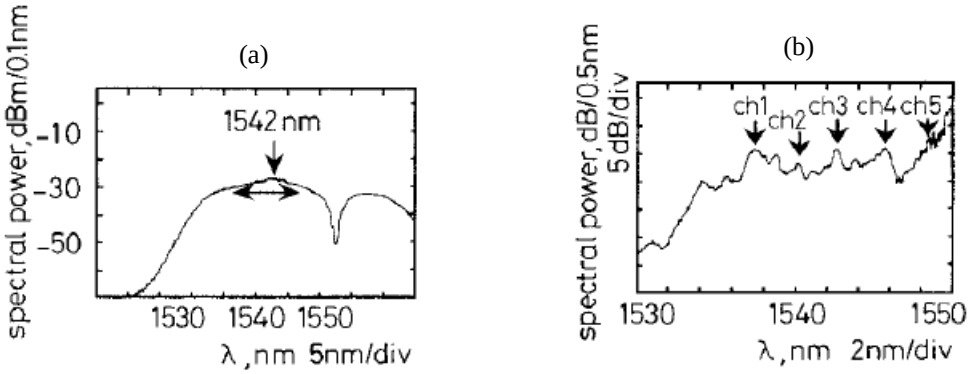

Figure 4.2: Optical spectrum (a) before and (b) after the NOLM switching of linearly-chirped pulses at 100 Gb/s. Figures extracted from [4].

fact, the impulse-response of the saturable absorber was about 10 ps [95], whereas for the NOLM-switch scheme in [4], the induced gate-width was about 2 ps.

In this chapter, I present the conditions for which the maximum tributary spectral-separation can be obtained when using a NOLM switch, and describe the physical interpretation of the spectral features that can be obtained under different chirp-rate and gate-width conditions. I begin by describing experiments that demonstrate the range of performance that is observed depending on the combination of chirp-rate and gating width. I then split the analysis of these measurements into two parts. Firstly, the simple cross-phase modulation (XPM) of the linearly-chirped pulses with the gating pulses is theoretically derived and experimentally observed. The interferometric effects in the NOLM, which lead to a finite switching-ratio of the switched linearly-chirped pulses, are then taken into consideration into the theoretical model, and numerical simulations of the NOLM switching are obtained. I conclude this chapter with an estimation of the multichannel crosstalk when the NOLM switch is operated under different chirp-rate and gate-width conditions.

4.1 Spectrum of NOLM-Gated Linearly-Chirped Pulses

The scheme proposed in Fig. 4.1 was experimentally implemented as shown in Fig. 4.3, in which the repetition rate of the OTDM signal was the same as that of the linearly-chirped pulses. We prepared ∼100 ps linearly-chirped pulses at 10 GHz, using the procedures described in Section 3.4.2, and coupled them to the signal port of the NOLM. At the control port of the NOLM we coupled 10-GHz pulses originated from an electroabsorption modulator followed by a pulse compressor based on a dispersion-decreasing fibre (EAM-DDF). The full-width at half-maximum (FWHM) of the pulses could thus be varied from 1-10 ps using adiabatic soliton compression assisted by distributed Raman amplification. Using this setup, we were able to observe the switched output for different cases of pulse width and control pulse peak power.

In Fig. 4.4 we present experimental data that demonstrates the time-to-frequency mapping of a tributary channel under different conditions of the control-pulse duration (gate temporal-width (τ)) and switch biasing-level (nonlinear phase-shift (ϕ_0)).

The cases presented in Fig. 4.4(a) and (b) correspond to control pulse widths of 2.5 and 9.5 ps respectively, whereas in both cases the maximum induced nonlinear phase-shift was π. The shape of the spectra of the two switched signals exhibit vastly different characteristics. In the instance that the shortest control pulses were used (case-a) a multi-lobed spectrum was obtained. By contrast, when broader control pulses were used for the same nonlinear phase shift (case-b) a cleanly carved switched spectrum, consisting of a well defined channel band, was obtained with a peak to pedestal extinction-ratio of ∼20 dB (which we associate with the finite switching extinction ratio of the NOLM). In case (c) the pulses were the same as in (b) but the induced maximum phase-shift was a factor of two higher in this instance. In this case a multi-lobed spectrum was again obtained.

It is to be anticipated that the existence of spectral sidebands on the switched pulses would result in a significant degradation in signal quality. For example, if the spectral sidebands extend into spectral regions, associated with neighboring channels, they would give rise to interchannel crosstalk and hinder any further signal processing. Moreover, any further processing of the switched signal using dispersive effects in optical fibres, as required for packet compression, would lead to severe pulse shape distortion.

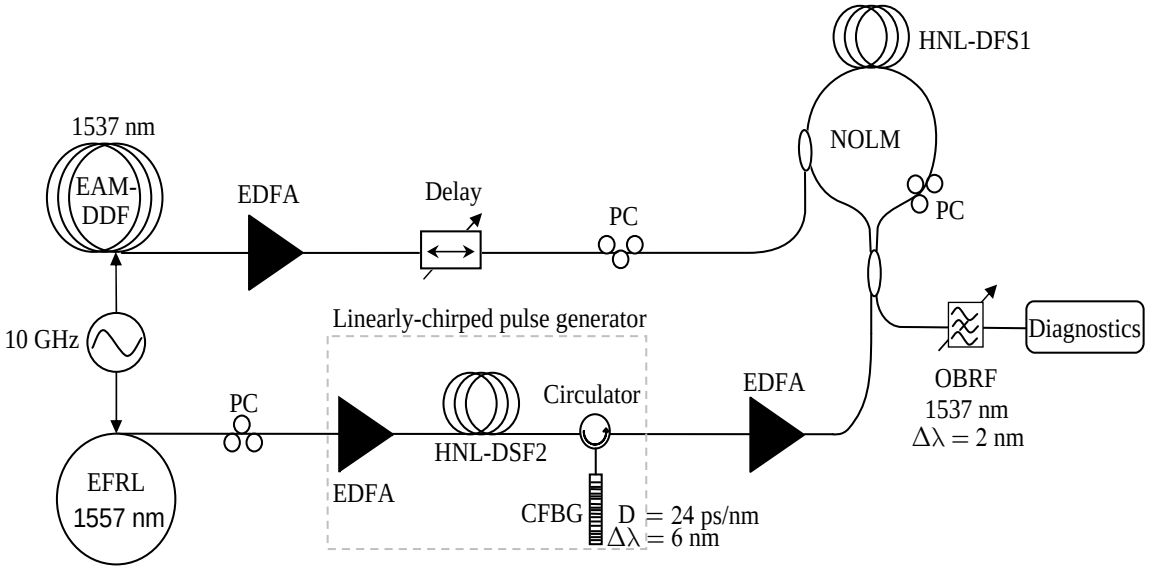

Figure 4.3: Experimental setup for the characterisation of optical gating of linearly-chirped pulses with a NOLM-switch.

From Fig. 4.4 it is thus apparent that the operation of the TDM-WDM converter is critically dependent on the interplay between the inherent chirp on the original broadband pulses and the strength of the nonlinear XPM interaction within the switch. In order to be able to gainfully design and use such converters it is essential to understand the switch operating conditions for which a sideband-free signal, with a high extinction ratio, can be achieved. In order to do this we need to study both the effects of XPM itself, and the role of the interferometric nature of the NOLM switch. The following section includes an analytical description of the XPM induced by the control pulses in the linearly-chirped pulses, and explains the origin of the beating features observed in Fig. 4.4.

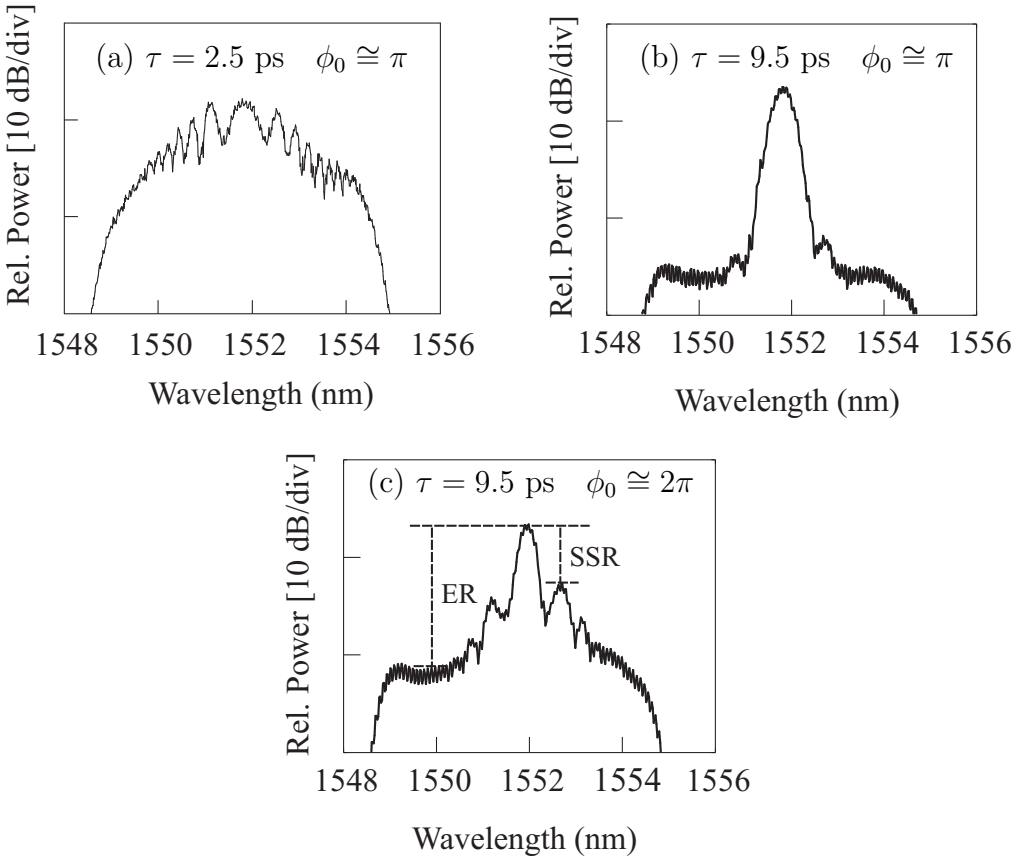

Figure 4.4: Measured spectra of pulses obtained by gating linearly chirped pulses in a NOLM for various modulating pulse widths and induced nonlinear phase shifts. (ER: NOLM extinction ratio, SSR: sideband suppression ratio)

4.1.1 XPM in Linearly-Chirped Pulses

In the analysis that follows we derive an expression for the evolution of the spectrum of the linearly-chirped pulses as they experience XPM during co-propagation with a single short data pulse through a length of fibre. In essence this analysis describes the nonlinear evolution of the linearly-chirped pulses as they travel in the clockwise direction within the NOLM, shown in Fig. 4.1. The analysis allows us to understand the origin of the sidebands, observed in Fig. 4.4, without (initially) the added complication of the effects of the interferometer. It will be shown that when a linearly-chirped pulse is switched by a much shorter Gaussian pulse, its power spectrum is modulated by two factors, one varying as a Gaussian and the other as a non-periodic modulation (see Eq. (4.19) below). The relative balance between these two effects ultimately determines the form of the resultant spectrum.

The electrical field of the cross-phase modulated signal is given by:

$$E(\tau) = E_{\mathrm{cp}}(\tau) \cdot \exp\left(i\phi_{\mathrm{xpm}}(\tau)\right), \tag{4.1}$$

where $E_{\mathrm{cp}}(\tau)$ is the flat-topped, linearly-chirped original pulse, and $\phi_{\mathrm{xpm}}(\tau)$ is the nonlinear phase shift induced by the switching pulse.

Here, for convenience, we have assumed the linearly-chirped pulse to be well approximated by a super-Gaussian shape of 4^{th} order, however it should be noted that the exact shape of the pulse envelope is not critical for the analysis as long as its width (τ_{cp}) is far longer than the width of the switching pulse (τ_0), i.e. $\tau_0 << \tau_{\mathrm{cp}}$:

$$E_{\mathrm{cp}}(\tau) = \sqrt{P_{\mathrm{cp}}} \exp\left(-\frac{\ln 2}{2}\left(\frac{2\tau}{\tau_{\mathrm{cp}}}\right)^8\right) \cdot \exp\left(-iC\tau^2\right) \tag{4.2}$$

where P_{cp} is the peak power, and C is the linear chirp-rate.

When the pulse is highly chirped so that $|C|\tau_{\mathrm{cp}}^2 >> 1$, there is an asymptotic solution for its complex spectrum, which is given by:

$$\widetilde{E}_{\mathrm{cp}}(\omega) = \sqrt{\frac{\pi P_{\mathrm{cp}}}{|C|}} \exp\left(-\frac{\ln 2}{2}\left(\frac{\omega}{C\tau_{\mathrm{cp}}}\right)^8\right) \cdot \exp\left(i\left(\frac{\omega^2}{4C} - \mathrm{sgn}(C)\frac{\pi}{4}\right)\right) \tag{4.3}$$

The derivation of Eq. (4.3) is given in Appendix C.

From Eq. (4.3) one can extract the magnitude and phase as:

$$\left|\widetilde{E}_{\mathrm{cp}}(\omega)\right|^2 = \frac{\pi P_{\mathrm{cp}}}{|C|} \exp\left(-\ln 2 \left(\frac{\omega}{C\tau_{\mathrm{cp}}}\right)^8\right) \tag{4.4}$$

and

$$\varphi_{\mathrm{cp}}(\omega) = \frac{\omega^2}{4C} - \mathrm{sgn}(C)\frac{\pi}{4} \tag{4.5}$$

For the cross-phase modulation form in Eq. (4.1), we considered the pulses in the line data stream to be Gaussian-like in shape, a reasonable assumption for the return-to-zero signal format. A mathematical description of the modulation is thus given by:

$$\phi_{\mathrm{xpm}}(\tau) = \phi_0 \cdot \exp\left(-\frac{\tau^2}{\tau_0^2}\right), \tag{4.6}$$

where ϕ_0 is the maximum phase-shift induced by the switching pulse in the nonlinear medium, and τ_0 is the half-width at $1/e$ of the maximum intensity of the same pulse.

Eq. (4.1) is in form similar to pulse self-phase modulation (SPM), for which the Fourier transform was derived using asymptotic analysis in [96]. In that case, an expression for the complex spectrum was obtained that was valid for large values of spectral broadening. However, the analysis followed in [96] assumed that the phase of the modulated field includes the SPM term only, and therefore cannot be applied to our case where the pulse undergoing phase modulation has a linear chirp. Consequently, in order to include the phase modulation, induced by XPM on a chirped pulse, we derived the spectrum for the case of small phase modulation ($\phi_0 \ll 1$), in which case Eq. (4.1) can be closely approximated by:

$$E(\tau) \cong E_{\mathrm{cp}}(\tau) + iE_{\mathrm{cp}}(\tau) \cdot \phi_{\mathrm{xpm}}(\tau) \tag{4.7}$$

We considered this assumption reasonable, as the experimental observation of the switched spectrum showed that spectral sidebands are still obtained for low values of nonlinear phase bias of the NOLM switch.

Now, the power spectrum of the electrical field is given by:

$$S(\omega) = \left| \int_{-\infty}^{\infty} E(\tau) \cdot \exp(i\omega\tau)\, d\tau \right|^2 . \tag{4.8}$$

Substituting Eq. (4.7) into Eq. (4.8) it follows that:

$$S(\omega) = \left|\widetilde{E}_{\mathrm{cp}}(\omega)\right|^2 + \left|\widetilde{E}_{\mathrm{xpm}}(\omega)\right|^2 + 2\left|\widetilde{E}_{\mathrm{cp}}(\omega)\right| \cdot \left|\widetilde{E}_{\mathrm{xpm}}(\omega)\right| \cdot \cos\left(\varphi_{\mathrm{cp}}(\omega) - \varphi_{\mathrm{xpm}}(\omega)\right) \tag{4.9}$$

where for simplicity of expression we have defined:

$$E_{\mathrm{xpm}}(\tau) \triangleq iE_{\mathrm{cp}}(\tau) \cdot \phi_{\mathrm{xpm}}(\tau), \tag{4.10}$$

and $\widetilde{E}_{\mathrm{cp}}, \widetilde{E}_{\mathrm{xpm}}$ were expressed in their phasor form where $\varphi_{\mathrm{cp}}, \varphi_{\mathrm{xpm}}$ represents their respective phase.

Substituting Eqs.(4.6) and (4.2) in Eq. (4.10) yields:

$$E_{\mathrm{xpm}}(\tau) = i\sqrt{P_{\mathrm{cp}}}\phi_0 \exp\left(-\frac{\tau^2}{\tau_0^2}\right) \cdot \exp\left(-iC\tau^2\right) \tag{4.11}$$

The waveform described in Eq. (4.11) has the form of a chirped Gaussian pulse with the same linear chirp-rate as the probe chirped pulse. The spectrum of Eq. (4.11) is analytically solved and given in, e.g. [34], by:

$$\widetilde{E}_{\mathrm{xpm}}(\omega) = \frac{\sqrt{P_{\mathrm{cp}}\pi}\phi_0\tau_0}{\sqrt[4]{1+C^2\tau_0^4}} \exp\left(-\frac{\tau_0^2\left(1-iC\tau_0^2\right)\omega^2}{4\left(1+C^2\tau_0^4\right)}\right) \cdot \exp\left(-i\frac{\arctan\left(C\tau_0^2\right)-\pi}{2}\right) \tag{4.12}$$

By expressing Eq. (4.12) in a phasor form one can extract the magnitude and phase as:

$$\left|\widetilde{E}_{\mathrm{xpm}}(\omega)\right|^2 = \frac{P_{\mathrm{cp}}\pi\phi_0^2\tau_0^2}{\sqrt{1+C^2\tau_0^4}} \exp\left(-\frac{\omega^2}{2\Delta\omega_{\mathrm{xpm}}^2}\right) \tag{4.13}$$

and

$$\varphi_{\mathrm{xpm}}(\omega) = \frac{\Delta\omega_{\mathrm{m}}^2}{4C\Delta\omega_{\mathrm{xpm}}^2}\omega^2 - \frac{\arctan\left(C\tau_0^2\right) - \pi}{2} \tag{4.14}$$

respectively. Where we have defined:

$$\Delta\omega_{\mathrm{xpm}} = \frac{\sqrt{\left(1 + C^2\tau_0^4\right)}}{\tau_0} \tag{4.15}$$

which, as shown in Appendix B, represents the total bandwidth of a Gaussian linearly-chirped pulse, in this case the gating pulses given in Eq. (4.11), and

$$\Delta\omega_{\mathrm{m}} = |C|\tau_0, \tag{4.16}$$

which represents the contribution of the chirp to the total bandwidth. The ratio between Eqs.(4.16) and (4.15) gives, therefore, the magnitude of the chirp contribution to the total bandwidth of the gated pulses and is consequently smaller than one.

Substituting Eqs.(4.13), (4.14) and Eqs.(4.4), (4.5) into Eq. (4.9) the power spectrum can be explicitly calculated as:

$$S(\omega) = \frac{\pi P_{\mathrm{cp}}}{|C|} \cdot \exp\left(-\ln 2\left(\frac{\omega}{C\tau_{\mathrm{cp}}}\right)^8\right) + \frac{P_{\mathrm{cp}}\pi\phi_0^2\tau_0^2}{\sqrt{1 + C^2\tau_0^4}} \cdot \exp\left(-\frac{\omega^2}{2\Delta\omega_{\mathrm{xpm}}^2}\right)$$

$$+ \frac{2\pi P_{\mathrm{cp}}\phi_0\tau_0}{\sqrt{|C|\sqrt{1 + C^2\tau_0^4}}} \cdot \exp\left(-\frac{\omega^2}{4\Delta\omega_{\mathrm{xpm}}^2}\right)\cos\left(\frac{1}{4C}\left(1 - \frac{\Delta\omega_{\mathrm{m}}^2}{\Delta\omega_{\mathrm{xpm}}^2}\right)\omega^2 + \theta_0\right) \tag{4.17}$$

where θ_0 is a constant phase term given by:

$$\theta_0 = -\frac{\pi}{2} - \mathrm{sgn}(C)\frac{\pi}{4} + \frac{\arctan\left(C\tau_0^2\right)}{2} \tag{4.18}$$

The last term in Eq. (4.17), which we label as $S_{\mathrm{ss}}(\omega)$, indicates that the spectral sidebands are generated through cross-phase modulation of the linearly-chirped pulses by Gaussian pulses, and it can be re-written for simplicity of analysis as:

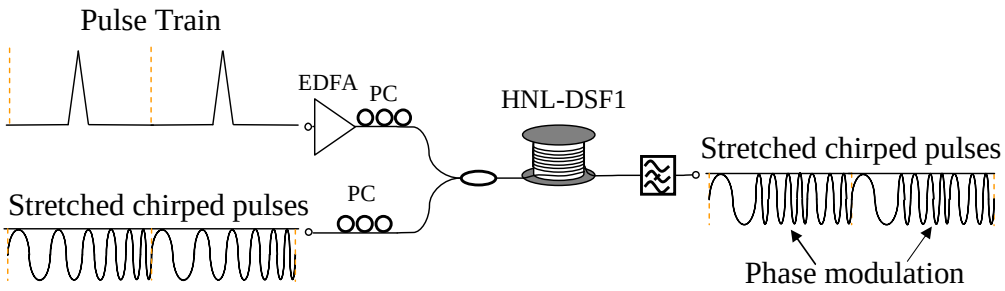

Figure 4.5: Experimental setup for the characterisation of XPM in linearly-chirped pulses.

$$S_{\mathrm{ss}}(\omega) \propto \exp\left(-\frac{\kappa_1}{2}\omega^2\right) \cdot \cos\left(\frac{\kappa_2}{2}\omega^2 + \theta_0\right) \tag{4.19}$$

where κ_1 is the curvature of the Gaussian at the centre frequency, and κ_2 is the chirp-rate of the cosine function.

This term indicates that the spectral envelope function is given by a chirp apodized by a Gaussian envelope, which describes well the spectrum observed in Fig. 4.4(a). Whilst the extent of the spectral sidebands depends on κ_1, which relates to the bandwidth of the Gaussian envelope, the number of sidebands under this envelope depends on the ratio between κ_1 and κ_2. Thus, if $\kappa_2 >> \kappa_1$ then a large number of lobes is produced, as a wide Gaussian envelope apodizes a fast chirp. If instead $\kappa_2 << \kappa_1$ then one main lobe with no sidebands is produced as the chirp is slow. For $\kappa_2 = \kappa_1$ it follows, from relating Eq. (4.19) to Eq. (4.17), that $C\tau_0^2 = 1$. For a fixed chirp-rate (C), Eq. (4.15) shows that the bandwidth affected by the XPM is minimum at $C\tau_0^2 = 1$. A physical interpretation is that if the bandwidth of the switching pulse ($1/\tau_0$) is larger than the bandwidth modulated ($\Delta\omega_{\mathrm{m}} = |C|\tau_0$), a one-to-one relation between time and frequency is impossible and spectral beats are generated since more than one frequency can occur at the same instant in time. At the opposite limit of a narrow switching pulse bandwidth compared to the modulated bandwidth (i.e. a broad switching pulse), the spectrum of the switched pulse is chirp-dominated and no spectral beating is generated.

In order to validate our theoretical derivation, we performed experimental measurements of the modulated spectrum using the setup shown in Fig. 4.5. The linearly-chirped pulses were prepared as illustrated in Fig. 4.3, for which $|C| = 0.021\,\mathrm{THz}^2$, and coupled together with 2-ps control pulses at a repetition rate of 10 GHz into

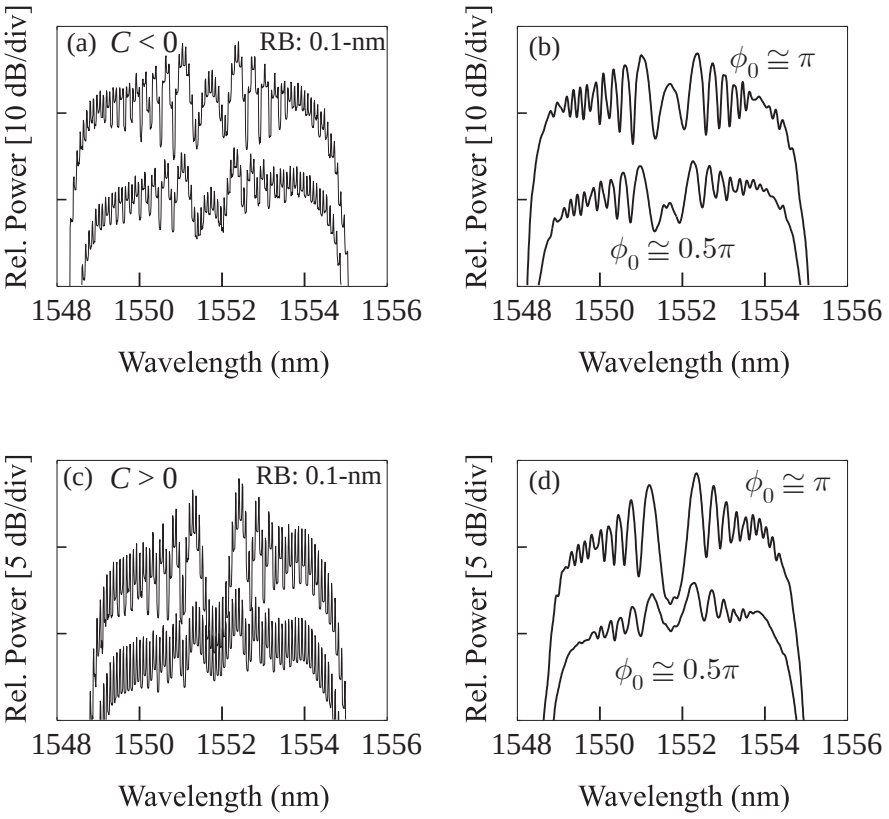

Figure 4.6: XPM spectra of linearly-chirped pulses (top: negatively chirped, bottom: positively chirped) after switching with 2 ps pulses and for various induced nonlinear phase-shifts. (a) and (c) measured power spectra, (b) and (d) retrieved spectral envelopes.

HNL-DSF1, resulting in a $|C|\tau_0^2$ product of 0.03. An amplifier at the input of the control pulses allowed the XPM strength to be varied. At the output the control pulses were filtered out. Figs. 4.6(a) and (c) show two resulting XPM spectra for low and high intensity control pulses, when the chirp-rate (C) was negative and positive, respectively. In order to compare these with our theoretical derivation, which gives the spectral envelope of a single pulse rather than the spectrum of a train of pulses, we needed to extract the corresponding spectral envelope from the measured spectrum. The Fourier transform of a train of pulses is the product of the spectral envelope with the spectral lines associated with the repetition rate of the pulses within the train. The separation of the spectrum into these two multiplicative terms (envelope and lines) was performed using cepstral analysis [1] [97]. The retrieved experimental spectra, using the cepstral algorithm, are shown in Figs. 4.6(b) and (d) for the two values

[1]The spectrum of a train of pulses can be represented as $X(\omega) = E(\omega)L(\omega)$, where $E(\omega)$ is the spectral envelope, $L(\omega)$ are the spectral lines. The cepstrum is given by $c = \mathcal{F}^{-1}(\log|X(\omega)|) = \mathcal{F}^{-1}(\log|E(\omega)|) + \mathcal{F}^{-1}(\log|L(\omega)|)$, where $\mathcal{F}^{-1}$ is the inverse Fourier transform. Filtering the cepstrum allows, therefore, to remove the spectral lines without affecting the spectral envelope.

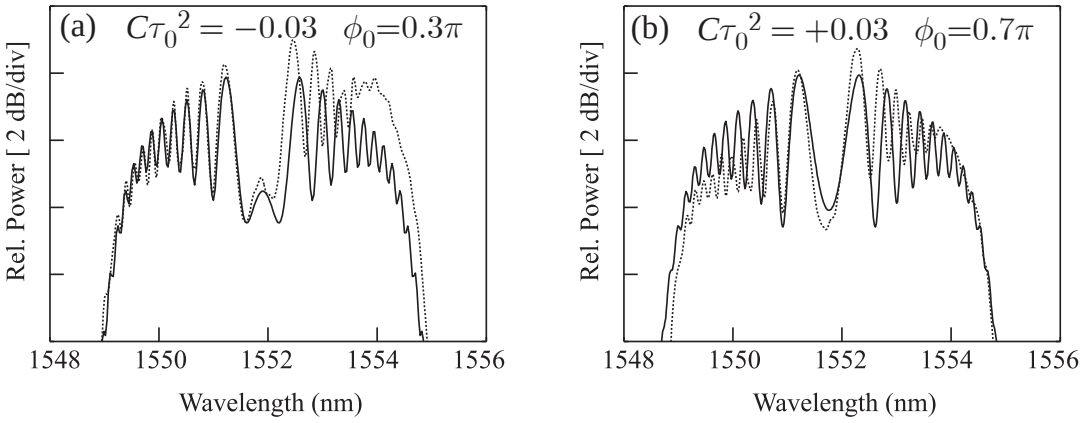

Figure 4.7: Comparison between a measured (dashed line) and a calculated (solid line) XPM spectral envelope. (a) negatively chirped, (b) positively chirped.

of peak phase shift. These traces were then compared to the calculated spectra given by Eq. (4.17). Fig. 4.7 shows this comparison for both cases of a negative and positive chirp-rate. For the theoretical model we used τ_0 equal to 1.2 ps (corresponding to a FWHM of 2 ps assuming a Gaussian pulse), τ_{cp} was 100 ps, and $|C|$ was 0.02 THz^2. The parameter P_{cp}, which represents the peak power of the linearly-chirped pulses, acts as scaling factor in Eq. (4.17), and therefore, vanishes when the spectrum is normalised by its energy integral. As can be seen, the theoretical model predicts, with good accuracy, the extension and position of spectral sidebands. The accuracy decreases, however, as the intensity of the XPM term (ϕ_0) increases, which relates to the small-phase approximation used in our theoretical derivation. We attribute the experimental spectral asymmetry to the non optimized operation of the chirped pulse generator.

4.1.2 Interferometric Effects in the NOLM-Switch

In the following we extend the discussion of phase modulation, presented in the previous section, to include the interferometric effects of the NOLM switch. For simplicity, as before, we have considered only the XPM effect in the nonlinear fibre in the NOLM and neglected any dispersive effects. The electrical field of the switched signal at the NOLM transmission port is, according to Appendix A, given by:

$$E(\tau) = \alpha_s E_{\mathrm{cp}}(\tau) \cdot \exp\left(i\phi_{\mathrm{xpm}}(\tau)\right) - (1-\alpha_s) E_{\mathrm{cp}}(\tau), \tag{4.20}$$

where E_{cp} and ϕ_{xpm} are described in Eq. (4.2) and (4.6) respectively, and α_s is the splitting ratio of the NOLM input coupler.

The performance of the NOLM was first modeled by numerically solving Eq. (4.20) for various settings of the control pulse width. At first we assumed a typical value for the NOLM extinction ratio of 25 dB, which is a realistic working level allowing for practical limits in the splitting-ratio balance for the NOLM coupler, and for imperfections in the alignment of the polarizations of the two counter-propagating beams. This corresponds to a splitting ratio parameter (α_s) of 0.527 (ignoring any polarization based effects). We fixed the maximum phase shift (ϕ_0) at π (corresponding to maximum switching efficiency), and the chirp-rate parameter (C) at -0.04 THz^2, again relating to reasonably practical values. Figs. 4.8(a-c) show the chirp, intensity profiles and spectra of the switched pulses for various values of the $C\tau_0^2$ product, and indicate that as the modulating pulsewidth (τ_0) increases, the chirp evolves gradually from a strong non-monotonic to a monotonic function. The simulation shown in Fig. 4.8(d) is for the same case as in Fig. 4.8(c), but assumes an infinite NOLM extinction (α_s= 0.5). No significant degradation to the pulse frequency chirp is observed between the two cases, apart from the tails of the switched pulse, where the switched pulse intensity is comparable to that of the residual intensity of the chirped pulses that have not been perfectly suppressed by the NOLM. The predictions from these calculations are in good agreement with the experimental performance characteristic shown in Fig. 4.4, and highlight the importance of a correct choice of chirp for a given data pulse width.

The NOLM gating of positively linearly-chirped pulses was also numerically investigated. In Fig. 4.9 I show numerical simulations of the gated pulse and its corresponding spectrum for a positive chirp-rate of $C = +0.04\,\mathrm{THz}^2$. The switching conditions were the same as those in Fig. 4.8. As can be seen, the general features of the spectral envelope are nearly identical in both the cases of a negative and positive chirp-rate, however, for large $C\tau_0^2$, the 3-dB bandwidth of the gated pulse is significantly larger for a positive chirp-rate. This relates to the largely different amount of chirp that is induced across the gated-pulse envelope. Fig. 4.8(d) shows that the gated pulse is nearly unchirped, whereas Fig. 4.9(d) shows that the gated pulse is instead largely chirped. The reason is that the chirp of the original pulses and the chirp induced by

XPM, which is always positive in the centre part of the gated pulse, cancel out for a negative chirp-rate, whereas they add up for a positive chirp-rate.

In the theoretical analysis of the previous section, the spectral beating originated by XPM in the linearly-chirped pulses was only mathematically confirmed. A physical interpretation is that the modulating pulse induces a non-monotonic chirp across the linearly-chirped pulse. Consequently, the same frequency component appears under the pulse envelope at different instants. In the spectrum, these temporal components of the same frequency interfere and spectral beats are formed with a periodicity according to the relation between the original chirp-rate and the chirp-rate induced by XPM.

I was puzzled by two aspects during the early stages of this work, one was that the suppression of the non-gated linearly-chirped pulse in a NOLM can be as large as 30 dB, and therefore the spectral interference should be greatly suppressed. However, as it can be seen in Figs. 4.4(a) and 4.8(a) the beating is significant.

It is anticipated that the spectral beating results from the interference between one component in the non-gated part of the linearly-chirped pulse, and another component of the same frequency in the central part of the gated pulse. This can be mathematically shown using the small-phase approximation ($\phi_{\mathrm{xpm}} << 1$) in Eq. (4.20), which approximates the electric field of a gated pulse to:

$$E(\tau) \cong (2\alpha_s - 1) E_{\mathrm{cp}}(\tau) + i\alpha_s E_{\mathrm{cp}}(\tau) \cdot \phi_{\mathrm{xpm}}(\tau) \tag{4.21}$$

The corresponding power spectrum is then given by:

$$\begin{aligned} S(\omega) = {} & (2\alpha_s - 1)^2 \left|\widetilde{E}_{\mathrm{cp}}(\omega)\right|^2 + \alpha_s^2 \left|\widetilde{E}_{\mathrm{xpm}}(\omega)\right|^2 \\ & + 2\alpha_s (2\alpha_s - 1) \left|\widetilde{E}_{\mathrm{cp}}(\omega)\right| \cdot \left|\widetilde{E}_{\mathrm{xpm}}(\omega)\right| \cdot \cos\left(\varphi_{\mathrm{cp}}(\omega) - \varphi_{\mathrm{xpm}}(\omega)\right) \end{aligned} \tag{4.22}$$

The first term in Eq. (4.22), which corresponds to the non-gated part of the linearly-chirped pulse, is in fact largely suppressed in a NOLM. For instance, considering $\alpha_s = 0.527$, the first-term extinction given by $10\log\left((2\alpha_s - 1)^2\right)$ is 25 dB, which corresponds to the NOLM extinction-ratio. The third-term in Eq. (4.22), which

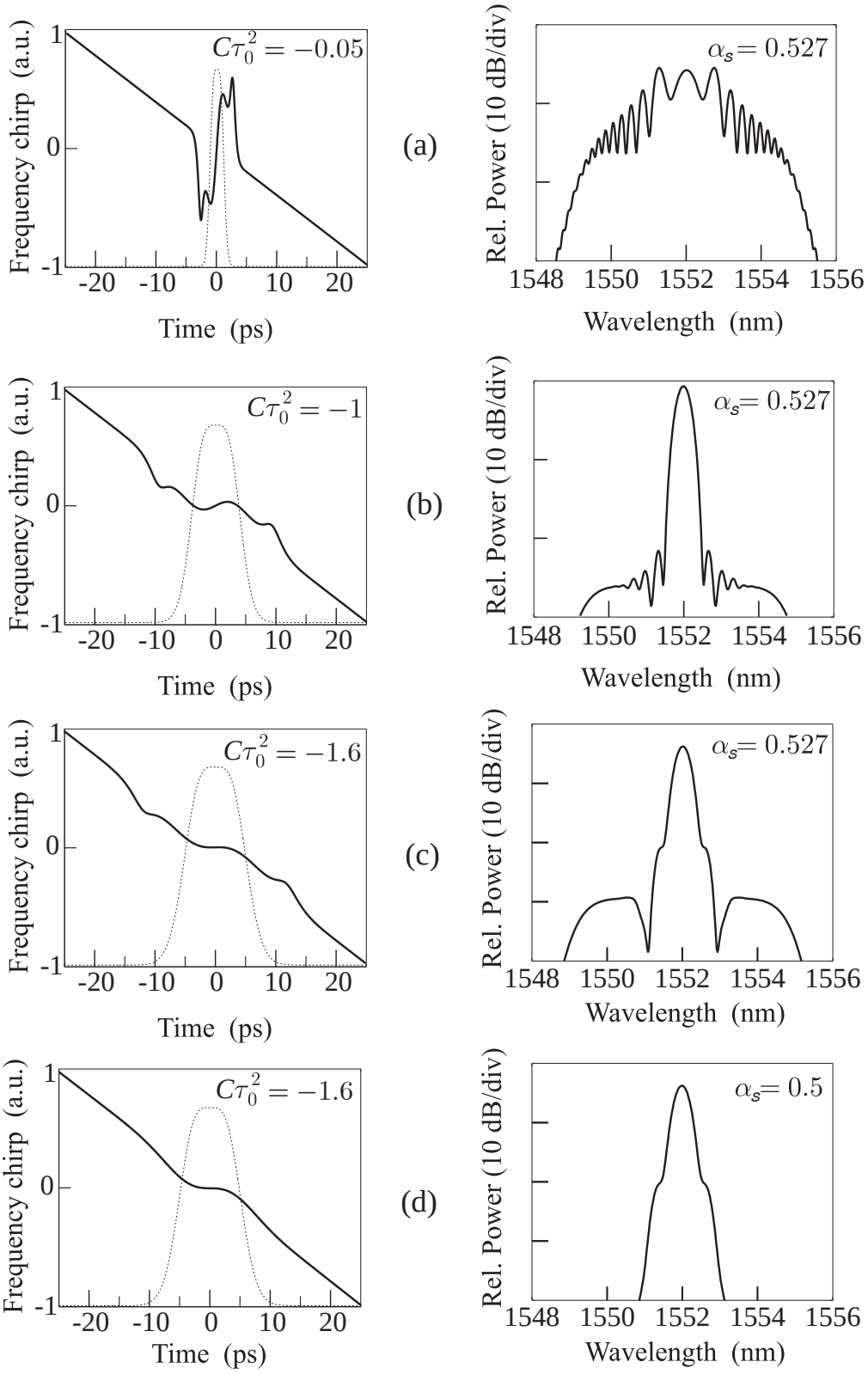

Figure 4.8: Numerical calculations of the NOLM switched pulse for different values of $C\tau_0^2$ and α_s when $\phi_0 = \pi$, $C = -0.04\,\mathrm{THz}^2$, and $\tau_{\mathrm{cp}} = 60\,\mathrm{ps}$. Left: Frequency chirp (solid line) and intensity envelope (dashed line). Right: The corresponding spectral envelopes.

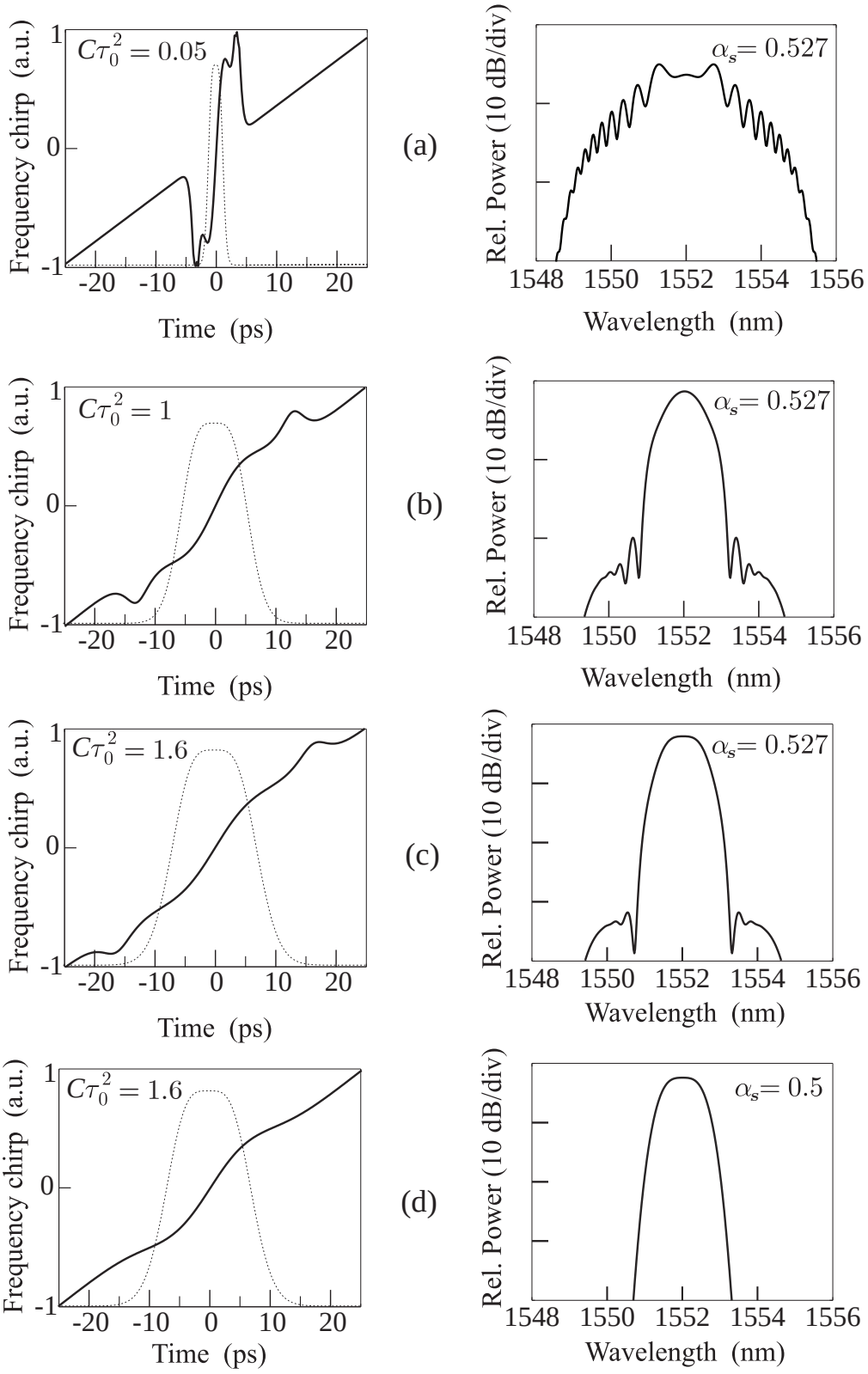

Figure 4.9: Numerical calculations of the NOLM switched pulse for different values of $C\tau_0^2$ and α_s when $\phi_0 = \pi$, $C = +0.04\,\mathrm{THz}^2$, and $\tau_{\mathrm{cp}} = 100\,\mathrm{ps}$. Left: Frequency chirp (solid line) and intensity envelope (dashed line) . Right: The corresponding spectral envelopes.

corresponds to the spectral beating, has, however, an extinction, which is given by $10\log(2\alpha_s(2\alpha_s-1))$, of 12 dB. Moreover, the second term, which corresponds to the ideal spectrum of the gated linearly-chirped pulse, has also an extinction of 6 dB. The contribution of the third term to the total spectrum is, therefore, dominant.

It can be inferred from Eq. (4.22) that for an ideal NOLM with an infinite extinction-ratio ($\alpha_s = 0.5$), the first and third term vanish, and therefore, spectral beats are not formed. This was confirmed by numerically solving Eq. (4.20). In Fig. 4.10 I show spectrograms on a logarithmic intensity scale with the corresponding pulse envelope and spectrum of a gated pulse. In Fig. 4.10(a) the NOLM extinction-ratio was 25 dB, whereas in Fig. 4.10(b) it was infinite. As can be seen, without residual transmission of the non-gated linearly-chirped pulse through the NOLM, the spectral beats disappear.

The other aspect I did not understand early on was that the amplitude of the non-monotonic chirp across the gated pulse did not relate to the bandwidth affected by the spectral beats. For example, in Fig. 4.8(a) the chirp inversion in the pulse affects only a small part of the spectrum of the original linearly-chirped pulses, which corresponds to the chirp amplitude across a temporal width of 60 ps. The spectral beats, however, extended over the full spectrum of the original linearly-chirped pulses, as can be seen in Fig. 4.8(a). This was obviously a misinterpretation of chirp, which is the deviation of the instantaneous-frequency, i.e. the average frequency-component at each instant, and therefore, does not show how the spectral content changes across the pulse envelope. This is clear in Fig. 4.10(a), which shows that the spectral content of the gated pulse is clearly wider than the residual spectrum of the linearly-chirped pulse, and consequently, spectral interference occurs over the full spectrum, even though the amplitude of the chirp inversion is small.

From the numerical simulations of Eq. (4.20), the peak-to-side-lobe ratio (or sideband-suppression ratio – SSR), which corresponds to the peak-power ratio between the centre-lobe and the first side-lobe in the gated-pulse spectrum, was also estimated. Fig. 4.11(a) shows this ratio as a function of the maximum induced phase-shift when the chirp-width product ($C\tau_0^2$) is equal to -1. For larger values than 0.8π, side-lobes appear over the 25 dB NOLM extinction-ratio limit (ER level). The results presented in this figure can be compared to the experimental observations of Figs. 4.4(b-c), where good agreement in terms of spectral shape between experiment and theory

are observed. In Fig. 4.11(b) we show the SSR estimation as a function of the modulating pulsewidth when the maximum phase-shift is π. A comparison of this figure with Eq. (4.17) shows that the strength of the sidebands follows the trend of the exponentially varying bandwidth of $S(\omega)$ and minimizes for $C\tau_0^2 = -1$. It is interesting to note that for values greater than -1.6 sidebands are no longer observed, and crosstalk suppression is dominated by the NOLM extinction ratio. Unfortunately, Eq. (4.17) which was derived for small values of ϕ_0 cannot fully describe this trend. Instead, it is best to examine the behavior of the chirp profile of the switched pulses.

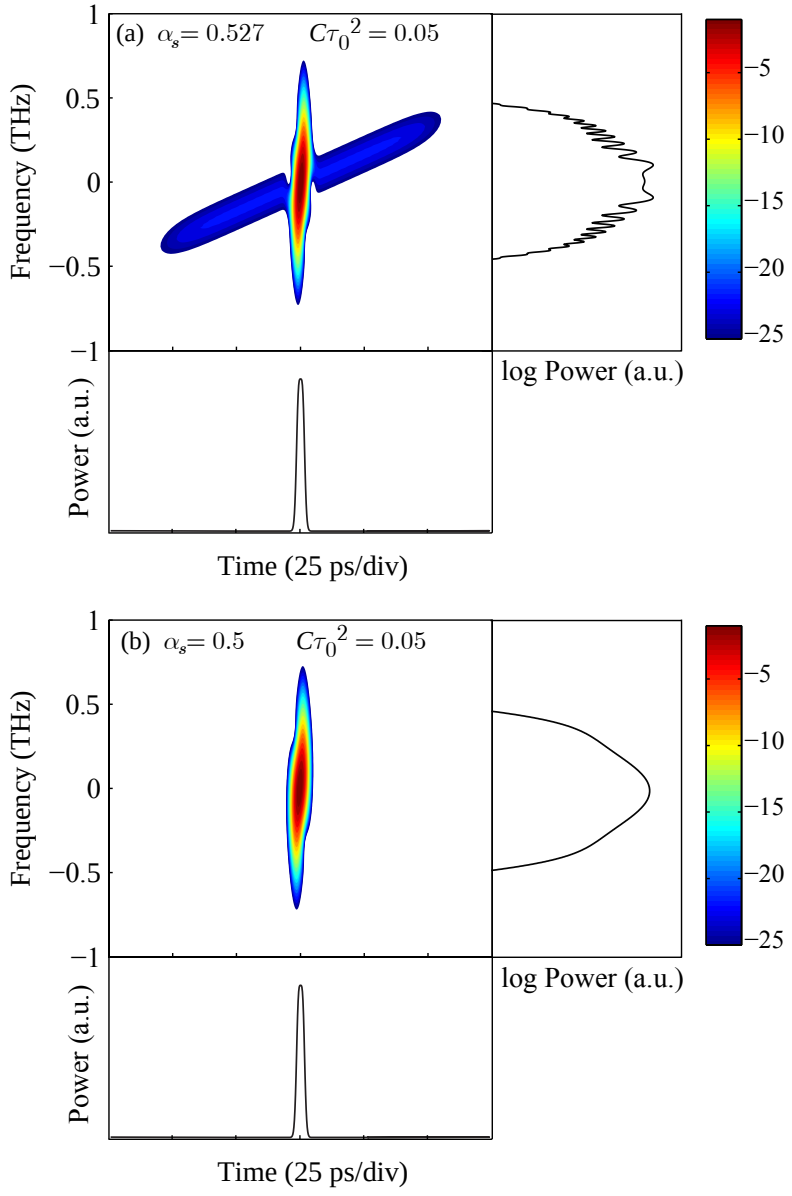

Figure 4.10: Numerical calculations of the spectrogram of the NOLM switched-pulse when $\phi_0 = \pi$, $C = +0.021\,\mathrm{THz}^2$, $\tau_0 = 1.5\,\mathrm{ps}$, and $\tau_{\mathrm{cp}} = 100\,\mathrm{ps}$. (a) 25-dB NOLM extinction-ratio, (b) infinite NOLM extinction-ratio.

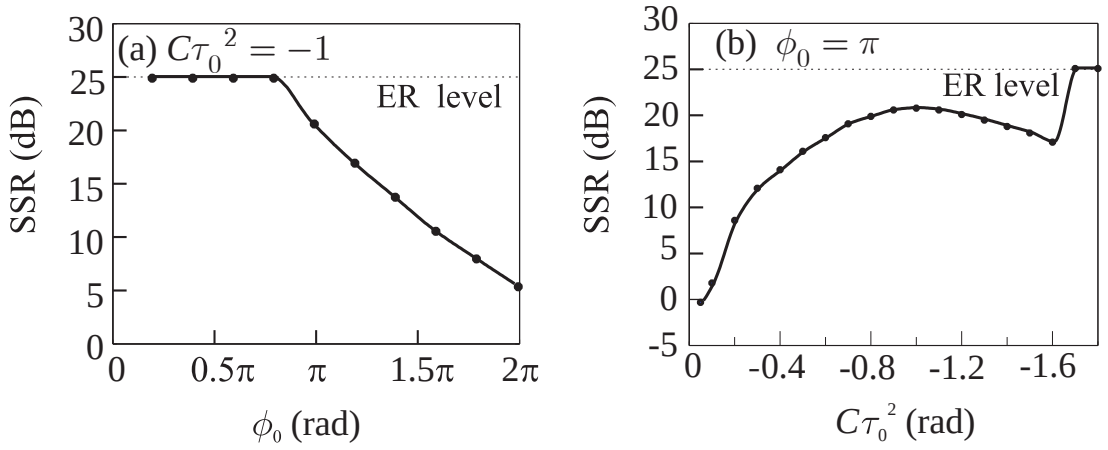

Figure 4.11: Spectral sideband suppression ratio as a function of (a) the nonlinear phase shift and (b) the chirp-width product. NOLM extinction ratio (ER): 25 dB.

The chirp function can be derived by first re-writing Eq. (4.20) in a single amplitude and phase form. It is only possible to obtain an analytical expression if we assume $\alpha_s = 0.5$, for which the NOLM extinction is infinite. Under this assumption, and using fundamental relations between circular functions, we have:

$$E(\tau) \propto \sin\left(\frac{\phi_0}{2}\exp\left(-\frac{\tau^2}{\tau_0^2}\right)\right) \cdot \exp\left(i\varphi(\tau)\right) \tag{4.23}$$

where the phase is given by:

$$\varphi(\tau) = \frac{\pi}{2} - C\tau^2 + \frac{\phi_0}{2}\exp\left(-\frac{\tau^2}{\tau_0^2}\right) \tag{4.24}$$

Eq. (4.23) shows that all-optical gating using a NOLM switch alters the pulse shape. It strongly affects the top of the pulse if the maximum phase-modulation is about π. If the application involved requires pulse shape preservation then the switching efficiency has to be traded-off, by operating the NOLM within the linear range of the sine function, for example considering NOLM operation at a maximum phase shift of 0.7π (rad). The chirp function can then be derived by taking the time derivative of Eq. (4.24), and is given by:

$$\delta\omega(\tau) = -\frac{\partial\varphi}{\partial\tau} = \left[2C + \frac{\phi_0}{\tau_0^2}\exp\left(-\frac{\tau^2}{\tau_0^2}\right)\right] \cdot \tau \tag{4.25}$$

A change in the sign of the chirp slope would give rise to temporal beating of certain frequency components and the formation of ripples in the spectral domain. This can be avoided when the chirp is monotonous, i.e.:

$$\frac{\partial \delta\omega}{\partial \tau} > 0 \quad \forall\, \tau \in\ ]-\infty, +\infty[, \tag{4.26}$$

for the case of a positive chirp-rate C. Substituting Eq. (4.25) in Eq. (4.26) yields:

$$C\tau_0^2 > \exp\left(-\frac{3}{2}\right) \cdot \phi_0 \tag{4.27}$$

When the switching efficiency is maximum ($\phi_0 = \pi$) relation (4.27) yields:

$$C\tau_0^2 > \exp\left(-\frac{3}{2}\right) \cdot \pi \cong 0.7, \tag{4.28}$$

As for the case of a negative chirp-rate C, the monotonicity is given by:

$$\frac{\partial \delta\omega}{\partial \tau} < 0 \quad \forall \tau \in\ ]-\infty, +\infty[, \tag{4.29}$$

Substituting Eq. (4.25) in Eq. (4.29) yields instead:

$$C\tau_0^2 < -\frac{\phi_0}{2} \tag{4.30}$$

and thus, when the switching efficiency is maximum ($\phi_0 = \pi$) relation (4.30) yields:

$$C\tau_0^2 < -\frac{\pi}{2} \cong -1.6, \tag{4.31}$$

in agreement with the numerical result of Fig. 4.11(b). Note that the limited NOLM extinction ratio and the assumption of $\alpha_s = 0.5$ that we have used in our analysis does not significantly affect the chirp of the switched pulses (as also shown in Figs. 4.8(c-d) and Figs. 4.9(c-d)).

4.2 NOLM Operating Conditions for TDM-to-WDM Conversion

Using Fig. 4.11(b) as a basis, it is now important to evaluate the relation between the total bandwidth required for producing switched pulses and the chirp-width product ($C\tau_0^2$). From Eq. (4.2) one can easily calculate the bandwidth of the linearly-chirped pulses as the first derivative of the phase, as is true for chirp-dominated signals, such as these pulses. The width of these pulses is equal to the period of the tributary signals ($1/B_{base}$), where B_{base} represents the tributary bit rate. Hence, their bandwidth is:

$$\Delta\omega_{\text{Total}} = \frac{2C}{B_{\text{base}}} \tag{4.32}$$

This can be expressed as a function of $C\tau_0^2$, as:

$$\Delta\omega_{\text{Total}} = \frac{2C\tau_0^2}{\tau_0^2 B_{\text{base}}} \tag{4.33}$$

which shows that for a given value of the $C\tau_0^2$ product, the bandwidth requirements for the linearly-chirped pulses are minimized when the pulse width of the aggregate data signal is maximum. For return-to-zero (RZ) signals, as required in ultrafast OTDM, the full-width at half-maximum (FWHM) of the pulses should not exceed one third of the duration of the bit slot, i.e. the maximum pulse width is:

$$\tau_0 = \frac{1}{3 \cdot 1.665 \cdot B_{\text{line}}} \tag{4.34}$$

where B_{line} is the line bit rate. Note that, as in Section IV.A, Gaussian pulses have been assumed, and the factor 1.665 is used for the conversion from FWHM to the half-width at the $1/e$ point. Introducing Eq. (4.34) in Eq. (4.33) yields:

$$\Delta\omega_{\text{Total}} = 2C\tau_0^2 \frac{(3 \cdot 1.665 \cdot B_{\text{line}})^2}{B_{\text{base}}} \tag{4.35}$$

or, expressed in terms of wavelengths:

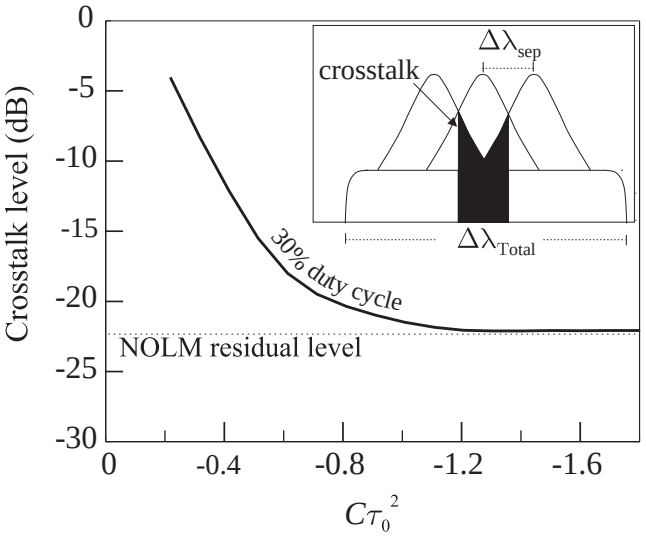

Figure 4.12: Crosstalk level between adjacent channels as a function of the chirp-width product for a NOLM with an extinction ratio of 25 dB. The crosstalk level is defined as the ratio of the peak power over the power in the shaded area (see inset).

$$\Delta\lambda_{\text{Total}} = \frac{\lambda^2}{\pi c} C\tau_0^2 \frac{(3 \cdot 1.665 \cdot B_{\text{line}})^2}{B_{\text{base}}} \tag{4.36}$$

where c is the speed of light in vacuum, and λ the wavelength of operation. For $\lambda =$ 1550 nm this yields:

$$\Delta\lambda_{Total}\,(\text{nm}) \cong 0.065 \cdot C\tau_0^2 \cdot \frac{B_{\text{line}}^2\,(\text{Gb/s})}{B_{\text{base}}\,(\text{Gb/s})} \tag{4.37}$$

Consequently the channel separation is given by the total bandwidth divided by the number of tributary channels $B_{\text{line}}/B_{\text{base}}$:

$$\Delta\lambda_{sep}\,(\text{nm}) \cong 0.065 \cdot C\tau_0^2 B_{\text{line}}\,(\text{Gb/s}) \tag{4.38}$$

As the channel separation is a function of the chirp-rate C, the crosstalk between adjacent channels can be a major impairment at low chirp-rates. In Fig. 4.12 we show a calculation of the channel extinction ratio, as estimated by calculating the crosstalk from its two nearest channels, as a function of the chirp-rate. It is clear from the curves in both Figs.4.11 and 4.12 that the best performance of a NOLM based TDM-WDM converter occurs when the chirp-width product is larger than -1.6.

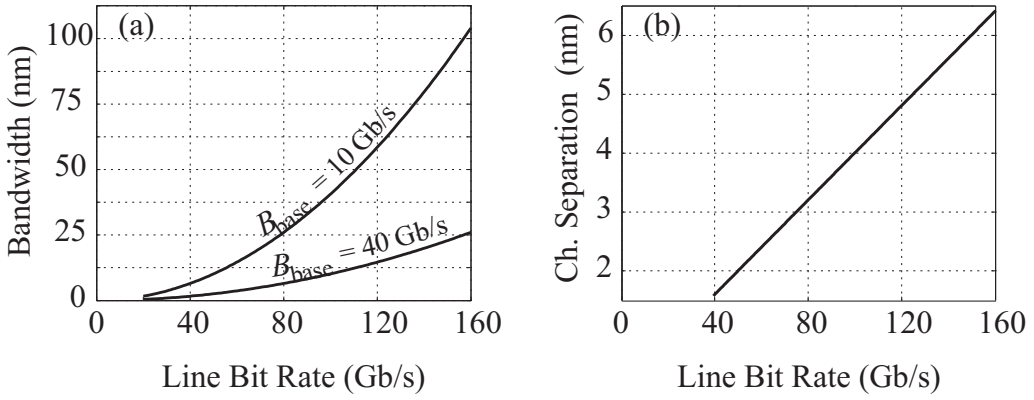

Figure 4.13: (a) Minimum bandwidth requirement for the linearly-chirped pulse for TDM-WDM conversion at $C\tau_0^2 = -0.6$ as a function of the aggregate OTDM bit rate. (b) The corresponding WDM channel separation.

However, such a high chirp-rate requires the generation and control of ultra-broad bandwidth linearly-chirped pulses. For example, 160-Gb/s operation with a tributary rate of 10 Gb/s would require linearly-chirped pulses with a total bandwidth in excess of 266 nm for the mapping of the 16 channels. A more reasonable approach would be to allow a compromise in the adjacent channel crosstalk to levels that can generally be tolerated by OTDM signals. For example, the OTDM signal extinction ratio is limited by the extinction of the $LiNbO_3$ data modulators which typically ranges between 15-20 dB. Fig. 4.12 shows that this value can be achieved by operating at a chirp-width product of -0.6. This reduces the bandwidth requirement for operation at 160 Gb/s to 100 nm. At a tributary rate of 40 Gb/s the required bandwidth would be just 25 nm. It is possible to shape an SPM-broadened spectrum, using for example a commercial dynamic-gain-equalizer, to produce a rectangular-like chirped pulse with a 30-nm bandwidth. In Ref.[98], using this approach, equalised time-to-wavelength mapping of 10 tributary channels of a 100-Gb/s OTDM signal onto a 22-nm bandwidth is demonstrated. Therefore, a practical implementation of this technique, at the line rate of 160 Gb/s operating on 40 Gb/s tributaries, should be possible. Fig. 4.13(a) shows the minimum bandwidth required for the TDM-WDM conversion as a function of the line bit rate for $C\tau_0^2 = -0.6$, and for the cases of 10 and 40 Gb/s tributaries. The corresponding channel separation is independent of the repetition rate of the tributary signals (Eq. (4.38)), and is shown in Fig. 4.13(b).

4.3 Summary and Discussion

In this chapter I described the optical gating of linearly-chirped pulses with a NOLM-switch for time-frequency signal-processing of an OTDM signal. It was shown that to convert an incoming OTDM-signal into a chirped-WDM replica with a one-to-one relation between the temporal and spectral waveforms, the chirp-rate C of the NOLM-signal pulses should be around $-1.6/\tau_0^2$, where τ_0 is the temporal-width of the pulses in the incoming OTDM-signal. Alternatively, the pulse duration τ_0 can be broadened to satisfy the same chirp-width product: $C\tau_0^2 \approx -1.6$. It was also shown that, for $|C|\tau_0^2 < 1$, intense multiple spectral-lobes are formed within the band of each tributary channel. The consequence is that any further signal-processing involving pulse compression results in severe pulse distortion. The physics of the spectral-lobe formation was unveiled and related to the interference between the spectral content in the gated pulse and the residual spectral-components in the non-gated linearly-chirped pulse. The XPM can also induce a non-monotonic chirp in the pulse, which leads to formation of low intensity spectral side-lobes for $C\tau_0^2 > -1$ when the chirp-rate C is negative.

Practical limitations, however, should be taken into account when increasing the chirp-width product. Increasing the chirp-rate can be challenging, as it implies broadening the spectrum of the linearly-chirped pulses while maintaining flat spectral-power-density. On the other hand, the incoming-pulse duration should be shorter than 1/3 of the bit period to prevent detrimental crosstalk-interference between adjacent tributary-channels. It was shown, though, that practical operation can be obtained with a minimum chirp-width product of 0.6 and a maximum incoming-pulse duty-cycle of 30%. Under these conditions, the estimated crosstalk-level was lower than -15 dB.

As an experimental validation of the discussion made above, the NOLM gating of a linearly-chirped pulse with a 40-Gb/s OTDM signal was experimentally measured. In the setup, outlined in Fig. 4.3, the 10-GHz control pulses were passively multiplexed to form a 40-GHz pulse stream. The chirp-rate (C) of the linearly-chirped pulses was as before $-0.021\,\mathrm{THz}^2$. Fig. 4.14(a) shows the optical spectrum of the 4 tributary-channels when the control-pulse duration was 2.5 ps, which corresponds to a chirp-width product of -0.05. Although mapping is achieved, the dominant feature in

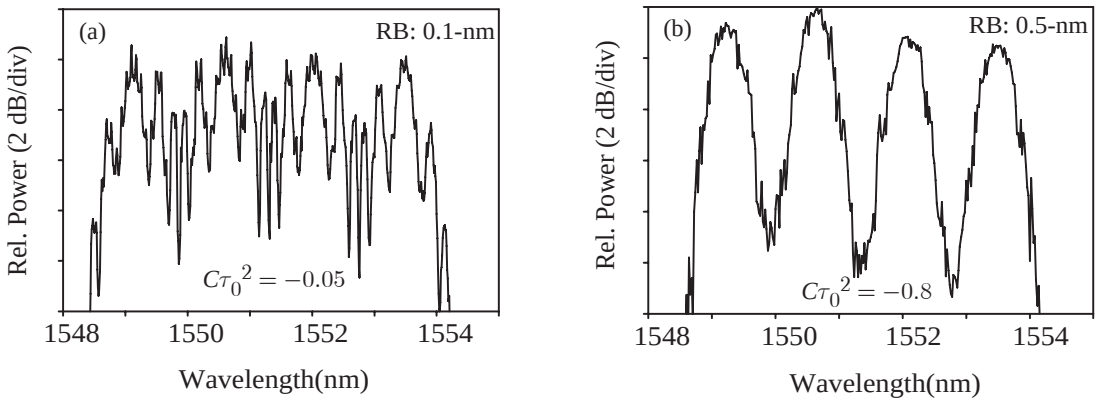

Figure 4.14: Optical spectrum of the chirped-WDM replica obtained by optical gating a linearly-chirped pulse with a 40-Gb/s OTDM signal in a NOLM switch. (a) $C\tau_0^2 = -0.05$, (b) $C\tau_0^2 = -0.8$.

the spectrum is the formation of side-lobes, and it is anticipated that the crosstalk between adjacent channels should be large. Fig. 4.14(b) shows the same but when the control-pulse duration was 10 ps, which corresponds instead to a chirp-width product of -0.8. Side-lobes are no longer observed (at least down to the -10-dB level), and the formed WDM channels have clean spectral features, which can be further processed. The results shown in these spectra confirm, therefore, the findings that were described in this chapter. The analysis and the concept developed in this chapter will be useful in all the experiments that will be presented in the following chapters of this thesis. NOLM switching of linearly-chirped pulses is next used for demultiplexing and add-drop filtering of OTDM signals, and in Chapter 6 for the compression and expansion of small packets of pulses.

Chapter 5

Time-Division-Multiplexing Functions Based on the Nonlinear Switching of Linearly-Chirped Pulses

Overview: In this chapter, I describe the experimental realization of time-division-multiplexing functions, namely channel demultiplexing and channel add/drop multiplexing, based on conversion between OTDM and mixed TDM-WDM signal formats and spectral filtering. I firstly introduce the principle-of-operation of each proposed scheme and compare them to widely reported OTDM techniques. Together with the experimental results I discuss the issues related to the technology required to implement these schemes, mainly the nonlinear gates and the optical filters. In the channel demultiplexing scheme a Kerr-shutter was used to gate the linearly-chirped pulses, whereas in the add/drop multiplexing scheme a NOLM-switch was used. Both experiments achieved error-free operation, however, the nonlinear-gating of the linearly-chirped pulses with a NOLM provided better performance.

5.1 Introduction

The ability to generate sub-picosecond pulses at gigahertz repetition-rates has made single-channel data rates well beyond the electronic processing-speed limit possible. Passive optical-delay-line arrays based on either fibre or planar waveguide technology provide the means to aggregate data into one single optical-carrier, up to unprecedented levels, based on time-division-multiplexing of ultra-short pulses. Optical time-division-multiplexing (OTDM) systems operating at data rates of $\sim$1 Tb/s have now been demonstrated [12, 99]. A major challenge is, however, to extract a signal channel at a base-rate from the multiplexed high bit-rate data stream at specific points in the transmission system where electronic signal-processing is required. A high-speed, all-optical data demultiplexer, which acts as a bridge between low bit-rate electrical signals and high bit-rate optical time-division-multiplexed (OTDM) signals, is therefore a key signal-processing device. More relevant in a network scenario is an all-optical add/drop multiplexer, which extracts an aggregated channel, clears the associated slot, and loads a new channel into the emptied slot. Substantial research work has been carried out to develop ultrafast switches that can operate at OTDM bit-rate speeds. It is also important, however, to investigate (de)multiplexing schemes that can, in a straightforward manner, process several aggregated channels simultaneously. Being able to process simultaneously several channels by simply adding passive components to the all-optical add/drop multiplexer can have a significant impact in its total power consumption and multiplexing capability. The scheme presented in this chapter can operate on multiple tributary-channels simply by adding more optical filtering elements to it.

5.2 OTDM Signal Demultiplexing Based on Kerr switching of Linearly-Chirped Pulses

Various schemes of ultrafast all-optical demultiplexing have been reported so far. The concept behind these schemes is depicted in Fig. 5.1(a). A clock signal is first extracted from the tributary channels of the incoming high-speed OTDM signal and used to drive an optical pulse-generator. The locally generated pulses are then synchronised with one tributary channel in the high-speed OTDM signal and used to

control the transmission of an ultrafast all-optical switch. The switch transmits only the bits aligned with the control pulses. It is, therefore, crucial that the transmission window induced by the control pulses does not exceed the bit-slot in the high-speed OTDM signal to prevent crosstalk from the adjacent channels.

Several all-optical switching technologies have been integrated in demultiplexing schemes and have shown ultra-high-speed operation. All-optical fibre-based demultiplexing techniques have been demonstrated using either cross-phase modulation [41] or four-wave mixing (FWM) [43]. Another attractive option for demultiplexing is with semiconductor optical amplifiers (SOAs). Demultiplexing with SOAs can be either based on FWM [100] or on phase modulation effects in a variety of interferometric structures [101]. Lithium niobate technology shows the advantage of circuit integration and no spontaneous-noise emission, and 160-Gb/s OTDM signal demultiplexing using cascaded second-order nonlinear effects in a periodically-poled waveguide has been achieved [102]. A very promising technology is the electroabsorption modulator (EAM) due to the possibility of monolithic integration with mode-locked laser diodes and photodiodes, and demultiplexing operation at 160 Gb/s has been reported [103]. Several other switching technologies have shown the capability to operate beyond the electronic speed, such as those based on inter-subband transition in semiconductor quantum-wells [11, 104].

It can be concluded that there is a host of technologies that can facilitate ultrafast switching. However, in all cases mentioned above, one channel could be processed per switching stage. Thus, the requirement to process multiple tributary-channels simultaneously may lead to complex system architectures, high power consumption, and complex synchronization schemes.

5.2.1 Concept of Demultiplexing using TDM-to-WDM Conversion

An approach that may simplify the simultaneous processing of several OTDM tributaries is based on the conversion of the OTDM signal onto a WDM signal in which the tributaries are mapped onto different frequency-channels. Mature optical filtering technologies can then be used to extract any of the tributary channels without affecting the remaining channels. Two main techniques have been proposed for OTDM onto

WDM demultiplexing. One technique uses linearly-chirped pulses precisely stretched to overlap all the tributary channels [21], thus providing a time-to-frequency mapping of the switch output, as illustrated in Fig. 5.1(b). The other technique is based on temporally interleaved clock-pulse streams at different wavelengths [18, 105], so that each clock-pulse stream synchronises with a tributary in the OTDM signal, as illustrated in Fig. 5.1(c). The latter has the advantage of producing transform-limited pulses, but a single source emitting pulses at alternate wavelengths is still a challenging research topic [106, 107], while interleaving different sources requires complex synchronisation schemes. The former technique has been demonstrated using a variety of nonlinear optical-switches by different groups, such as FWM in fibre [21, 108], XPM in fibre [20, 98], and the fibre NOLM-switch [4].

In this chapter, we demonstrate this demultiplexing scheme using linearly-chirped rectangular pulses shaped in a linearly-chirped fibre-Bragg-grating and nonlinear switching in a fibre Kerr-gate. The data demultiplexing is, therefore, based on mapping each

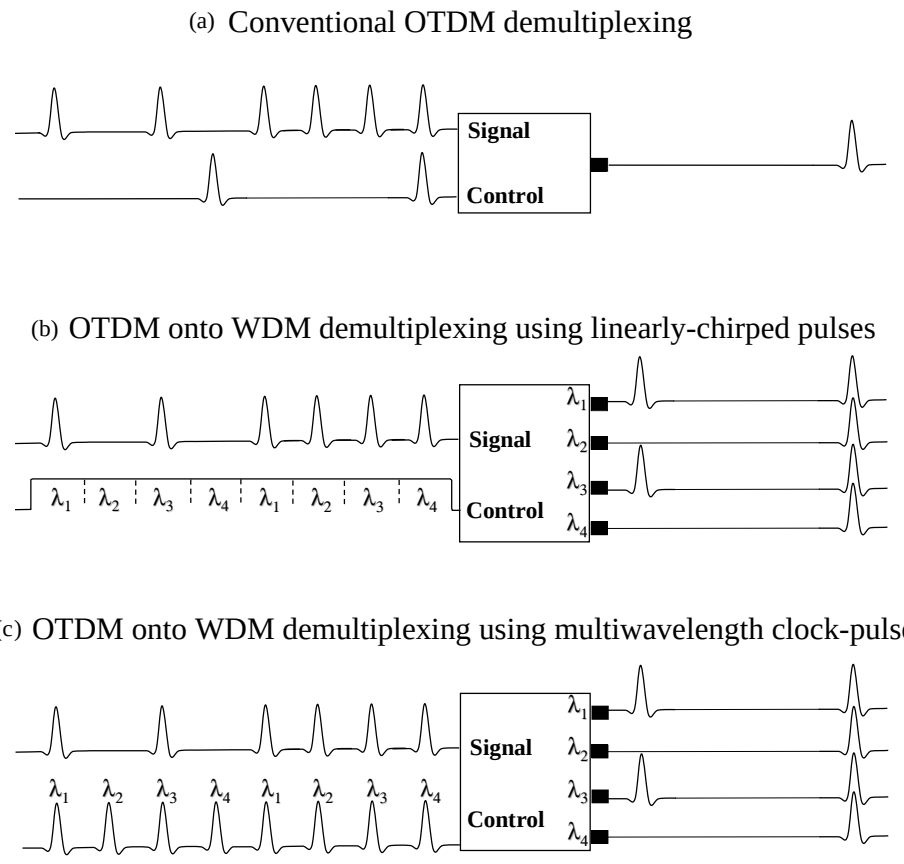

Figure 5.1: Principle of operation of the two OTDM demultiplexing techniques.

individual OTDM channel onto a different wavelength through nonlinear switching of the chirped square pulse in the Kerr gate, see Fig. 5.1(b). The individual channels can then be separated by passive filtering in the wavelength domain. This scheme can provide good tolerance to timing jitter if passive filters with square passbands are used to separate the individual demultiplexed channels.

5.2.2 Experimental Setup and Results for 40-Gb/s Demultiplexing

Our experimental setup is shown in Fig. 5.2. 2.5-ps pulses at a 10-GHz repetition rate were generated using an actively mode-locked fibre ring laser (ML-FRL) operating at 1558.5 nm and then split into two separate pulse trains. The first pulse train entered the chirped rectangular pulse generator comprising a highly nonlinear fibre (HNL-DSF2) and a linearly-chirped fibre Bragg gating (LCFBG). In the chirped rectangular pulse generator, the soliton pulses were firstly spectrally broadened to around 20 nm (-3 dB bandwidth) via self-phase modulation in the dispersion-shifted highly-nonlinear fibre. As described in Section 3.4.2, the pulses were then shaped by subsequent reflection from the LCFBG into ∼140 ps wide rectangular pulses with an almost-rectangular spectral profile of 6-nm bandwidth, which corresponds to a linear-chirp slope of 23 ps/nm. The temporal and spectral shapes are identical (in this case almost-rectangular) for highly linearly-chirped pulses, as shown in Appendix C.

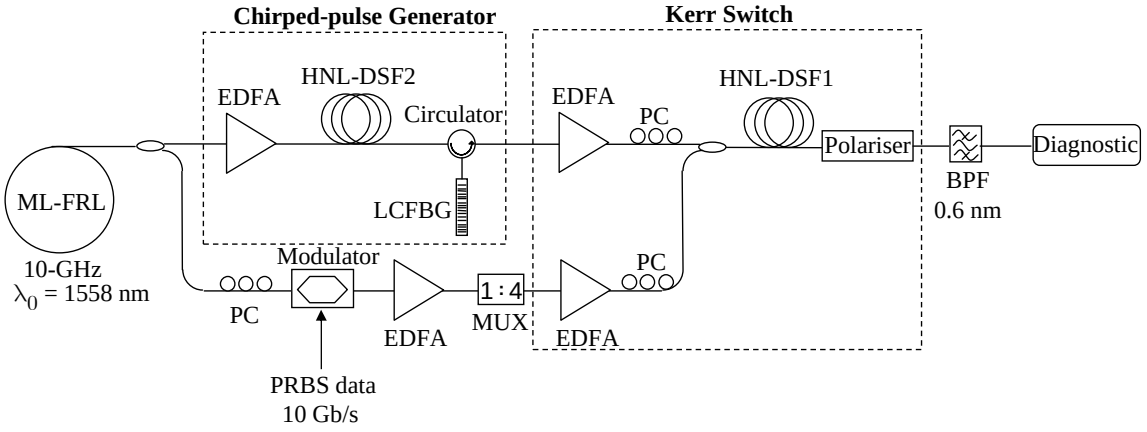

Figure 5.2: Experimental setup for 40 to 10-Gb/s OTDM onto WDM demultiplexing using linearly-chirped pulses in a Kerr Switch.

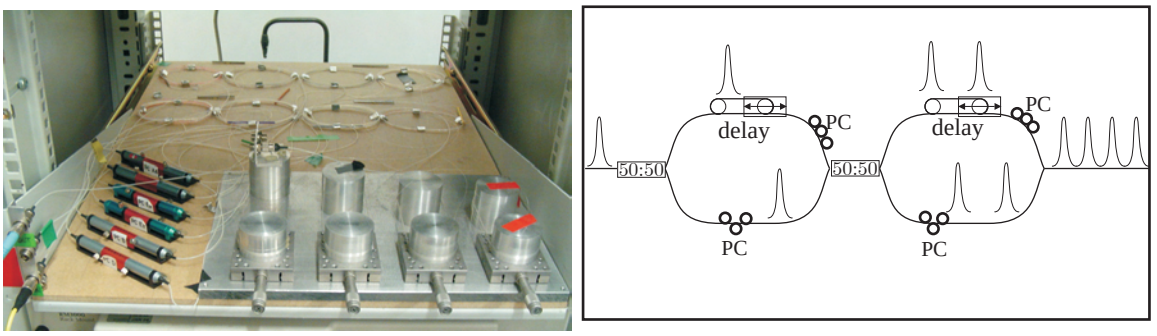

Figure 5.3: Time-division-multiplexer based on unbalanced Mach-Zehnder interferometers in cascade.

The second train of pulses was firstly modulated at 10 Gb/s with a $2^{31} - 1$ pseudo-random binary data sequence (PRBS) and was then passively multiplexed through a 1:4 fibre-based multiplexer (see Fig. 5.3) to a rate of 40 Gb/s. The multiplexer is based on unbalanced Mach-Zehnder interferometers in cascade [109]. Each stage doubles the bit-rate by interleaving two copies of its inputs shifted by a multiple integer of half of the bit-period. The input bit-rate increases therefore n-times in 2^n-stages. To generate a PRBS multiplexed-sequence, and thus avoid long sequences of zeros, each stage should approximately shift its inputs by a half pattern-length [110]. For example, considering the $2^7 - 1$ PRBS sequence, whose pattern length is 12.8 ns at 10 Gb/s, the first stage should shift its inputs by 6.4 ns plus half of the input bit-period (50 ps), the second-stage by 3.2 ns plus 25 ps, and the subsequent stages by half the shift of their preceding stage. As it can be seen in the photograph in Fig. 5.3, each fibre-stretching-delay, which is formed by a pair of metal cylinders and optical fibre wound around them, has approximately half the length of the preceding one, and therefore its fixed delay is subsequently halved. As one cylinder is fixed and the other is mounted on a movable stage, the delay can be finely tuned around a few tens of picoseconds. This multiplexer only provides $2^7 - 1$ PRBS multiplexed-sequences, since larger data sequences require impractical lengths for the fibre-stretching-delay. Furthermore, this multiplexer scheme can only be used in laboratory experiments for proof-of-principle demonstrations, since the multiplexed channels originate from the same data encoder. In a real-system implementation each channel originates from a different data encoder and they are multiplexed together in a parallel arrangement of optical-delay-lines shifted by a half bit-period.

The 40 Gb/s data and the rectangular linearly-chirped pulses were then amplified to

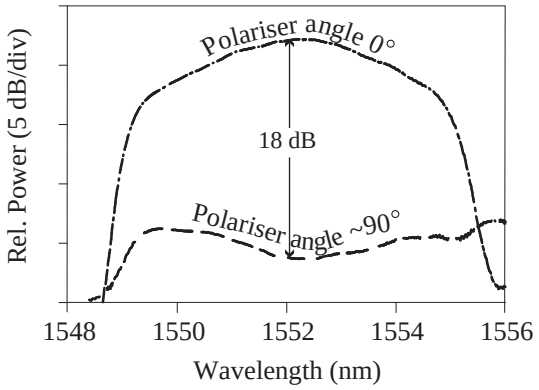

Figure 5.4: Probe suppression in the Kerr-switch when aligned to orthogonal axis.

an average power of 24 dBm and 15 dBm respectively, and coupled together using a 3-dB coupler into a fibre Kerr-switch which was based on a highly nonlinear fibre and a fibre polariser. As a one-to-one relation exists between the spectral and temporal waveforms of the linearly-chirped pulses, the polarisation extinction of the probe (linearly-chirped pulses) through the Kerr-switch can be directly estimated from the optical-spectrum measurement shown in Fig. 5.4. As can be seen, the polarisation extinction across the spectrum of the linearly-chirped pulses was only about 15 dB, although the polarisation extinction of the polariser alone was measured to be 35 dB. A possible explanation relates to the random birefringence of the highly-nonlinear-fibre in the Kerr-switch, which eventually causes any linear polarisation-state at the fibre input to change to an elliptical polarisation-state after propagating through the fibre.

In Fig. 5.5 numerical calculations of the transmittance through the polariser, which corresponds to the ratio between the energy of the electric field that passes through the polariser and the total energy of the incident electric-field, are shown as a function of the polarisation state of the incident electric-field. The calculations were carried out for a polariser with a 35-dB extinction-ratio, similar to the one I used in my experiments. The ellipticity angle is given by the phase difference between the two orthogonal components of the electric-field vector and relates to different electric-field polarisation states. For instance, the electric-field vector is linearly polarised when the two orthogonal components are in-phase, which corresponds to an ellipticity angle of zero. For ellipticity angles different from zero, the electric-field vector rotates along

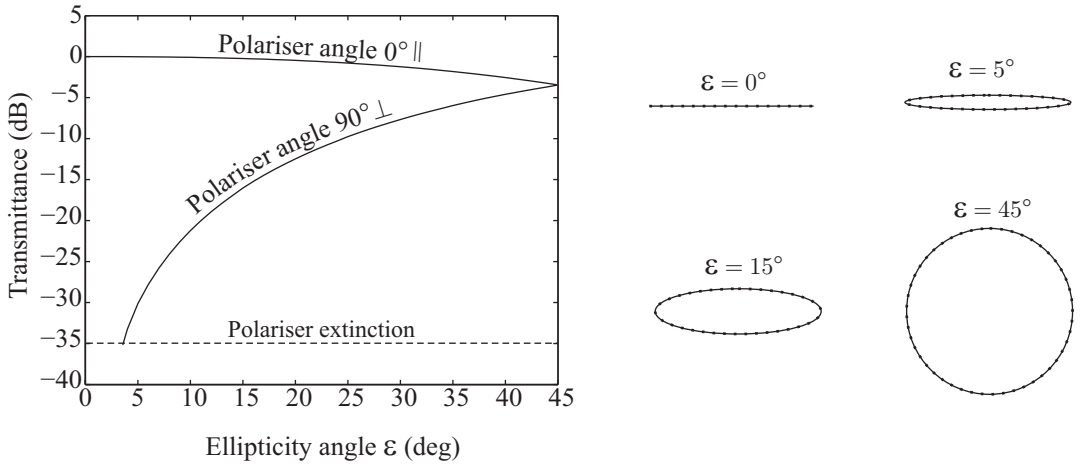

Figure 5.5: Probe polarisation extinction in the Kerr-switch as function of the state-of-polarisation at the output of the highly-nonlinear fibre.

the direction of its wavefront propagation. The relation between the ellipticity angle and the rotation of the electric-field is illustrated in Fig. 5.5.

It is, thus, clear that the maximum transmittance occurs when the electric-field vector is linearly polarised and oscillates in the direction of the polariser axis. On the other hand, the transmittance is minimum when the electric-field vector is linearly polarised and oscillates orthogonally to the direction of the polariser axis. The polarisation extinction is given by the difference between the transmittance when the polariser axis is either parallel (polariser angle 0°) or orthogonal (polariser angle 90°) to the electric field. As it can be seen in Fig. 5.5, the polarisation extinction is dominated by the polariser only when the ellipticity angle is lower than ∼4°. For larger ellipticity angles the polarisation extinction decreases drastically. The polarisation controller at the probe input of the Kerr-switch transforms any polarisation state into a linear polarisation state that can be oriented over 90°. However, due to the random birefringence of the highly-nonlinear-fibre in the Kerr-switch, a certain degree of polarisation ellipticity is expected after the fibre. This can vary largely in non-polarisation maintaining fibres, even in the case of low-birefringence fibres. A possible solution to improve the Kerr-switch extinction is either to use polarisation-maintaining fibres or a small length of low-birefringence fibre. For example, in [41] the Kerr-switch was based on a 20-m low-birefringence highly-nonlinear fibre.

The polarisation of the linearly-chirped pulses was thus set to the minimum transmittance through the Kerr-switch. In the Kerr-switch the control pulses (40 Gb/s

data) induced nonlinear polarisation-rotation via cross-phase modulation of the overlapping part of the linearly-chirped pulses. The output of the Kerr-switch consisted, therefore, of a replica of the 40-Gb/s data carved onto the linearly-chirped pulses and the residual of the control pulses not reflected by the polariser. Finally, each of the spectrally mapped OTDM channels was filtered out using a tunable passive filter with a 0.6-nm bandwidth.

Bit-error-rate (BER) and eye-diagram measurements were carried out to quantify the demultiplexer performance. Fig. 5.6 shows the combined spectrum of the original 40-Gb/s signal and the rectangular linearly-chirped pulses after the polariser, which shows the spectral mapping of the individual tributary channels, as well as the eye diagrams of the original 40-Gb/s signal and of each of the demultiplexed channels. The eye-diagram of the 40-Gb/s OTDM original resembles that of a nonreturn-to-zero signal due to the low bandwidth of the utilised electrical-receiver (∼20 GHz). As shown in the figure, the quality of the demultiplexed channel eye-diagrams is very close to that of the original signal for channels 2 and 4, while significant amplitude noise degradation is observed for channels 1 and 3. This can also be observed in the BER curves shown in Fig. 5.7. Nevertheless, error-free demultiplexing of all-four channels was readily achieved with a power penalty of 1.5 dB, see Fig. 5.7. The noise degradation in channels 1 and 3 is likely to originate from a bit-to-bit change in the state-of-polarisation set within the 10:40-Gb/s passive multiplexer. In

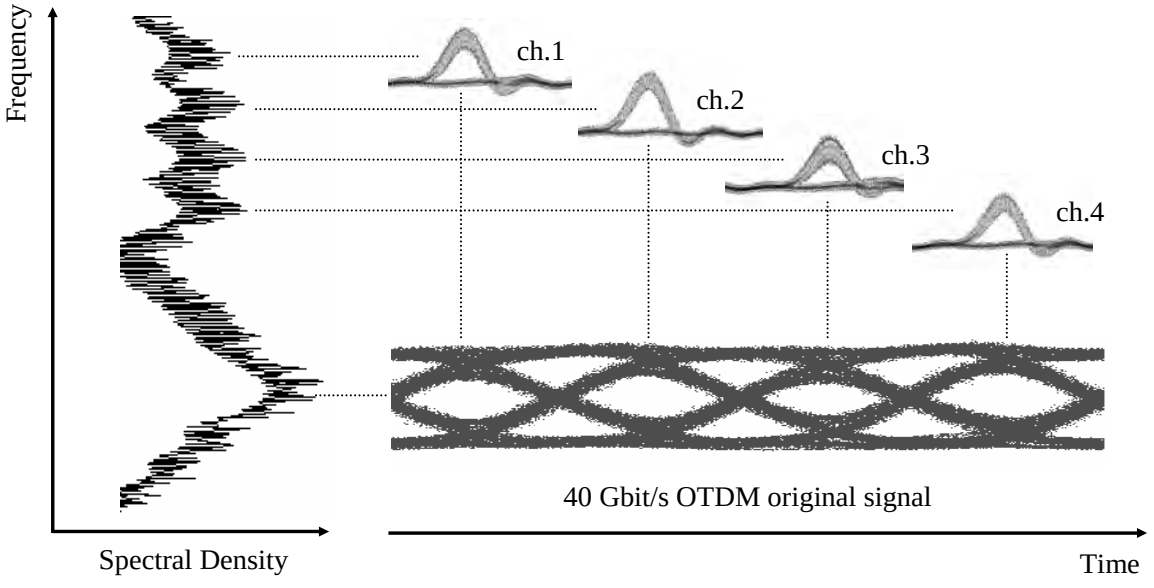

Figure 5.6: Eye diagrams of the original 40-Gb/s signal and 10-Gb/s demultiplexed channels, and the corresponding optical spectrum after the Kerr gate.

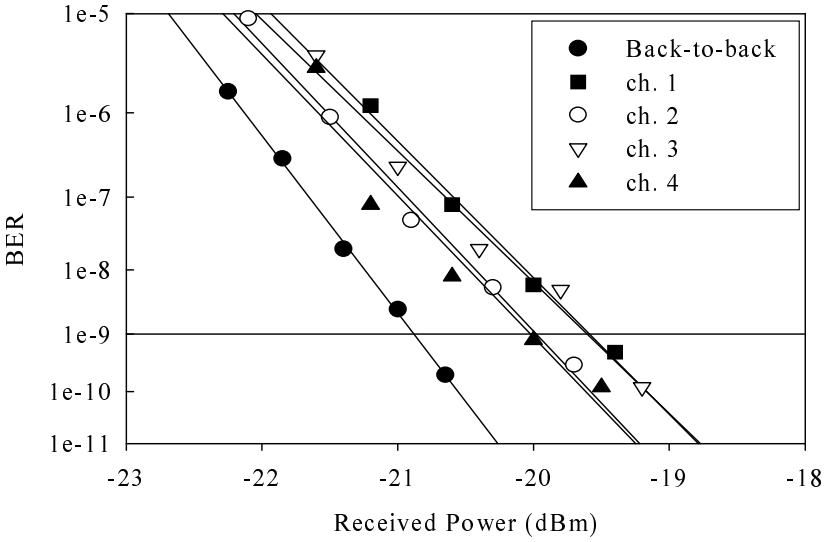

Figure 5.7: Measured bit error rate for 40:10 Gb/s demultiplexing.

later experiments, a polariser was used after the multiplexer to ensure that all the multiplexed channels have the same state-of-polarisation. In this instance, however, a polariser was not used after the multiplexer.

5.3 OTDM Signal Add-drop Multiplexing Based on NOLM Switching of Linearly-Chirped Pulses

Demultiplexing of a high-speed OTDM signal onto low bit-rate signals, which can then be converted into electrical signals, can be necessary either at the network edge-routers or at the end-user receiver. In the network, add and drop of tributary channels from a high-speed OTDM signal is likely to be a more essential function, since it allows sharing of the high-speed optical medium with other users at intermediate network nodes. Although there is some similarity between the two functions, time-division add-drop multiplexing (TADM) is a more sophisticated application because it is used to remove and aggregate tributaries from an ultra-high speed signal without affecting any of the adjacent channels. Moreover, in contrast to demultiplexing, the processed signal needs to keep a high on-off extinction ratio and signal-to-noise ratio. The practical implementation of the TADM function requires copying the data in a

specific tributary channel into a separate signal, clearing the corresponding bit-slot, and finally coupling a new tributary channel into the cleared bit-slot.

Several groups have previously demonstrated TADM based on three different concepts: nonlinear switching, multiple wavelength conversion and ultrafast electro-optic modulation. TADM devices based on nonlinear switching are normally 4-port systems. The two input ports contain the data signal and a synchronized clock at the tributary rate, which is responsible for changing the state of the switch. The data signal is then transmitted to either of the two output ports depending on whether the switch is excited or not. A synchronised add channel can then be inserted into the cleared channel slot. Several nonlinear switching mechanisms have been proposed for TADM, such as wavelength shifting [111], polarization rotation [112–114] and cross-phase modulation in a nonlinear loop mirror [115–117]. Although this technique has the advantage of a simple configuration, the typical extinction-ratio of the switching window, as defined by the nonlinear transfer function of the switch, in most cases gives only limited clearing efficiency within the dropped channel time-slot.

In multiple wavelength conversion schemes two wavelength translation processes are used [118–120]. Two clock signals at different wavelengths are prepared, one at the repetition rate of a single tributary, the other a (N-1)×multiplexed clock signal, where N is the total number of tributary channels. The clock signals are synchronized to the incoming data stream, and clock and data are coupled into a wavelength converter which separates the data into two different wavelengths. A further stage of wavelength conversion is necessary if it is required to maintain the original wavelength for both of the separated signals.

The approach based on ultrafast modulators has the advantage of low total-power consumption, but requires separate modulators for the drop and add functions [121].

Although all the previous techniques are capable of operating at very high bit rates, the associated dropped channel suppression ratios are typically less than 25 dB. This can be a severe limitation to cascaded add/drop multiplexing. Reference [122] reports a study of the requirements in terms of the dropped channel time-slot suppression and pulse peak-to-pedestal ratio for the added channel when cascading TADMs. It shows that in a realistic cascaded add-drop operation at 40 Gb/s, where it is not always the same channel that is dropped, an extremely high pulse peak-to-pedestal

ratio, in excess of 40 dB, is necessary to guarantee error-free performance within a 1-dB power penalty for slot suppression values under 25 dB. It also shows that the pulse quality of the added channel can be relaxed if the time-slot clearing efficiency is increased, for example for the same system a suppression ratio of 35 dB reduces the peak-to-pedestal extinction of the added channel to 33 dB. Beyond 35-dB slot suppression there is no significant improvement, and the quality of the added pulse is the dominant factor that affects scaling to higher bit-rates. Therefore time-slot suppression ratios in excess of 30 dB are a key requirement when cascading add/drop nodes.

In this chapter I demonstrate a novel TADM technique operating at 40 Gb/s based on the principle of TDM-to-WDM conversion that is capable of providing a time-slot suppression ratio of more than 35 dB. Whilst TADM normally requires critical synchronization and state-of-the-art ultrafast switches, high suppression-ratio wavelength add-drop multiplexing (WADM) can readily be achieved using commercially available passive optical filters. In the TADM approach reported in this thesis the incoming OTDM signal is first converted into a mixed TDM-WDM replica, which maps the individual tributary channels onto discrete separate wavelengths whilst retaining the critical pulse-timing information, opening the possibility to process the signal directly within the frequency domain (and additionally within the time domain if required). A dropped-channel time-slot suppression ratio of 35 dB can readily be achieved by this means. Moreover, since it is possible to create relatively complex filters with well defined phase and amplitude responses over large bandwidths, e.g. using fibre Bragg grating technology, all the tributary channels can be processed simultaneously in a single fibre without the need for additional channel synchronization, making the device power-efficient.

5.3.1 Concept of TADM using TDM-to-WDM Conversion

The proposed TADM technique is illustrated in Fig. 5.8. An incoming transmitted high-speed TDM signal is first converted into a mixed time-wavelength multiplexed format. The specific technological approach that we have adopted to perform the TDM-WDM conversion is detailed in Chapter 4 and shown in Fig. 5.9(a), and is based on the nonlinear switching of linearly-chirped pulses in a low pulse walk-off,

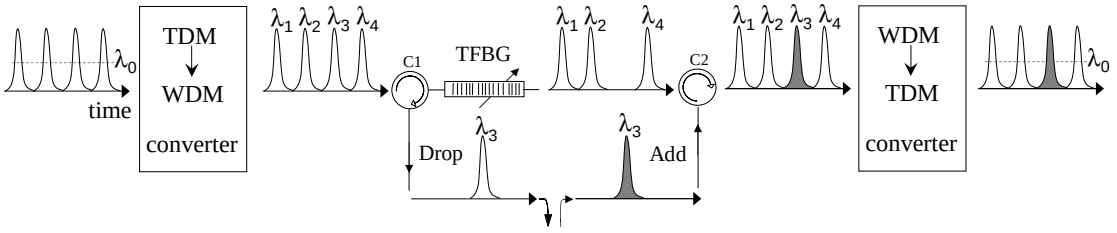

Figure 5.8: Concept of the OTDM add/drop multiplexer based on time-to-wavelength conversion. (C1: circulator 1; C2: circulator 2)

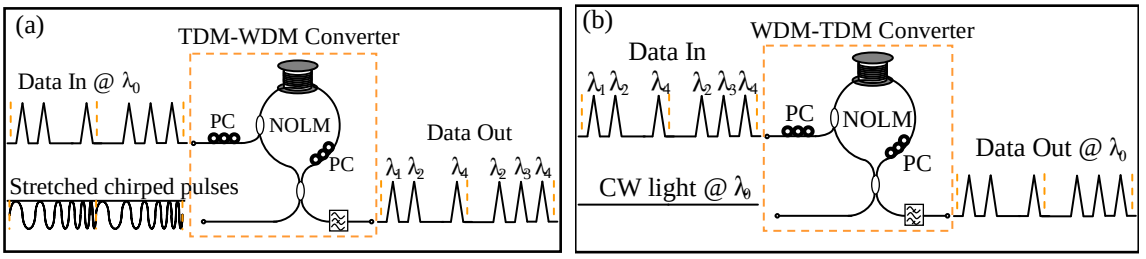

Figure 5.9: Schematic diagram of (a) the TDM to mixed TDM-WDM converter, (b) the mixed TDM-WDM to pure TDM converter, both using a NOLM switch.

broadband NOLM. The dual time-wavelength mapping of the data signal, after the NOLM, allows the use of spectral filters (as well as ultrafast switches if desired) for the manipulation of the signal. For example, add/drop multiplexing in a mixed format signal can be performed using a reflective fibre Bragg grating (FBG) filter in a two circulator configuration commonly used in WADM (Fig. 5.8). The tunable FBG (TFBG) filter is centered at the wavelength of one of the tributary channels which is reflected to port 3 of circulator 1. The signal transmitted through the FBG filter into port 2 of circulator 2 corresponds to the remaining tributary channels with one time slot (and the corresponding wavelength) cleared out. A new channel can be added to the cleared time slot and within an empty spectral region. Furthermore, this process can be extended to any of the remaining tributary channels simply by cascading more TFBG stages within the set-up. A final conversion back onto a pure, single wavelength TDM signal might be necessary if the add/drop multiplexer is in the mid span of a transmission line. Fig. 5.9(b) shows a diagram of the WDM-TDM converter which is used in this work and which is based on carving a CW-beam at the desired wavelength with the mixed TDM-WDM signal representation, using a NOLM designed for broadband operation with low interchannel temporal walk-off, such as that in Fig. 5.10, which uses a nonlinear fibre with ultra-low dispersion between 1500

and 1600 nm.

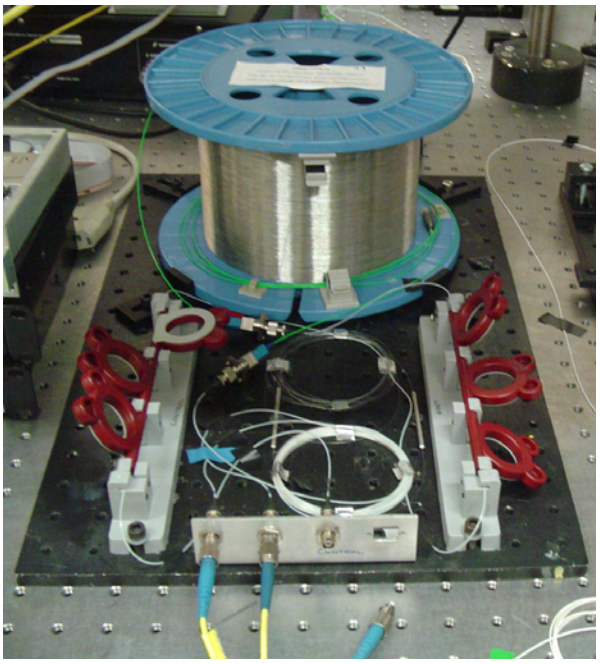

Figure 5.10: Nonlinear optical loop mirror using a 1-km long dispersion-shifted highly nonlinear fibre.

5.3.2 Time and Wavelength Add/Drop Port

Once the signal has been converted into a mixed TDM-WDM format, it can be processed either in the time or the wavelength domain. For add/drop multiplexing, I have used spectral processing, since it allows for the use of passive spectral filters using mature technology originally developed for WDM systems. Several devices for WDM add/drop multiplexing have been proposed and demonstrated using various filtering technologies such as arrayed waveguide gratings, fibre Bragg gratings, Mach-Zehnder filters, and ring resonators. All can filter out an individual channel without affecting the other channels aggregated in the same optical fibre. One essential feature of an add-drop multiplexer is high drop-channel suppression, since the accumulation of crosstalk can lead to severe signal degradation. The application of FBGs for wavelength add-drop multiplexing has already been studied extensively (e.g. see [123]). FBG add/drop filters are now available with a peak reflectivity well over 99.9%, whereas significant design improvements have helped to overcome what were traditionally thought to be limitations in the performance of these devices, such as

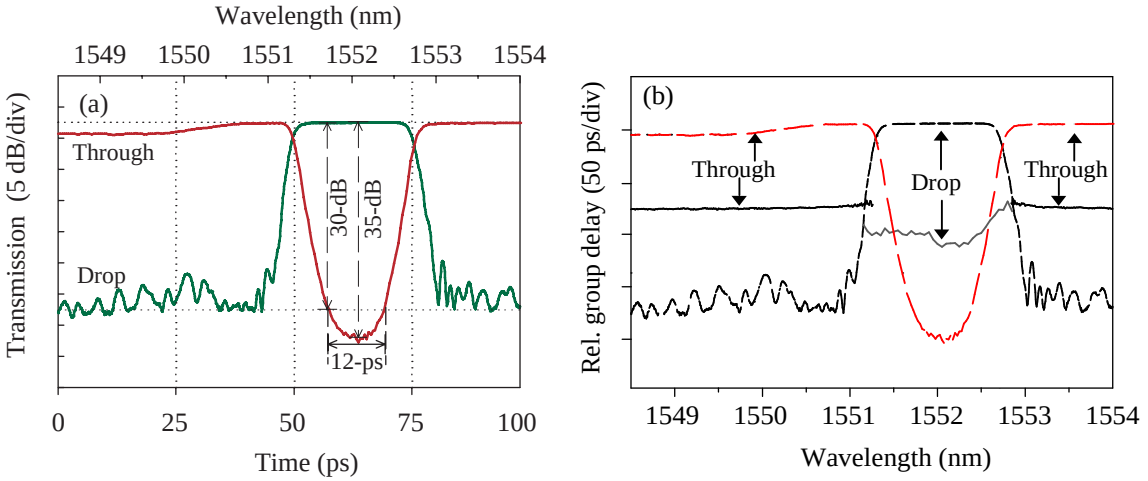

Figure 5.11: Experimental characterization of the add/drop port. (a) Intensity measurements of the through and drop ports, (b) corresponding relative group-delay measurements (for reference the intensity plots are also shown in this graph).

in-band dispersion [66]. Furthermore, recent research effort has moved towards the development of tunable FBG technology suitable for dynamic WDM networks [3].

As shown in Chapter 3, the temporal envelope of a highly-chirped pulse mirrors the spectral envelope when it is stretched in a dispersive fibre. Therefore, when an FBG carves the spectrum of a linearly-chirped pulse, a temporal window with similar features is produced. The duration of the temporal window is defined by the pulse chirp-rate. For our particular system, we have used pulses with a linear chirp-rate of 6 nm over 100 ps, and an FBG with a square passband of 1.5 nm. By measuring the spectral characteristics of the FBG, its behaviour in time can also be predicted. This is shown in Fig. 5.11, which illustrates that the bandwidth of the FBG corresponds to a switching window of 25 ps (100 ps over 6 nm times 1.5 nm).

For reference, the spectral traces shown in the figure were taken with a resolution bandwidth of 0.01 nm which corresponds to a temporal resolution of 170 fs (100 ps over 6 nm times 0.01 nm). These traces also show that the FBG had a maximum transmission-loss at the bandgap centre of 35 dB, which corresponds to a reflectivity of 99.97%. Overall the channel suppression was better than 30 dB within a 12-ps window. The square-like shape of the FBG reflectivity produces a square-like temporal window, which ensures that the channel is dropped without distortion while imposing high suppression on the adjacent channels. Channel distortion can still be induced by inherent dispersion in the reflection and transmission bands of the add/drop FBG filter. It is, therefore, essential to use dispersion-less FBG filters for

add/drop multiplexing [67]. However, dispersion-less FBG filters with large bandwidths, as required for this add/drop scheme (i.e. bandwidths of ∼1.5 nm), can be challenging to fabricate. According to Eq. (2.23), in order to achieve a large FBG bandwidth the amplitude of the refractive-index modulation should be large, whereas the grating length should be short. Furthermore, to achieve a nearly constant group-delay across the reflection bandwidth, all light should be reflected from the same point within the FBG. Therefore, the fabrication of broadband dispersion-less FBG filters require a large and sharp index-modulation to be induced. For instance, the broadest dispersion-less FBGs with a reflectivity higher than 99.9% fabricated in our laboratories to date have had a bandwidth of about 1 nm. A more practical approach is to use a chirped FBG, since in this case both high reflectivity and wide bandwidth can be achieved in a straightforward manner. The inherent FBG dispersion can then be compensated for with a dispersive fibre or another chirped FBG with the opposite dispersion. This was the approach used in this work. In Fig. 5.11(b), the measured relative-group-delay of the combined chirped-FBG and dispersive fibre is shown. As can be seen, in the transmission band, which affects the through channels, the group delay is nearly constant, whereas in the reflection band, which affects the drop and add channels, the group delay changes slightly in the long-wavelength side of the band. Further details and complete characterisation of the drop-channel, when pulses signals are used, is given in the next section which describes the overall system performance.

In order to be able to drop any of the tributary channels, the FBG was mounted on a tuning device which uses mechanical stress to alter the effective grating period, so that the FBG centre wavelength can be tuned to match any of the tributary channels. In Figs. 5.12(a) and (b), two different mounts for the add/drop FBGs used in the laboratory experiments performed in this thesis are shown. In Fig. 5.12(a) the FBG is mounted on a beam that can be bent and, consequently, force grating-period compression. This shifts the Bragg wavelength of the FBG to shorter wavelengths. Tuning over 40 nm could be achieved with the devices used in my experiments, although it has now been demonstrated that the same technique can provide tuning over 100 nm [3]. In Fig. 5.12(b) the FBG is instead glued on one end to a fixed stage and on the other end to a translation stage. The translation stage is aligned to move in the FBG axial-direction, which can induce a tensile-strain of the FBG and, consequently, elongate the grating period. This shifts the Bragg wavelength to longer

wavelengths. However, because of the limited mechanical elasticity of silica, the FBG cannot be stretched by more than 1% (corresponding to a tuning of $1-1.5$ nm), without running the risk of breaking the FBG. Nevertheless, this is a simple mounting technique which has proven valuable to precisely tune the original Bragg-wavelength in several experiments.

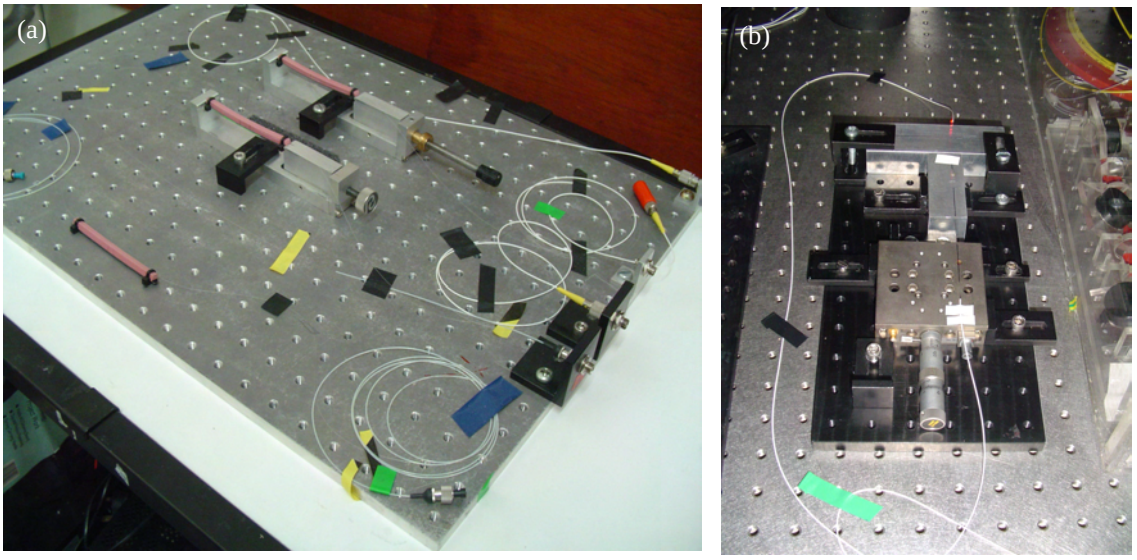

Figure 5.12: Tunable mounts used to shift the centre wavelength of the add/drop FBG filters. (a) Beam bending; (b) Fibre stretching.

5.3.3 Experimental Setup and Results for 40-Gb/s TADM

The complete setup of the OTDM add/drop multiplexer that we used for our demonstration experiments is shown in Fig. 5.13. The 40 Gb/s RZ-OTDM transmitter consisted of a gain-switched diode laser producing pulses with a full-width at half-maximum of 9.5 ps ($\tau_0 = 5.7$ ps assuming Gaussian pulses) at 10 GHz and a centre wavelength of 1546 nm. The pulses were externally modulated with a $2^{31}-1$ PRBS data sequence and then multiplexed to a line-rate of 40 Gb/s. Fig. 5.14(a) shows the corresponding spectrum and eye-diagrams. At the add-drop multiplexer input, the 40-Gb/s data was amplified to an average power of 20 dBm and launched into the control port of a highly-nonlinear fibre (HNLF) optical loop mirror (NOLM). Details of the HNLFs used are given in Table 2.1. The signal to the NOLM comprised 100-ps linearly-chirped super-Gaussian pulses at a 10-GHz repetition rate and a flat top bandwidth of 6 nm, which corresponds to a chirp-rate (C) of $+0.024$ ps^{-2}. Under these conditions the NOLM switch was operated at a chirp-width product ($C\tau_0^2$) of

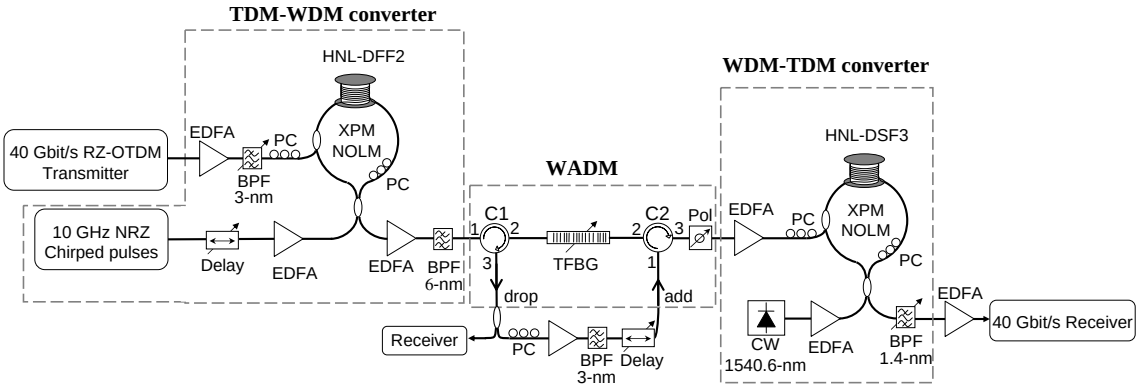

Figure 5.13: Experimental setup for time division add/drop multiplexing at 40 Gb/s. (WADM: wavelength add/drop multiplexer, TFBG: tunable fibre-Bragg-grating, EDFA: erbium doped fibre amplifier, PC: polarization controller, BPF: band-pass filter)

0.8. The chirped pulses were amplified to an average power of 15 dBm and launched into the signal port of the NOLM. After switching in the NOLM these pulses were carved into a TDM-WDM replica of the original data as shown in Fig. 5.14(b). The 3-dB bandwidth of each channel was 0.7 nm and the spacing between them 1.4 nm. Fig. 5.15 shows simultaneous traces observed while running the experimental setup. In this photograph, the optical-spectrum-analyser (top) shows the TDM-WDM signal, whereas the digital-communications-analyser (bottom) shows the eye-diagram of the original 40-Gb/s TDM data. By filtering out the original 40-Gb/s signal with a 6-nm bandpass filter, a suppression ratio between the switched and original signals of ∼30 dB was achieved.

The temporal waveform of the switched signal was assessed by measuring its autocorrelation. As shown in Fig. 5.16, the envelope and period of the individual pulses is the same in the original and converted signals, suggesting that TDM-WDM conversion has not affected the quality of the signal. The TDM-WDM signal was then injected into the tunable fibre-Bragg-grating (TFBG), in the WDM add/drop multiplexer, using the circulator arrangement shown in Fig. 5.13. The drop port was then port 3 of C1 and the add port of a new 10-Gb/s channel was port 1 of C2. Figs.5.14(c) and (d) show the spectra and eye diagrams of the through and dropped channels, respectively. The spectrum of the through channels shows more than 30-dB suppression of the dropped channel, which confirms high-quality channel clearing. The

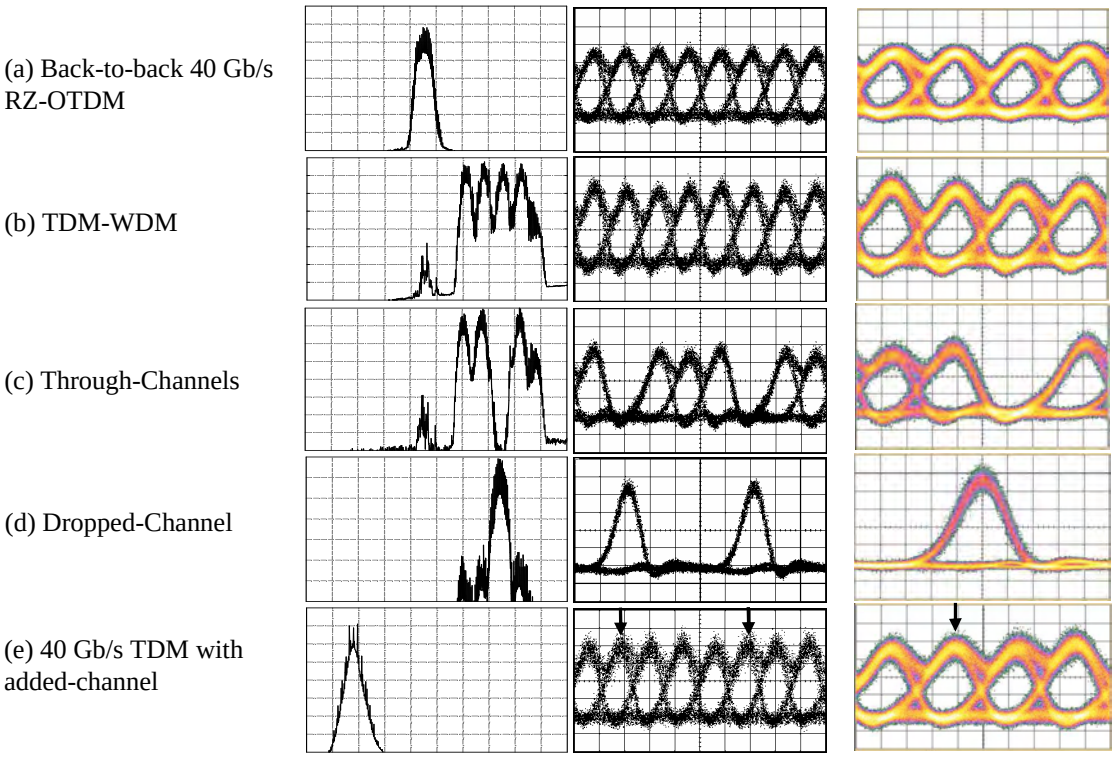

Figure 5.14: Spectra and eye diagrams at different stages of the OTDM add/drop multiplexer. Left: optical spectra (vert. scale: 5 dB/div, horiz. scale: 2 nm/div, span: 1537-1557 nm, RB: 0.01 nm). Right: eye diagrams (horiz. scale: 20 ps/div).

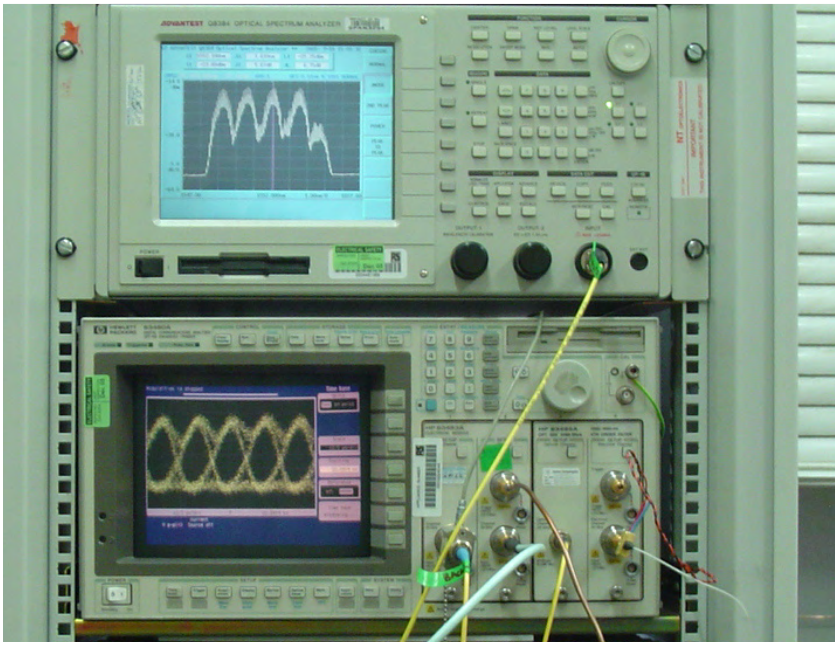

Figure 5.15: Optical spectrum of the Mixed TDM-WDM signal (top), and eye-diagram of the original 40-Gb/s OTDM signal (bottom).

dropped channel is depicted in Fig. 5.14(d), where one can see that the extinction ratio between this channel and the rest of the band was >25 dB.

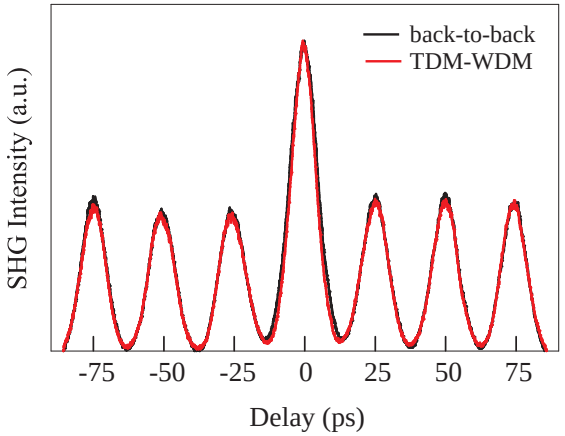

Figure 5.16: Autocorrelation traces of the incoming 40-Gb/s OTDM signal and the converted mixed TDM-WDM signal.

As discussed in the previous section, the tunable fibre-Bragg-grating (TFBG) in the WDM add/drop multiplexer consisted of a chirped FBG, which allows for a combination of large bandwidth and high reflectivity. Fig. 5.17 shows a detailed schematic of the drop port together with measurements of the group-delay across the TFBG reflective bandwidth, when the signal is reflected off the grating (CFBG), and after subsequent propagation in a dispersion compensating fibre (CFBG+SSMF). As can be seen, the group-delay is linear across the reflective bandwidth of the CFBG, except near the long-wavelength edge. The estimated dispersion associated with the linear group-delay was -96 ps/nm. A standard single-mode-fibre (SSMF) with a dispersion coefficient of +17 ps/nm/km was used to compensate for the dispersion of the CFBG. The length of the SSMF that compensates for the estimated dispersion is therefore 5.7 km. The combined dispersion of the CFBG and SSMF was nearly zero across a large part of the grating stopband but not near the long-wavelength edge, where the dispersion of the CFGB is nearly zero. The effect of the residual dispersion across the drop port was assessed by comparing the pulse characteristics at the input and output of the system. The pulses in the dropped channel were measured using FROG and compared against the pulses in the same channel at the input-port.

Fig. 5.18(a) shows the temporal intensity-envelope on a logarithmic scale and the frequency-chirp of the FROG-retrieved pulses, where the pulses in the dropped channel are shown by the solid-line and the input-port pulses by the dashed-line. Fig. 5.18(b) shows the corresponding spectra and relative group-delays. As can be seen, the observed pulse-distortion was very small since the envelope and chirp of both the input- and drop-port pulses were in good agreement. It needs, however, to be noted that the

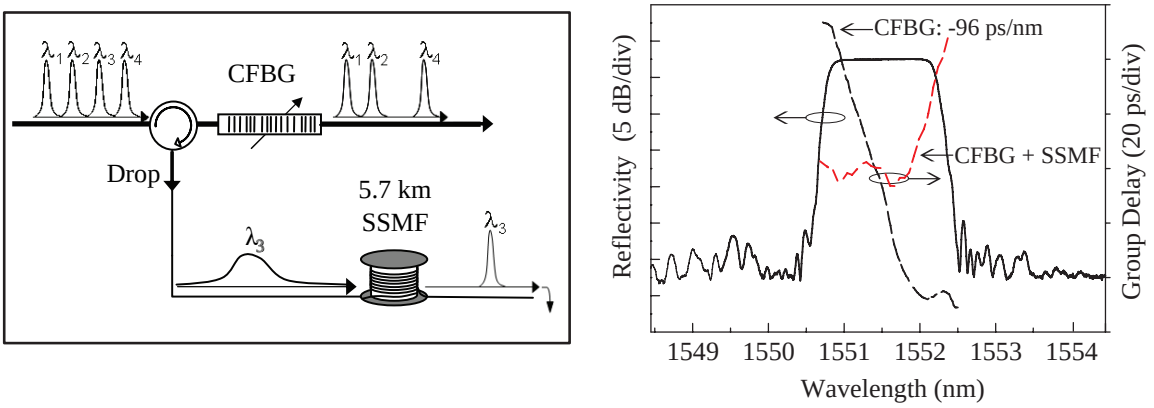

Figure 5.17: Schematic diagram of the WDM add/drop multiplexer drop-port and group-delay measured across the CFBG stopband.

spectrometer used in the FROG instrument had a fairly poor input-power dynamic-range of 15 dB, and hence the features on the retrieved pulses below the 15-dB peak-intensity level are most likely spurious. Nevertheless, it shows that the pulse duration was recovered to ∼9 ps at the output of the drop-port. This was also confirmed by independently measuring the pulse intensity-autocorrelation traces, which are shown in Fig. 5.19. As can be seen, the autocorrelations have the same full-width at the half-maximum of 13 ps, which assuming Gaussian pulses corresponds to a pulse-duration of 9 ps. The drop-channel pulses show, however, wider wings when compared to the input-port pulses, which could have been induced by the non-compensated dispersion near the long-wavelength edge of the grating stopband. Although some pulse distortion was possibly induced, the measurements confirmed good pulse quality.

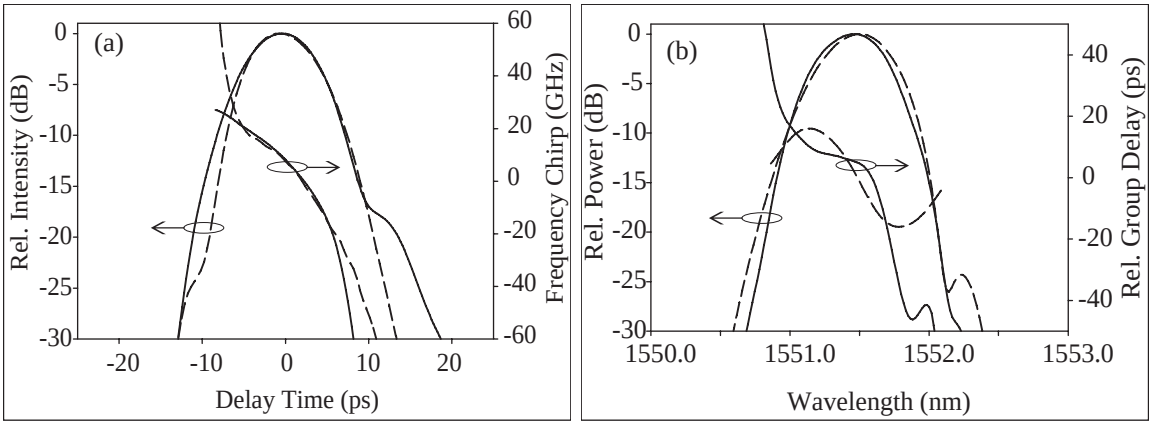

Figure 5.18: Temporal and spectral intensities retrieved from SHG-FROG spectrograms for the pulses in the dropped-channel (solid line) and the pulses at the WDM add/drop multiplexer input (dashed line). (a) Temporal envelope and frequency chirp, (b) Spectral envelope and group delay.

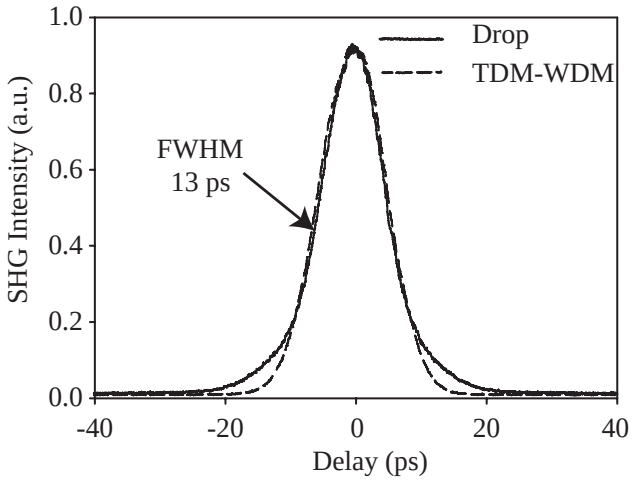

Figure 5.19: Autocorrelation traces of the pulses in the dropped-channel (solid line) and the pulses in the mixed TDM-WDM signal (dashed line) at the input of the WDM add/drop multiplexer.

In order to demonstrate the add function of the multiplexer we then coupled a signal onto the remaining channels in the line, which were transmitted through the TFBG. As long as it was temporally synchronized with the rest of the data, this signal could be operating at any wavelength. In our case, and for practical reasons, we chose to re-inject the same channel to the add port. This represents the worst case for coherent crosstalk between the residual channel energy transmitted through the FBG filter and the newly added channel. However, the high reflectivity of the FBG used (99.97%) reduced the crosstalk noise level to less than the typical laser or nonlinear-switch noise level. A tunable optical delay line was used on the add channel to ensure that these pulses were injected into the cleared time slot.

In our scheme, a further stage of nonlinear switching was used to convert the signal from mixed TDM-WDM back to TDM format. The signal was first coupled to a fibre polarizer to equalize the state-of-polarization of all channels. The TDM-WDM signal, with a new added channel, was then amplified to an average power of 18 dBm and used as the NOLM control to switch a continuous-wave beam at 1540.6 nm. At the output of the NOLM a 1.4-nm bandpass filter isolated the switched signal from the control, yielding the spectrum shown in Fig. 5.14(e). Open eye diagrams were obtained, albeit with a slight increase in amplitude noise.

To assess the add/drop operation, we measured bit error rates (BER) before and after the add/drop multiplexer, using a 40 -Gb/s receiver comprising a 40:10-Gb/s electro-absorption-modulator-based demultiplexer. Fig. 5.20 shows the achieved BER

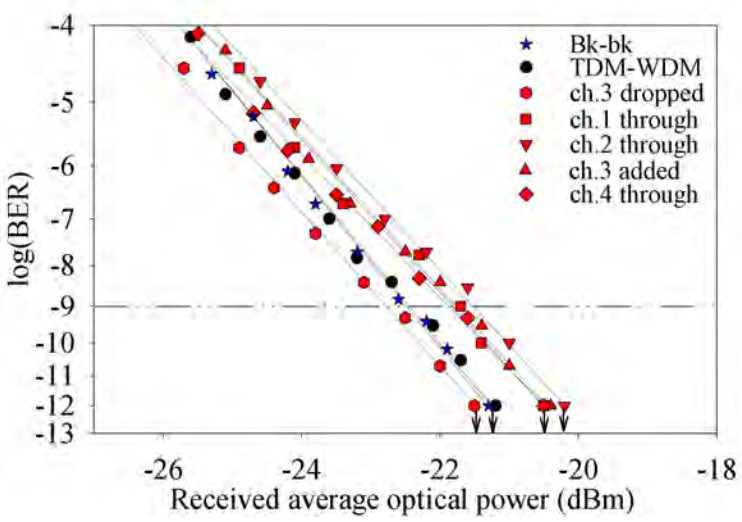

Figure 5.20: Measured BER versus received optical power for the 40-Gb/s OTDM add/drop multiplexer.

performance in comparison to the 40-Gb/s back-to-back signal. Error-free operation was achieved within a 2-dB power penalty for all cases, and no degradation due to crosstalk was observed for the added channel. As for the dropped channel, a BER improvement was observed which is mainly due to the reduction of the significant intersymbol-interference that existed on the original 40-Gb/s signal.

A very attractive feature of the scheme proposed herein, compared to time domain techniques, is the potential for the simultaneous dropping of several tributary channels by simply cascading tuneable FBG filters. For example, dropping of two channels is possible using the arrangement of circulators and TFBGs shown in Fig. 5.21(a). In Fig. 5.21(b) measurements of the transmission of the through and drop ports are shown. Fig. 5.21(a) also shows eye diagrams of the through channels after two tributary channels have been dropped off from the 40-Gb/s OTDM signal, confirming the practicality of the system. Unfortunately, the dispersion in the reflective bandwidth of the particular TFBGs used in this instance, which is shown in Fig. 5.21(b), changes drastically from about -50 ps/nm to +50 ps/nm within a 1-nm interval, and therefore cannot be compensated for with a dispersive fibre. This led to a significant degradation of the quality of the dropped channels and impaired the possibility of further investigating this scheme.

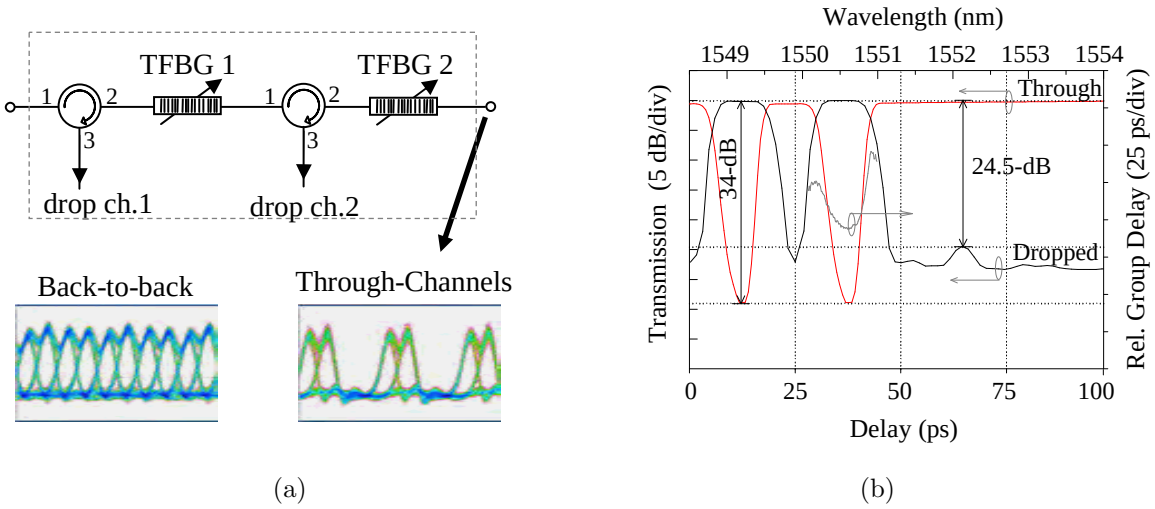

(a) (b)

Figure 5.21: Simultaneous time-division add/drop multiplexing of two tributary channels. (a) WDM add/drop multiplexer scheme and measured eye-diagrams (25 ps/div), (b) experimental characterisation of the transmission and relative group-delay of the through and drop ports.

5.4 Summary and Discussion

In this chapter, I have experimentally demonstrated time-division demultiplexing and add/drop multiplexing based on the nonlinear gating of linearly-chirped pulses. The technique relies on the generation of linearly-chirped pulses, which are synchronous to and run at the rate of the data clock, and have a duty cycle of 100%. The linearly-chirped pulses also have a wide flat spectrum and a rectangular temporal envelope stretched to overlap all the tributary channels. These pulses are then injected into the signal-port of an ultrafast switch. The switch is controlled by the OTDM-signal pulses, and consequently, each tributary gates the chirped-pulse at a different instantaneous frequency. The OTDM signal is thus converted into a mixed TDM-WDM replica at the switch output. The signal can then be processed either in the temporal or spectral domains.

This technique was first applied to the demonstration of all-optical demultiplexing of the four 10-Gb/s constituent channels of a 40-Gb/s OTDM data signal using a fibre Kerr-switch and a passive optical filter as the demultiplexer. Error-free demultiplexing was achieved with a power penalty of ~1.5 dB relative to the 10-Gb/s base rate back-to-back. The power-penalty observed was mainly due to the poor polarisation extinction in the fibre Kerr-switch. The effect of the residual birefringence of the

non-polarisation maintaining highly-nonlinear fibre was investigated numerically. It was concluded that even a small residual birefringence can degrade significantly the polarisation extinction of the Kerr-switch. This can be minimized by either using a polarisation-maintaining highly-nonlinear fibre or by shortening the length of the highly-nonlinear fibre.

The multiplexing-format conversion technique was then applied to the demonstration of time-division add/drop multiplexing (TADM) of all 10-Gb/s constituent channels of a 40-Gb/s OTDM signal. TADM occurs typically at intermediate nodes in the optical network, and high quality of the throughput OTDM-signal is an utmost requirement. Therefore, instead of a Kerr gate, nonlinear gating of the linearly-chirped pulses in a NOLM-switch was considered in this case, so that a high on-off extinction of the switched signal could be achieved. The 40-Gb/s OTDM data pulses were then converted into 4-WDM channels, each carrying 10-Gb/s data. By using an FBG filter we were able to drop these channels with a suppression ratio better than 30 dB and add new channels to the line, without affecting the quality of the remaining channels. A second NOLM-switch converts the 4-WDM channels onto a single optical-carrier, and produces a throughput OTDM-signal with approximately the same bandwidth as the original 40-Gb/s OTDM signal. In the TADM experiments, the linearly-chirped pulses had a chirp-rate of $+0.024\,\mathrm{ps}^{-2}$, and the pulse-width of the original OTDM pulses was 9.5 ps, corresponding to a chirp-width product of $\sim$0.8 for the NOLM gate. This condition ensured distortion-free OTDM-to-WDM conversion with a spectral channel crosstalk-level lower than 20 dB, see Fig. 4.12 in Chapter 4. With this technique, it is straightforward to achieve serial dropping of tributary-channels, by simply cascading more than one FBG filter. The simultaneous dropping of two OTDM channels was demonstrated in a proof-of-principle experiment.

The application of this scheme to higher bit-rates requires the generation of linearly-chirped pulses with an even wider spectrum. The chirp-rate increases with the width of the spectrum and, consequently, the spectral channel-separation also increases. This also allows nonlinear gating with shorter OTDM-data pulses, and therefore, appropriate OTDM-to-WDM conversion can be achieved at higher bit-rates. The linearly-chirped pulse bandwidth requirement as a function of the OTDM line bit-rate is plotted in Fig. 4.13 in Chapter 4. For instance, TADM operation at 160 Gb/s requires a bandwidth of 25 nm at a tributary bit-rate of 40 Gb/s. This can be easily

generated through SPM in the normal-dispersion regime of a highly-nonlinear fibre. However, as discussed in Chapter 3, it is challenging to generate flat spectral-density, which is required to uniformly map the tributary channels into the spectral domain, over a broad spectrum. Beside the pulse pre-shaping technique demonstrated in Chapter 3, the SPM-broadened spectrum can also be flattened using a dynamic-gain-equaliser, as shown in [98].

The time division add/drop multiplexing technique demonstrated in this chapter has, therefore, the potential to operate at higher bit-rates and benefits from the flexibility to process the signal either in the temporal or spectral domains, which can allow a number of complex multiplexing functions using passive optical components.

Chapter 6

Packet Compression and Expansion Based on NOLM Switching of Linearly-Chirped Pulses

Overview: In this chapter, I describe a novel scheme for all-optical packet compression and expansion. The technique relies upon the switching of linearly-chirped rectangular pulses with the original TDM packet. The switching maps the individual adjacent data bits of the TDM packet onto pulses with different wavelengths. A dispersive linear element, in our case an optical fibre, can then be used to control both the separation and width of these pulses and to create a time compressed or expanded version of the original packet. This technique has the potential to achieve operation at ultra-high bit-rates up to Tb/s. The packet length, however, is limited by the bandwidth of the original linearly-chirped pulses. In Chapter 4, the linearly-chirped pulse bandwidth required to adequately convert an incoming signal into a mixed TDM-WDM replica was estimated as a function of the signal bit-rate. In this chapter, it is shown that in order to adequately compress/expand the pulses of the mixed TDM-WDM replica a wider bandwidth can be required, which limits in practice the operable packet length.

In the future, different networks may be connected through an all-optical gateway. The gateway function is to harmonise the data format of the different networks. For instance, different networks may use different signal formats (e.g. RZ or NRZ)[1], multiplexing formats (TDM, WDM or CDM), modulation formats (e.g. ASK or PSK), bit-rates, modulation clocks, and so on. It is unlikely that networks supporting different services will use the same transmission technique. For example, transoceanic systems are likely to continue using WDM, as a large amount of data can be aggregated in a straightforward manner and long-haul transmission is achieved without complex and expensive regeneration schemes, while access networks may opt for high-speed TDMA or/and CDMA, because these technologies can provide among other advantages, spectrum efficient utilisation, simpler network management and control, and higher security. The different manner in which the bandwidth is shared in TDMA and CDMA systems makes a universal technological approach unlikely. For example, an ultra-high speed ethernet can be layered more easily on TDMA, while a metropolitan network, based on broadcast and select data, is more easily layered on CDMA. Therefore, the most reasonable scenario for optical access-networks is interconnected network-islands, where the island technology is chosen according to the data communication services. Hence, all-optical devices to convert signals between different networks are likely to become a key technology.

Bit-rate expansion and compression is a technique of major relevance in this suggested scenario. For instance, a high-speed backbone network operating at 100 Gb/s, may connect different local-area-networks operating at 10 Gb/s. The capacity available on the backbone network can be fully utilised if the network node can burst packets at the high-speed rate of the backbone network, which requires a time-slot (packet) multiplexing approach. Networks based on the packet compression and expansion scheme were proposed in [5, 8, 124, 125].

[1]RZ: return-to-zero, NRZ: noreturn-to-zero, CDM: code division multiplexing, ASK: amplitude shift-keying, PSK: phase shift-keying.

6.1 Review of Packet Compression and Expansion Schemes

Several schemes for all-optical packet compression and decompression have been proposed so far. In this section, I briefly describe the operating principle and the achieved operation of the various proposed schemes.

The two basic schemes proposed for optical packet compression and expansion are shown in Fig. 6.1. In Fig. 6.1(a), the operation principle of a packet compression scheme based on a recirculating loop is illustrated [5, 126]. The loop has a round-trip time (T_r) corresponding to the difference between the bit-period of the input (T_{in}) and output (T_{out}) packets. Consequently, when the first bit in the packet travels once around the loop, the second bit is delayed only by the difference between the input bit-period and the round-trip time. Subsequent loop trips do the same for the following bits in the packet. At the loop output, several replicas of the same packet are formed, and an on/off switch is used to gate only one of them.

Since the various bits of the packet travel around the loop a different number of times, an optical amplifier has to be included in the loop to compensate for the power splitting and insertion losses. If an erbium-doped fibre amplifier (EDFA) is to be used for this purpose, then the loop length is typically longer than 10 m. This limits the maximum input bit-rate to approximately 30 Mb/s. A packet compression scheme based on a recirculating loop with a semiconductor optical amplifier, which allows higher input bit-rates, was proposed in [127].

A drawback of the recirculating loop scheme is that the number of loop trips is approximately the same as the number of bits in the compressed packet. Consequently, the signal-to-noise ratio degradation due to in-band spontaneous emission noise accumulation increases with the packet size, which imposes a practical limit on the packet size. In [126], bit-rate compression from 25 Mb/s to 5 Gb/s, of 10-bit packets, was successfully demonstrated.

Recently, a 4-fold compression of packets of 12000 bits at 2.5 Gb/s was successfully demonstrated, using a recirculating loop with a semiconductor optical amplifier [128]. In this scheme, the loop round-trip time is much larger than the input bit-period, and thus the loop stores a large number of bits; in this demonstration about 3000

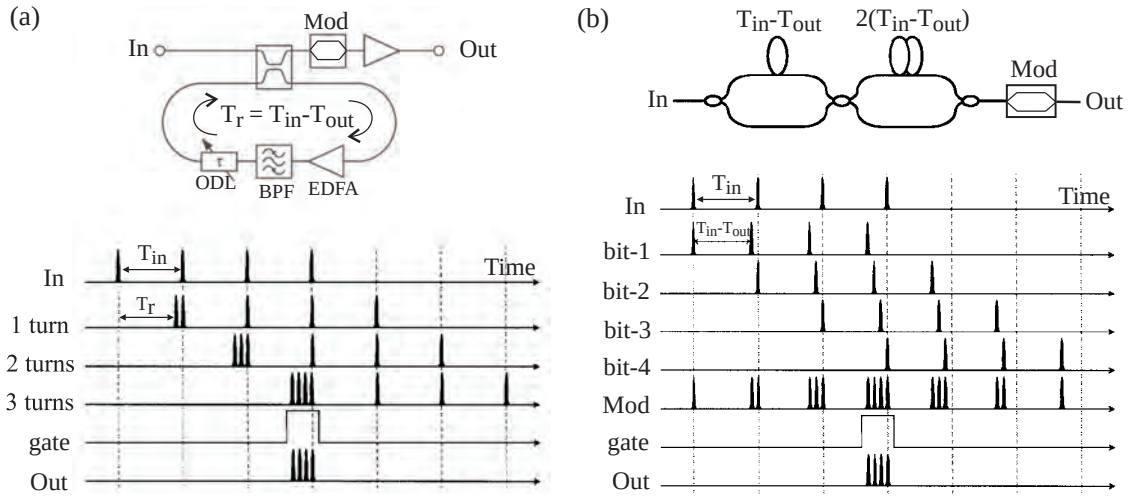

Figure 6.1: Packet compression schemes proposed by different groups: (a) the recirculating loop, (b) the optical-delay-line lattice. Mod: on/off modulator, EDFA: erbium doped fibre amplifier, ODL: optical-delay-line, BPF: bandpass filter. Figures were adapted from [5, 6].

bits at 2.5 Gb/s were stored in the loop. The loop length is adjusted so that after a loop round-trip the bits in the loop are interleaved with incoming bits at the desired output repetition-rate. This scheme allows for compression of large size packets in a few loop-trips. For instance, in this demonstration only 4 loop-trips were used to compress a 12000-bit packet. The bit sequence, however, is scrambled in relation to the input packet. This, consequently, requires either complex electronic control of the packet routing, or expansion of the packet using a reverse operation scheme before further processing.

One drawback common to all schemes based on the recirculating loop technique is that, for ultra-high output bit-rates, the loop length has to be controlled by locking the phase difference between the input and output packet clocks, as small loop length variations can introduce significant timing jitter and, consequently, cause detrimental intersymbol interference.

In Fig. 6.1(b), the operating principle of a packet compressor and decompressor based on an optical-delay-line lattice is illustrated [6]. The optical-delay-line lattice consists of consecutive stages of delayed Mach-Zehnder interferometers. In a stage, the signal is first split into two separate paths, which have a delay difference of $2^{m-1}(T_{in} - T_{out})$, where m is the sequential order of the stage, T_{in} and T_{out} are the input and output bit-period, respectively, and then coupled together, as is shown in Fig. 6.1(b). In n-stages, each bit is thus split 2^n times and repeats with a period of $T_{in} - T_{out}$. The

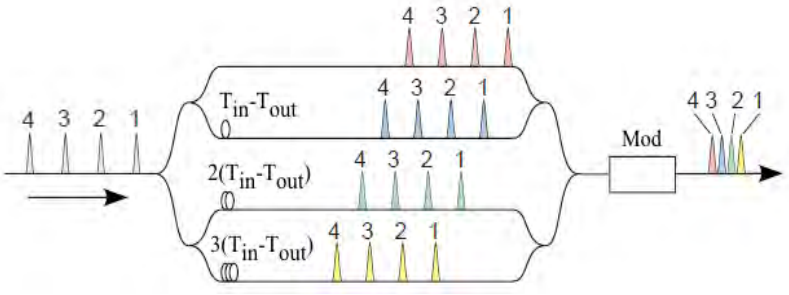

Figure 6.2: Packet compression scheme based on a parallel arrangement of the optical-delay-line lattice. Mod: on/off modulator.

superposition of the copies of all bits, at the optical-delay-line lattice output, holds a compressed version of the entire input packet, which can then be gated with an intensity modulator. The optical-delay-line lattice can be used, in the opposite direction, for packet expansion. In this case, the lattice produces n-copies of the entire compressed packet, which repeat with a period of $T_{out} - T_{in}$. An ultra-fast switch is then used to gate individual bits at the output period (T_{out}), which produces an expanded version of the input packet. Using this scheme, compression and decompression of a 16-bit packet, between 100 Mb/s and 100 Gbit/s, was successfully demonstrated in [6].

One drawback of this scheme, is a large degradation of the signal-to-noise ratio, in the case of large size packets, due to the low power of the gated packet as a consequence of splitting the packet in several stages. Furthermore, for ultra-high output bit-rates, the delay time at each stage has to be controlled to avoid large jitter-induced interference, using for example a scheme similar to the one suggested in [129].

The optical-delay-line lattice scheme has also been implemented with a parallel arrangement of the optical-delay-lines [130], as illustrated in Fig. 6.2. Another version of this scheme is based on the supercontinuum generation [131]. In this scheme, the input packet is spectrally broadened, in a highly-nonlinear fibre, into a wide spectrum which is then sliced in as many channels as the bits in the packet, and which are subsequently separated into different optical paths. This substitutes the initial power splitting stage in Fig. 6.2. After the modulator, a further stage of wavelength conversion is required to convert the packet back onto a single carrier-wavelength. Packet compression and decompression of 4-bit packets between 10 Gb/s and 40 Gb/s was demonstrated using this scheme.

Although an outstanding research effort has been made by several groups, which I briefly described in this section, an all-optical packet compression/decompression scheme compliant with the future optical packet-switched networks is yet to be proposed. This scheme should provide packet compression and expansion between any input and output bit-rates, adapt to different packet lengths, minimize the need for long-period packet buffering, and operate at any packet rate, among other network operation requirements.

In this chapter, I investigate the possibility of packet compression and expansion through the temporal lens-effect induced in a dispersive medium on packets chirped via the NOLM switching of linearly-chirped pulses. This scheme is not proposed as a solution to the aforementioned limitations of previous schemes, but rather as a novel approach, which has the potential to operate at ultra-high bit-rates. Since the packet and the individual pulses are simultaneously compressed or expanded, the maximum compression or expansion ratio is not limited by the input pulse duration. Moreover, the packets are compressed or expanded in a single path, which avoids additional circuitry to stabilize the pulse position. I describe next the theoretical aspects behind the temporal lens-effect of packets chirped through the NOLM switching of linearly-chirped pulses.

6.2 Theory

Temporal scaling of a waveform can be achieved by imparting a quadratic phase-modulation on it and, subsequently, propagating it through a dispersive medium, which results in the temporal lens-effect [132–134]. The operating principle of the

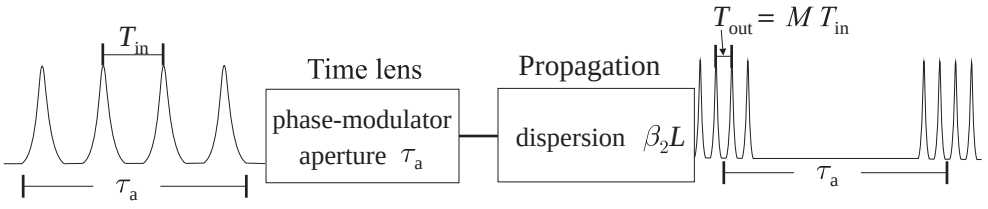

Figure 6.3: Schematic of the packet compression/expansion scheme based on the temporal lens-effect. τ_a is the temporal window in which the quadratic phase-modulation is applied (equivalent to the aperture of a spatial lens).

packet compression/expansion system based on the temporal lens-effect is illustrated in Fig. 6.3.

The temporal imaging system in [132, 134] was first proposed for single-shot measurement of ultrafast waveforms using low-speed detectors and, therefore, designed to exactly reproduce the waveform temporal features on a much longer temporal scale. In telecommunications, however, the exact reproduction of the temporal features of the incoming packets may not be crucial. If critical parameters such as the signal format and the level of intersymbol-interference are not changed, then compression and expansion of the incoming packets through the temporal lens-effect can be used.

6.2.1 Temporal Lens-Effect via NOLM Switching of Linearly-Chirped Pulses

NOLM-switching of linearly-chirped pulses with an incoming packet produces a chirped replica of this packet at the NOLM output. Although this is different from a pure quadratic phase-modulation across the packet, the subsequent propagation of the NOLM-produced chirped packets in a dispersive medium leads to their temporal compression or expansion. The operating principle of packet compression and expansion based on the temporal lens-effect via NOLM-switching of linearly-chirped pulses is shown in Figs. 6.4 and 6.5, respectively. The incoming unchirped packet of pulses, to be compressed or expanded, is used to control a nonlinear optical gate, in this case a fibre-based NOLM switch. Into the NOLM signal-port are injected linearly-chirped pulses at the packet repetition-rate with the duty-cycle of the full packet length. In the NOLM, just the part of the signal temporally overlapping with the control pulses is switched to the gate output-port. Consequently, at the NOLM output, each pulse in the packet is carried upon a different centre-frequency.

Packet compression or expansion can, then, subsequently occur either in a positive or negative dispersion medium depending on the sign of the chirp-rate across the packet. In a positively chirped packet, the pulse centre-frequency increases with time, as shown in Fig. 6.4(b), whereas in a negatively chirped packet it decreases, as shown in Fig. 6.5(b). A positively/negatively chirped packet, for example, compresses in a positive/negative dispersion medium.

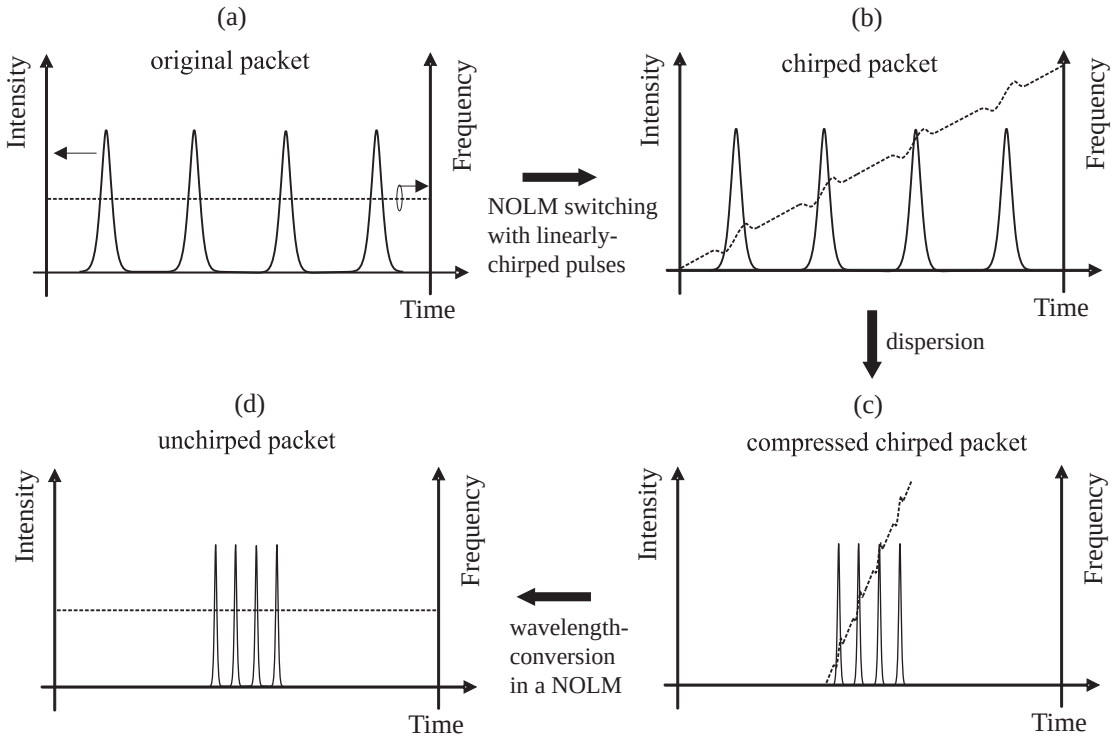

Figure 6.4: Basic operating principle of the proposed packet compressor.

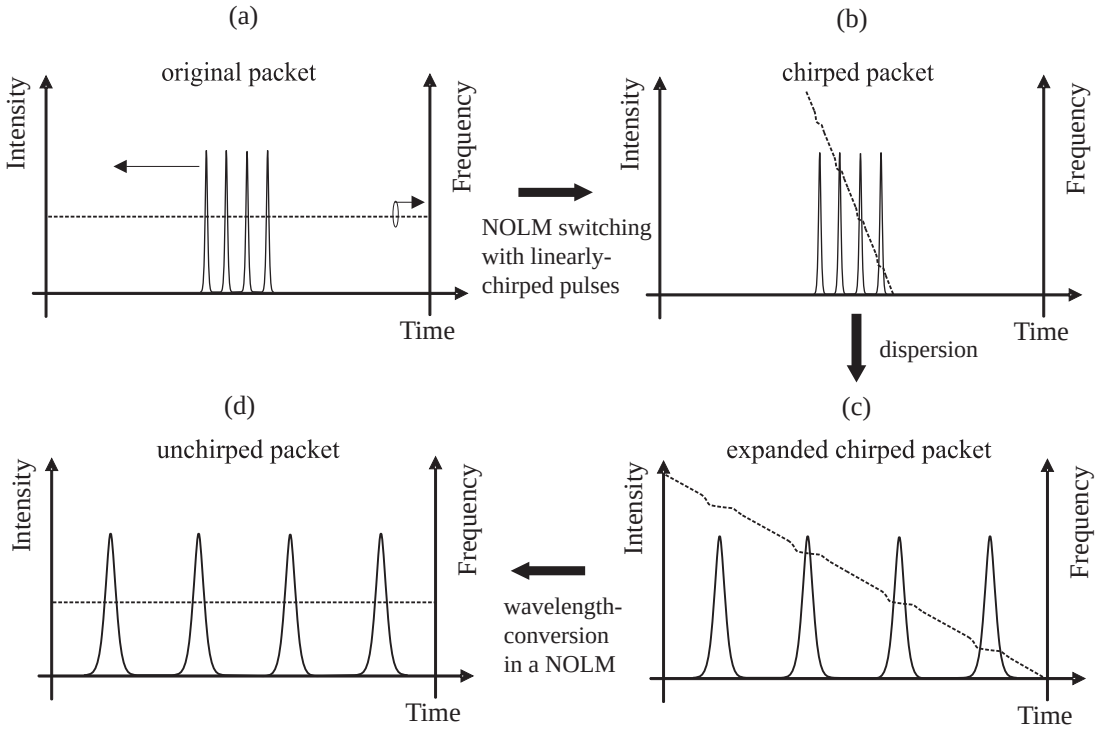

Figure 6.5: Basic operating principle of the proposed packet decompressor.

However, as described in Chapter 4, the chirp-rate in the NOLM switched pulses is different from that of the input linearly-chirped pulses, since it results from the superposition of the phase of the linearly-chirped pulses with the cross-phase modulation induced by the control pulses, see Figs. 4.8 and 4.9. As illustrated in Fig. 6.4(b), the chirp-rate in the switched pulses is larger than the chirp-rate in the input linearly-chirped pulses, when the chirp is positive. In contrast, the chirp-rate in the switched pulses is smaller than the chirp in the input linearly-chirped pulses, when the chirp is negative, as shown in Fig. 6.5(b). The explanation is that cross-phase modulation imposes a positive chirp onto the part of the signal overlapped by the centre of the control pulses[2]. The superposition of the two chirps adds up, therefore, when the input chirp is positive, this results in a larger chirp in the pulse, while it subtracts when the input chirp is negative resulting in a smaller overall chirp. The difference between the centre frequencies of consecutive switched pulses is, however, given by the chirp-rate of the linearly-chirped pulses, since cross-phase modulation by the peak of the control pulses induces no chirp into the signal.

Although compression and expansion can be achieved either with positive or negative chirp, it is now intuitive that positive chirp may be advantageous for compression, while negative chirp may benefit expansion. The reason is that, for a negatively chirped packet, the chirp in the switched pulse is small, and therefore the pulse compresses little. In contrast, for a positively chirped packet, the chirp in the switched pulse is large, and consequently the pulse can be further compressed, see Fig. 6.4(c). On the other hand, a small amount of chirp in the switched pulses results in a slower pulse broadening, and therefore, overlapping between adjacent pulses can be avoided during the packet expansion, see Fig. 6.5(c). This intuitive interpretation is confirmed in the next section by means of numerical simulations. The system operating conditions are also assessed and described in the next section.

[2]The physical interpretation is that in positive refractive-index materials, the refractive-index increases proportionally to the pulse intensity due to the nonlinear Kerr effect, consequently, in the leading edge (rising edge) the phase velocity decreases with time, which corresponds to a red-shift, while in the trailing edge (falling edge) the phase velocity increases with time, which corresponds to a blue-shift.

6.2.2 Operating Conditions

A few aspects were considered as crucial to the successful implementation of this scheme. One was the chirp-rate and dispersion required to either compress or expand packets to a certain output bit-rate. Another one was the operating conditions required to prevent the individual pulses from overlapping the adjacent bits during compression or expansion. In particular, the minimum chirp-rate which ensures that the final pulse-duration is smaller than 30% of the output bit-period needed to be evaluated, thus preventing a significant increase of the intersymbol-interference level. The last aspect was the variation of the output bit-period across the packet induced by the dispersion slope, when standard telecom single-mode fibres are used as the dispersive medium in which compression/expansion occurs.

6.2.2.1 Dispersion Required for Packet Compression/Expansion

The quadratic phase-modulation across the linearly-chirped pulses, used in the NOLM switching, can be written as:

$$\phi = -CT^2, \tag{6.1}$$

where C is the chirp coefficient, T is the time.

The difference between the instantaneous centre-frequency of two consecutive NOLM-switched pulses is, consequently, given by:

$$\Delta\omega = -\left.\frac{\partial\phi}{\partial T}\right|_{T=T_{\text{in}}} = 2CT_{\text{in}} \tag{6.2}$$

where T_{in} is the delay between two consecutive pulses in the input packet.

The chirp-rate (CR) can then be defined as the ratio between the instantaneous-frequency shift and the associated time interval, and can be written as:

$$CR = \frac{\Delta\omega}{T_{\text{in}}} = 2C \tag{6.3}$$

As the optical spectrum is typically measured in the wavelength domain, it can be more convenient to express the chirp-rate as:

$$CR(\text{nanometer/picosecond}) = \frac{\Delta\lambda}{\Delta T} = -\frac{\lambda_0^2 C}{\pi c} \tag{6.4}$$

where λ_0 is a nominal wavelength, c is the speed of light in vacuum.

Subsequently, during dispersive propagation, the delay between these two consecutive pulses changes by:

$$\Delta T = \Delta\omega\beta_2 L \tag{6.5}$$

where $\beta_2 L$ is the total dispersion of the propagation medium.

Let us define the time-lens system magnification factor M as:

$$M = \frac{T_{\text{out}}}{T_{\text{in}}} = \frac{B_{\text{in}}}{B_{\text{out}}} \tag{6.6}$$

where $T_{\text{in/out}}$ represents the input/output bit period, and $B_{\text{in/out}}$ represents the input/output bit rate, respectively. It follows that $M > 1$ corresponds to a waveform expansion, which for a stream of data pulses produces a reduction of the input bit-rate, while $0 < M < 1$ corresponds to a waveform compression, which for a stream of data pulses produces an increase of the input bit-rate. Thus, the packet expansion factor is given by $F_e = M$, while the packet compression factor is given by $F_c = \frac{1}{M}$.

Using Eq. (6.6), the delay between two consecutive pulses, before and after magnification, can be written in terms of the magnification factor itself as:

$$\Delta T = (M-1)\,T_{\text{in}} \qquad \boxed{T_{\text{in}}} \quad \boxed{T_{\text{out}} = M\,T_{\text{in}}} \tag{6.7}$$

Replacing Eq. (6.2) in Eq. (6.5) and then in Eq. (6.7), it follows that the second-order dispersion required to magnify the waveform by M, is given by:

$$\beta_2 L = \frac{M-1}{2C} \tag{6.8}$$

The chirp-rate of the linearly-chirped pulses defines, thus, the dispersion required to achieve a certain magnification factor. The focal dispersion f_D of the time-lens system, or the total dispersion that results in maximum waveform compression, is given as $M \longrightarrow 0$ by:

$$f_D = -\frac{1}{2C} \tag{6.9}$$

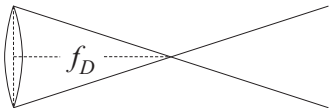

Waveform compression occurs, therefore, for a total dispersion smaller than the focal dispersion.

6.2.2.2 Minimum Chirp-Rate Required for Pulse Compression

A critical aspect of our packet compression/expansion scheme based on the temporal lens-effect is that the pulse-width of the individual pulses in the packet may compress/expand by a factor different from that of the bit-rate increase/decrease. Consequently, the adjacent pulses may overlap and detrimental interference may arise. To assess the conditions for an ideal image formation, which happens when the magnification of both the packet bit-rate and the duration of the individual pulses is the same, the propagation of the individual pulses in the packet was studied.

The exact normalised electric-field of the pulses shown in Figs. 6.4 and 6.5, when considering a NOLM with an infinite switching-ratio, was derived in Chapter 4 and is given by:

$$U(0,\tau) = \sin\left(\frac{\pi}{2}\exp\left(-\frac{\tau^2}{\tau_0^2}\right)\right)\exp\left(i\frac{\pi}{2} - iC\tau^2 + i\frac{\pi}{2}\exp\left(-\frac{\tau^2}{\tau_0^2}\right)\right) \tag{6.10}$$

The problem of estimating the pulse duty-cycle of compressed or expanded pulses, as a function of the initial duty-cycle and the time lens chirp-rate, cannot therefore be solved analytically. According to [34], the dispersive propagation of an arbitrary waveform can be calculated by numerically solving:

$$U(L,\tau) = \int_{-\infty}^{+\infty} \widetilde{U}(0,\omega)\exp\left(i\frac{\beta_2 L\omega^2}{2} - i\omega\tau\right)d\omega \tag{6.11}$$

The total dispersion required for a waveform magnification of M is given by Eq. (6.8), and replacing this in Eq. (6.11) it follows that:

$$U(L,\tau) = \int_{-\infty}^{+\infty} \widetilde{U}(0,\omega) \exp\left(i\frac{1-M}{4MC}\omega^2 - i\omega\tau\right) d\omega \tag{6.12}$$

The pulse duty-cycle in the magnified waveform is obtained by estimating the pulse full-width at half-maximum (τ_1) from Eq. (6.12), which can be approximated, for an arbitrary pulse, by the root-mean-square of the pulse intensity-envelope width, as shown in [34]. Hence, considering Eq. (6.6) and energy conservation during the dispersive propagation, the output pulse duty-cycle (σ_1) can be estimated by:

$$\sigma_1 = \frac{\tau_1}{T_{\text{out}}} = \frac{\tau_1}{T_{\text{out}}}\frac{\sigma_0 T_{\text{in}}}{\tau_0} = \frac{\sigma_0}{M}\frac{\tau_1}{\tau_0} = \frac{\sigma_0}{M}\sqrt{\frac{\int_{-\infty}^{+\infty} \tau^2 \left|U(L,\tau)\right|^2 d\tau}{\int_{-\infty}^{+\infty} \tau^2 \left|U(0,\tau)\right|^2 d\tau}} \tag{6.13}$$

where τ_0 and σ_0 are the input pulse full-width at half-maximum and input pulse duty-cycle, respectively. Eq. (6.12) and the integrals in Eq. (6.13) have to be calculated numerically.

Figures 6.6(a) and (b) show the output pulse duty-cycle (σ_1) as a function of the chirp-rate of the linearly-chirped pulses ($2C$) and the input pulse duty-cycle (σ_0) for packet compression from 10 to 40 Gb/s via the NOLM switching of linearly-chirped pulses. Whilst case (a) considers positively chirped packets after the NOLM switch, case (b) considers negatively chirped packets. Comparing Figs. 6.6(a) and (b), it can be seen that an output duty-cycle smaller than 30% can be obtained with lower chirp-rate and input duty-cycle values for positively chirped packets. This confirms that a positive chirp-rate is better in packet compression. Figures 6.7(a) and (b) show the same calculations for the packet expansion from 40-Gb/s to 10-Gb/s. In this case, lower chirp-rate and input duty-cycle values can be found for negatively chirped packets. This confirms that a negative chirp-rate opposes better the pulse broadening during packet expansion.

The minimum chirp-rate of the linearly-chirped pulses, for which the output pulse duty-cycle is smaller than 30%, can then be extracted from the contour maps obtained

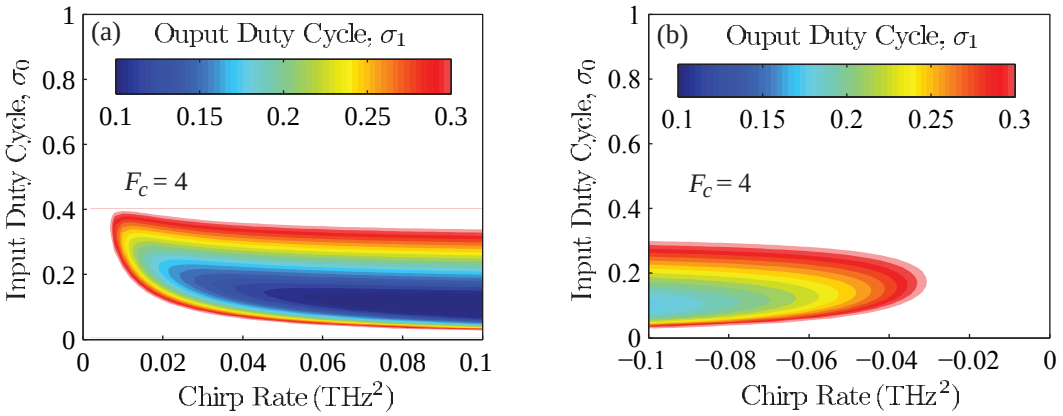

Figure 6.6: Output pulse duty-cycle as a function of the packet chirp-rate and the input pulse duty-cycle for 4-fold compression of 10-Gb/s packets via the NOLM switching of linearly-chirped pulses. (a) positively chirped packets, (b) negatively chirped packets.

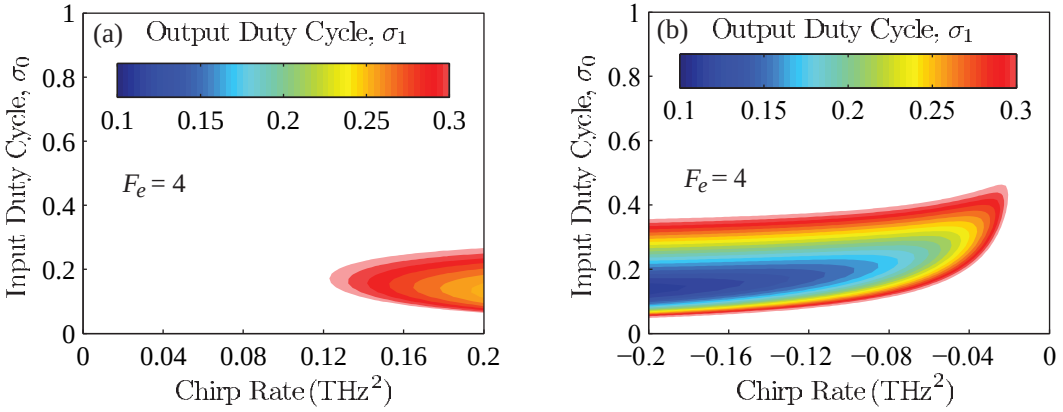

Figure 6.7: Output pulse duty-cycle as a function of the packet chirp-rate and the input pulse duty-cycle for 4-fold expansion of 40-Gb/s packets via the NOLM switching of linearly-chirped pulses. (a) positively chirped packets, (b) negatively chirped packets.

from Eq. (6.13). Figures 6.8(a) and (b) show, then, the minimum chirp-rate required to produce output pulses with a duty-cycle smaller than 30% as a function of the packet magnification factor. Whilst, Fig. 6.8(a) shows the case of compression of 10-Gb/s input packets, Fig. 6.8(b) shows the case of expansion of high-speed bit-rate packets to 10-Gb/s output packets. For example, for a compression factor of 100, which corresponds to output packets with a bit-rate of 1 Tb/s, the time-lens chirp-rate has to be about 0.28 THz^2. In Fig. 6.8(b) the slow down of high-speed bit-rate packets to 10 Gb/s was considered. It is interesting that the plotted curve, resulting from Eq. (6.13), fits $C\tau_0^2 \approx -1.2$, where τ_0 is the pulse full-width at half-maximum for an input pulse duty-cycle of 30%. For example, for an expansion factor of 100, which corresponds to slowing down the bit-rate from 1 Tb/s to 10 Gb/s, the input pulse-period is 1 ps, for which the pulse-width τ_0 for a 30% duty-cycle is 300 fs, and

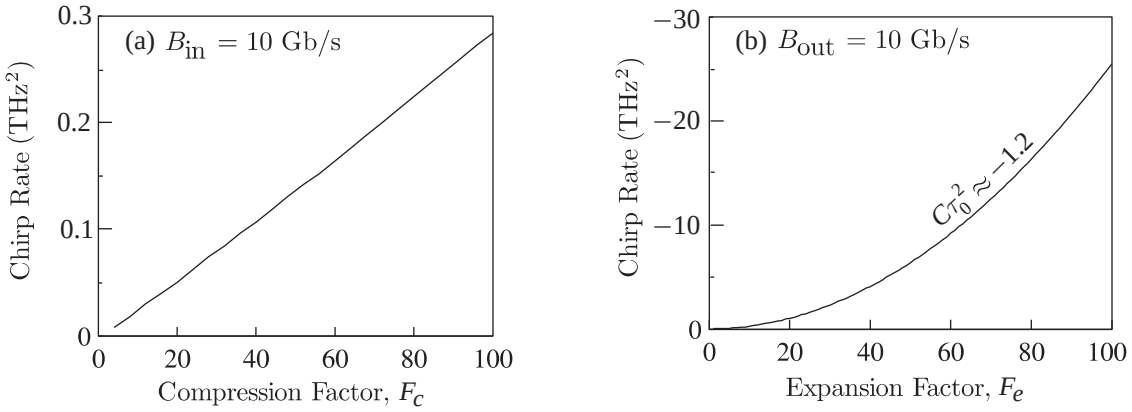

Figure 6.8: The minimum chirp rate of the NOLM time lens, for which the output duty-cycle is smaller than 30%, as a function of the packet magnification factor. (a) Compression of 10 Gb/s input packets, and (b) expansion to 10 Gb/s output packets.

therefore the minimum chirp-rate required to keep the output pulse duty-cycle under 30%, according to $C\tau_0^2 \approx -1.2$, is $-26\,\text{THz}^2$.

It may not be intuitive why packet expansion requires a much larger time-lens chirp-rate than packet compression. The reason is that in packet expansion the pulses in the input high-speed bit-rate packets are closely spaced and, therefore, a larger chirp-rate is required to shift the pulse instantaneous centre-frequency by the same amount as for low-speed bit-rate input packets in packet compression. The bandwidth of the time-lens (the chirp-rate times the temporal aperture) required to compress or expand similar size packets is, however, about the same.

6.2.2.3 Deviation from a Second-Order Dispersion Medium

Waveform compression or expansion after the NOLM-switch can be achieved in a dispersive medium, such as a dispersive fibre or a pair of diffraction gratings. The fibre-based approach offers less overall power loss, higher robustness and more compact packaging in comparison to bulk diffraction gratings. In particular, chirped fibre Bragg gratings can provide identical control of the total dispersion using a suitable tuneable mounting. However, fibre Bragg gratings have a relatively narrow operational bandwidth. Compression or expansion of large packets can require a large operational bandwidth, and therefore the use of a dispersive transmission fibre was selected for my work. Although transmission fibre has low loss and a wide operational bandwidth, it has a significant dispersion slope that can induce distortion in

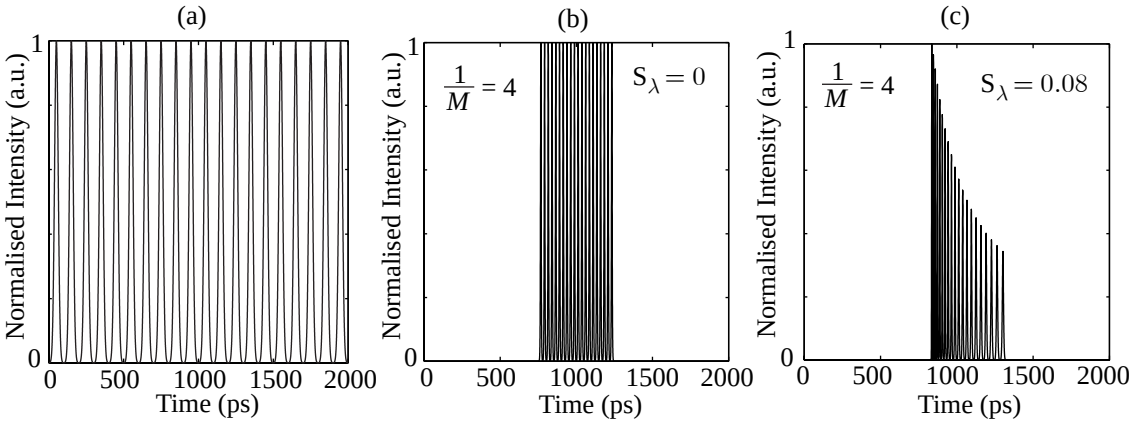

Figure 6.9: The effect of the dispersion slope of dispersive transmission fibre in the 4-fold compression of 10 Gb/s packets. (a) The initial packet with 20-bits at 10 Gb/s, (b) compressed packet considering zero dispersion slope, and (c) compressed packet considering a dispersion slope of 0.08 ps/nm^2/km .

a linearly-chirped waveform. In this section, I describe and discuss the effect of the dispersion slope on the individual pulse position in the temporally magnified packet.

Figure 6.9 shows a numerical simulation of the 4-fold compression of a packet of 20 bits at 10 Gb/s. The initial packet is shown in Fig. 6.9(a), while Fig. 6.9(b) shows the compressed packet considering a dispersion slope coefficient (S_λ) of zero, and Fig. 6.9(c) shows the effect of the typical dispersion slope of dispersive transmission fibre, $S_\lambda = 0.08$ ps/nm^2/km, in the compressed packet. As can be seen, in case (c) the magnification is different for each pulse in the packet. Furthermore, the spacing between pulses changes across the packet. The pulse spacing deviation from a constant repetition period is derived for the case of a generic temporal magnification in the following paragraphs.

Let us begin by considering the propagation delay between two consecutive pulses with two different centre frequencies ω_1 and ω_2, which, assuming a propagation medium with a length L, is given by [34]:

$$\Delta T_{1-2} = L\left(\frac{1}{v_g(\omega_1)} - \frac{1}{v_g(\omega_2)}\right) = L\left(\beta_1\left(\omega_1\right) - \beta_1\left(\omega_2\right)\right) \tag{6.14}$$

where $v_g(\omega)$ is the group velocity at the frequency ω in the propagation medium, and $\beta_1(\omega)$ is the corresponding first-order derivative of the mode propagation constant at the frequency ω.

Considering a third-order dispersive medium, which is characterised by the second-order dispersion coefficient $\beta_2(\omega)$ and the frequency independent third-order dispersion coefficient β_3, the value of β_1, about the frequency ω_0, is given by:

$$\beta_1(\omega) = \beta_1(\omega_0) + \beta_2(\omega_0)(\omega - \omega_0) + \frac{\beta_3}{2}(\omega - \omega_0)^2 \tag{6.15}$$

Consequently, Eq. (6.14) can be written as:

$$\Delta T_{1-2} = L(\omega_1 - \omega_2)\left[\beta_2(\omega_0) + \beta_3(\omega_\mathrm{p} - \omega_0)\right] = L(\omega_1 - \omega_2)\beta_2(\omega_\mathrm{p}) \tag{6.16}$$

where:

$$\omega_\mathrm{p} = \frac{\omega_1 + \omega_2}{2}$$

is the intermediate instantaneous frequency between ω_1 and ω_2, and is obviously a function of the position of each two consecutive pulses in the linearly chirped packet. Consequently, the magnification factor, given by Eq. (6.8), is a function of the instantaneous frequency across the chirped packet, as shown in Fig. 6.9(c).

The deviation on the period between two consecutive pulses across the magnified packet is given by the third-order dispersion term in Eq. (6.16):

$$\Delta T_d = \Delta T_{1-2} - \Delta T_{1-2}(\beta_3 = 0) = (\omega_1 - \omega_2)(\omega_\mathrm{p} - \omega_0)L\beta_3 \tag{6.17}$$

The frequency difference between two consecutive pulses in the packet $(\omega_1 - \omega_2)$ is well defined by the time lens chirp-rate $(2C)$, and given by Eq. (6.2). Subsequently, Eq. (6.17), using Eq. (6.8), can be re-written as a function of the magnification factor and the medium dispersion coefficients; the resulting equation can then be divided by the output pulse-period T_out defined in Eq. (6.6), and consequently, the relative deviation from the output pulse-period is obtained as:

$$\frac{\Delta T_d}{T_\mathrm{out}} = \frac{M-1}{M}\frac{\beta_3}{\beta_2(\omega)}(\omega_\mathrm{p} - \omega_0) \tag{6.18}$$

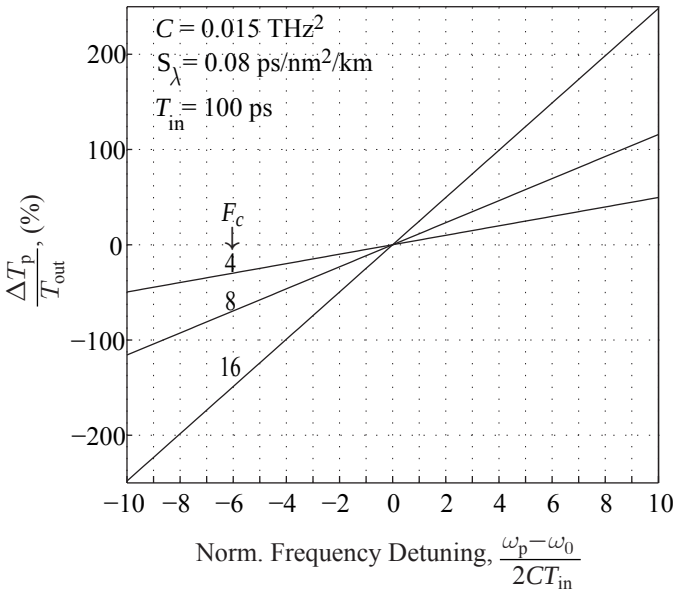

Figure 6.10: Relative deviation of the output pulse-period, induced by the fibre dispersion slope (S_λ), as a function of the normalised instantaneous-frequency detuning across the packet for a 4/8/16 times compressed packet. The frequency detuning is normalised by the centre-frequency shift between consecutive pulses in the packet ($2CT_{\text{in}}$) and, therefore, corresponds to the bit position relative to the position for which the effect of the dispersion slope is zero.

The frequency difference $(\omega_{\text{p}} - \omega_0)$ corresponds to the frequency detuning from the position for which Eq. (6.8) holds. In other words, for the two consecutive pulses with intermediate instantaneous frequency ω_0, the output period is exactly M times the input period, while for the other pair of pulses in the packet the period changes.

Figure 6.10 shows the relative deviation of the pulse period across the pulse position in a packet of 20 bits compressed from 10 Gb/s to 40 Gb/s, 80 Gb/s, and 160 Gb/s. It can be seen, that for a typical value of the dispersion slope of dispersive transmission fibre, a large deviation from the targeted pulse period is induced. For example, for 40 Gb/s compressed packets the bit period changes from approximately 12 ps to 35 ps across the 20-bit packet. For 80 Gbs and 160 Gb/s compressed packets some of the bits in the packet completely overlap as the pulse period deviation exceeds 100%. In our experimental demonstration of this scheme we operated 4-bit packets, because of the bandwidth limit of the linearly-chirped pulses, and therefore the dispersion slope effect was noticeable but small. However, implementation of this scheme on longer packets requires the strict use of a second-order dispersion medium, as can be concluded from Fig. 6.10.

6.3 Experiments

6.3.1 Packet Compression Experiments

In my earliest attempt at packet compression using the scheme illustrated in Fig. 6.4, neither the theory described in the previous section nor the theory of NOLM switching of linearly-chirped pulses had been developed. At that early stage, compression/expansion of the duration and period of the pulses of a mixed TDM-WDM signal was naively assumed to simultaneously occur in a dispersive fibre, due to the linear chirp-rate of the linearly-chirped pulses coupled into the NOLM switch.

Because the operating conditions described in the previous section were not obeyed, these early experiments did not show clean packet compression performance through temporal lens-effect. The obtained eye-diagrams and autocorrelation traces were noisy and distorted, mainly due to large intersymbol-interference between adjacent pulses. However, these experiments are essential to understand the evolution of my thesis work. In the following section, I describe these early experimental results that led us to theoretically and experimentally investigate further the NOLM switching of linearly-chirped pulses and the temporal lens-effect. The description of optimised experiments that have followed the conditions identified by the theoretical analysis follow in Section 6.3.1.2.

6.3.1.1 Packet compression under a weak temporal lens-effect using solitonic effects

In a first attempt to experimentally demonstrate our packet compression scheme, a time lens with a chirp-rate of $0.013\,\mathrm{THz}^2$ and a temporal aperture of 360 ps was used. A 10-Gb/s data stream consisting of 8-ps modulated pulses, which corresponds to an input pulse duty-cycle of 0.08, was used to control a NOLM-switch and, thus, produce 4-bit chirped packets. By referring back to Section 6.2, we can see that the chirp induced across each pulse via the NOLM switching of linearly-chirped pulses under these operating conditions is insufficient to achieve significant pulse compression. As was shown in Fig. 6.6(a), a 4-fold packet compression with a time lens chirp-rate of $0.013\,\mathrm{THz}^2$ requires a minimum input pulse duty-cycle of $\sim$0.2.

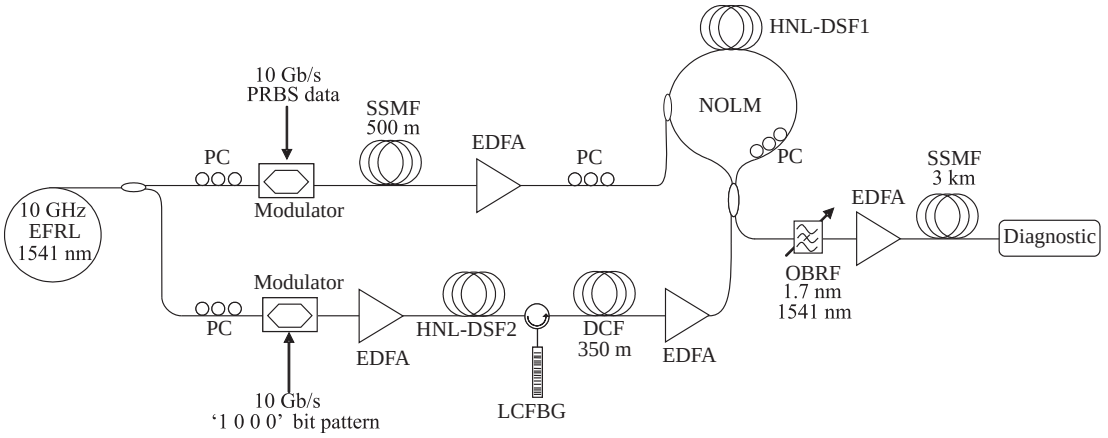

Figure 6.11: Experimental setup for packet compression at 2.5 Gpacket/s using a time lens with a chirp-rate of $-0.017\,\mathrm{nm/ps}$ ($0.013\,\mathrm{THz}^2$) and a temporal aperture of 360 ps.

Since pulse compression could not be achieved with the time lens alone, I considered the use of solitonic effects to aid to the compression of the pulses and accompany the bit-rate compression. The experimental setup is shown in Fig. 6.11. In this scheme, the first pulse train was modulated with a pseudo-random data sequence in order to generate a 10-Gb/s TDM signal. The data pulses were broadened from 2.5 ps to 8 ps via propagation through 500 meters of standard single-mode fibre and then amplified to an average power of 21 dBm and coupled onto the NOLM via its control port. The linearly-chirped pulses were generated as described in Section 3.4.2, but dispersed in an extra length of dispersion compensating fibre (DCF, D = $-110\,\mathrm{ps/nm/km}$), so that the total dispersion of the LCFBG and DCF was about $-60\,\mathrm{ps/nm}$, which broadened the pulses to 360 ps. The corresponding chirp-rate was, therefore, $-0.017\,\mathrm{nm/ps}$ ($0.013\,\mathrm{THz}^2$). The linearly-chirped rectangular pulses were then amplified to an average power of 10 dBm and injected into the signal port of the NOLM. The cross-phase modulation induced by the data pulses on the rectangular chirped signal switched the overlapping part of the chirped pulses to the NOLM output port, thereby generating 4-WDM channels at 2.5 Gb/s. A 1.7-nm optical band-rejection filter (OBRF) consisting of two cascaded fibre-Bragg-gratings, whose transmission is shown in Fig. 6.12, was used to filter out the original 10-Gb/s TDM signal. The optical spectrum of the switched signal after the filter and amplifier is shown in Fig. 6.13. As can be seen, 4 WDM channels were carved on the chirped pulse spectrum, which is shown in detail in Fig. 6.13(b). The rejection filter removes, only partially, the original TDM signal since the -3-dB bandwidth of the fibre mode-locked laser pulses was about 1.4 nm. Although the residual TDM signal does not add amplitude noise (due to frequency

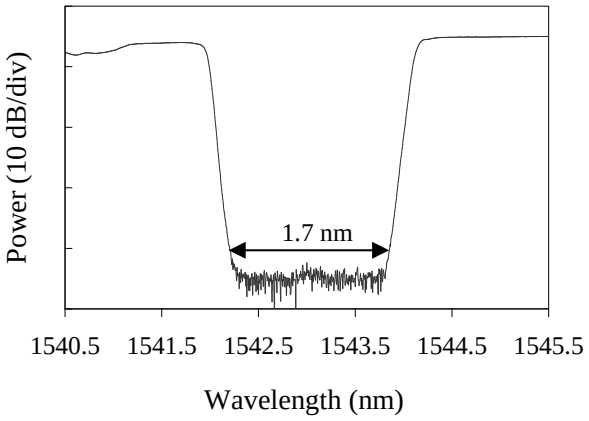

Figure 6.12: Transmission spectrum of the rejection filter using two cascaded FBGs. The combined bandwidth could be tuned from 1 nm to 1.7 nm.

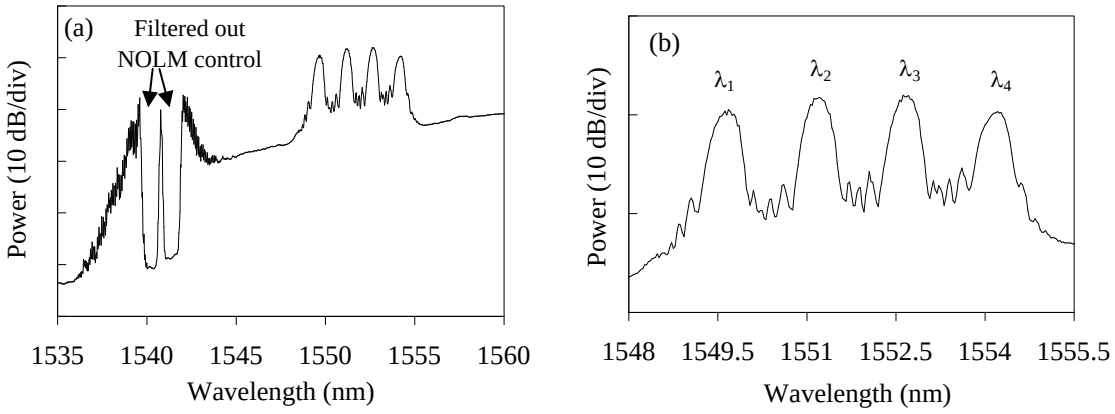

Figure 6.13: Optical spectrum of the chirped pulses after the NOLM switch. (a) Large spectral span, (b) small spectral span around the spectrum of the 4 WDM channels.

beating) to the detected switched signal (since the frequency difference between the residual and switched signals (∼1 THz) greatly exceeds the bandwidth of electronic receivers), the gain competition between both signals during subsequent amplification can lead to a poor signal-to-noise ratio of the switched signal. This is evidenced in Fig. 6.14(b), which shows the switched signal after the NOLM and is compared to the signal before switching Fig. 6.14(a).

The duration of the switched pulses was measured by second-harmonic intensity autocorrelation and is shown in Fig. 6.15(a). Assuming a Gaussian shape, the pulse duration was about 8 ps, which corresponds to a duty-cycle of 8% at the bit-rate of 10 Gb/s. The switched pulses were then propagated through 3 km of SSMF (D = 15 ps/nm/km). According to Eq. (6.8), for the chirp-rate used, −0.017 nm/ps,

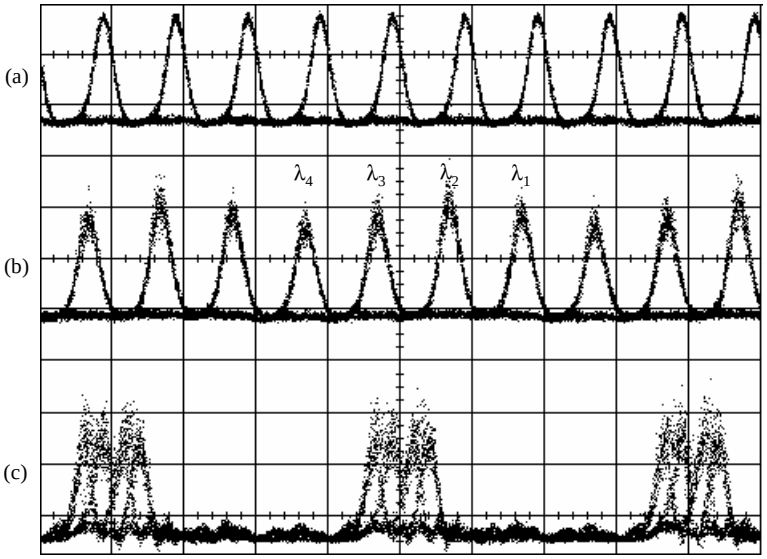

Figure 6.14: Oscilloscope traces of (a) the 10-Gb/s TDM signal used to control the NOLM switch, (b) 4-bit packets switched from the chirped pulses, and (c) the 4-bit packets compressed in 3 km of SSMF. The time scale division is 100 ps/div.

a 4-fold packet compression occurs at 3 km, while the focal length is 3.9 km. As mentioned earlier, in order to simultaneously achieve compression of the individual pulses and packet, the signal was amplified to an average power of 24 dBm at the input of the 3 km-long SSMF. The autocorrelation trace of the higher-order soliton, which was detected at the output of the SSMF is shown in Fig. 6.15(b) for only one of the four channels. The pulse duration was thus compressed to 3.2 ps (assuming a sech^2 shape). However, a higher-order soliton has a large pedestal, clearly visible in this autocorrelation trace. Consequently, although the compressed pulse duration corresponds to a pulse duty-cycle of 13% in the 40-Gb/s TDM signal, the associated pedestal can produce large distortion. This is clear in Fig. 6.15(c), which shows the autocorrelation of the 4-bit 40-Gb/s signal, whose corresponding oscilloscope trace is shown in Fig. 6.14(c). As can also be seen, the side pulses are broader than the centre pulse, which indicates that the pulses may not be equally spaced in the 4-bit 40-Gb/s packets.

To better assess the conditions required for packet compression through the temporal lens-effect, the study of packets with only 2 pulses was carried out in subsequent experiments. The previous experimental setup was, therefore, modified to that shown in Fig. 6.16. The main changes were: the 2.5-ps pulses at the 10 GHz repetition-rate from the erbium fibre-ring laser (EFRL) were neither data modulated

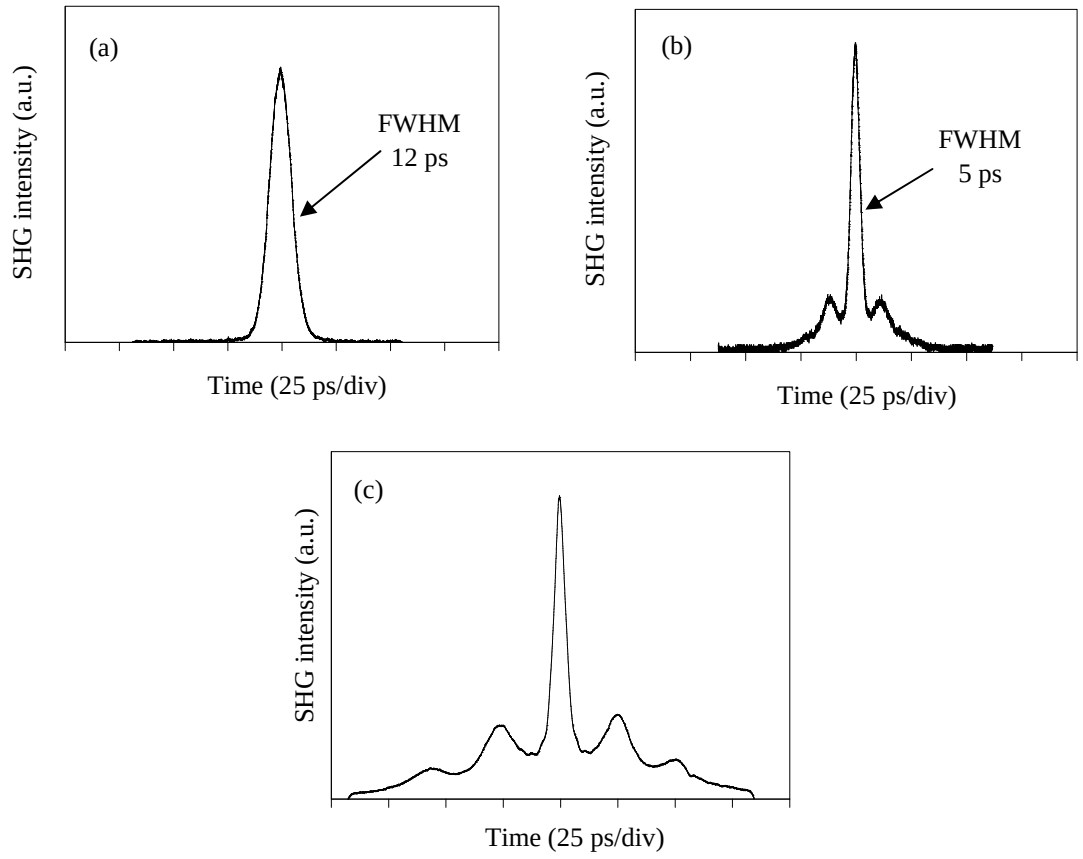

Figure 6.15: Autocorrelation traces of the (a) switched pulses, (b) higher-order soliton pulses generated in the 3 km of SSMF, and (c) 4-bit packets compressed in the 3 km of SSMF.

nor broadened to 8 ps; the linearly-chirped pulses were instead shaped into ∼120-ps wide rectangular pulses with a 6-nm bandwidth, which corresponds to a linear chirp-rate of $-0.05\,\mathrm{nm/ps}$ ($0.04\,\mathrm{THz}^2$). Hence, the NOLM switching of the rectangular linearly-chirped pulses generated 2-pulse packets spaced by 100 ps at 2.5 Gpacket/s. In Figure 6.17(c), the oscilloscope trace of the switched chirped pulses is shown, while Figs. 6.17(a) and (b) show the 10-GHz pulse stream used to control the NOLM switch and the 120-ps linearly-chirped rectangular pulses, respectively.

Figure 6.18 shows the optical spectrum at the NOLM output port before the rejection filter. As can be seen, the linearly-chirped pulse spectrum, spanning from 1549 nm to 1555 nm, was modulated by the overlapping control pulses, in this case two pulses, due to cross-phase modulation (XPM). The XPM spectrum is shown in detail in Fig. 6.18(b). The spectral beats in between the two channels were explained in Chapter 4 to be due to the spectral field interference between the switched chirped

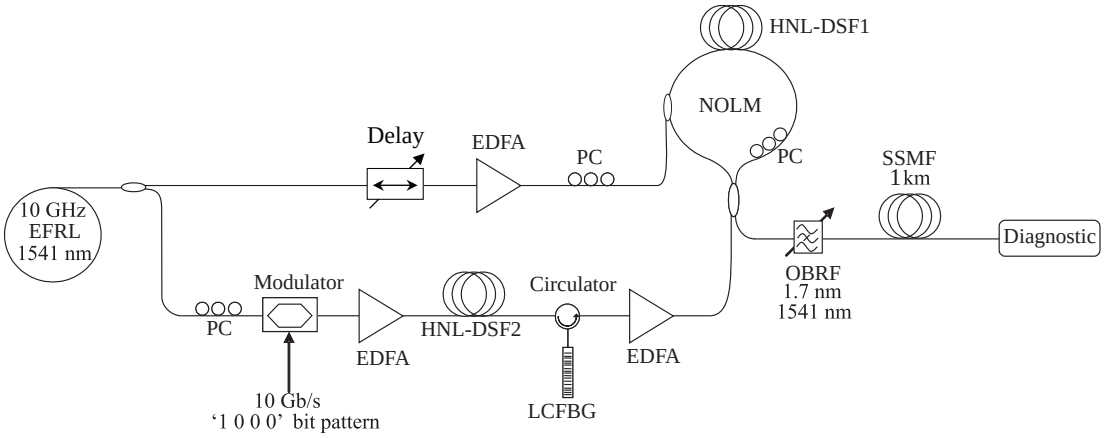

Figure 6.16: Experimental setup for packet compression at 2.5 Gpacket/s using a time lens with a chirp rate of -0.05 nm/ps and a time aperture of 120 ps.

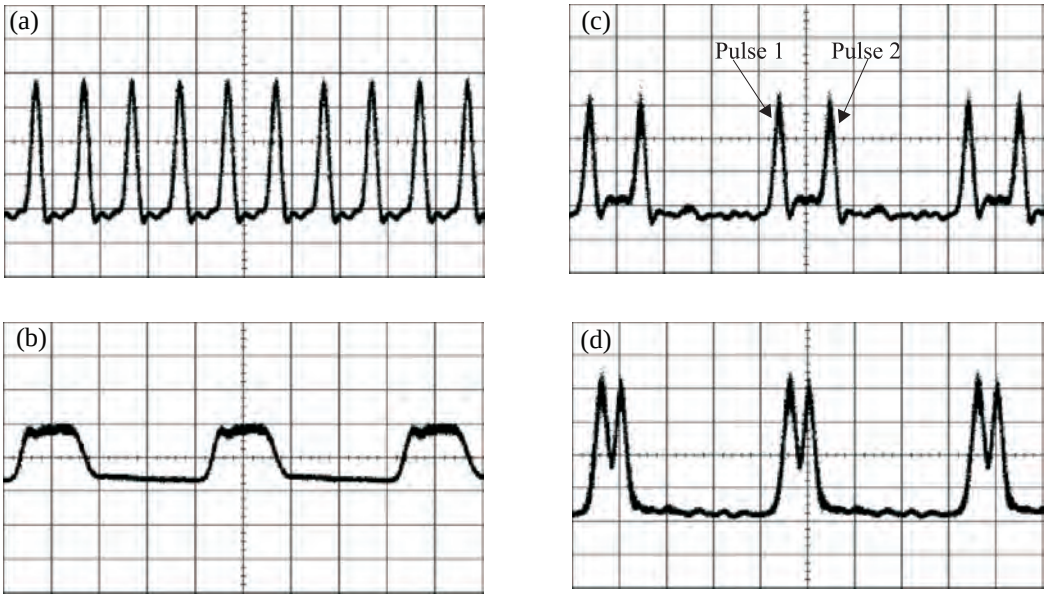

Figure 6.17: Oscilloscope traces of (a) the 10 GHz NOLM control pulses, (b) the time lens aperture, (c) the switched packet of two pulses, (d) the packet compressed in 1 km of SSMF. The time scale division is 100 ps/div.

pulses and the residual transmission of the chirped signal through the NOLM output port. In Fig. 6.18(a), it can also be seen that the overlapping between the control pulses and the linearly-chirped signal, in the fibre in the NOLM, produces four-wave mixing (FWM). The FWM spectrum shows two channels, however, the FWM efficiency is different for the two channels, because the difference in walk-off time, in the nonlinear fibre, between the control pulse and the various parts of the chirped signal. Spectral beats are also observed in the FWM spectrum, the periodicity of which approximately doubles that of the XPM spectrum. The beat formation is

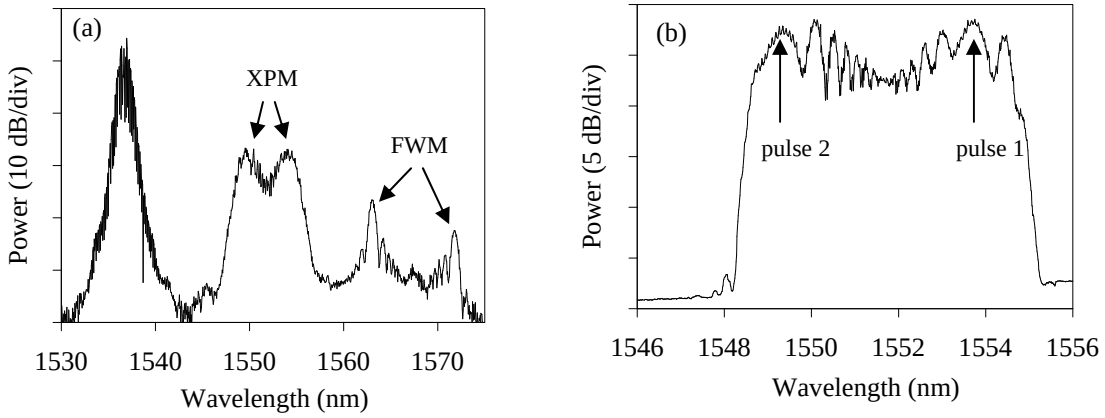

Figure 6.18: Optical spectrum after the NOLM time lens. (a) Large spectral span, (b) small spectral span around the XPM spectrum.

similarly caused by spectral field interference, while its period is given by the chirp in the switched pulses, which is twice that of the XPM pulses. This can be inferred by observing that the channel spacing in the FWM spectrum is twice that of the channels in the XPM spectrum. The doubling of the chirp is clear, the linearly-chirped pulse acts as the FWM pump, which experiences anomalous dispersion in the highly nonlinear fibre, for which phase matching is possible. Therefore, FWM occurs between two photons of each frequency in the linearly chirped pulse and a photon from the control pulse. The separation between two FWM generated frequencies is, thus, twice the separation of the pump frequencies.

Figure 6.19 shows the autocorrelation trace of the switched pulses before and after propagation in 1-km SSMF (D = 14 ps/nm/km), corresponding to figures (c) and (d) in Fig. 6.17 respectively. According to Eq. (6.8), for the time lens chirp-rate used, the packet compression factor is about 3. As can be seen, the duration of the autocorrelation of the switched pulses before propagation is 6.5 ps which, for a Gaussian shape, corresponds to a pulse duration of 4.5 ps. The switched pulses are, therefore, broader than the 2.5-ps control pulses, which is due to the walk-off between the control and signal pulses in the NOLM. Fig. 6.19(b) shows that although the packet of two pulses compressed (also clear in Fig. 6.17(d)), the individual pulses broadened significantly, which led to severe interference.

Taking into consideration that the packets were positively chirped, since compression occurs in the anomalous dispersion regime, it can be inferred from Fig. 6.6(a), noting that the input duty-cycle is about 5% (4.5-ps pulses), that to achieve a 4-fold packet

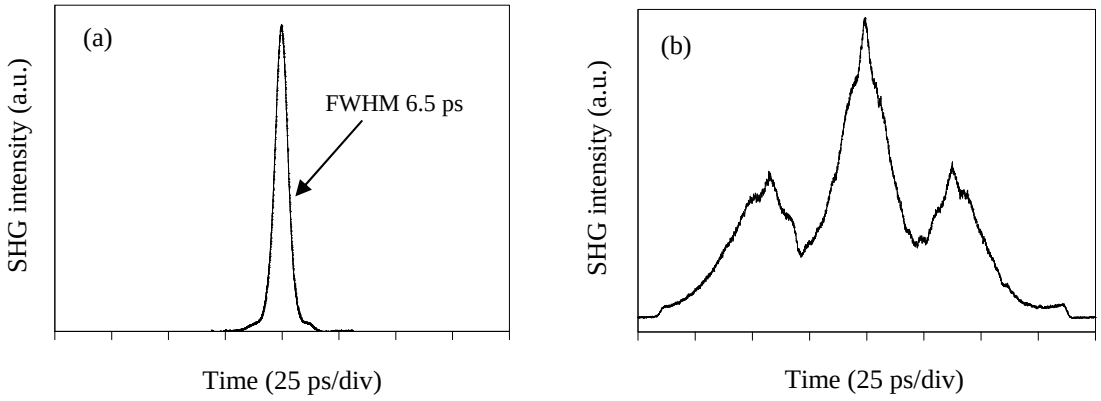

Figure 6.19: Autocorrelation traces of (a) the switched packet of two pulses, and (b) the packet compressed in 1 km of SSMF.

compression, and to keep the pulse duty-cycle below 30%, the minimum chirp-rate required is about 0.06 THz^2 (-0.08 nm/ps), which is larger than the chirp-rate of the time lens used (-0.05 nm/ps).

In a subsequent study of the compression of 2-pulse packets through the temporal lens-effect, the use of separate sources for the generation of the TDM signal and the linearly-chirped pulses was considered, hoping to minimize the interference between the switched pulses and any residual transmission of the original TDM signal. An available solution, was to use a short-pulse laser that was being developed in the Laboratory [135]. The source was based on pulse compression of 13-ps pulses, produced by carving a CW-beam in an electro-absorption modulator, in a dispersion-decreasing fibre with Raman gain, which produced 1.3-ps soliton pulses. This thesis would be incomplete without mentioning the following event. Whilst I was measuring the spectrum of the NOLM switched signal, the Raman pumps were inadvertently turned off by a colleague who immediately apologised and quickly turned the pumps back on. During this I saw, in the optical spectrum analyser, that channels without spectral beating were formed when the pumps were off, while severe spectral beating appeared when the pumps were on. Now, while the pumps were off, pulse compression did not occur, and therefore, the NOLM control pulse duration was about 13 ps. On the other hand, when the pumps were on, the pulse duration was 1.3 ps. To confirm that indeed the control pulse duration affected the system performance, the experimental setup in Fig. 6.16 was used, but 20 ps pulses generated with an electro-absorption modulator were used to control the NOLM switch. The measured optical spectrum

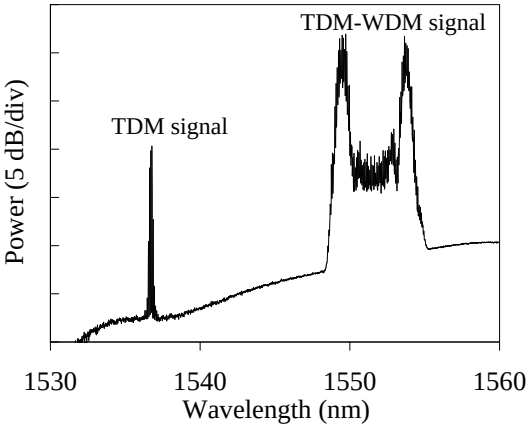

Figure 6.20: Optical spectrum of the chirped pulses after the NOLM time lens. Resolution 0.01 nm.

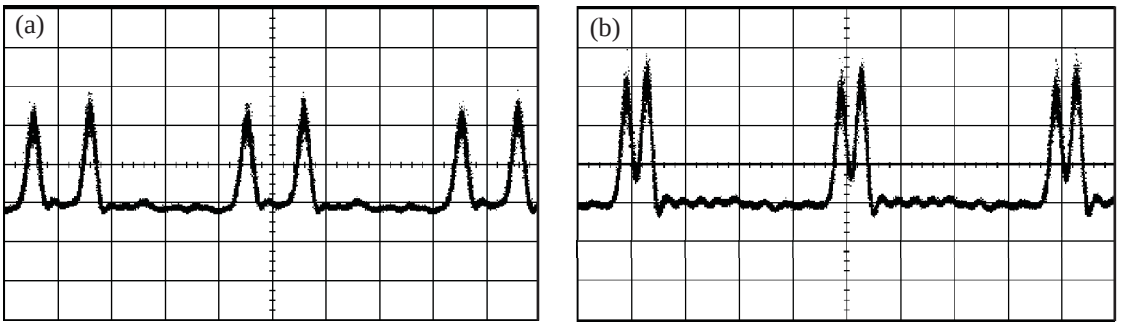

Figure 6.21: Oscilloscope traces of (a) the 2-bit packets switched from the chirped pulses, and (b) the packets compressed in 1 km of SSMF. The time scale division is 100 ps/div.

of the switched signal is shown in Fig. 6.20, and can be compared against the spectrum in Fig. 6.18. In Fig. 6.20 the channels, in the TDM-WDM signal, are spectrally separated and the spectral beats are no longer present. In-between the two channels, the residual chirped-signal transmitted through the output port of the NOLM can be seen. The suppression of the residual signal is limited by the finite switching-ratio of the NOLM switch and cross-phase modulation between the control pulses and the chirped signal in counter-propagating directions in the NOLM.

It has to be appreciated that this fortuitous accidental observation prompted us to further investigate the relation between the lens chirp-rate and the control pulse duration.

The switched pulses were then propagated through the 1 km of SSMF to produce 3-fold packet compression. The oscilloscope and autocorrelation traces before and after compression are shown in Figs.6.21 and 6.22, respectively. In Fig. 6.21(a) I show the

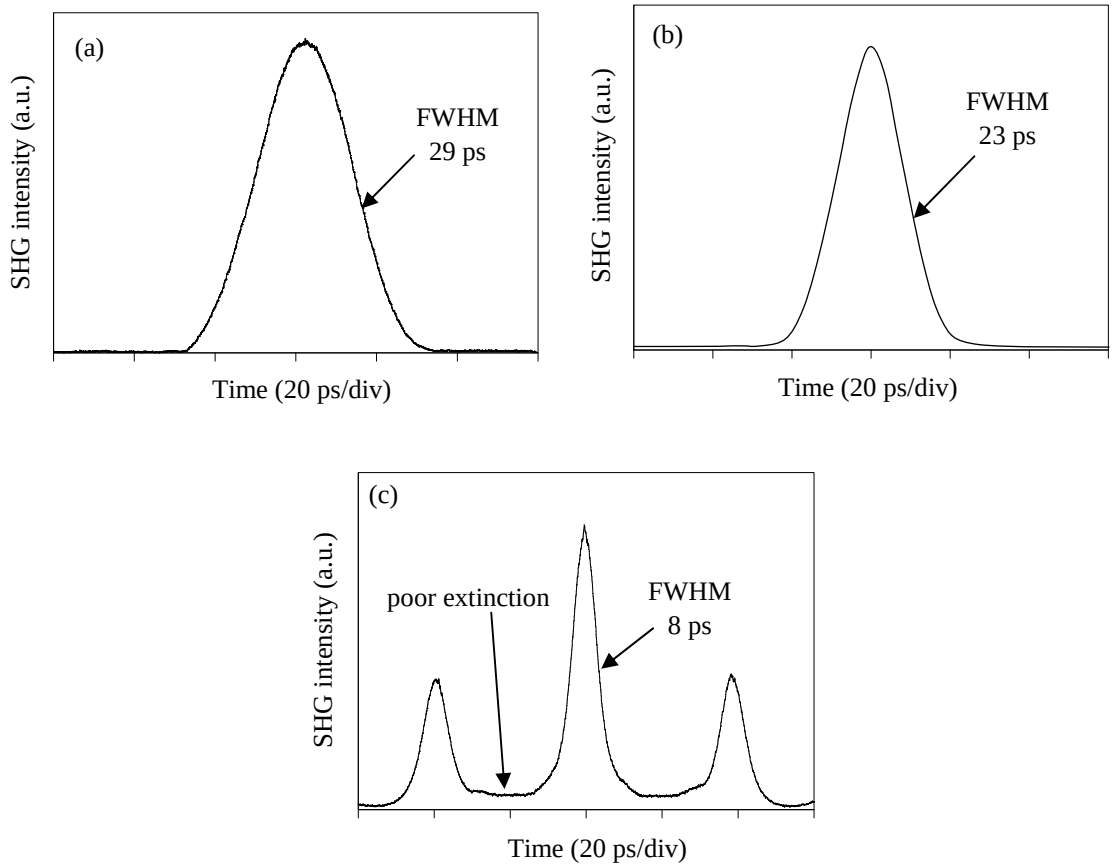

Figure 6.22: Autocorrelation traces of (a) control pulses, (b) switched pulses, and (c) 2-bit packets compressed in 1 km of SSMF.

switched signal consisting of a packet of two pulses transmitted through the time lens aperture, and in (b) the switched pulses after compression in the 1 km of SSMF. In Fig. 6.22(a) I show the autocorrelation of the control pulses, and a pulse duration of 20 ps (assuming Gaussian transform-limited pulses) can be estimated. The switched pulses are shown in Fig. 6.22(b) with a pulse duration of 16 ps. It can be observed, that the pulse duration of the switched pulse is larger than the duration of the control pulse for short control pulses, and it is smaller for long control pulses. This is so, because the phase to intensity conversion in the NOLM switch produces a shorter pulse than the phase modulating pulse, however, for short modulating pulses the walk-off time between the modulation and the signal can be larger than the modulating pulse duration. The compressed packet after the SSMF is shown in Fig. 6.21(b), and the corresponding autocorrelation in Fig. 6.22(c). The pulses were compressed to 5.2 ps, and thus, a 3-fold packet and pulse compression was simultaneously achieved. Furthermore, the side pulses, in the autocorrelation, have the same duration as the

central pulse. The poor extinction in-between pulses is, as explained before, due to the poor adjustment of the polarisation in the NOLM to compensate the counter-propagation XPM. These results are in good agreement with the simulations of a 4-fold packet compression shown in Fig. 6.6(a), when an input duty-cycle of 16% and a chirp-rate of $0.04\,\mathrm{THz}^2$ is considered.

6.3.1.2 Packet compression under a strong temporal lens-effect

Having found the experimental conditions to induce temporal packet compression based purely on the temporal lens-effect, a demonstration of compression of 4-bit packets from 10 to 40 Gb/s was planned. The experimental setup is shown in Fig. 6.23. The data source consisted of an electro-absorption modulator gate operating at 1542.9 nm and producing 20-ps pulses at a 10-GHz repetition rate which were modulated externally with a 2^7-1 bits pseudo-random binary sequence. These data pulses were amplified to an average power of 20 dBm and launched into the control port of the highly nonlinear fibre NOLM1 switch. The signal to NOLM1 comprised 360-ps

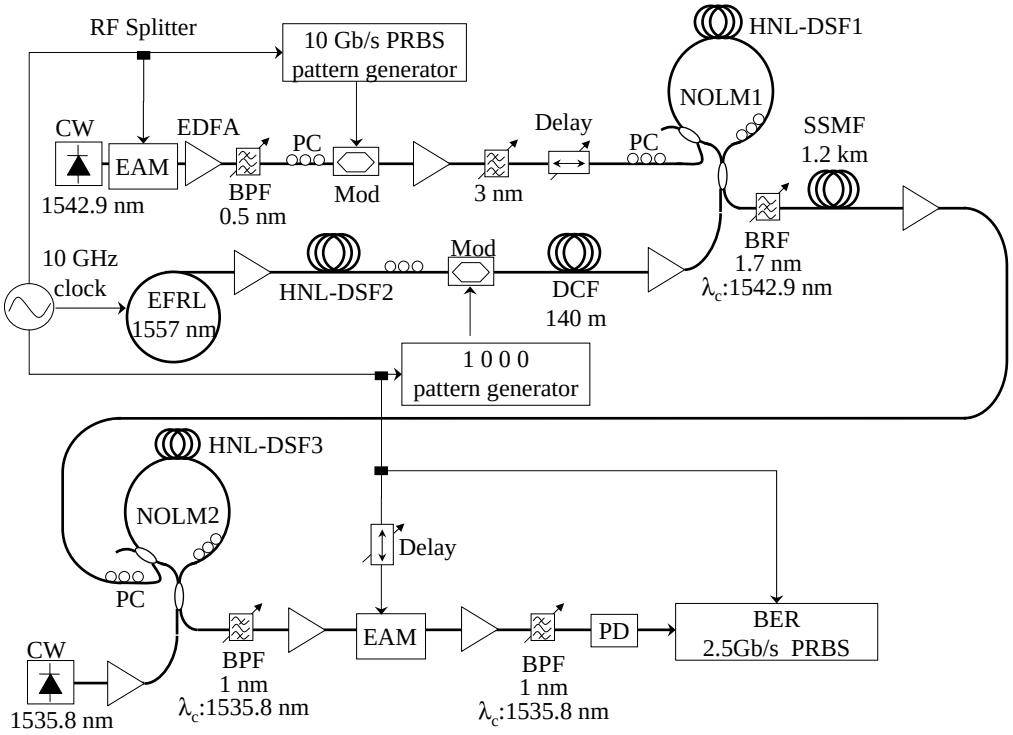

Figure 6.23: Experimental setup for packet compression at 2.5 Gpacket/s using a time lens with a chirp rate of $-0.037\,\mathrm{nm/ps}$ and a time aperture of 360 ps.

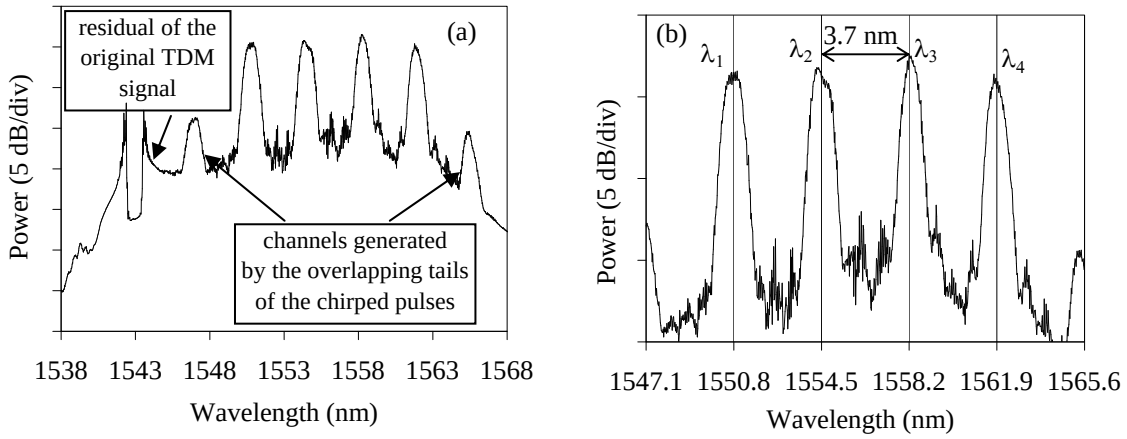

Figure 6.24: Optical spectrum of the 10-Gb/s 4-bit chirped-packets at 2.5 Gpacket/s with a resolution of 0.1 nm in (a) a large spectral-scale, (b) a small spectral-scale.

linearly-chirped rectangular pulses at a 2.5-GHz repetition rate, which determines the packet rate. They were formed as a result of the nonlinear propagation of 2.5-ps pulses, generated from an actively mode-locked erbium-fibre ring-laser (EFRL) operating at 1557 nm, in the normal dispersion regime of HNL-DSF2 (see Table 2.1). The pulses at the output of HNL-DSF2 had a −3-dB bandwidth of 13.5 nm and a pulse width of about 7 ps. An additional length of dispersion compensating fibre (DCF, dispersion of −190 ps/nm/km at the wavelength of 1550 nm, and a length of 140 m) was then used to linearly stretch the pulses to the desired width of 360 ps. Since the pulse propagation occurred only in the normal dispersion regime, the chirp introduced in the pulses was linear, and therefore, the chirp-rate could be estimated by dividing the spectral bandwidth of the pulses (13.5 nm) by their pulse width (360 ps), yielding a value of $-0.037\,\mathrm{nm/ps}$ ($C = 0.015\,\mathrm{THz}^2$). The 6-nm linearly-chirped fibre Bragg grating used before to shape the chirped pulses, was removed this time, so that a larger chirp-rate could be achieved. The chirped pulses were then amplified to an average power of 15 dBm and coupled into the NOLM signal input port. At the NOLM output port a 1.7-nm band rejection filter, centred at 1542.9 nm, filtered out the control signal, while passing the switched signal, which represented a chirped WDM replica of the original 10-Gb/s TDM data extending over the full 13.5 nm bandwidth of the rectangular chirped pulses. The optical spectrum of the signal after NOLM1 is shown in Fig. 6.24. As can be seen, 4-WDM channels were carved into the spectrum of the chirped signal, while the original 10 Gb/s TDM signal was reasonably filtered out by the rejection filter as the −3-dB bandwidth of the data pulses generated from the EAM source is less than 1 nm. In Fig. 6.24(b) I show the

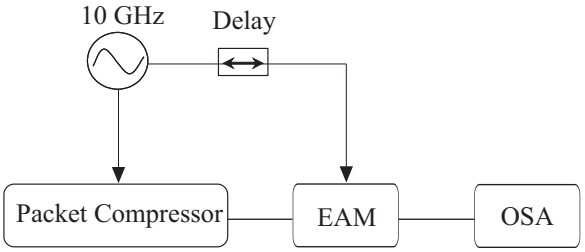

Figure 6.25: Schematic diagram of the linear spectrographic technique used for the complete characterisation of the switched chirped pulses.

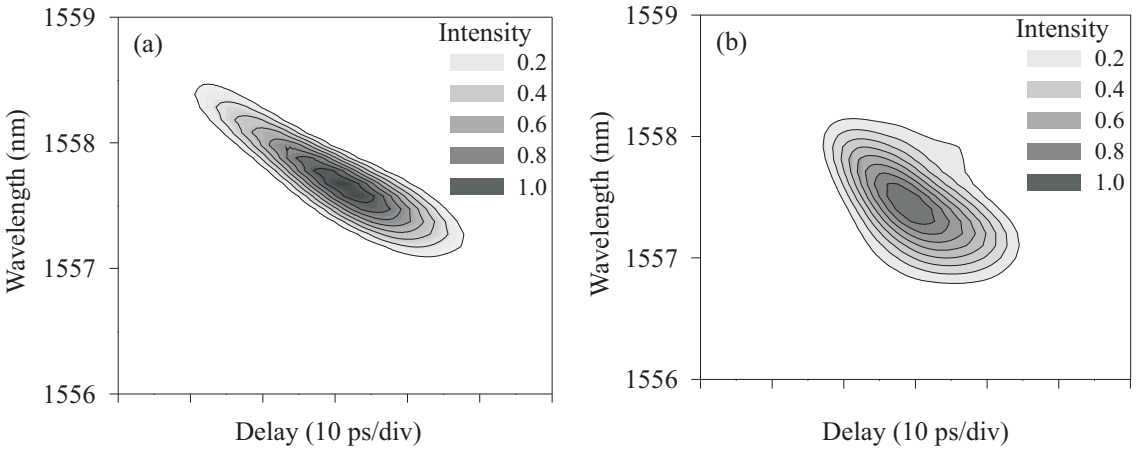

Figure 6.26: Spectrogram of the 10-Gb/s chirped switched-pulses (a) before and (b) after compression in the 1.2-km SSMF.

spectrum of the 4 chirped WDM channels, on a smaller spectral span, so that the channel spacing can be appreciated. A spacing of 3.7 nm was measured, which is in good agreement with the chirp rate of the NOLM time lens of -0.037 nm/ps. It can also be seen that unwanted channels are formed on the side of the 4 WDM channels. These appeared because the linearly-chirped pulses overlapped with more than four data pulses. As described in Chapter 3, the dispersive stretching of SPM pulses can produce long leading and trailing tails. As discussed previously, since the frequency difference between the unwanted channels and the 4 WDM channels (which is larger than 460 GHz (3.7 nm)) is far greater than the electronic bandwidth of the receiver, any coherent crosstalk is filtered out by the receiver.

After NOLM1, the duration of the switched pulses was about 16 ps. The switched signal was then launched into a standard single mode fibre (SSMF, dispersion of 17 ps/nm/km, length of 1.2 km), which was used as the dispersive compression element. The length of SSMF required for a 4-fold packet compression can be confirmed

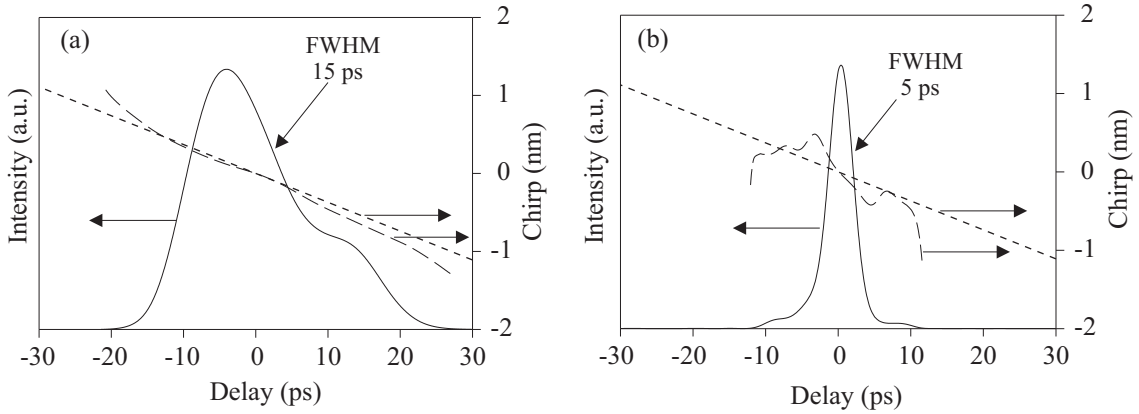

Figure 6.27: Retrieved intensity envelope and chirp (a) before and (b) after after compression in the 1.2-km SSMF. The dashed line is the chirp of the time lens (−0.037 nm/ps).

from Eq. (6.8). The focal length in the SSMF is the inverse of the product of the chirp-rate and the fibre dispersion, according to Eq. (6.9), and is equal to 1.6 km.

The switched pulses before and after the compression fibre were measured with a frequency resolved optical gating (FROG) device, which uses an electro-absorption modulator (EAM) for optical gating, developed in the Laboratory [136], see Fig. 6.25. The acquisition of the optical spectrum as a function of the delay time produces a spectrogram of the cross-correlation between the field of the switched chirped pulses and the EAM gate. The amplitude and phase of the chirped pulses can be mathematically retrieved from the spectrogram using blind deconvolution algorithms. The measured spectrograms of a switched channel are shown in Figs.6.26(a) and (b), before and after the compression fibre, respectively. The retrieved intensity envelope and chirp are shown in Fig. 6.27. As can be seen, a pulse compression factor of 3 was achieved, and the chirp rate in the pulse increased during compression, which is in agreement with Fig. 6.4. The dashed curve gives the original chirp of the time lens, and for the pulse before compression the deviation of the chirp of the pulse from the chirp of the lens was negligible. This is expected, as the pulse transform-limited bandwidth is much smaller than the chirp imparted by the lens.

The asymmetric shape of the intensity envelope of the switched pulses is due to the original shape of the linearly chirped pulses at the NOLM1 input. In Fig. 6.28, oscilloscope traces of the linearly chirped rectangular pulses at the signal port input of the NOLM1 are shown. In Fig. 6.28(a) the repetition rate of the mode-locked laser pulses was gated down to 1.25 GHz, so that the amplitude variation in the individual pulse can be appreciated. Even though the temporal resolution of the oscilloscope

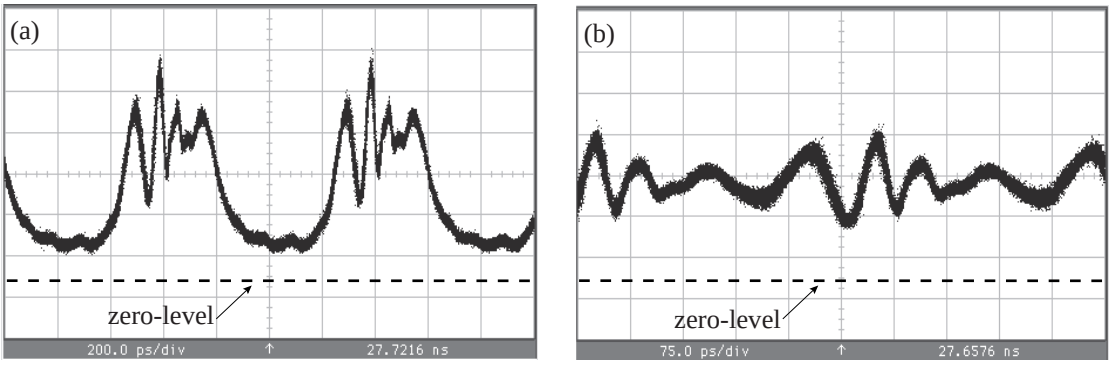

Figure 6.28: Oscilloscope traces of the linearly-chirped pulses with a repetition rate of 1.25 GHz (a), and 2.5 GHz (b).

trace is less than 15 ps, it can be seen that the pulse envelope has large variations in amplitude, which are due to the Fourier transformation of the self-phase modulation rippling, as described in Chapter 3. Consequently, gating across such an envelope can produce largely asymmetric pulses, similar to that in Fig. 6.27(a). In Fig. 6.28(b) the oscilloscope trace of the linearly-chirped pulses at the repetition-rate of 2.5 GHz is shown. At this pulse rate, the amplitude should appear essentially as CW for a linearly-chirped pulse with a rectangular intensity profile.

After the compression fibre, although pulse and packet compression were achieved, the compressed data is in a TDM-WDM mixed multiplexing format (see Fig. 6.4(c)), and any further propagation in the presence of chromatic dispersion would change the pulse repetition period. A second NOLM was then used to clean the chirp across the compressed packet and to convert it back onto a single wavelength. The fibre in NOLM2 was a standard dispersion shifted fibre (DSF3, zero dispersion at 1549 nm, dispersion coefficient of +0.07 ps/nm/km at 1550 nm, nonlinear coefficient of 2.4 $W^{-1}km^{-1}$, and length of 1 km). The signal launched into NOLM2 was a continuous wave beam centred at 1535.8 nm, whereas the control signal was provided by the compressed packets amplified to an average power of 20 dBm. At the output of the NOLM a 1 nm bandpass filter isolated the switched signal from the control signal.

Fig. 6.29 shows the autocorrelation traces of the initial 10 Gb/s TDM signal, injected into the packet compressor, and the final 4-bit 40 Gb/s TDM packets. Fig. 6.29(a) shows the expected autocorrelation of a binary sequence with an equal probability of symbols, as the maximum amplitude of the side pulses is half that of the central pulse. In Fig. 6.29(b), the measured autocorrelation (solid curve) was plotted

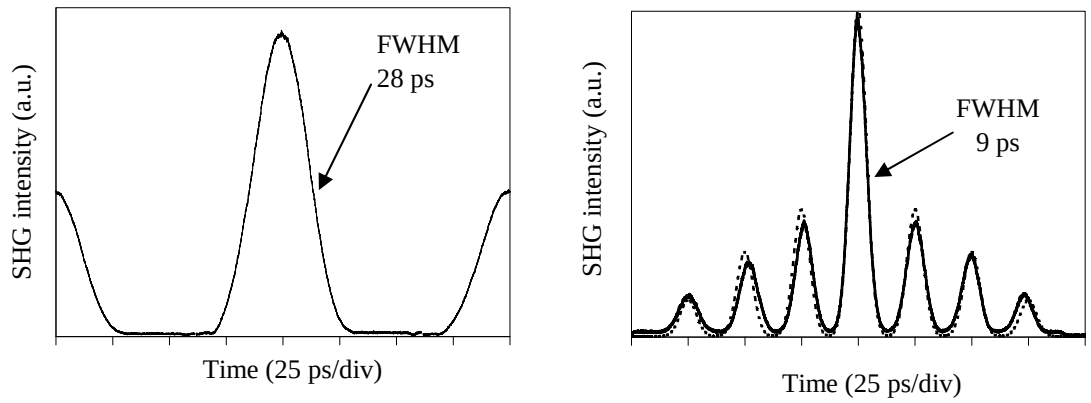

Figure 6.29: (a) Autocorrelation trace of the input 10-Gb/s TDM signal, (b) measured (solid line) and theoretical (dashed line) autocorrelation traces of the compressed 4-bit packets at 40 Gb/s and 2.5 Gpacket/s.

against the theoretical autocorrelation (dashed curve) of 4-bit packets at 40 Gb/s and 2.5 Gpacket/s with equal probability of ones and zeros, and were found in good agreement. The measured autocorrelation is readily understandable; as the measured signal consists of packets with a duration of 100 ps, and a repetition period of 400 ps, the corresponding autocorrelation function should have a triangular envelope with a duration at the base of 200 ps. In other words, since between every 4 bits there are empty time-slots, a delay of N bits in the autocorrelation corresponds to an overlap of 4-N bits only, and therefore, for a 1-bit delay the amplitude is 3/4 of the '1' ratio (0.375), for a 2-bit delay the amplitude is 2/4 of the '1' ratio (0.25), and for a 3-bit delay the amplitude is 1/4 of the '1' ratio (0.125). Therefore, the maximum amplitude of the side pulses decreases linearly to zero in an interval of 100 ps from the centre of the central pulse, as shown in Fig. 6.29(b). The duty-cycle increased from 20% to 25% during the packet compression, and it can be estimated that a 3-fold pulse compression occurs, which confirms the results obtained with the FROG technique.

The corresponding oscilloscope traces and eye diagrams (infinite persistence trace) are shown in Fig. 6.30. The packet periodicity can be appreciated in Fig. 6.30(b). Although a clear eye opening of the final compressed packet can be observed in Fig. 6.30(d), the amplitude noise is greater than that in Fig. 6.30(c), which results from the two nonlinear switching processes involved. In particular, the residual signal from the first switch, which consists of the unremoved control pulses and the unwanted switched channels, is optically mixed with the WDM channels via self-phase modulation effects in the second switch. Furthermore, the lack of a 14 nm

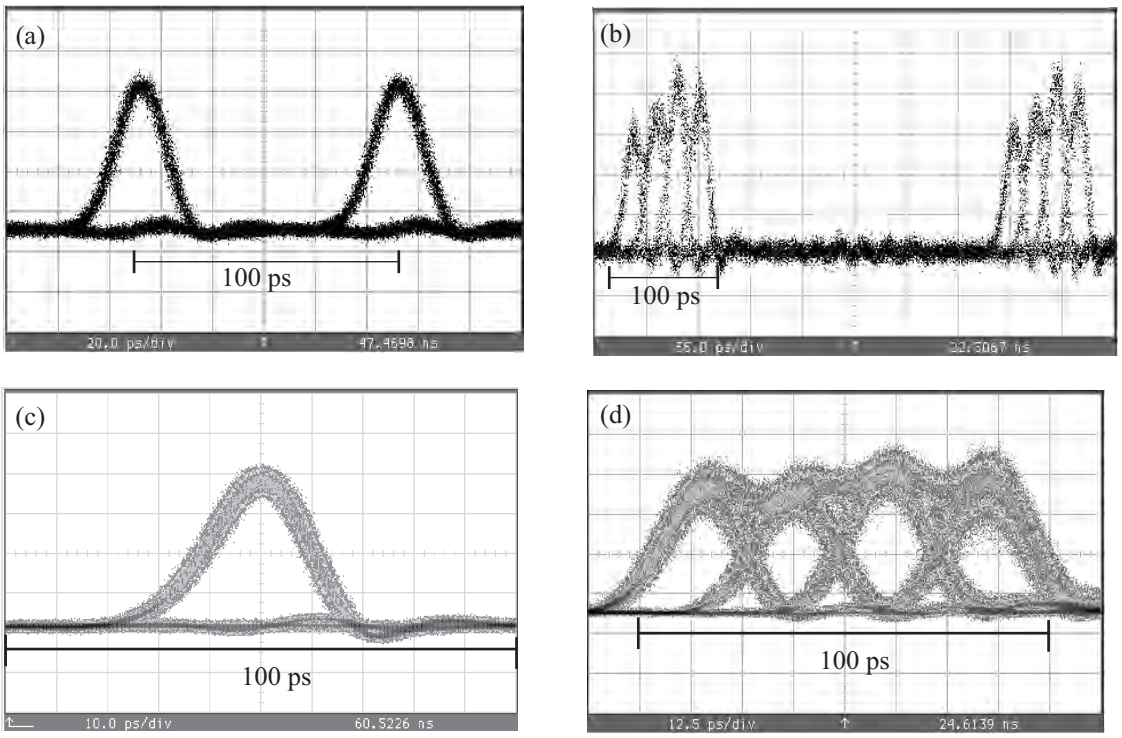

Figure 6.30: Measured eye diagrams of the input 10 Gb/s TDM signal ((a) and (c)), and the compressed 4-bit packets at 40 Gb/s and 2.5 Gpacket/s ((b) and (d)). In (a) and (b) the display persistence was 900 ms, while in (c) and (d) it was infinite.

filter to remove the out-of-band amplified spontaneous emission noise at the control port of the second switch results in a low in-band signal-to-noise ratio for the switched signal. The peak power imbalance between the different bits in the packet results mainly from the non flat shape of the linearly-chirped pulse at the input of the NOLM. The observed amplitude noise is different at each bit slot, which can be attributed to slightly different walk-off values between bit slots allocated to different centre wavelengths.

The spectrum of the final 4-bit compressed packets is shown in Fig. 6.31. Whilst Fig. 6.31(a) shows the measured spectrum, Fig. 6.31(b) shows the corresponding calculated spectrum. In the simulation, 5.7-ps hyperbolic secant (sech) pulses, in a sequence of 16 packets of 4 bits at 2.5 Gpacket/s and a bit rate of 40 Gb/s, were considered. The simulated timing jitter of the sech pulse source was 200 fs, while the standard deviation of the pulse-to-pulse amplitude fluctuation was taken to be 5%. Also, the spectral resolution of the optical spectrum analyser was included, to reproduce the relative amplitude of the spectral lines. As can be seen, the main characteristics of the measured spectrum are confirmed in the simulation. The spectral

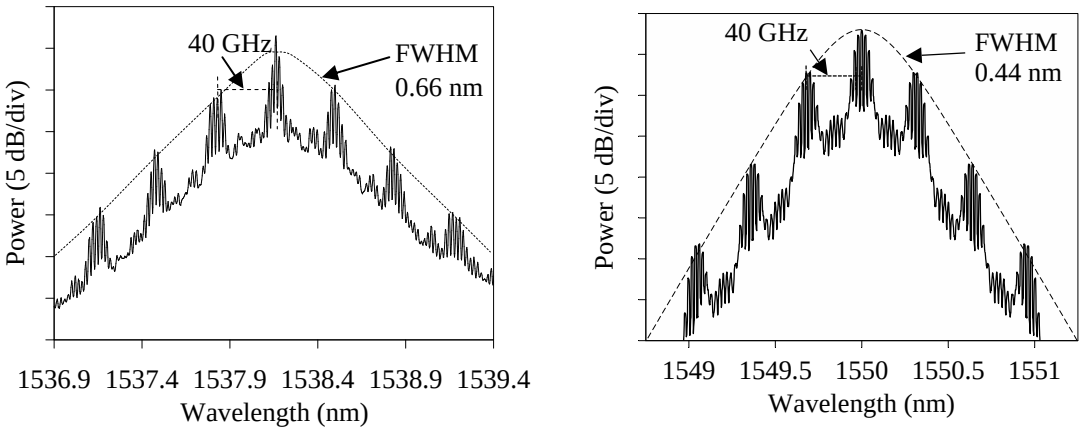

Figure 6.31: Optical spectrum of the 4-bit packets at 40 Gb/s and 2.5 Gpacket/s converted into a single carrier wavelength. In (a) the measured spectrum, (b) the simulated spectrum. The optical-spectrum-analyser resolution was 0.01 nm.

lines have 40 GHz periodicity (corresponding to the bit rate) and a sinc-shape. The full bandwidth of the sinc-shaped lines (i.e. the bandwidth between the first zeros) is 20 GHz, which corresponds to the rectangular envelope of the 100 ps packets. The sinc-shaped lines themselves consist of discrete 2.5 GHz lines, which correspond to the packet repetition rate. However, the width of the spectral envelope (dashed curve), which corresponds to the transform limited bandwidth of the individual pulses, is significantly larger for the measured spectrum. It is to be noted, that the edges of the pulse retrieved in Fig. 6.27(b) are steeper than a sech or Gaussian pulse, and therefore its transform limited bandwidth is expected to be larger.

In order to assess the noise properties of the packet compressor, we performed bit error rate (BER) measurements at the baseline rate of 10 Gb/s. We performed these measurements first after NOLM1 by filtering out each of the spectral channels shown in Fig. 6.24, and then after NOLM2. For this measurement, an EAM-based demultiplexer with a switching window of 20 ps was used, as shown in Fig. 6.23. The eye diagrams measured after demultiplexing each bit slot of the 4-bit packet at 40 Gb/s are shown in the insets in Fig. 6.32. All the BER measurements are plotted in Fig. 6.32 with respect to the back-to-back setup and compared in terms of the received power. Error-free performance was achieved in all cases. The power penalty after NOLM1 for the different channels varied between 2.7 and 4 dB, whereas after NOLM2 the power penalty varied between 6.5 and 8 dB. In the latter case, the channel converted from 1550.8 nm to 1535.8 nm shows the biggest penalty, which we consider to be due to the larger walk-off time between these wavelengths in NOLM2.

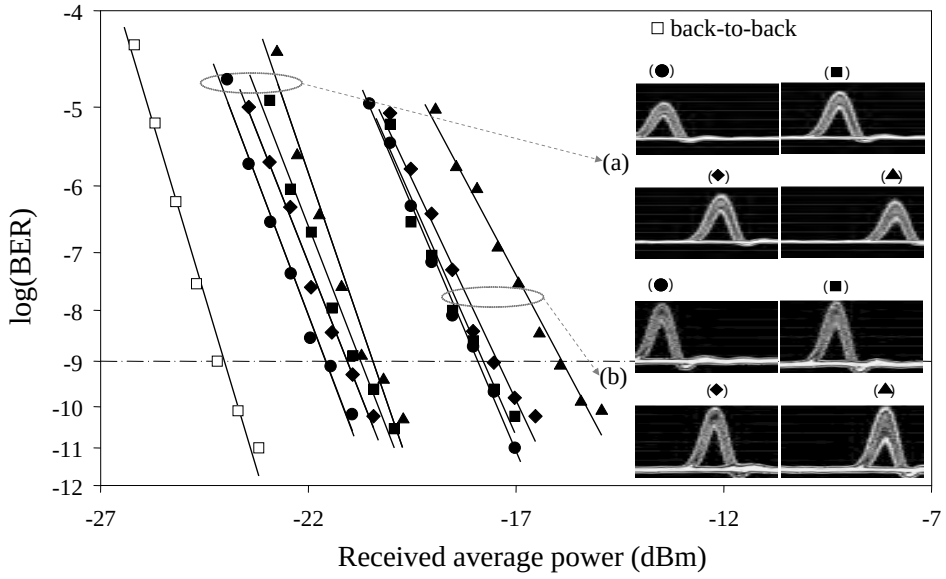

Figure 6.32: Bit error-rate measurements for the 4-bit packets at 40 Gb/s and 2.5 Gpacket/s (a) chirped-WDM packets, (b) converted to TDM packets.

Packet compression up to 80 Gb/s was attempted using the same experimental setup. The only component modified was the compression fibre, whose length was increased to 1.4 km. This is in agreement with Eq. (6.8), when considering an 8-fold packet compression, and the dispersion coefficient of the SSMF (17 ps/nm/km).

The autocorrelation trace of the 80-Gb/s compressed packets was measured, and is shown in Fig. 6.33(a) by the solid line. It is compared against the theoretical autocorrelation (dotted line), which was obtained for a sequence of 16 packets of 4 bits at 2.5 Gpacket/s and a bit rate of 80 Gb/s. A random binary-sequence with equal probability of symbols was considered, while the individual bits were 4.6-ps hyperbolic secant pulses. It can be seen from Fig. 6.33(a) that the amplitude difference between the theoretical and measured autocorrelation traces increases for the farthest pulses from the central pulse. A possible explanation is that the relative pulse position deviation induced by the slope dispersion of the SSMF increases with the bit rate (as shown in Fig. 6.10). Furthermore, the pulse period in the compressed packet is a linear function of the time, which can explain the increasing of the amplitude difference as a function of the autocorrelation delay time. In Fig. 6.33(b), the theoretical autocorrelation of packets of 4 bits at 80 Gb/s with 3-ps pulses, which corresponds

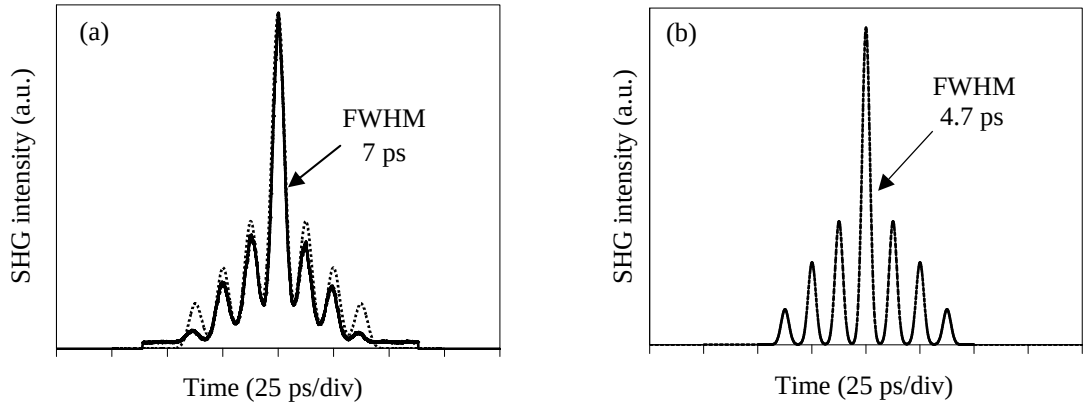

Figure 6.33: Autocorrelation trace of the 4-bit packets at 80 Gb/s and 2.5 Gpacket/s. In (a) the measured trace (solid line), and theoretical trace (dashed line) considering a pulse duty-cycle of 37%. In (b) the theoretical trace considering a pulse duty-cycle of 25%.

to a duty-cycle of 25%, is shown.

It is clear that the chirp-rate available (-0.037 nm/ps) was insufficient to compress the individual pulses to a duty-cycle lower than 30%, for which intersymbol interference is negligible. From Fig. 6.8(a) it can be established that the lens chirp-rate, as a function of the packet compression factor (F_c), is approximately given by $0.0026F_c$ (THz^2), for the NOLM time-lens. Using this relation, the minimum chirp-rate for an 8-fold packet compression is $0.02\,\mathrm{THz}^2$ (-0.025 nm/ps), which is less than the chirp-rate available (-0.037 nm/ps). However, as it can be inferred from Fig. 6.6(a), the minimum chirp-rate that gives an output duty-cycle smaller than 30% requires the input pulse duty-cycle to be in a small interval around 35%, while a lower input pulse duty-cycle requires a higher chirp-rate. Hence, packet compression keeping the pulse duty-cycle under 30% should eventually be possible, using the same time lens, by increasing the input pulse duty-cycle from 20% to 30%.

Measured eye diagrams of the 80 Gb/s compressed packets are shown in Fig. 6.34. Whilst Fig. 6.34(a) shows the packet periodicity, Fig. 6.34(b) shows the eye diagram in detail. Although, large signal-to-noise ratio degradation results from the two nonlinear switching processes, the signal distortion observed in the measured eye diagrams is mainly due to the limited bandwidth of the receiver used ($\sim$40 GHz), which induces large intersymbol interference. In [137], it is shown that a large penalty due to intersymbol interference is observed in a receiver with a bandwidth smaller than 50% of the bit rate for the return-to-zero signal format, and to avoid a penalty larger

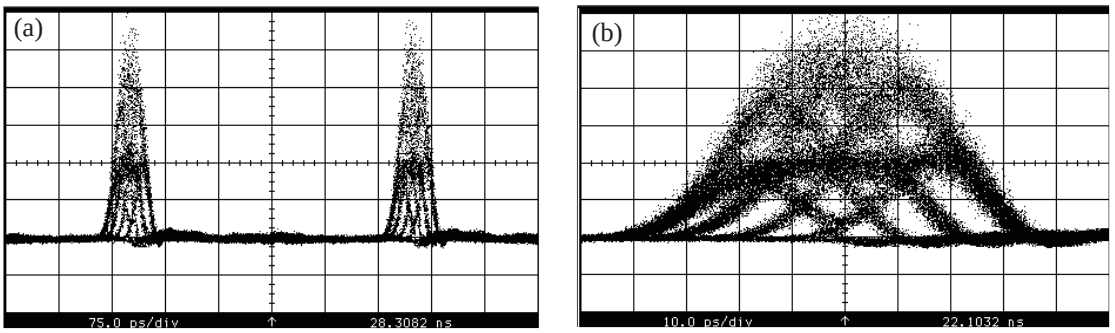

Figure 6.34: Measured eye diagrams of the 80 Gb/s compressed packets. The time scale division was 75 ps in (a), and 10 ps in (b).

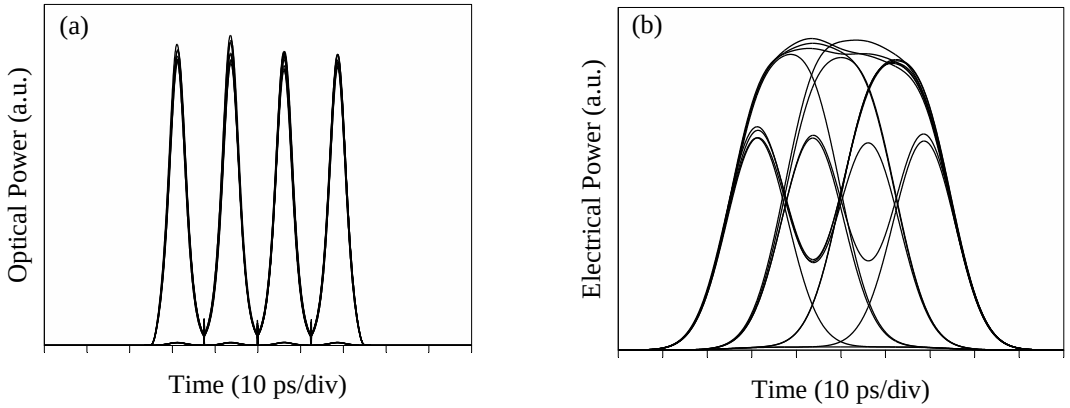

Figure 6.35: Theoretical eye diagrams of the 80 Gb/s compressed packets. (a) Optical sampling oscilloscope, and (b) 40 GHz electrical sampling oscilloscope.

than 1 dB the receiver bandwidth should be larger than 70% of the bit rate. Therefore, for an 80 Gb/s signal, a minimum receiver bandwidth of ∼60 GHz is required to avoid significant intersymbol interference.

The effect of the limited receiver-bandwidth on the measured eye-diagrams was simulated, considering a 40-GHz low-pass Gaussian filter for the transfer function of the electrical receiver. In order to assess the degradation induced by the bandwidth of the electrical receiver, well-sampled eye diagrams were also simulated, as are eye diagrams measured with an optical sampling oscilloscope, for which the sampling bandwidth is much larger than the bandwidth of the optical signal.

In Fig. 6.35(a) I show the eye diagram of 16 packets of 4 bits at 80 Gb/s, with 4.6-ps sech pulses. As the pulse duty-cycle is about 37%, a slight intersymbol interference is observed at the tail crossing-point, although, this has negligible impact in terms of

signal degradation. In Fig. 6.35(b) the intersymbol interference is clearly visible and, as in Fig. 6.34(b), a two-level eye diagram is formed. As the phase-coherence time of the optical signal was neglected in the simulation, only the intersymbol interference between pulses with identical phase is observed. In other words, only the case of in-phase interference between pulses was simulated. It is reasonable to expect that out-of-phase pulse interference can produce other levels in the simulated eye diagram, such as those observed in Fig. 6.34(b). In Fig. 6.34(b), the effect of the compression fibre dispersion-slope is clear; the pulses at the front of the packet overlap more than pulses at the back.

The measured optical spectrum of the compressed 80 Gb/s packets, after being converted into a single carrier wavelength in NOLM2, is shown in Fig. 6.36(a), and is

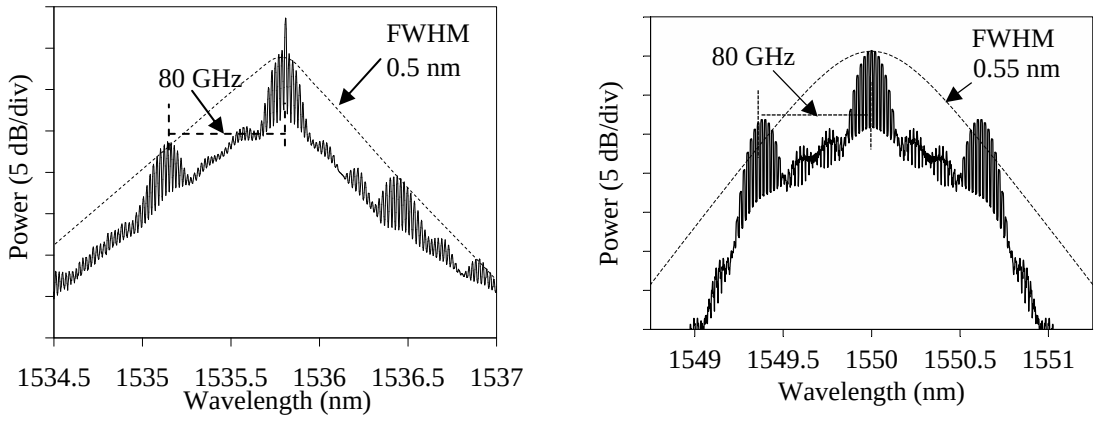

Figure 6.36: Optical spectrum of the 4-bit packets at 80 Gb/s and 2.5 Gpacket/s converted into a single carrier wavelength. In (a) the measured spectrum, (b) the simulated spectrum. The optical-spectrum-analyser resolution was 0.01 nm.

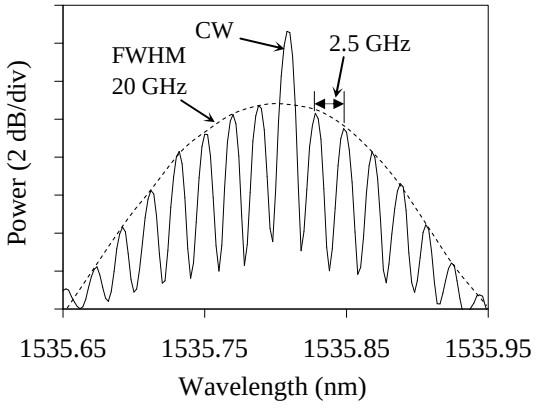

Figure 6.37: Measured optical spectrum of the central sinc-shaped spectral line on a larger spectral scale.

compared against the simulated spectrum in Fig. 6.36(b). As can be seen, the main characteristics of the measured spectrum are confirmed in the simulation. The spectral lines have 80 GHz periodicity (corresponding to the bit-rate) and a sinc-shape. The full bandwidth of the sinc-shaped lines (i.e. the bandwidth between the first zeros) is ∼40 GHz, which corresponds to the rectangular envelope of the 50-ps packets. The optical spectrum of the central sinc-shaped spectral line is shown on a larger spectral scale in Fig. 6.37. The sinc-shaped lines themselves consist of discrete 2.5 GHz lines, which correspond to the packet repetition rate. Note that the CW component in the centre of the optical spectrum is due to the finite NOLM switching-ratio. The shape of the spectral envelope (dashed curve), which corresponds to the transform-limited bandwidth of the individual pulses, is, however, significantly different for the measured and simulated spectra. This is an indication that the shape of the measured pulses is different to the hyperbolic secant pulse-shape considered in the simulation.

6.3.2 Packet Expansion Experiments

Packet expansion may be required to allow the reverse operation of packet compression when packets move from a high-speed to a low-speed network. Packet expansion may also be useful at the receiver-end to adapt the speed of the signal to the bandwidth of the receiver. In this section, I describe our experimental results on bit-rate expansion of 4-bit packets from 40 to 10 Gb/s using the temporal lens-effect via the NOLM switching of linearly-chirped pulses.

Figure 6.38 shows the experimental setup used to expand 4-bit packets at 2.5 Gpacket/s from 40 Gb/s to 10 Gb/s. In the laboratory, the incoming 40 Gb/s packets were generated using 10-ps pulses at a repetition-rate of 10 GHz from a gain-switched laser diode operating at 1540 nm. The gain-switched laser was injection-locked by an external CW-laser operating at 1539.8 nm, which greatly reduces the pulse-to-pulse timing-jitter [138]. The pulses were then modulated with a 10-Gb/s binary-sequence obtained by adding three zero-bits after each bit of a $2^7 - 1$ pseudo-random binary-sequence, which results in a $2^7 - 1$ PRBS data-stream at 2.5 Gb/s .

The pulse data-stream was then amplified to compensate for losses in the modulator and was subsequently fed into a 1:4 multiplexer. The OTDM-multiplexer's fibre-delay-lattice was designed to produce a multiplexed bit-sequence which is also

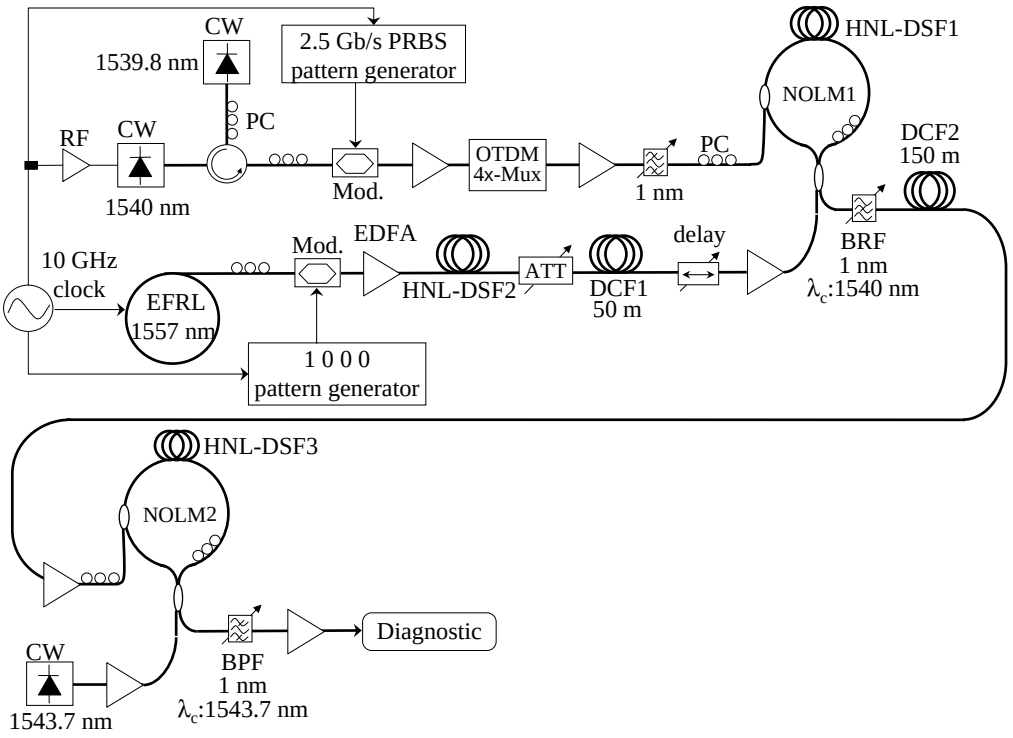

Figure 6.38: Experimental setup for expansion of 4-bit packets from 40 to 10 Gb/s at 2.5 Gpacket/s using a chirp-rate of −0.16 nm/ps and a time-lens aperture of ∼100 ps.

a pseudo-random sequence. Consequently, the multiplexed signal consisted of 40-Gb/s 4-bit packets at 2.5 Gpacket/s, which are shown in Fig. 6.39. Fig. 6.39(a) shows their low persistence eye-diagrams on a large temporal scale (100 ps/div), whereas Fig. 6.39(b) shows the infinite persistence eye-diagram on a small temporal scale (12.5 ps/div). In Fig. 6.40, the corresponding optical-spectrum and intensity-autocorrelation traces are shown. As can be seen, the time-bandwidth product of the gain-switched pulses was 1.2 (assuming a Gaussian pulse-shape), which suggests that the pulses were chirped. The optical spectrum does not show the same spectral features as the spectrum of the 40-Gb/s 4-bit compressed-packets, shown in Fig. 6.31, in the previous section. The explanation is that, in the case of the compressed-packets, the pulse phase was coherent across a large number of packets due to the phase-coherence of the CW-laser source, whereas in the case of the multiplexed-packets, the pulse-to-pulse phase is totally uncorrelated because adjacent pulses in the packet followed a different optical-path in the multiplexer. Therefore, the spectral modes originate from random-phase interference, and consequently, the fine features of the resulting spectrum are unrelated to the repetition-rate of the packet stream. Still,

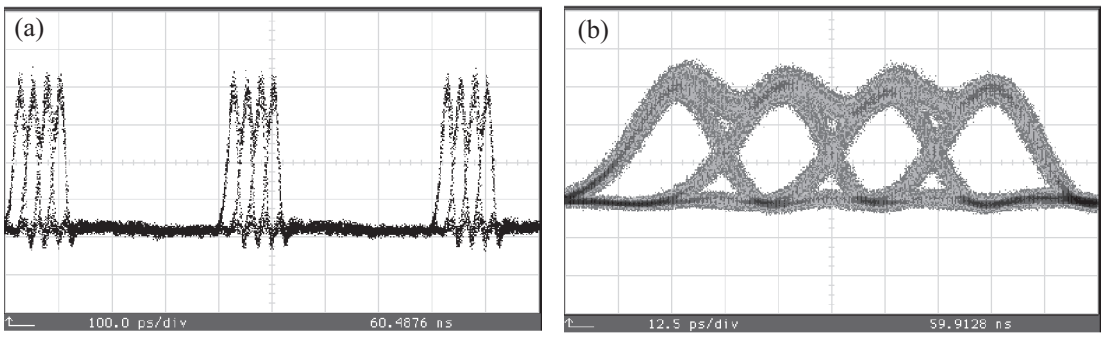

Figure 6.39: Eye diagrams of the incoming 40-Gb/s 4-bit packets at 2.5 Gpacket/s measured in (a) a large temporal scale (100 ps/div) and low persistence, (b) a small temporal scale (12.5 ps/div) and infinite persistence.

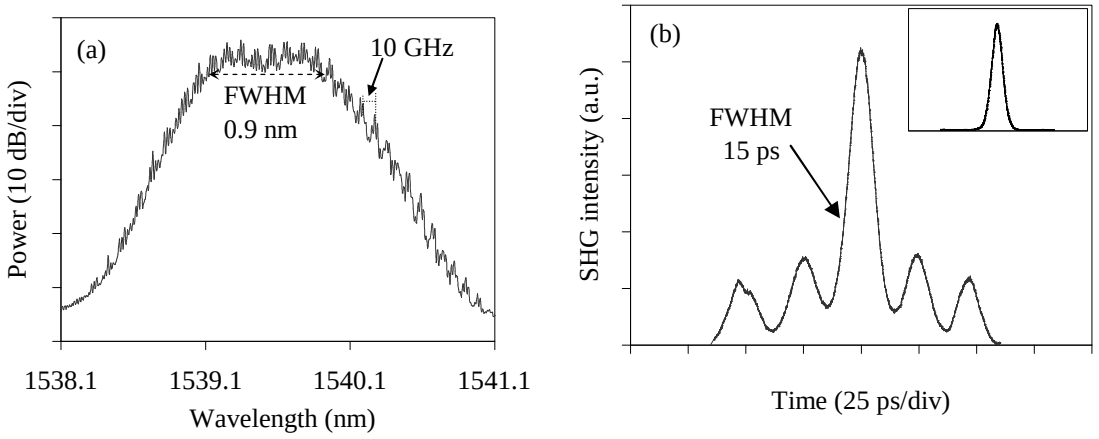

Figure 6.40: (a) Optical spectrum of the incoming 40-Gb/s 4-bit packets at 2.5 Gpacket/s with a resolution of 0.01 nm; (b) intensity autocorrelation of the 40-Gb/s 4-bit packets, and inset the intensity autocorrelation of the 10-GHz gain-switched pulses.

2.5 GHz spectral modes are observed, which corresponds to the packet repetition-rate. Figure 6.40(b) shows the autocorrelation trace of the multiplexed 40-Gb/s 4-bit packets together with the autocorrelation trace of the gain-switched pulses in the inset; the temporal scale used in the two traces of Fig. 6.40(b) is the same, so that they can be compared directly.

The 40-Gb/s 4-bit packets were then amplified and injected into the NOLM1 control-port, whereas ∼100-ps linearly-chirped pulses at the repetition rate of 2.5 GHz were injected into the NOLM1 signal-port. The linearly-chirped pulses were prepared by chirping 2.5-ps pulses, originating from an actively mode-locked fibre laser, whose pulse repetition-rate was gated down from 10 to 2.5 GHz using an external modulator. Chirping of the pulses was achieved in the highly-nonlinear fibre HNL-DSF2 via strong self-phase modulation in the normal-dispersion regime as described in Chapter 3. The

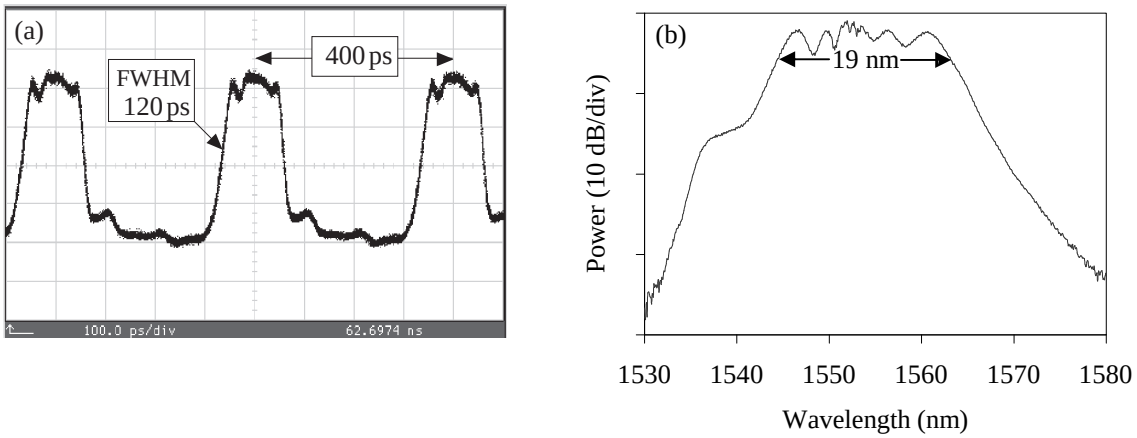

Figure 6.41: (a) Oscilloscope trace of the 120-ps linearly chirped-pulses at a repetition of 2.5 GHz in a temporal scale of 100 ps/div; (b) the corresponding optical spectrum with a resolution of 0.1 nm.

pulse envelope was subsequently stretched in the DCF1 (D=−110 ps/nm/km). The generated pulses are shown in Fig. 6.41, where Fig. 6.41(a) shows the pulse oscilloscope trace on a temporal scale of 100 ps/div, and Fig. 6.41(b) shows the corresponding optical spectrum with a spectral resolution of 0.1 nm. As can be seen, the chirped-pulse duration was 120 ps, which is much larger than the impulse response of the 30-GHz receiver used, and the −3-dB bandwidth was 19 nm; the corresponding chirp-rate was, therefore, −0.16 nm/ps (0.13 THz^2). As the envelope of the linearly-chirped pulses was stretched in a negative dispersion fibre (the DCF1), the chirp-rate was positive.

In NOLM1, the transmission of the linearly-chirped pulses was controlled by the 40-Gb/s 4-bit packets, and therefore, at the output-port of the NOLM1, a chirped replica of the packets was obtained together with the original packets. A 1-nm rejection filter, which was composed of two tuneable fibre-Bragg-gratings, subsequently removed the original packets, whilst the chirped packets were unaffected by the filter. The optical spectrum of the chirped-packets, after this filter, is shown in Fig. 6.42. As can be seen four channels were formed, which correspond to the number of bits per packet; the measured 4-nm channel-spacing confirms the previously estimated chirp-rate of −0.16 nm/ps, since it is equal to the chirp-rate times the 40-Gb/s bit-period (25 ps). As the transform-limited bandwidth of 10-ps Gaussian pulses is only 0.35 nm, the spectral-width of each channel was chirp-dominated, and therefore, according to Appendix B, can be approximately estimated by the chirp-rate times the pulse-width (10 ps) as 1.6 nm.

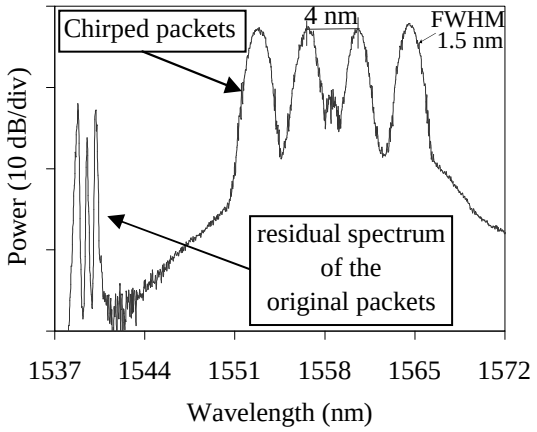

Figure 6.42: Optical spectrum of the 4-bit 40-Gb/s chirped-packets after NOLM1 with a resolution of 0.1 nm.

The net dispersion required for a 4-fold expansion of the packets is given by Eq. (6.8). The 40-Gb/s chirped-packets were thus expanded in the 150-m long DCF2, the dispersion coefficient of which was -110 ps/nm/km. As the packets were positively chirped, the pulse propagation-speed decreases from the leading edge to the trailing edge of the packet in a positive dispersion fibre, which leads to the packet expansion from 40 to 10 Gb/s.

The expanded chirped-packets were then mapped onto a single wavelength, thus generating unchirped-packets that could be further transmitted. These were obtained by using the chirped packets to control the carving of a CW-beam centred at 1543.7 nm in NOLM2, as shown in Fig. 6.38. The CW-beam wavelength was chosen to be different from the original-packet wavelength (1540 nm), so that noise degradation induced by the residual component from the original packets, which passed through the filter, was avoided. A 1-nm bandpass filter at the output of NOLM2 transmitted the unchirped expanded-packets only. Fig. 6.43(a) shows the optical spectrum of the unchirped expanded-packets, whereas Fig. 6.43(b) shows the spectrum in a larger spectral scale so that the residual signals from both NOLM switching stages can be appreciated. As can be seen, the unchirped expanded-packets had a 3-dB bandwidth of 0.18 nm, and spectral lines with a periodicity of 10 GHz, which show that phase coherent 10-Gb/s packets were produced.

The autocorrelation of the 10-Gb/s 4-bit unchirped-packets was also measured and is compared against that of the original packets in Fig. 6.44(a) and with the chirped-packets in Fig. 6.44(b). From the duration (FWHM) of the autocorrelation of the

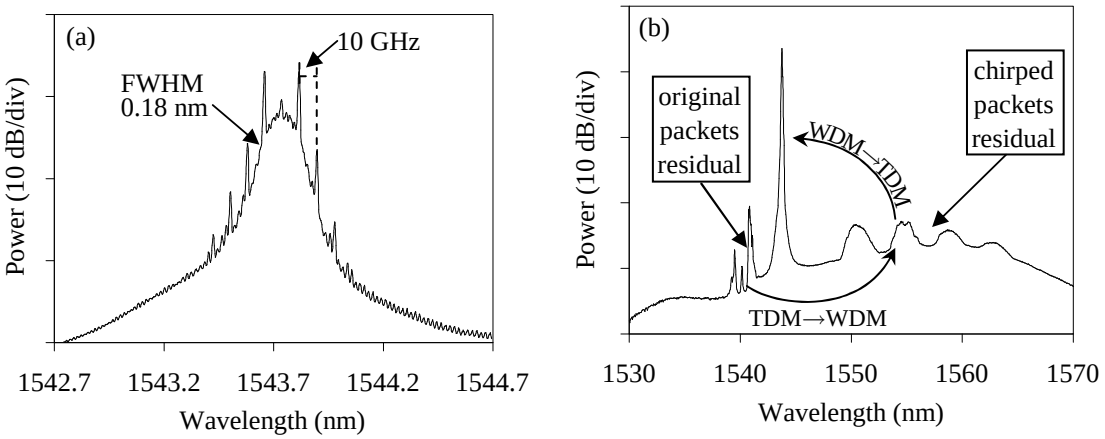

Figure 6.43: Optical spectrum of the final 4-bit 10-Gb/s expanded packets at 2.5 Gpacket/s (a) with a resolution of 0.01 nm in a small spectral-scale, (b) with a resolution of 0.1 nm in a large spectral-scale.

unchirped expanded-pulses, it can be estimated, assuming a Gaussian pulse-shape, for which the deconvolution-factor is 0.707, that the duration (FWHM) of the expanded pulses was 28 ps. However, the corresponding time-bandwidth product would be 0.63 rather than 0.44 as for an unchirped Gaussian-pulse, which implies that the pulse shape was almost certainly non-Gaussian. In fact, it was observed that the shape of the expanded pulses is strongly dependent on the average power of the NOLM1 control-pulses. It was possible to measure the expanded pulse-envelope directly on the electrical-sampling-oscilloscope, using a 30-GHz receiver with an impulse response of about 20 ps; the pulses were measured for different average-power levels (P_c) of the NOLM1 control-pulses, and are shown in Fig. 6.45. The left-column shows the envelope of the switched chirped-pulses before expansion, whereas the right-column

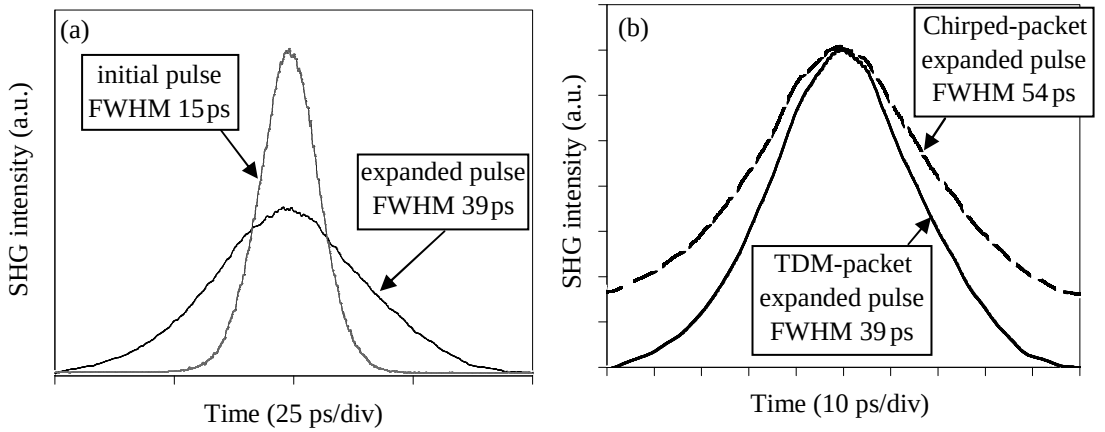

Figure 6.44: Intensity autocorrelations of (a) incoming versus outgoing packet-pulses, (b) chirped versus unchirped expanded-pulses.

shows the same pulses after expansion. The amplitude histograms show the noise generated when NOLM1 was biased at different P_c power levels. As can be seen, the amplitude noise was minimum at an average power of 15 dBm, which corresponds to the power level required for maximum switching-efficiency. However, the pulse envelope after expansion changed into a rectangular-like shape as the control power increased to the maximum switching-efficiency, and for higher power levels a valley was gradually formed in the centre of the pulse. It is thus expected that the time-bandwidth product of these rectangular-like expanded pulses can be much larger than that of a transform-limited Gaussian pulse.

The different shapes of the expanded-pulse envelope can be explained by the Fourier transform effect of linearly-chirped pulses propagating in a dispersive fibre. Since the spectral shape of the switched channels is a function of the intensity of the control pulses in NOLM1, the temporal shape of the chirped pulses after propagation in a dispersive fibre changes accordingly. Different spectral-shapes of chirped-pulses carved in NOLM1 are shown in Fig. 6.46 for a control average-power of 10 and 13 dBm at a repetition-rate of 2.5 GHz. The measured spectra were fitted to 15-point moving-average curves, so that the shape of the spectral envelopes could be better appreciated. As can be seen, the spectral shape is nearly Gaussian at 10 dBm, while it changes to nearly parabolic at 13 dBm. Subsequent dispersive propagation of such chirped-pulses with different spectral envelopes leads to the Fourier transformation of their temporal envelope, as shown in Fig. 6.45.

Consequently, as the pulse can change its temporal envelope significantly during expansion, it is difficult to estimate the exact pulse-duration from its autocorrelation trace. However, from the autocorrelation traces in Fig. 6.44, it can be inferred that the expanded pulse-envelope is certainly non-rectangular, since its intensity autocorrelation is non-triangular. It is thus reasonable to assume that the pulse duration of the expanded pulse in Fig. 6.44 is upper-bounded by the deconvolution-factor of a parabolic pulse, which is 0.8. Therefore, the expanded-pulse duration was at most 31 ps (39 ps times 0.8), which corresponds to a maximum expansion-factor of $\sim$3 (from 10 to 31 ps). The pulse duration of the expanded chirped-pulse is, however, longer than the expanded pulse after NOLM2, as is shown in Fig. 6.44(b). For the chirped-pulse the maximum pulse-duration was 43 ps (54 ps times 0.8), which instead corresponds to a maximum expansion-factor of $\sim$4. The pulse-duration compression

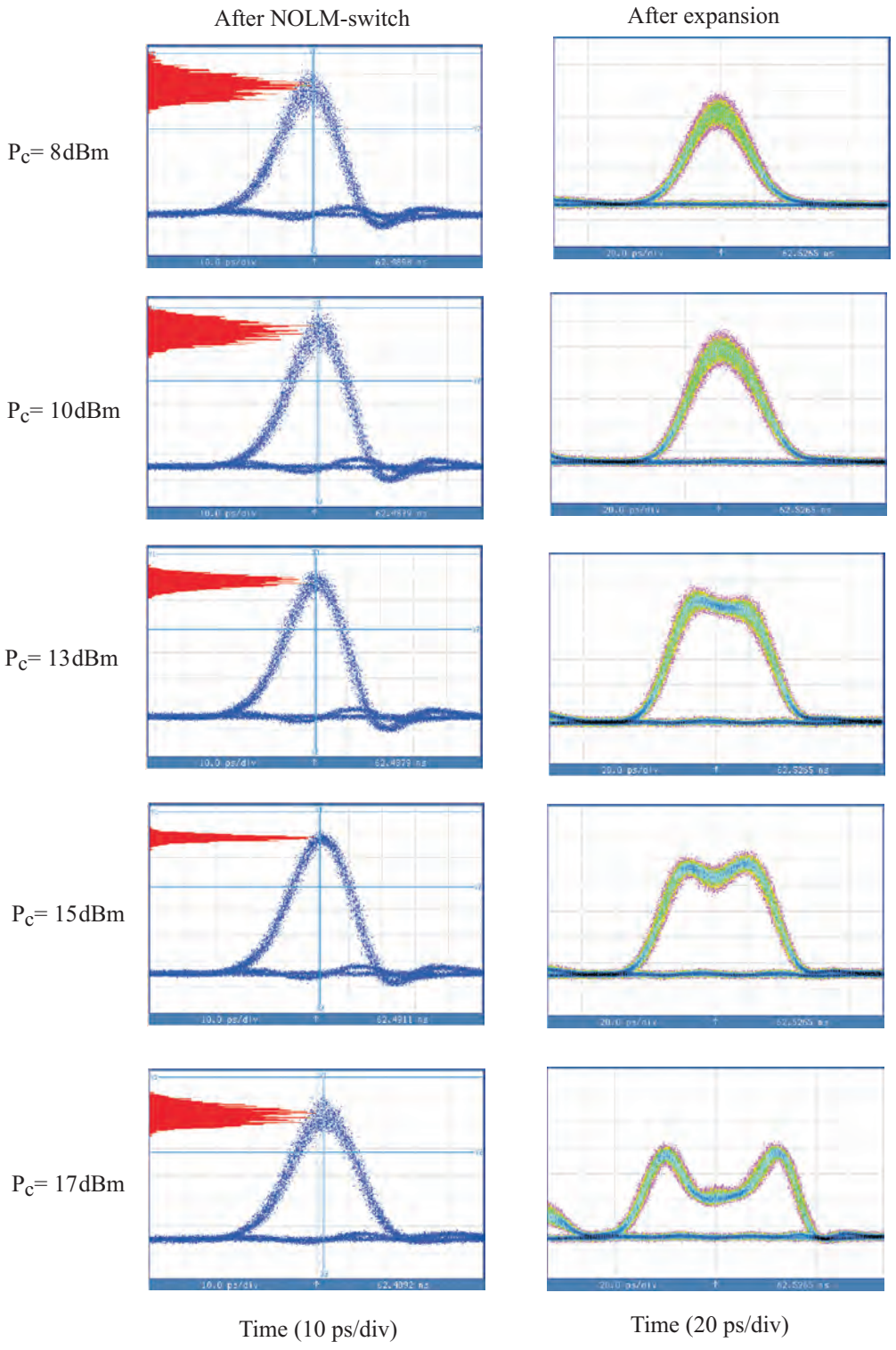

Figure 6.45: Oscilloscope traces of a chirped-pulse before (left column) and after (right column) expansion in the DCF2 for different average-power levels of the NOLM1 control-pulses.

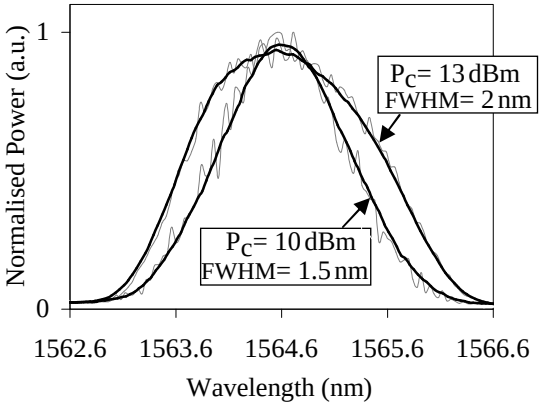

Figure 6.46: Optical spectra of carved chirped pulses for two different average-power levels of the NOLM1 control-pulses plotted in the linear scale.

in NOLM2 was because the induced switching-window was shorter than the duration of the control pulses, which generally happens in a NOLM when the pulse duration is significantly larger than the walk-off time. In this case the control-pulse duration was about 40 ps and the largest walk-off between control and signal in NOLM2 was about 10 ps, and therefore the switching-window broadening induced by the walk-off was negligible. The anomalous dispersion in the NOLM2 fibre eventually also induced some pulse compression.

Eye-diagrams of the unchirped expanded-packets are shown in Figs. 6.47(a) and (b). In Fig. 6.47(a) low persistence eye-diagrams are shown on a time scale-division of 50 ps/div. As can be seen the bit-rate of the expanded packets was 10 Gb/s. In Fig. 6.47(b) infinite persistence eye-diagrams are shown in a time-scale-division of 40 ps/div. Even though the zero-level extinction is high, the pulses show significant

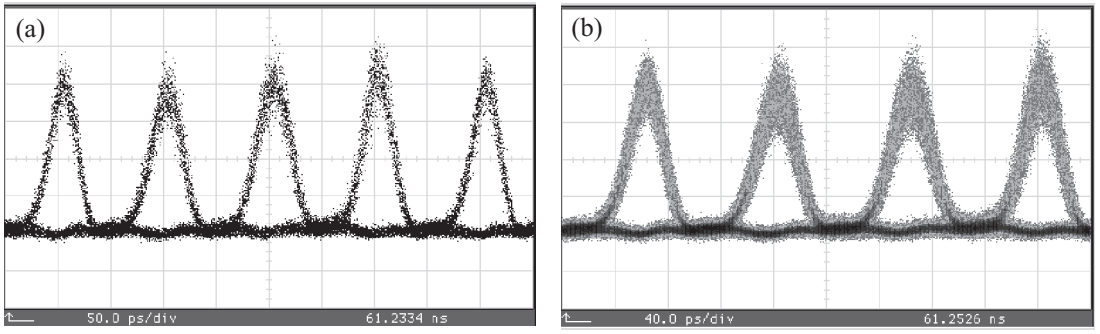

Figure 6.47: Eye diagrams of the outgoing 10-Gb/s 4-bit packets at 2.5 Gpacket/s measured on (a) a temporal scale of 50 ps/div and low persistence, (b) a temporal scale of 40 ps/div and infinite persistence.

amplitude noise degradation. Several factors may have contributed to this degradation, such as poor filtering and ASE-noise accumulation, which are evident in Fig. 6.43. More relevant, however, is that NOLM1 was operated well below its maximum switching-efficiency to prevent the expanded-pulse envelope evolving into a rectangular shape as shown in Fig. 6.45. The average power of the NOLM1 control-pulses was then about 16 dBm, which corresponds to 10 dBm per channel, and as it can be seen in Fig. 6.45, large amplitude noise is generated at this power level.

The pulse-width evolution during a 4-fold packet expansion has been numerically investigated and described in Section 6.2.2.2. Therein, Figs. 6.7(a) and (b) compared the expansion of positively and negatively chirped-packets, and in particular it is shown that negatively-chirped packets require a much smaller chirp-rate (the minimum chirp-rate is about $-0.04\,\mathrm{THz}^2$). Unfortunately, packet expansion with negatively chirped-pulses was not attempted in these experiments. The work presented in Section 6.2.2.2 was a subsequent numerical investigation of the results obtained in these experiments. It should thus be taken into account that some details given in this chapter were not completely understood at the time of these experiments.

Instead, Fig. 6.7(a) shows that for positively-chirped packets the minimum chirp-rate, which keeps the pulse duty-cycle under 30%, is $0.14\,\mathrm{THz}^2$, which is about the same chirp-rate as for the experimentally prepared linearly-chirped pulses. The acceptable input pulse duty-cycle is, however, around 20%, whilst in the experiment the input pulses were 10 ps, and therefore, at a bit-rate of 40 Gb/s the input duty-cycle was ∼40%. Consequently, as the pulse and packet expansion-factors were both around 4 (before NOLM2), the duty-cycle of the expanded pulses was also larger than 30%. With negatively chirped-pulses, according to Fig 6.7(b), it would have been possible to compress the duty-cycle from 40% to 30% during the 4-fold expansion with a chirp-rate of $-0.04\,\mathrm{THz}^2$.

6.4 Summary and Discussion

In this chapter, I examined the possibility of packet compression/expansion through the temporal lens-effect on linearly-chirped packets, presenting both numerical and experimental results. The packet compression/expansion scheme relies on the NOLM

switching of linearly-chirped pulses with the original packets, which produces linearly-chirped packets at the repetition-rate of the linearly-chirped pulses. The chirped packets can then be compressed/expanded in a dispersive fibre. A further NOLM switching stage gates a CW-signal with the chirped packets and, consequently, removes the chirp across the compressed/expanded packets.

One main aspect of this scheme to be taken into consideration is the evolution of the individual pulses during packet compression/expansion in the dispersive fibre. Pulse and packet compression/expansion factors were theoretically shown to be different and, consequently, a careful choice of the operational parameters has to be made to prevent the onset of adjacent pulse interference.

As for return-to-zero signals pulse interference increases largely for a pulse duty-cycle larger than 30%, the criteria to achieve an output pulse duty-cycle lower than 30% were introduced. The output duty-cycle as a function of the input duty-cycle and chirp-rate was numerically investigated. To facilitate the practical system implementation, the minimum chirp-rate required to achieve the above duty-cycle criteria was estimated.

The required chirp-rate defines the maximum packet length that can be either compressed or expanded. For instance, from Fig. 6.8, the minimum chirp-rate required for packet compression from 10 Gb/s to 1 Tb/s is about -0.3 nm/ps. A packet length of 1 ns would then require linearly-chirped pulses with a total bandwidth of about 300 nm. It is thus clear, due to practical limitations either in generating such linearly-chirped pulses or in performing NOLM switching over such wide bandwidth, that this technique can only operate with small packets. System implementation of this scheme would require additional grooming of the small packets into larger packets eventually requiring the use of a recirculating loop scheme.

Packet compression of 4-bit packets at 2.5 Gpacket/s from 10 to 40 Gb/s was experimentally demonstrated. The pulse durations before and after compression were measured from the corresponding autocorrelation traces and the results showed a good agreement with the theoretical predictions. The packet compressor performance was also measured in terms of bit-error rates for all 4-bit slots in the packet, with error-free performance achieved for all cases.

Packet expansion of 4-bit packets at 2.5 Gpacket/s from 40 to 10 Gb/s was also experimentally demonstrated. Again, the measured pulse duration after expansion showed a good agreement with the theoretical predictions. Significant pulse shape distortion induced due to the Fourier transformation of the temporal envelope of the NOLM switched chirped pulses was, however, observed. For instance, at the maximum switching efficiency, the pulse shape evolved into a rectangular shape during the packet expansion. To maintain the pulse shape, the NOLM switch was operated at a low bias-level, which produced a signal with large amplitude noise and, consequently, error-free performance could not be obtained.

Chapter 7

Conclusions and Future Directions

7.1 Conclusions

The multiplexing format conversion of a high-speed OTDM signal into a mixed TDM-WDM format allows for flexible optical-signal-processing by manipulating the signal in both the temporal and spectral domains. For example, network functions such as OTDM channel demultiplexing and add/drop multiplexing can, then, either be performed with ultrafast switches (conventional approach) or with passive optical filters, whose technology has been widely developed in the context of WDM networks. Also, in the mixed TDM-WDM format, the aggregate-rate of the original OTDM signal can be compressed/expanded on a packet basis in a dispersive element such as a chirped fibre-Bragg-grating or a dispersive fibre. Hence, the ability to convert between time multiplexed and wavelength multiplexed signals could allow for the construction of optical subsystems capable of relatively complex all-optical functions.

The optical-signal-processing schemes proposed in this thesis can be divided into three stages. The first stage is an OTDM-to-WDM converter, which shifts the carrier wavelength of each tributary channel onto a different wavelength without affecting the temporal multiplexing. The aim is to map the OTDM channels into the wavelength domain, providing a straight one-to-one relation between wavelength and time. The second stage can either be an optical filter, a dispersive fibre, or a combination of both, when processing the signal in the spectral domain. The third stage is a WDM-to-OTDM converter, which shifts the carrier wavelength of each tributary to the

same wavelength and, consequently, converts the processed signal back to its original OTDM format.

The OTDM-to-WDM conversion is based on the nonlinear switching of linearly-chirped pulses, whose linear chirp encompasses the full range of channel wavelengths that need to be generated, and whose pulse duration temporally overlaps each multiplexed OTDM channel. The linearly-chirped pulses are then fed into an all-optical switch, whereas the OTDM channels are used as control pulses to switch the linearly-chirped pulses in regions of temporal overlap. The WDM-to-OTDM conversion, instead, is based on the nonlinear switching of a CW-signal with the processed mixed TDM-WDM signal.

A major challenge in the practical implementation of this scheme is the generation of linearly-chirped pulses with a rectangular temporal envelope and a wide spectral bandwidth with flat spectral density. Although linearly-chirped pulses can readily be generated by propagating highly intense pulses in the normal dispersion regime of a highly nonlinear fibre, their temporal envelope can evolve into a largely oscillating profile after dispersive stretching due to the Fourier transformation effect, which occurs when highly linearly-chirped pulses are strongly dispersed. A pulse pre-shaping technique was proposed to assist the nonlinear evolution of the highly intense pulses into a linearly-chirped rectangular pulse with a wide rectangular spectral envelope. Generation of linearly-chirped rectangular pulses with a bandwidth of about 15 nm was demonstrated using this technique.

The investigation of NOLM switching of the linearly-chirped pulses revealed that a minimum NOLM-control pulse duration is required to ensure a one-to-one relation between the temporal and spectral waveforms after the switching. In particular, the chirp-rate parameter (C) of the linearly-chirped pulses and the NOLM-control pulse-width (τ_0) should satisfy the chirp-width product $|C|\tau_0^2 \geq 1.6$. For $|C|\tau_0^2 << 1$, intense multiple spectral-lobes were observed within the band of each tributary channel. In this case, any further signal-processing, involving pulse compression, results in severe pulse distortion. The physics of the spectral-lobe formation was identified and related to the interference between the spectral content in the gated pulse and the residual spectral-components in the non-gated linearly-chirped pulse.

Increasing the chirp-width product can, however, be challenging, since it implies the generation of linearly-chirped pulses with wider optical spectrum, and so, practical limitations should be taken into account. Operating the NOLM switch at a chirp-width product of between 0.8 and 1 was shown to be a reasonable approach. In this regime, a spectral side-lobe suppression larger than 20 dB, and an adjacent channel crosstalk-level lower than −20 dB were shown. For a chirp-width product of −1 the spectral bandwidth occupied by each channel was also shown to be a minimum.

Another means to overcome the need to generate very broad bandwidth linearly-chirped pulses is to increase the NOLM-control pulse duration, which increases quadratically the chirp-width product. Although, the pulse duration should be kept shorter than 1/3 of the bit-period to prevent a significant increase in intersymbol-interference between adjacent channels.

In this thesis early experimental work, all-optical demultiplexing of the four 10-Gb/s constituent channels of a 40-Gb/s OTDM signal was demonstrated using a fibre Kerr-switch to gate the linearly-chirped pulses. Error-free operation was achieved with a power penalty of ∼1.5 dB relative to the back-to-back. The noise degradation was attributed to the poor polarisation-extinction of the fibre Kerr-switch, while the various performance of the different demultiplexed channels was attributed to the use of a non-polarisation maintaining 10:40 Gb/s multiplexer.

Taking into consideration the above operational conditions, 40-Gb/s OTDM signal add/drop multiplexing was experimentally demonstrated. Time-division add/drop multiplexing with a suppression-ratio for the dropped channel of better than 30 dB, without affecting the quality of the remaining channels, was demonstrated using a highly reflective fibre-Bragg-grating filter. Error-free operation was achieved with a power penalty of 1 dB, where the noise degradation was mainly due to the two NOLM switching stages used for TDM-to-WDM and WDM-to-TDM conversion.

The most challenging aspects in the practical implementation of this scheme was the stable generation of linearly-chirped pulses with a flat spectral-density, and the use of filtering components which could accomodate the spectral bandwidth of the WDM channels, but which eventually did not efficiently filter out the control pulses after the first NOLM. When the residual energy of these pulses was transmitted into

the second-NOLM, significant noise degradation was produced through the nonlinear mixing between the residual pulses and the second-NOLM control pulses.

Packet compression/expansion through the temporal lens-effect of linearly-chirped packets was also investigated. The linearly-chirped packets are first produced via the NOLM switching of linearly-chirped pulses. These chirped packets can then be compressed/expanded in a dispersive fibre, and a further NOLM switch is used to gate a CW-signal with the chirped packets, which removes the chirp across the packets.

The evolution of the individual pulses during packet compression/expansion in the dispersive fibre was thoroughly investigated, and pulse and packet compression/ expansion factors were shown to be different. To avoid significant interference between adjacent pulses, the initial duty-cycle of the pulses in the packet should be increased to about 30%, and the minimum chirp-rate of the linearly-chirped pulses should be $0.0028F_c$ (THz^2) for packet compression, where F_c is the compression factor, and $-0.0026F_e^2$ (THz^2) for packet expansion, where F_e is the expansion factor. The total dispersion required for a $F_c(F_e)$-fold packet compression(expansion) is then given by Eq. (6.8).

Taking into account these conditions, 4-bit packet compression at 2.5 Gpacket/s from 10 to 40 Gb/s was experimentally demonstrated. The packet compressor performance was measured and error-free operation was achieved for all the four channels in the packet. Packet expansion of 4-bit packets at 2.5 Gpacket/s from 40 to 10 Gb/s was also experimentally demonstrated. In this case, significant pulse shape distortion was observed at the maximum NOLM switching efficiency, which is due to the Fourier transformation of the temporal envelope of the pulses in the chirped packet. To maintain the pulse shape, the NOLM switch was operated at a low bias-level, which produced a signal with large amplitude noise and, consequently, error-free performance could not be obtained.

7.2 Future Directions

The desirable progress of this thesis work would be the experimental demonstration of operation of the above schemes at higher bit-rates (e.g. 160 Gb/s). The main challenge is the generation of linearly-chirped rectangular pulses with higher

chirp-rates, which relates to the development of flat spectral-density supercontinuum sources. Recently, a few techniques based either on similariton generation in highly nonlinear-fibre amplifiers [139] or parabolic pulse seeding into a conventional highly-nonlinear fibre [140] have shown flat spectral-density over more than 20 nm. Other techniques that can eventually produce a wider flat spectrum is the shaping of a SPM-broadened spectrum with a dymanic-gain-equaliser, which however can only provide limited spectral shaping. The pre-shaping technique proposed in this thesis is another possibility, but wider spectrum generation requires further investigation.

The optical gating of the linearly-chirped pulses at the above speed (160 Gb/s) requires the use of an ultrafast switch. Still, the NOLM switch is likely to be the most suitable choice. However, to assure constant switching efficiency over the wide bandwidth of the linearly-chirped pulses, highly nonlinear fibres with reduced higher-order dispersion terms should be used [141]. A problem that has affected the NOLM switching performance in this thesis experiments is the cross-phase modulation between the counter-propagating signals in the NOLM. This is likely to become a major impairment at higher bit-rates, and a NOLM scheme that eliminates the contribution of the counter-propagation XPM should be considered [48]. Another possible solution for the ultrafast gating of linearly-chirped pulses is $LiNbO_3$ integrated devices [142]. The efficiency of cascaded quadratic nonlinear interactions in $LiNbO_3$, which can mimic all-optical $\chi^{(3)}$ phenomena [143], has dramatically increased due to advances in the waveguide design and fabrication processes, and switching operation over 100 Gb/s has already been demonstrated [144].

More complex time-division multiplexing schemes based on a lattice of optical filters and delay lines, such as time-slot interchange could be implemented using the scheme proposed in this thesis. In contrast to time division add/drop multiplexing, where a channel is first dropped and a new channel is subsequently added into the empty time-slot, time-slot interchange consists on swapping the time-slot of two or more channels, which may be an essential function in future network routers [145]. Future developments in planar waveguide technology could greatly facilitate the implementation of complex lattices of optical filters and delay lines [146], which would allow circuit integration of these schemes and, consequently, improve the operation stability.

Appendix A

Model of a NOLM with Finite Switching-Ratio

The switching-ratio of a NOLM is defined as the ratio between the intensity of the light in the on and off states, and is mainly limited by the imperfect splitting-ratio of the NOLM input-coupler. As the NOLM switch consists of a balanced Sagnac-interferometer, as shown in Fig. 2.2, the components in the common optical path in the loop impose the same loss on the clock-wise and anti-clock-wise beams. Unless a bad splice within the common path induces a larger scattering-loss in one of the directions, no additional degradation of the switching-ratio should occur.

To model the NOLM finite switching-ratio, typical measured values of the input coupler splitting-ratio should be taken into consideration. The input coupler can then be modelled as follows:

$$\begin{pmatrix} E_3 \\ E_4 \end{pmatrix} = \begin{pmatrix} \sqrt{\alpha_{13}} & i\sqrt{\alpha_{23}} \\ i\sqrt{\alpha_{14}} & \sqrt{\alpha_{24}} \end{pmatrix} \cdot \begin{pmatrix} E_1 \\ E_2 \end{pmatrix} \tag{A.1}$$

where α_{mn} is the light splitting-ratio when the coupling occurs between ports m and n. E_m is the electric field at the input of the port m, where $m = 1, 2$, and E_n is the electric field at the output of the port n, where $n = 3, 4$, in the case of a 4-port coupler.

The transfer function of the NOLM switch is then given by:

$$\begin{pmatrix} E_{2out} \\ E_{1out} \end{pmatrix} = \begin{pmatrix} \sqrt{\alpha_{24}} & i\sqrt{\alpha_{23}} \\ i\sqrt{\alpha_{14}} & \sqrt{\alpha_{13}} \end{pmatrix} \cdot \begin{pmatrix} \exp(i\phi) & 0 \\ 0 & 1 \end{pmatrix} \cdot \begin{pmatrix} \sqrt{\alpha_{13}} & i\sqrt{\alpha_{23}} \\ i\sqrt{\alpha_{14}} & \sqrt{\alpha_{24}} \end{pmatrix} \cdot \begin{pmatrix} E_{1in} \\ E_{2in} \end{pmatrix} \tag{A.2}$$

where ϕ is the amplitude of the cross-phase modulation induced by the NOLM control field.

The light-off state corresponds to $\phi = 0$, and assuming that the input signal is totally injected via port-1 ($E_{1in} = E_0$ and $E_{2in} = 0$), Eq. (A.2) is written as:

$$\begin{pmatrix} E_{2out} \\ E_{1out} \end{pmatrix} = \begin{pmatrix} \sqrt{\alpha_{24}\alpha_{13}} - \sqrt{\alpha_{23}\alpha_{14}} \\ 2i\sqrt{\alpha_{14}\alpha_{13}} \end{pmatrix} \cdot E_0 \tag{A.3}$$

In contrast, the light-on state corresponds to $\phi = \pi$ and, therefore, in this case Eq. (A.2) is written as:

$$\begin{pmatrix} E_{2out} \\ E_{1out} \end{pmatrix} = - \begin{pmatrix} \sqrt{\alpha_{24}\alpha_{13}} + \sqrt{\alpha_{23}\alpha_{14}} \\ 0 \end{pmatrix} \cdot E_0 \tag{A.4}$$

The NOLM switching-ratio can then be estimated by:

$$\epsilon = \left| \frac{E_{2out,ON}}{E_{2out,OFF}} \right|^2 = \left| \frac{\sqrt{\alpha_{24}\alpha_{13}} + \sqrt{\alpha_{23}\alpha_{14}}}{\sqrt{\alpha_{24}\alpha_{13}} - \sqrt{\alpha_{23}\alpha_{14}}} \right|^2 \tag{A.5}$$

Considering the following typical values for the splitting-ratio of the *Oplink* 3-dB couplers used in this thesis experimental work:

$\alpha_{13} = 3.2\,\text{dB}$, $\alpha_{14} = 2.9\,\text{dB}$, $\alpha_{23} = 2.8\,\text{dB}$, $\alpha_{24} = 3.1\,\text{dB}$,

the estimated NOLM switching-ratio is $\epsilon_{dB} \cong 29\,\text{dB}$, which is in good agreement with experimentally obtained values. Eq. (A.2) can therefore be used to model a NOLM with finite switching-ratio, and the cross-phase modulation term in the matrix can be replaced by the numerical solution of the nonlinear Schrödinger equation to take into account the complete set of nonlinear and dispersive effects in the fibre in the loop.

Appendix B

Spectral-Width of Linearly-Chirped Pulses

In this thesis, the bandwidth of a linearly-chirped pulse is repeatedly estimated by the product of chirp-rate and pulse-duration, which corresponds to the chirp amplitude within the pulse envelope. However, it can be wrong to estimate the spectral-width from the chirp amplitude when the pulse chirp is non-linear [147]. For example, the beating (field interference) of two sinusoidal waveforms produces a period waveform, whose spectrum consists of the two sinusoidal oscillation-frequencies. Its instantaneous-frequency, however, sweeps to much higher frequencies, and consequently, the beating chirp amplitude is much larger than the spectral-width. The explanation is that the high instantaneous-frequency appears under the beating envelope at instants of destructive-interference (zero beating-amplitude), and therefore, does not appear in the spectrum.

In this appendix it is shown that the spectral-width is generically given by two contributions: the derivative of the pulse amplitude-envelope, and the chirp times the pulse amplitude-envelope.

The spectral width of a generic signal can be better estimated by the second-moment of the frequency [147]:

$$\sigma_\omega^2 = \frac{1}{2\pi E} \int_{-\infty}^{+\infty} \omega^2 \left| \widetilde{F}(\omega) \right|^2 d\omega \tag{B.1}$$

where E is the total signal energy, ω is the angular frequency, and $\widetilde{F}(\omega)$ the spectrum complex-amplitude.

In Eq.(B.1) the module square of the spectrum can be expressed as the product of the spectrum complex-conjugates, and using the convolution theorem Eq.(B.1) can then be written as:

$$\sigma_\omega^2 = \frac{1}{2\pi E} \int_{-\infty}^{+\infty} \omega^2 \mathcal{F}\left[F(\tau) * \overline{F}(-\tau)\right] d\omega. \tag{B.2}$$

where $\mathcal{F}$ represents the Fourier transform, and the over-line means complex conjugate. In Eq.(B.2), it was taken that the Fourier transform of the complex-conjugate is the conjugated of the *reflected* Fourier-transform [148]: $\mathcal{F}\left[\overline{\widetilde{F}}(\omega)\right] = \overline{F}(-\tau)$.

Expressing the convolution and Fourier transform integrals, it follows that:

$$\sigma_\omega^2 = \frac{1}{2\pi E} \int_{-\infty}^{+\infty} \omega^2 \int_{-\infty}^{+\infty} \int_{-\infty}^{+\infty} F(\tau') \cdot \overline{F}(\tau' - \tau)\, d\tau' e^{i\omega\tau} d\tau d\omega, \tag{B.3}$$

which can be re-written in the following form:

$$\sigma_\omega^2 = -\frac{1}{E} \int_{-\infty}^{+\infty} \int_{-\infty}^{+\infty} F(\tau') \cdot \overline{F}(\tau' - \tau)\, d\tau' \cdot \underbrace{\frac{i^2}{2\pi} \int_{-\infty}^{+\infty} \omega^2 e^{-i\omega\tau} d\omega}_{\substack{\text{second derivative of the} \\ \text{delta function:} \\ \frac{d^2\delta(\tau)}{d\tau^2}}} d\tau \tag{B.4}$$

and therefore:

$$\sigma_\omega^2 = -\frac{1}{E} \int_{-\infty}^{+\infty} \int_{-\infty}^{+\infty} F(\tau')\, \overline{F}(\tau' - \tau)\, d\tau' \cdot \delta^{(2)}(\tau)\, d\tau. \tag{B.5}$$

Considering the following property of the delta function [148]:

$$\int_{-\infty}^{+\infty} f(x)\, \delta^{(n)}(x)\, dx = (-1)^n f^{(n)}(0) \tag{B.6}$$

Eq.(B.4) is simplified to:

$$\sigma_{\omega}^{2} = -\frac{1}{E}\int_{-\infty}^{+\infty} F(\tau')\left.\frac{d^{2}\overline{F}(\tau'-\tau)}{d\tau^{2}}\right|_{\tau=0} d\tau' = -\frac{1}{E}\int_{-\infty}^{+\infty} F(\tau')\frac{d^{2}\overline{F}(\tau')}{d\tau'^{2}}d\tau' \tag{B.7}$$

To obtain the relation between spectral-width and chirp, let us consider the pulse complex-amplitude envelope in terms of its amplitude and phase:

$$F(\tau) = A(\tau)\, e^{i\phi(\tau)} \tag{B.8}$$

The second derivative in Eq.(B.7) can then be expressed by:

$$\frac{d^{2}\overline{F}(\tau)}{d\tau^{2}} = \left(\frac{d^{2}A}{d\tau^{2}} - 2i\frac{dA}{d\tau}\frac{d\phi}{d\tau} - iA\frac{d^{2}\phi}{d\tau^{2}} - A\left(\frac{d\phi}{d\tau}\right)^{2}\right) e^{-i\phi(\tau)} \tag{B.9}$$

Substituting Eq.(B.9) in Eq.(B.7) it follows that:

$$\sigma_{\omega}^{2} = -\frac{1}{E}\int_{-\infty}^{+\infty}\left(A\frac{d^{2}A}{d\tau^{2}} - 2iA\frac{dA}{d\tau}\frac{d\phi}{d\tau} - iA^{2}\frac{d^{2}\phi}{d\tau^{2}} - A^{2}\left(\frac{d\phi}{d\tau}\right)^{2}\right)d\tau \tag{B.10}$$

Integrating the first term by parts , it results that:

$$\int_{-\infty}^{+\infty} A\frac{d^{2}A}{d\tau^{2}}d\tau = \underbrace{\cancel{A\frac{dA}{d\tau}\Big|_{-\infty}^{+\infty}}}_{\text{bounded function}} - \int_{-\infty}^{+\infty}\left(\frac{dA}{d\tau}\right)^{2}d\tau \tag{B.11}$$

Whilst considering the second and third terms, and integrating the second term by parts, it follows that:

$$\int_{-\infty}^{+\infty}\left(2iA\frac{dA}{d\tau}\frac{d\phi}{d\tau}+iA^2\frac{d^2\phi}{d\tau^2}\right)d\tau=\int_{-\infty}^{+\infty}\left(i\frac{dA^2}{d\tau}\frac{d\phi}{d\tau}+iA^2\frac{d^2\phi}{d\tau^2}\right)d\tau$$
$$=\underbrace{iA^2\frac{d\phi}{d\tau}\Big|_{-\infty}^{+\infty}}_{\text{bounded function}}-\cancel{\int_{-\infty}^{+\infty}iA^2\frac{d^2\phi}{d\tau^2}d\tau}+\cancel{\int_{-\infty}^{+\infty}iA^2\frac{d^2\phi}{d\tau^2}d\tau} \tag{B.12}$$

Consequently, Eq.(B.10) is simplified to:

$$\sigma_\omega^2=\frac{1}{E}\underbrace{\int_{-\infty}^{+\infty}\left(\frac{dA}{d\tau}\right)^2d\tau}_{\text{amplitude derivative}}+\frac{1}{E}\underbrace{\int_{-\infty}^{+\infty}A^2\left(\frac{d\phi}{d\tau}\right)^2d\tau}_{\text{phase derivative}} \tag{B.13}$$

It can then be confirmed that there are two contributions to the spectral-width, one from the derivative of the amplitude envelope, and the other from the chirp of the instantaneous-frequency.

Using Eq.(B.13), the spectral-width of a linearly-chirped Gaussian pulse, whose amplitude and phase are given by:

$$A(\tau)=\sqrt{P_0}\exp\left(-\frac{\tau^2}{2\tau_0^2}\right)\quad\text{and}\quad\phi(\tau)=-C\tau^2\quad\text{respectively,}$$

is next derived.

The energy (E) of a Gaussian-pulse expressed in this form is $\sqrt{\pi}P_0\tau_0$. Substituting this in Eq.(B.13), calculating the first derivative of the amplitude and phase, and solving the integrals, it follows that:

$$\sigma_\omega^2=\frac{1}{2\tau_0^2}+2C^2\tau_0^2 \tag{B.14}$$

Eq.(B.14) corresponds to the variance of the Gaussian-pulse spectrum, i.e. the half-width at ∼0.6 of the maximum spectral-intensity. More commonly, for it is of easier experimental measurement, the full-width at half-maximum (3-dB bandwidth) is used, which relates to the variance as it follows:

$$\Delta\omega_{\mathrm{FWHM}} = \sqrt{8\ln(2)} \cdot \sigma_{\omega} = \sqrt{\frac{4\ln(2)}{\tau_0^2} + 16\ln(2)C^2\tau_0^2} \tag{B.15}$$

τ_0 is the half pulse-duration at $1/e$ of the peak intensity, and it relates to the pulse duration at half-maximum according to [34]:

$$\tau_{\mathrm{FWHM}} = 2\sqrt{\ln(2)}\tau_0 \tag{B.16}$$

Substituting Eq.(B.16) in Eq.(B.15) it follows that:

$$\Delta\omega_{\mathrm{FWHM}} = \sqrt{\left[\frac{4\ln(2)}{\tau_{\mathrm{FWHM}}}\right]^2 + 4C^2\tau_{\mathrm{FWHM}}^2} \tag{B.17}$$

Eq.(B.17) was verified for the case of a transform-limited Gaussian pulse ($C = 0$), by extracting from the equation the duration-bandwidth product, which yields:

$$\Delta\nu_{\mathrm{FWHM}} \cdot \tau_{\mathrm{FWHM}} = \frac{4\ln(2)}{2\pi} \approx 0.44 \tag{B.18}$$

In contrast, for a highly-chirped Gaussian pulse the second term in the square-root dominates, and therefore, Eq.(B.17) can be approximately written as:

$$\Delta\omega_{\mathrm{FWHM}} \approx 2C\tau_{\mathrm{FWHM}}, \tag{B.19}$$

which confirms that the 3-dB bandwidth is approximately given by the chirp-rate times the pulse duration.

Appendix C

Complex Spectrum of a Linearly-Chirped Pulse

In this appendix, the derivation of the Fourier transform of a linearly-chirped super-Gaussian pulse given by Eq. (4.2) is presented. In the most general case, the spectrum of this pulse cannot be described in a closed mathematical form. However, when the pulse is highly chirped, so that one can safely assume that the phase is rapidly varying across the pulse envelope, an approximate solution can be found using the method of stationary phase.

Expressing the linearly-chirped pulse in the following general form:

$$E_{\mathrm{cp}}(\tau) = |E_{\mathrm{cp}}(\tau)| \exp\left(-iC\tau^2\right), \tag{C.1}$$

the corresponding Fourier transform can be written as:

$$\widetilde{E}_{\mathrm{cp}}(\omega) = \int_{-\infty}^{\infty} E_{\mathrm{cp}}(\tau) \cdot \exp(i\omega\tau)\, d\tau = \int_{-\infty}^{\infty} |E_{\mathrm{cp}}(\tau)| \exp\left(-iC\tau^2 + i\omega\tau\right) d\tau \tag{C.2}$$

Substituting the variable τ by $T\tau_{\mathrm{cp}}$, Eq. (C.2) can be written as:

$$\widetilde{E}_{\mathrm{cp}}(\omega) = \tau_{\mathrm{cp}} \int_{-\infty}^{\infty} |E_{\mathrm{cp}}(T\tau_{\mathrm{cp}})| \exp\left(-iC\tau_{\mathrm{cp}}^2 T^2 + i\omega\tau_{\mathrm{cp}} T\right) dT \tag{C.3}$$

In Eq. (C.3) the phase goes to infinity in the asymptotic limit $|C|\tau_{\mathrm{cp}}^2 \to \infty$. Consequently, the integrand oscillates rapidly and cancels over most of the range. Cancellation, however, does not occur in the neighborhood of a stationary point (T_{sp}), at which:

$$\left(\frac{\partial\varphi\left(T,\omega,C\right)}{\partial T}\right)_{T=T_{\mathrm{sp}}} = 0 \quad \text{or} \quad T_{\mathrm{sp}} = \frac{\omega}{2C\tau_{\mathrm{cp}}} \tag{C.4}$$

Therefore, by using the method of stationary phase [149], Eq. (C.3) can be approximated by:

$$\widetilde{E}_{\mathrm{cp}}\left(\omega\right) \simeq \tau_{\mathrm{cp}}\left|E_{\mathrm{cp}}\left(T_{\mathrm{sp}}\tau_{\mathrm{cp}}\right)\right| \cdot \int_{-\infty}^{\infty} \exp\left(-iC\tau_{\mathrm{cp}}^2 T_{\mathrm{sp}}^2 + i\omega\tau_{\mathrm{cp}}T_{\mathrm{sp}} - iC\tau_{\mathrm{cp}}^2\left(T-T_{\mathrm{sp}}\right)^2\right) dT \tag{C.5}$$

Calculating Eq. (C.5) at the stationary point given in (C.4) yields:

$$\widetilde{E}_{\mathrm{cp}}\left(\omega\right) \simeq \tau_{\mathrm{cp}}\left|E_{\mathrm{cp}}\left(\frac{\omega}{2C}\right)\right| \cdot \exp\left(i\frac{\omega^2}{4C}\right) \int_{-\infty}^{\infty} \exp\left(-iC\tau_{\mathrm{cp}}^2\left(T-T_{\mathrm{sp}}\right)^2\right) dT \tag{C.6}$$

The integral in Eq. (C.6) is explicitly evaluable, and therefore the complex spectrum of a highly linearly-chirped pulse is then given by:

$$\widetilde{E}_{\mathrm{cp}}\left(\omega\right) \simeq \sqrt{\frac{\pi}{|C|}}\left|E_{\mathrm{cp}}\left(\frac{\omega}{2C}\right)\right| \exp\left(i\left(\frac{\omega^2}{4C} - \mathrm{sgn}(C)\frac{\pi}{4}\right)\right) \tag{C.7}$$

Substituting Eq. (4.2) in Eq. (C.7), the complex spectrum of a highly linearly-chirped super-Gaussian pulse can be obtained, and is given by:

$$\widetilde{E}_{\mathrm{cp}}\left(\omega\right) \simeq \sqrt{\frac{\pi P_{\mathrm{cp}}}{|C|}} \exp\left(-\frac{\ln 2}{2}\left(\frac{\omega}{C\tau_{\mathrm{cp}}}\right)^8\right) \exp\left(i\left(\frac{\omega^2}{4C} - \mathrm{sgn}(C)\frac{\pi}{4}\right)\right), \tag{C.8}$$

which proves Eq. (4.3).

Appendix D

Fourier transformation of Linearly-Chirped Pulses

A second-order dispersive medium can be modeled by the following transfer function [150]:

$$H(\omega) = \exp\left[i\frac{\beta_2 L}{2}\omega^2\right] \tag{D.1}$$

where L is the length of the dispersive medium, and β_2 the dispersion coefficient.

The inverse Fourier transform of Eq. (D.1) holds the impulse response of the dispersive medium, and is given by:

$$h(t) \propto \exp\left[\frac{i}{2\beta_2 L}t^2\right] \tag{D.2}$$

The propagation of a pulse through the dispersive medium can then be calculated as the convolution of an input pulse $x(t)$ and the medium impulse response $h(t)$, which, using the convolution integral, is given by:

$$y(t) = x(t) * h(t) \propto \int_{-\infty}^{+\infty} x(\tau)\exp\left[\frac{i}{2\beta_2 L}(t-\tau)^2\right]d\tau \tag{D.3}$$

Expanding the phase term in the integral, Eq. (D.3) can be re-written as:

$$y(t) \propto \exp\left[\frac{i}{2\beta_2 L}t^2\right] \int_{-\infty}^{+\infty} x(\tau) \exp\left[\frac{i}{2\beta_2 L}\tau^2\right] \exp\left[-\frac{i}{\beta_2 L}t\tau\right] d\tau \tag{D.4}$$

Assuming that the initial pulse is a linearly-chirped pulse, $x(t)$ can be expressed by:

$$x(t) = |x(t)| \cdot \exp\left[iCt^2\right] \tag{D.5}$$

where C is the linear-chirp coefficient. The phase term $\omega_0 t$, where ω_0 is the optical-carrier angular frequency, has been omitted for simplicity. This only implies that the angular frequency ω below is the offset angular frequency from ω_0.

Substituting Eq. (D.5) in Eq. (D.4), it follows that:

$$y(t) \propto \exp\left[\frac{i}{2\beta_2 L}t^2\right] \int_{-\infty}^{+\infty} |x(\tau)| \exp\left[iC\tau^2 + \frac{i}{2\beta_2 L}\tau^2\right] \exp\left[-\frac{i}{\beta_2 L}t\tau\right] d\tau \tag{D.6}$$

The quadratic phase term $\tau^2/2\beta_2 L$ in Eq. (D.6) can be neglected when $C \gg 1/2\beta_2 L$, since the quadratic phase of the linearly-chirped pulse in Eq.(D.5) is, consequently, much larger than this term. Eq. (D.6) can then be approximated by:

$$y(t) \propto \exp\left[\frac{i}{2\beta_2 L}t^2\right] \int_{-\infty}^{+\infty} x(\tau) \exp\left[-\frac{i}{\beta_2 L}t\tau\right] d\tau \tag{D.7}$$

Using the variable substitution $\omega = t/\beta_2 L$ in the integral, Eq. (D.7) can be re-written as:

$$y(t) \propto \exp\left[\frac{i}{2\beta_2 L}t^2\right] \int_{-\infty}^{+\infty} x(\tau) \exp\left[-i\omega\tau\right] d\tau = \exp\left[\frac{i}{2\beta_2 L}t^2\right] X\left(\frac{t}{\beta_2 L}\right) \tag{D.8}$$

where $X(\omega)$ is the Fourier transform of $x(t)$.

The intensity of the propagated pulse is then given by:

$$|y(t)|^2 \propto |X(\omega)|^2, \tag{D.9}$$

which is proportional to the input pulse spectrum.

The condition for the Fourier transformation of a linearly-chirped pulse is, as shown above, given by:

$$\beta_2 L \gg \frac{1}{2C} \tag{D.10}$$

Taking into consideration that for a highly linearly-chirped pulse the pulse duration (ΔT) and bandwidth ($\Delta\omega$) relate to the linear-chirp coefficient (C) according to Eq. (B.19) in Appendix B, the Fourier transformation condition can be re-written as:

$$\beta_2 L \gg \frac{\Delta T}{\Delta\omega} \tag{D.11}$$

Bibliography

[1] T. Okuno, M. Onishi, T. Kashiwada, S. Ishikawa, and M. Nishimura, "Silica-based functional fibers with enhanced nonlinearity and their applications," *IEEE Journal on Selected Topics in Quantum Electronics*, vol. 5, no. 5, pp. 1385 – 1391, 1999.

[2] N. J. Doran and D. Wood, "Nonlinear-optical loop mirror," *Optics Letters*, vol. 13, no. 1, pp. 56–58, 1988.

[3] M. Mokhtar, C. Goh, S. Butler, S. Set, K. Kikuchi, D. Richardson, and M. Ibsen, "Fibre Bragg gratings compression-tuned over 110nm," *Electronics Letters*, vol. 39, no. 6, pp. 509–511, 2003.

[4] K. Uchiyama, H. Takara, T. Morioka, S. Kawanishi, and M. Saruwatari, "100 Gbit/s multiple-channel output all-optical demultiplexing based on TDM-WDM conversion in a nonlinear optical loop mirror," *Electronics Letters*, vol. 32, no. 21, pp. 1989–1991, 1996.

[5] A. Hasegawa, H. Toda, M. Shikata, Y. Ozeki, T. Suzaki, Y. Ueno, and K. Tajima, "Experimental demonstration of the compressed optical packet multiplexing scheme," *Journal of Optical Networking*, vol. 11, no. 7, pp. 221–235, 2002.

[6] P. Toliver, K. Deng, I. Glesk, and P. Prucnal, "Simultaneous optical compression and decompression of 100-Gb/s OTDM packets using a single bidirectional optical delay line lattice," *IEEE Photonics Technology Letters*, vol. 11, no. 9, pp. 1183–1185, 1999.

[7] P. Vetter, D. Goderis, L. Verpooten, and A. Granger, "Systems aspects of APON/VDSL deployment," *IEEE Communications Magazine*, vol. 38, no. 5, pp. 66–72, May 2000.

[8] V. W. S. Chan, K. L. Hall, E. Modiano, and K. A. Rauschenbach, "Architectures and technologies for high-speed optical data networks," *Journal of Lightwave Technology*, vol. 16, no. 12, pp. 2146–2168, 1998.

[9] D. J. Blumenthal, "Routing packets with light," *Scientific American*, vol. 284, pp. 96–99, 2001.

[10] A. Takada and J. H. Park, "Architecture of ultrafast optical packet switching ring network," *Journal of Lightwave Technology*, vol. 20, no. 12, pp. 2306–2315, 2002.

[11] H. Ishikawa, T. Simoyama, H. Yoshida, S. Sekiguchi, V. Achanta, J. Kasai, and T. Mozume, "Intersubband transition all optical switches for 160Gb-1Tb/s OTDM systems," in *OSA Trends in Optics and Photonics Series*, vol. 95 A, 2004, pp. 631–633.

[12] M. Nakazawa, "Tb/s OTDM Technology," in *Proc. European Conference on Optical Communication (ECOC)*, vol. 2, 2001, pp. 184–187.

[13] J. Holonyak, N. and M. Feng, "The transistor laser," *IEEE Spectrum*, vol. 43, no. 2, pp. 50–55, Feb. 2006.

[14] S. Watanabe, S. Takeda, K. Hironishi, F. Futami, and T. Chikama, "All-optical 3R regeneration of WDM signals using WDM-OTDM-WDM conversions in two-stage nonlinear fiber loop interferometers," in *Proc. European Conference on Optical Communication (ECOC)*, vol. 3, 2000, pp. 297–9.

[15] M. A. Summerfield, J. Lacey, A. J. Lowery, and R. S. Tucker, "All-optical TDM to WDM conversion in a semiconductor optical amplifier," *Electronics Letters*, vol. 30, no. 3, pp. 255–256, 1994.

[16] C. Joergensen *et al.*, "All-optical 40 Gbit/s OTDM to 2×20 Gbit/s WDM signal-format translation," *Electronics Letters*, vol. 32, no. 15, pp. 1384–1386, 1996.

[17] D. Norte and A. E. Willner, "All-optical data format conversions and reconversions between the wavelength and time domains for dynamically reconfigurable WDM networks," *Journal of Lightwave Technology*, vol. 14, no. 6, pp. 1170–1182, 1996.

[18] B. Li, K. Guan, and P. Ye, "Multi-wavelength clock operation of NOLM for OTDM-WDM conversion," in *Proceedings of 2nd Optoelectronics and Communications Conference OECC '97, 8-11 July 1997*, 1997, pp. 542–3.

[19] H. Sotobayashi, W. Chujo, and K. Kitayama, "Photonic gateway: TDM-to-WDM-to-TDM conversion and reconversion at 40 Gbit/s (4 channels × 10 Gbit/s)," *Journal of the Optical Society of America B*, vol. 19, pp. 2810–2816, 2002.

[20] K. Uchiyama, H. Takara, K. Mori, and T. Morioka, "160 Gbit/s all-optical time-division demultiplexing utilising modified multiple-output OTDM demultiplexer(MOXIC)," *Electronics Letters*, vol. 38, no. 20, pp. 1190–1191, 2002.

[21] H. Sotobayashi, W. Chujo, and T. Ozeki, "80 Gbit/s simultaneous photonic demultiplexing based on OTDM-to-WDM conversion by four-wave mixing with supercontinuum light source," *Electronics Letters*, vol. 37, no. 10, pp. 640–642, 2001.

[22] P. L. Kelley, "The nonlinear index of refraction and self-action effects in optical propagation," *IEEE Journal of Selected Topics in Quantum Electronics*, vol. 6, pp. 1259–1264, 2000.

[23] A. Melloni, M. Martinelli, and A. Fellegara, "Frequency characterization of the nonlinear refractive index in optical fiber," *Fiber and Integrated Optics*, vol. 18, pp. 1–13, 1999.

[24] M. Asobe, "Nonlinear optical properties of chalcogenide glass fibers and their application to all-optical switching," *Optical Fiber Technology*, vol. 3, pp. 142–148, 1997.

[25] K. Kikuchi, "All-optical signal processing using fiber nonlinearity," in *Proc. IEEE/LEOS Annual Meeting Conference*, vol. 2, 2002, pp. 428 – 9.

[26] J. Leong, P. Petropoulos, S. Asimakis, H. Ebendorff-Heidepriem, R. Moore, K. Frampton, V. Finazzi, X. Feng, J. Price, T. Monro, and D. Richardson, "A lead silicate holey with γ=1860 $W^{-1}km^{-1}$ at 1550 nm," in *Proc. Optical Fiber Communications Conference (OFC)*, 2005, paper PDP22.

[27] A. Fitt, K. Furusawa, T. Monro, C. Please, and D. Richardson, "The mathematical modelling of capillary drawing for holey fibre manufacture," *Journal of Engineering Mathematics*, vol. 43, no. 2, pp. 201–227, 2002.

[28] F. Poletti, V. Finazzi, T. Monro, N. Broderick, V. Tse, and D. Richardson, "Inverse design and fabrication tolerances of ultra-flattened dispersion holey fibers," *Optics Express*, vol. 13, pp. 3728–3736, 2005.

[29] J. H. Lee, "All-optical signal processing devices based on holey fiber," *IEICE Transactions on Electronics*, vol. E88-C, no. 3, pp. 327–334, 2005.

[30] M. J. Holmes, D. L. Williams, and R. J. Manning, "Highly-nonlinear optical fibers for all optical processing applications," *IEEE Photonics Technology Letters*, vol. 7, no. 9, pp. 1045–1047, 1995.

[31] T. Okuno, M. Hirano, T. Nakanishi, and M. Onishi, "Highly-nonlinear optical fibers and their applications," *SEI Technical Review*, no. 62, pp. 34–40, 2006.

[32] T. Kato, Y. Suetsugu, and M. Nishimura, "Estimation of nonlinear refractive index in various silica-based glasses for optical fibers," *Optics Letters*, vol. 20, no. 22, pp. 2279–2281, 1995.

[33] A. Boskovic, S. V. Chernikov, J. R. Taylor, L. Gruner-Nielsen, and O. A. Levring, "Direct continuous-wave measurement of n_2 in various types of telecommunication fiber at 1.55 μm," *Optics Letters*, vol. 21, no. 24, pp. 1966–1968, 1996.

[34] G. P. Agrawal, *Nonlinear Fiber Optics, Third edition.* Academic Press, 2001.

[35] E. M. Dianov and V. M. Mashinsky, "Germania-based core optical fibers," *Journal of Lightwave Technology*, vol. 23, no. 11, pp. 3500–3508, 2005.

[36] B. Ainslie and C. Day, "A review of single-mode fibers with modified dispersion characteristics," *Journal of Lightwave Technology*, vol. 4, no. 8, pp. 967–979, 1986.

[37] M. Takahashi, R. Sugizak, J. Hiroishi, M. Tadakuma, Y. Taniguchi, and T. Yagi, "Low-loss and low-dispersion-slope highly nonlinear fibers," *Journal of Lightwave Technology*, vol. 23, no. 11, pp. 3615–3624, 2005.

[38] K. Kikuchi, "Ultra-high speed optical signal processing through third-order fiber nonlinearity," *Proceedings of SPIE*, vol. 5725, pp. 220–234, 2005.

[39] M. Saruwatari, "All-optical signal processing for terabit/second optical transmission," *IEEE Journal of Selected Topics in Quantum Electronics*, vol. 6, no. 6, pp. 1363–1374, 2000.

[40] L. Oxenlowe, K. Berg, A. Clausen, J. Seoane, A. Siahlo, P. Jeppesen, M. Schmidt, M. Schilling, and Q. Le, "Specialty fibers for 160, 320 and 640 Gb/s signal processing," in *Proc. Conference on Lasers and Electro-Optics (CLEO)*, vol. 2, 2004.

[41] S. Watanabe, R. Okabe, F. Futami, R. Hainberger, C. Schmidt-Langhorst, C. Schubert, and H. Weber, "Novel fiber Kerr-switch with parametric gain: Demonstration of optical demultiplexing and sampling up to 640 Gb/s," in *Proc. European Conference on Optical Communication (ECOC)*, 2004, paper Th4.1.6 (Postdeadline paper), pp. 12–13.

[42] J. Li, B.-E. Olsson, M. Karlsson, and P. A. Andrekson, "OTDM demultiplexer based on XPM-induced wavelength shifting in highly nonlinear fiber," *IEEE Photonics Technology Letters*, vol. 15, no. 12, pp. 1770–1772, 2003.

[43] T. Morioka, H. Takara, S. Kawanishi, T. Kitoh, and M. Saruwatari, "Error-free 500 Gbit/s all-optical demultiplexing using low-noise, low-jitter supercontinuum short pulses," *Electronics Letters*, vol. 32, no. 9, pp. 833–834, 1996.

[44] K. Otsuka, "Nonlinear antiresonant ring interferometer," *Optics Letters*, vol. 8, no. 9, pp. 471–473, 1983.

[45] Z. Wang, C. Lin, K.-K. Chow, Y.-C. Ku, and A. Bjarklev, "Wavelength-tunable dispersion-imbalanced loop mirror based on dispersion-flattened high-nonlinearity photonic crystal fiber and its application in suppression of the incoherent interferometric crosstalk," *IEEE Photonics Technology Letters*, vol. 17, no. 9, pp. 1911–1913, Sept. 2005.

[46] K. Blow, N. Doran, and B. Nelson, "Demonstration of the nonlinear fibre loop mirror as an ultrafast all-optical demultiplexer," *Electronics Letters*, vol. 26, pp. 962–964, 1990.

[47] H. Shi and J. Lin, "Theoretical analysis on polarization deviation and switch window optimization in nonlinear optical loop mirror demultiplexer," *Journal of Lightwave Technology*, vol. 17, no. 12, pp. 2572–2576, 1999.

[48] T. Sakamoto and K. Kikuchi, "Nonlinear optical loop mirror with an optical bias controller for achieving full-swing operation of gate switching," *IEEE Photonics Technology Letters*, vol. 16, no. 2, pp. 545–547, 2004.

[49] T. Morioka, M. Saruwatari, and K. Nakagawa, "All-optical Kerr switching techniques and applications," in *Proc. IEEE Global Telecommunications Conference*, 1990, pp. 1311–17.

[50] T. Morioka and M. Saruwatari, "Ultrafast all-optical switching utilizing the optical Kerr effect in polarization-maintaining single-mode fibers," *IEEE Journal on Selected Areas in Communications*, vol. 6, no. 7, pp. 1186–1198, Aug. 1988.

[51] G. Muslu and H. Erbay, "Higher-order split-step Fourier schemes for the generalized nonlinear Schrödinger equation," *Mathematics and Computers in Simulation*, vol. 67, no. 6, pp. 581–595, 2005.

[52] J. A. C. Weideman and B. M. Herbst, "Split-step methods for the solution of the nonlinear Schrödinger equation," *SIAM Journal of Numerical Analysis*, vol. 23, no. 3, pp. 485–507, 1986.

[53] G. Strang, "On the construction and comparison of difference schemes," *SIAM Journal of Numerical Analysis*, vol. 5, no. 3, pp. 506–517, 1968.

[54] O. V. Sinkin, R. Holzlner, J. Zweck, and C. R. Menyuk, "Optimization of the split-step Fourier method in modeling optical fiber communication systems," *Journal of Lightwave Technology*, vol. 21, no. 1, pp. 61–68, 2003.

[55] C. Francia, "Constant step-size analysis in numerical simulation for correct four-wave-mixing power evaluation in optical fiber transmission systems," *IEEE Photonics Technology Letters*, vol. 11, no. 1, pp. 69–71, 1999.

[56] G. Bosco, A. Carena, V. Curri, R. Gaudino, P. Poggiolini, and S. Benedetto, "Suppression of spurious tones induced by the split-step method in fiber

systems simulation," *IEEE Photonics Technology Letters*, vol. 12, no. 5, pp. 489–491, 2000.

[57] K. O. Hill and G. Meltz, "Fiber Bragg grating technology fundamentals and overview," *Journal of Lightwave Technology*, vol. 15, pp. 1263–1276, 1997.

[58] A. D. Kersey, M. A. Davis, H. J. Patrick, M. LeBlanc, K. P. Koo, C. G. Askins, M. A. Putnam, and E. J. Friebele, "Fiber grating sensors," *Journal of Lightwave Technology*, vol. 15, no. 8, pp. 1442–1463, 1997.

[59] P. J. Lemaire, R. M. Atkins, V. Mizrahi, and W. A. Reed, "High pressure H, loading as a technique for achieving ultra-high UV photosensitivity and thermal sensitivity in GeO, doped optical fibres," *Electronics Letters*, vol. 29, no. 13, pp. 1191–1193, 1993.

[60] A. Othonos, "Fiber Bragg gratings," *Review of scientific instruments*, vol. 68, no. 12, pp. 4309–4341, 1997.

[61] P. St. J. Russell, J. L. Archambault, and L. Reekie, "Fibre gratings," *Physics World*, pp. 41–46, October 1993.

[62] D. Hand and P. St. J. Russell, "Photoinduced refractive-index changes in germanosilicate fibers," *Optics Letters*, vol. 15, no. 2, pp. 102–104, 1990.

[63] T. Erdogan, "Fiber grating spectra," *Journal of Lightwave Technology*, vol. 15, no. 8, pp. 1277–1294, Aug. 1997.

[64] M. Ibsen, R. Feced, P. C. Teh, J. H. Lee, M. R. Mokhtar, P. Petropoulos, M. N. Zervas, D. J. Richardson, and D. N. Payne, "Advanced fibre Bragg gratings and where they are going," in *Australian Conference on Optical Fibre Technology*, 8-11 July 2002, invited.

[65] B. Malo, S. Theriault, D. Johnson, F. Bilodeau, J. Albert, and K. Hill, "Apodized in-fibre Bragg grating reflectors photoimprinted using a phase mask," *Electronics Letters*, vol. 31, no. 3, pp. 223–225, 1995.

[66] R. Feced, M. Durkin, M. Ibsen, and M. Zervas, "An efficient inverse scattering algorithm for the design of nonuniform fiber Bragg gratings," *IEEE Journal of Quantum Electronics*, vol. 35, no. 8, pp. 1105–1111, 1999.

[67] M. Ibsen, R. Feced, P. Petropoulos, and M. Zervas, "99.9% reflectivity dispersion-less square-filter fibre Bragg gratings for high speed DWDM networks," in *Proc. Optical Fiber Communications Conference (OFC)*, 2000, paper PD21.

[68] T. Inui, T. Komukai, and M. Nakazawa, "Highly efficient tunable fiber Bragg grating filters using multilayer piezoelectric transducers," *Optics Communications*, vol. 190, pp. 1–4, April 2001.

[69] D. Starodubov, V. Grubsky, and J. Feinberg, "Ultrastrong fiber gratings and their applications," *Proceedings of SPIE*, vol. 3848, pp. 178–185, 1999.

[70] P. Petropoulos, M. Ibsen, A. Ellis, and D. Richardson, "Rectangular pulse generation based on pulse reshaping using a superstructured fiber Bragg grating," *Journal of Lightwave Technology*, vol. 19, no. 5, pp. 746–752, May 2001.

[71] J. H. Lee, P. C. Teh, P. Petropoulos, M. Ibsen, and D. J. Richardson, "Timing jitter tolerant all-optical modulator and demultiplexing systems incorporating pulse-shaping fiber Bragg gratings," in *Proc. Optical Fiber Communications Conference (OFC)*, 2001, paper PD30.

[72] A. M. Weiner, "Femtosecond pulse shaping using spatial light modulators," *Review of Scientific Instruments*, vol. 71, no. 5, pp. 1929–1960, 2000.

[73] K. Winick and J. Roman, "Design of corrugated waveguide filters by Fourier transform techniques," *IEEE Journal of Quantum Electronics*, vol. 26, no. 11, pp. 1918–1929, 1990.

[74] F. Ghiringhelli, "Fundamental properties of Bragg gratings and their application to the design of advanced structures," Ph.D. dissertation, University of Southampton, 2003.

[75] J. Skaar and K. Risvik, "A genetic algorithm for the inverse problem in synthesis of fiber gratings," *Journal of Lightwave Technology*, vol. 16, no. 10, pp. 1928–1932, Oct. 1998.

[76] P. Hill and B. Eggleton, "Strain gradient chirp of fibre Bragg gratings," *Electronics Letters*, vol. 30, no. 14, pp. 1172–1174, 1994.

[77] T. Imai, T. Komukai, and M. Nakazawa, "Dispersion tuning of a linearly shirped fiber Bragg grating without a center wavelength shift by applying a strain gradient," *IEEE Photonics Technology Letters*, vol. 10, no. 6, pp. 845–847, 1998.

[78] Y. Song, D. Starodubov, Z. Pan, Y. Xie, A. Willner, and J. Feinberg, "Tunable WDM dispersion compensation with fixed bandwidth and fixed passband center wavelength using a uniform FBG," *IEEE Photonics Technology Letters*, vol. 14, no. 8, pp. 1193–1195, 2002.

[79] J. Kwon, Y. Jeon, and B. Lee, "Tunable dispersion compensation with fixed center wavelength and bandwidth using a side-polished linearly chirped fiber Bragg grating," *Optical Fiber Technology*, vol. 11, no. 2, pp. 159–166, 2005.

[80] R. Trebino, K. DeLong, D. Fittinghoff, J. Sweetser, M. Krumbügel, B. Richman, and D. Kane, "Measuring ultrashort laser pulses in the time-frequency domain using frequency-resolved optical gating," *Review of Scientific Instruments*, vol. 68, no. 9, pp. 3277–3295, 1997.

[81] M. Sugiyama, M. Do, F. Futami, S. Watanabe, and H. Onaka, "A low drive voltage $LiNbO_3$ phase and intensity integrated modulator for optical frequency comb generation and short pulse generation," in *Proc. European Conference on Optical Communication (ECOC)*, vol. 2, 2004, pp. 198–199.

[82] K. R. Tamura, H. Kubota, and M. Nakazawa, "Fundamental of stable continuum generation at high repetition rates," *IEEE Journal of Quantum Electronics*, vol. 36, no. 7, pp. 773–779, 2000.

[83] M. Nakazawa, K. R. Tamura, H. Kubota, and E. Yoshida, "Coherence degradation in the process of supercontinuum generation in an optical fiber," *Optical Fiber Technology*, no. 4, pp. 215–223, 1998.

[84] K. R. Tamura and M. Nakazawa, "54-fs, 10-GHz soliton generation from a polarization-maintaining dispersion-flattened dispersion-decreasing fiber pulse compressor," *Optics Letters*, vol. 26, pp. 762–764, 2001.

[85] Y. Takushima, F. Futami, and K. Kikuchi, "Generation of over 140-nm-wide super-continuum from a normal dispersion fiber by using a mode-locked

semiconductor laser source," *IEEE Photonics Technology Letters*, vol. 10, no. 11, pp. 1560 – 2, 1998.

[86] N. Nishizawa and M. Yoshida, "Generation and characterization of widely broadened super continuum using highly nonlinear fibers and fiber laser," in *Proc. Optical Fiber Communications Conference (OFC)*, 2002, paper WR2.

[87] S. Watanabe and F. Futami, "All-optical signal processing using highly-nonlinear optical fibers," *IEICE Transactions on Electronics*, vol. E84-c, no. 5, pp. 553–563, 2001.

[88] D. Anderson, M. Desaix, M. Lisak, and M. Quiroga-Teixeiro, "Wave breaking in nonlinear-optical fibers," *Journal of the Optical Society of America B*, vol. 9, no. 8, pp. 1358–1361, 1992.

[89] V. I. Kruglov, A. C. Peacock, J. M. Dudley, and J. D. Harvey, "Self-similar propagation of high-power parabolic pulses in optical fiber amplifiers," *Optics Letters*, vol. 25, pp. 1753–1755, 2000.

[90] Y. Ozeki, K. Taira, K. Aiso, Y. Takushima, and K. Kikuchi, "Highly flat super-continuum generation from 2 ps pulses using 1km-long erbium-doped fibre amplifier," *Electronics Letters*, vol. 38, no. 25, pp. 1642 – 3, 2002.

[91] T. Hirooka and M. Nakazawa, "Parabolic pulse generation by use if a dispersion decreasing fiber with normal group-velocity dispersion," *Optics Letters*, vol. 29, no. 5, pp. 498–500, 2004.

[92] P. J. Almeida, P. Petropoulos, M. Ibsen, and D. J. Richardson, "Generation of ultra-flat SPM-broadened spectra in a highly nonlinear fiber using pulse pre-shaping in a fiber Bragg grating," in *Proc. Optical Fiber Communications Conference (OFC)*, vol. 1, 2005, pp. 259 – 61.

[93] K. Uchiyama, S. Kawanishi, and M. Saruwatari, "100-Gb/s multiple-channel output all-optical OTDM demultiplexing using multichannel four-wave mixing in a semiconductor optical amplifier," *IEEE Photonics Technology Letters*, vol. 10, no. 6, pp. 890–2, 1998.

[94] H. Sotobayashi, W. Chujo, and T. Ozeki, "Bi-directional photonic conversion between 4 × 10 Gbit/s OTDM and WDM by optical time-gating wavelength

interchange," in *Proc. Optical Fiber Communications Conference (OFC)*, 2001, paper WM5.

[95] I. Ogura, Y. Hashimoto, H. Kurita, T. Shimizu, and H. Yokoyama, "Picosecond all-optical gate using a saturable absorber in mode-locked laser diodes," *IEEE Photonics Technology Letters*, vol. 10, no. 4, pp. 603–605, 1998.

[96] R. Cubeddu, R. Polloni, C. A. Sacchi, and O. Svelto, "Self phase modulation and "Rocking" of molecules in trapped filaments of light with picosecond pulses," *Physical Review A*, vol. 2, no. 5, pp. 1955 –1963, 1970.

[97] A. V. Oppenheim and R. W. Schafer, "Homomorphic analysis of speech," *IEEE Transactions on Audio and Electroacoustics*, vol. 16, no. 2, pp. 221–226, 1968.

[98] K. Uchiyama and T. Morioka, "All-optical time-division demultiplexing experiment with simultaneous output of all constituent channels from 100 Gbit/s OTDM signal," *Electronics Letters*, vol. 37, no. 10, pp. 642–643, 2001.

[99] M. Nakazawa, T. Yamamoto, and K. R. Tamura, "1.28Tbit/s-70km OTDM transmission using third- and fourth-order simultaneous dispersion compensation with a phase modulator," *Electronics Letters*, vol. 36, no. 24, pp. 2027–2029, 2000.

[100] I. Shake, H. Takara, K. Uchiyama, I. Ogawa, T. Kitoh, T. Kitagawa, M. Okamoto, K. Magari, Y. Suzuki, and T. Morioka, "160 Gbit/s full optical time-division demultiplexing using FWM of SOA-array integrated on PLC," *Electronics Letters*, vol. 38, no. 1, pp. 37–38, 2002.

[101] C. Schubert, J. Berger, S. Diez, H. J. Ehrke, R. Ludwig, U. Feiste, C. Schmidt, H. G. Weber, G. Toptchiyski, S. Randel, and K. Petermann, "Comparison of interferometric all-optical switches for demultiplexing applications in high-speed OTDM systems," *Journal of Lightwave Technology*, vol. 20, no. 4, pp. 618–624, 2002.

[102] Y. Fukuchi, T. Sakamoto, K. Taira, and K. Kikuchi, "All-optical time-division demultiplexing of 160 Gbit/s signal using cascaded second-order nonlinear effect in quasi-phase matched $LiNbO_3$ waveguide device," *Electronics Letters*, vol. 39, no. 10, pp. 789 – 90, 2003.

[103] H.-F. Chou, Y.-J. Chiu, W. Wang, J. Bowers, and D. Blumenthal, "Compact 160-Gb/s demultiplexer using a single-stage electrically gated electroabsorption modulator," *IEEE Photonics Technology Letters*, vol. 15, no. 10, pp. 1458–1460, Oct. 2003.

[104] T. Simoyama, H. Yoshida, J. Kasai, T. Mozume, A. Gopal, and H. Ishikawa, "InGaAs-AlAs-AlAsSb coupled quantum well intersubband transition all-optical switch with low switching energy for OTDM systems," *IEEE Photonics Technology Letters*, vol. 15, no. 10, pp. 1363–1365, Oct. 2003.

[105] M. Duelk, S. Fischer, E. Gamper, W. Vogt, E. Gini, H. Melchior, W. Hunziker, M. Puleo, and R. Girardi, "Full 40 Gbit/s OTDM to WDM conversion: Simultaneous four channel 40:10 Gbit/s all-optical demultiplexing and wavelength conversion to individual wavelengths," in *Proc. Optical Fiber Communications Conference (OFC)*, 1999, paper PD17.

[106] J. Vasseur, M. Hanna, J. Dudley, and J.-P. Goedgebuer, "Alternate multiwavelength modelocked fiber laser," *IEEE Photonics Technology Letters*, vol. 16, no. 8, pp. 1816–1818, Aug. 2004.

[107] J. Vasseur, M. Hanna, J. Dudley, and J. Barry, "Numerical and theoretical analysis of an alternate multiwavelength mode-locked fiber laser," *IEEE Photonics Technology Letters*, vol. 17, no. 11, pp. 2295–2297, Nov. 2005.

[108] T. Morioka, S. Kawanishi, H. Takara, and M. Saruwatari, "Multiple-output, 100 Gbit/s all-optical demultiplexer based on multichannel four-wave mixing pumped by a linearly-chirped square pulse," *Electronics Letters*, vol. 30, no. 23, pp. 1959–60, 1994.

[109] L. Boivin, M. Wegmueller, M. C. Nuss, and W. H. Knox, "110 Channels 2.35 Gb/s from a Single Femtosecond Laser," *IEEE Photonics Technology Letters*, vol. 11, no. 4, pp. 466–468, 1999.

[110] Pritel, Inc. Naperville, Illinois, USA. (2003) Optical Clock Multiplier. [Online]. Available: http://www.pritel.biz/pdf/ocm.pdf

[111] J. Li, B.-E. Olsson, M. Karlsson, and P. Andrekson, "OTDM add-drop multiplexer based on XPM-induced wavelength shifting in highly nonlinear fiber," *Journal of Lightwave Technology*, vol. 23, no. 9, pp. 2654–2661, 2005.

[112] C. Schubert, C. Schmidt, S. Ferber, R. Ludwig, and H. Weber, "Error-free all-optical add-drop multiplexing at 160 Gbit/s," *Electronics Letters*, vol. 39, no. 14, pp. 1074 – 6, 2003.

[113] J. Turkiewicz, E. Tangdiongga, H. Rohde, W. Schairer, G. Lehmann, G. Khoe, and H. de Waardt, "Simultaneous high speed OTDM add-drop multiplexing using GT-UNI switch," *Electronics Letters*, vol. 39, no. 10, pp. 795 – 6, 2003.

[114] E. Tangdiongga, J. Turkiewicz, H. Rohde, W. Schairer, G. Lehmann, E. Sikora, Y. Zhou, A. Lord, D. Payne, G. Khoe, and H. de Waardt, "160 Gbit/s OTDM add-drop networking using 275 km installed fibres," *Electronics Letters*, vol. 40, no. 9, pp. 552 – 4, 2004.

[115] A. Poustie and K. Blow, "Demonstration of an all-optical Fredkin gate," *Optics Communications*, vol. 174, pp. 317 – 320, 2000.

[116] J. H. Lee, T. Tanemura, Y. Takushima, and K. Kikuchi, "All-optical 80-Gb/s add-drop multiplexer using fiber-based nonlinear optical loop mirror," *IEEE Photonics Technology Letters*, vol. 17, no. 4, pp. 840 – 2, 2005.

[117] E. Verdurmen, Y. Zhao, E. Tangdiongga, J. Turkiewicz, G. Khoe, and H. De Waardt, "Error-free all-optical add-drop multiplexing using HNLF in a NOLM at 160 Gbit/s," *Electronics Letters*, vol. 41, no. 6, pp. 349 – 350, 2005.

[118] L. Rau, S. Rangarajan, W. Wang, and D. Blumenthal, "All-optical add-drop of an OTDM channel using an ultra-fast fiber based wavelength converter," in *Proc. Optical Fiber Communications Conference (OFC)*, vol. 1, 2002, pp. 259 – 61.

[119] A. Buxens, H. N. Poulsen, A. T. Clausen, and P. Jeppesen, "All-optical OTDM-to-WDM signal-format translation and OTDM add-drop functionality using bidirectional four wave mixing in semiconductor optical amplifier," *Electronics Letters*, vol. 36, no. 2, pp. 156–158, 2000.

[120] S. Fischer, M. Dulk, E. Gamper, W. Vogt, W. Hunziker, E. Gini, H. Melchior, A. Buxens, H. Poulsen, and A. Clausen, "All-optical regenerative OTDM add-drop multiplexing at 40 Gb/s using monolithic InP Mach-Zehnder interferometer," *IEEE Photonics Technology Letters*, vol. 12, no. 3, pp. 335 – 7, 2000.

[121] H.-F. Chou, J. Bowers, and D. Blumenthal, "Compact 160-Gb/s add-drop multiplexer with a 40-Gb/s base rate using electroabsorption modulators," *IEEE Photonics Technology Letters*, vol. 16, no. 6, pp. 1564 – 6, 2004.

[122] K. Jepsen, H. Poulsen, A. Clausen, A. Buxens, and K. Stubkjaer, "Investigation of cascadability of add-drop multiplexers in OTDM systems," in *Proc. European Conference on Optical Communication (ECOC)*, vol. 1, 1998, pp. 619 – 20.

[123] I. Riant, "Fiber Bragg gratings for optical telecommunications," *Comptes Rendus Physique*, vol. 4, no. 1, pp. 41–49, 2003.

[124] P. Toliver, I. Glesk, R. J. Runser, K.-L. Deng, B. Y. Yu, and P. R. Prucnal, "Routing of 100 Gb/s words in a packet-switched optical networking demonstration (POND) node," *Journal of Lightwave Technology*, vol. 16, no. 12, pp. 2169–2180, 1998.

[125] S. Aleksic, "An ultra-fast photonic ring network employing Optical Packet Compression-Time Division Multiplexing (OPC-TDM) scheme," *Electrical Engineering*, vol. 83, pp. 223–229, 2001.

[126] H. Toda, F. Nakada, M. Suzuki, and A. Hasegawa, "An optical packet compressor based on a fiber delay loop," *IEEE Photonics Technology Letters*, vol. 12, no. 6, pp. 708–710, 2000.

[127] K. Lee, S. Lee, and J. Park, "New architecture of optical cell compressor and expander for WDM/TDM switching systems," in *Proc. Conference on Lasers and Electro-Optics (CLEO)*, 1999, paper FE3.

[128] S. Rangarajan, H. N. Poulsen, and D. J. Blumenthal, "All-optical packet compression of variable length packets from 40 to 1500-B using a gated fiber loop," *IEEE Photonics Technology Letters*, vol. 18, no. 2, pp. 322–324, 2006.

[129] K. Uchiyama, K. Nonaka, and H. Takara, "Subpicosecond timing control using optical double-pulses correlation measurement," *IEEE Photonics Technology Letters*, vol. 16, no. 2, pp. 626–628, 2004.

[130] H. Takenouchi, R. Takahashi, K. Takahata, T. Nakahara, and H. Suzuki, "40-Gb/s 32-bit optical packet compressor-decompressor based on an optoelectronic

memory," *IEEE Photonics Technology Letters*, vol. 16, no. 7, pp. 1751–1753, 2004.

[131] H. Sotobayashi, K. Kitayama, and T. Ozeki, "40 Gbit/s photonic packet compression and decompression by supercontinuum generation," *Electronics Letters*, vol. 37, no. 2, pp. 110–111, 2001.

[132] B. H. Kolner and M. Nazarathy, "Temporal imaging with a time lens," *Optics Letters*, vol. 14, no. 12, pp. 630–632, June 1989.

[133] B. H. Kolner, "Space-time duality and the theory of temporal imaging," *IEEE Journal of Quantum Electronics*, vol. 30, no. 8, pp. 1951–1963, 1994.

[134] C. Bennet and B. Kolner, "Upconversion time microscope demonstrating 103× magnification of femtosecond waveforms," *Optics Letters*, vol. 24, pp. 783–785, 1999.

[135] T. Kogure, J. H. Lee, and D. J. Richardson, "Wavelength and duration tunable 10 GHz 1.3ps pulse source using dispersion decreasing fiber based distributed Raman amplification," *IEEE Photonics Technology Letters*, vol. 16, pp. 1167–1169, 2004.

[136] M. A. F. Roelens, M. Forzati, A. Djupsjobacka, P. Petropoulos, A. Berntson, and D. J. Richardson, "High quality pulse and device characterisation using EAM-based frequency resolved optical gating," in *Proc. European Conference on Optical Communication (ECOC)*, no. 3, 2005, pp. 397–398.

[137] M. Pfennigbauer, M. Pauer, P. J.Winzer, and M. M. Strasser, "Performance optimization of optically preamplified receivers for Return-to-zero and Non Return-to-zero coding," *International Journal of Electronics and Communications*, vol. 56, no. 4, pp. 261–267, 2002.

[138] D.-S. Seo, D. Y. Kim, and H.-F. Liu, "Timing jitter reduction of gain-switched DFB laser by external injection-seeding," *Electronics Letters*, vol. 32, no. 1, pp. 44–45, 1996.

[139] Y. Ozeki, Y. Takushima, K. Aiso, K. Taira, and K. Kikuchi, "Generation of 10 GHz similariton pulse trains from 1.2 km-long erbium-doped fibre amplifier

for application to multi-wavelength pulse sources," *Electronics Letters*, vol. 40, no. 18, pp. 1103 – 4, 2004.

[140] F. Parmigiani, C. Finot, K. Mukasa, M. Ibsen, M. Roelens, P. Petropoulos, and D. J. Richardson, "Ultra-flat SPM-broadened spectra in a highly nonlinear fiber using parabolic pulses formed in a fiber Bragg grating," *Optics Express*, vol. 14, pp. 7617–7622, 2006.

[141] C. H. Kwok, S. H. Lee, K. K. Chow, C. Shu, C. Lin, and A. Bjarklev, "Widely tunable wavelength conversion with extinction ratio enhancement using PCF-based NOLM," *IEEE Photonics Technology Letters*, vol. 17, pp. 2655–2657, 2005.

[142] K. Gallo, J. Prawiharjo, F. Parmigiani, P. Almeida, P. Petropoulos, and D. Richardson, "Processing ultrafast optical signals in broadband telecom systems by means of cascaded quadratic nonlinearities," in *the 8th International Conference on Transparent Optical Networks*, 2006, invited.

[143] G. Stegeman, D. Hagan, and L. Torner, "$\chi^{(2)}$ cascading phenomena and their applications to all-optical signal processing, mode-locking, pulse compression and solitons," *Optical and Quantum Electronics*, vol. 28, no. 12, pp. 1691–1740, 1993.

[144] Y. Fukuchi and K. Kikuchi, "Novel design method for all-optical ultrafast gate switches using cascaded second-order nonlinear effect in quasi-phase matched $LiNbO_3$ devices," *IEEE Photonics Technology Letters*, vol. 14, no. 10, pp. 1409 – 11, 2002.

[145] K. Onohara, H. Sotobayashi, K. Kitayama, and W. Chujo, "Photonic time-slot and wavelength-grid interchange for 10-Gb/s packet switching," *IEEE Photonics Technology Letters*, vol. 13, no. 10, pp. 1121–1123, Oct. 2001.

[146] K. Takiguchi, M. Itoh, and T. Shibata, "Optical-signal-processing device based on waveguide-type variable delay lines and optical gates," *Journal of Lightwave Technology*, vol. 24, no. 7, pp. 2593–2601, July 2006.

[147] L. Mandel, "Interpretation of instantaneous frequencies," *American Journal of Physics*, vol. 42, no. 10, pp. 840–846, 1974.

[148] R. Bracewell, *The Fourier Transform and Its Applications*, S. Rao and D. Damstra, Eds. McGraw-Hill, 1986.

[149] F. W. J. Olver, *Asymptotics and Special Functions*. London: Academic Press, 1974.

[150] T. Jannson, "Real-time Fourier transformation in dispersive optical fibers," *Optics Letters*, vol. 8, no. 4, pp. 232–234, 1983.

List of Publications

P. J. Almeida, P. Petropoulos, F. Parmigiani, M. Ibsen, and D. J. Richardson, OTDM Add-Drop Multiplexer Based on Time-Frequency Signal Processing, Journal of Lightwave Technology **24**, 2720–2732 (2006), invited.

J. Prawiharjo, K.Gallo, B.C.Thomsen, M.A.F.Roelens, **P.J.Almeida**, N.G.R.Broderick, and D. Richardson, Frequency resolved optical gating in a quasi-phase-matched $LiNbO_3$ waveguide, IEEE Photonics Technology Letters **17**, 849–851 (2005).

P. J. Almeida, P. Petropoulos, B. Thomsen, M. Ibsen, and D. Richardson, All-optical packet compression based on time to wavelength conversion, IEEE Photonics Technology Letters **16**, 1688 – 90 (2004).

P.J. Almeida, F. Parmigiani, M. Ibsen, K. Mukasa, P. Petropoulos, and D. J. Richardson, 35 dB Channel Suppression in OTDM Add-Drop Multiplexing Based on Time-Frequency Signal Processing, in *Proc. Optical Fiber Communications Conference (OFC)* (2006).

K. Gallo, J. Prawiharjo, F. Parmigiani, **P. Almeida**, P. Petropoulos, and D. Richardson, Processing ultrafast optical signals in broadband telecom systems by means of cascaded quadratic nonlinearities, in *the 8th International Conference on Transparent Optical Networks* (2006), invited.

D. Richardson, J. Leong, F. Parmigiani, **P. J. Almeida**, M. Ibsen, and P. Petropoulos, Recent developments in fibre technology and its application within high speed optical communications, in *the 3rd International Symposium on System Construction of Global Network Oriented Information Electronics (IGNOIE-COE05)* (2006), invited.

P. J. Almeida, P. Petropoulos, M. Ibsen, and D. J. Richardson, Generation of ultra-flat SPM-broadened spectra in a highly nonlinear fiber using pulse pre-shaping in a fiber Bragg grating, in *Proc. Optical Fiber Communications Conference (OFC)* **1**, 259 – 61 (2005).

F. Parmigiani, P.Petropoulos, **P.J.Almeida**, M.Ibsen, and D.J.Richardson, Amplitude and timing jitter reduction using a fiber NOLM incorporating a fiber Bragg grating based pulse shaper, in *Proc. Optical Fiber Communications Conference (OFC)* (2005).

J. Prawiharjo, K.Gallo, B.C.Thomsen, M.A.F.Roelens, **P.J.Almeida**, N.G.R.Broderick, and D. Richardson, Blind-FROG in a quasi-phase-matched $LiNbO_3$ waveguide, in *Proc. Optical Fiber Communications Conference (OFC)* (2005).

P. J. Almeida, P. Petropoulos, M. Ibsen, M. Mokhtar, B. Thomsen, and D. Richardson, All-optical TDM add-drop multiplexer based on time to wavelength conversion, in *Proc. European Conference on Optical Communication (ECOC)* **3**, 438–9 (2004).

P.J. Almeida, P.Petropoulos, M.Ibsen, and D.J.Richardson, High-speed optical signal processing systems based on the switching of broadband frequency-chirped pulses, in *IoP Meeting on Nonlinear Optics in Communications* (2004).

P. J. Almeida, J. Lee, M. Ibsen, P. Petropoulos, B. Thomsen, P. Teh, F. Parmigiani, and D. Richardson, All-optical TDM data demultiplexing based on a highly nonlinear fiber Kerr gate using a linearly chirped rectangular control, in *Proc. CLEO/QELS* (2003).

R. Llorente, J.H.Lee, **P.J.Almeida**, M.Ibsen, D.J.Richardson, J.Marti, and F.Ramos, Novel orthogonal wavelength division multiplexing (OWDM) scheme: Theory and experiment, in *Proc. LEOS annual meeting* (2003).

F. Parmigiani, P.Petropoulos, **P.Almeida**, M.Ibsen, J.H.Lee, and D.J.Richardson, A direct assessment of the performance of pulse shaping superstructured fiber gratings using an optical sampling oscilloscope, in *Proc. Optical Fiber Communications Conference (OFC)* (2003).